Title

Developing Genetically Encoded Optical Tools for Imaging Brain Circuits and Pharmacology

Author

Dong, Chunyang

Publication Date

2023

Peer reviewed|Thesis/dissertation

Developing Genetically Encoded Optical Tools for Imaging Brain Circuits and Pharmacology

By

CHUNYANG DONG

DISSERTATION

Submitted in partial satisfaction of the requirements for the degree of

DOCTOR OF PHILOSOPHY

in

Biochemistry, Molecular, Cellular and Developmental Biology

in the

OFFICE OF GRADUATE STUDIES

of the

UNIVERSITY OF CALIFORNIA

DAVIS

Approved:

_____

Dr. Lin Tian, Chair

_____

Dr. Brian C. Trainor

_____

Dr. Vladimir Yarov-Yarovoy

_____

Dr. Jennifer L. Whistler

Committee in Charge

2023

Dedication and Acknowledgements

I dedicate this thesis to my wife, Zihan Jia (Regina), and our children, Lucas and Lewis, as well as our supportive families who have helped us achieve our career goals peacefully in a distant country. Their unwavering support and love throughout my graduate career made this journey more purposeful and fulfilling.

I would also like to express my gratitude to my mentor, Dr. Lin Tian, who is like a second family member to me. Her pioneering vision and tailored guidance have played a pivotal role in the successful completion of this thesis and my growth as an independent scientist.

I would like to extend my sincere gratitude to my collaborators, in the order of my dissertation chapters, Dr. Yulong Li, Dr. David E. Olson, Dr. William C. Wetsel, Dr. Won Chan Oh, Dr. John A. Gray, Dr. Jonathan S Marvin, Dr. Luke D Lavis, Dr. Henry A Lester, Dr. Thomas L Kash, Dr. Vladimir Yarov-Yarovoy, Dr. Viviana Gradinaru, Dr. Loren L Looger, Dr. Jennifer L. Whistler, Dr. Bo Li, Dr. Lakshmi A Devi, Dr. Hugo A Tejeda, Dr. Michael R. Bruchas, and Dr. Matthew R. Banghart. I appreciate your lab's contributions to the projects and all the groundbreaking discoveries we have published together, and I have learned so much from your various disciplines during my Ph.D. training. Your guidance has been invaluable in helping me become a well-rounded candidate for my next career stage. Thank you all for your support throughout my dissertation journey.

Without the aid of my dissertation committee members, Dr. Brian C. Trainor, Dr. Vladimir Yarov-Yarovoy, and Dr. Jennifer L. Whistler, I would not have made it this far. Their assistance, feedback, and suggestions throughout the dissertation process have

been invaluable. Their guidance helped me refine my research and provided the necessary support to complete this work. Thank you for your strong and steady commitment and support.

Finally, I want to express my heartfelt gratitude to the lab members of the Tian Lab, who have supported me throughout this academic journey. When I joined the lab as a second-year undergraduate, I had the privilege of working alongside Dr. Gerard Joey Broussard, Dr. Elizabeth K Unger, Dr. Tommaso Patriarchi, Dr. Ruqiang Liang, Dr. Grace Or Mizuno, Stelios Papadopoulos, Shelby Wong, Carolyn Davis, David Jaffe, Leon Palao III, and Karan Mahe. They provided me with the knowledge, skills, and support during the first era of the lab, which laid a strong foundation for my later research projects. During the second lab era, which saw the addition of new scientists, postdocs, graduate students, and undergraduates, including Dr. Alessio Andreoni, Dr. Junqing Sun, Dr. Emily Wright, Dr. Akash Pal, Dr. Julie Chouinard, Dr. Kwun Nok Mimi Man, Dr. Rochelin Dalangin, Adriana Hernandez, Azariah Coblentz, Cameron Larson, Erin Scott, Jacob Roshgadol, Kiran Long-Iyer, Nikki Tjahjono, Yihan Jin, Yiwei Hua, Sherin Lajevardi, Ziwei Qiu, Margo Le, Peter Freitas, Sally Ho, Lily Trouchon, and my undergraduate trainee Darren Kirin Lo, who contributed their expertise and created a lively, knowledgeable and supportive lab environment. Thank you all for helping me accomplish my graduate school training and for being an integral part of my journey.

Abstract

Preface:

Within the context of the broader biological / life sciences field, my thesis work focused on the interdisciplinary area of neuroscience. By integrating biochemistry, synthetic biology, and pharmacology, I developed an innovative molecular toolkit that enables non-invasive, real-time monitoring of various neuromodulator activities with high specificity and spatiotemporal resolution through optical imaging in the brain of behaving animals. With focuses on both biogenic amines and neuropeptides, the described molecular tools offer sub-cellular targetability and sub-second precision readouts, leading to new insights into physiological and pathological processes of neuromodulation, novel therapies and diagnostics of daily life, and potentially leading to mapping brain computations. Most technologies and results described in the thesis have been patented and published in high-impact peer-reviewed journals, such as *Cell* and *Science*, with one manuscript submitted to *Nature Neuroscience*, and one preliminary study.

Main Dissertation Abstract:

The brain is an intricate organ that controls various functions, such as perception, behavior, mood, and cognition, through interactions between neurons, astrocytes with neurotransmitters (NT), and neuromodulators (NM). The recent advancements in fluorescence imaging and genetic engineering have allowed researchers to study neural

activity, neurochemicals, and drug-specific receptor conformations at a cellular and subcellular level.

Imaging neuronal spikes is crucial in the study of neural circuits and behavior. Neuronal spikes, or action potentials, are brief electrical signals traveling along nerve fibers and are the primary means neurons communicate. Researchers can directly visualize and quantify these electrical signals in living animals with high spatiotemporal resolution using genetically encoded calcium indicators (GECIs) and genetically encoded voltage indicators (GEVIs). This ability to image neuronal spikes in real-time in behaving animals offers new possibilities for dissecting neural circuits and understanding the mechanisms behind behavior across different species. In the past ten years, GECIs and GEVIs have revolutionized systems neuroscience by allowing for the mesoscopic recording of intracellular calcium as a proxy for electrical activity and directly reporting spiking patterns and subthreshold voltage activity.

Calcium and voltage imaging are valuable tools for monitoring neurons' calcium and electrical activity, but they have limitations when studying neuromodulation. Neuromodulation involves controlling neural activity through signaling molecules like hormones, NT, NM, and growth factors. This is a crucial aspect of brain function, enabling communication between neurons and coordination of brain regions. Neuromodulation fine-tunes neural circuits and influences brain functions like learning, memory, perception, and behavior. For instance, dopamine in the striatum controls reinforcement learning and habit formation, while serotonin affects mood, anxiety, and sleep. Neuromodulation also plays a crucial role in treating neurological and psychiatric

disorders, with drugs altering NT levels or neuromodulatory patterns, such as antidepressants targeting the serotonin system and antipsychotics targeting the dopamine system. However, the release of NM may not be directly coupled to neuronal activation because NM is often released from non-synaptic locations, can have diffuse effects on multiple neurons, and can be released in response to non-neuronal signals.

Many groups have pioneered the effort and developed technologies for measuring the bulk release of NM, including micro-dialysis, opto-dialysis, amperometry, and mass spectrometry. However, the traditional methods either need direct measurements of specific NM or need to be higher in spatiotemporal resolution. Therefore, to better dissect the complex dynamics of neuromodulation, it is necessary to invent new technologies for monitoring NM release with sub-cellular and sub-second spatiotemporal resolution in real-time.

My graduate thesis focused on engineering genetically encoded neurochemical indicators (GENIs) and using optical imaging to study NM release. By genetically encoding the indicators, we can achieve specific cell-type targeting of the indicators and pinpoint the release pattern of specific NM in a highly specific manner, providing sub-second temporal- and sub-cellular spatial- resolution. This enables researchers to accurately measure the real-time release of NM, including their precise location and release dynamics in behaving animals. Overall, using GENIs and optical imaging to study NM release has greatly advanced our understanding of the complex processes involved in synaptic communication and has opened new avenues for exploring the mechanisms underlying neural and physiological diseases.

In the opening chapter, I delve into the current collection of GENIs, recent advances in NM dynamic studies, and the impact of drugs and environmental stimuli on neuromodulation via fluorescence imaging with GENIs developed by our lab and others. I present the methodology of engineering GENIs that allow real-time tracking of various neural activities and specific receptor conformations affected by drugs. I also use mathematical modeling to explore the engineering and optimization methods for these indicators. Further, the GENI engineering methods can be utilized for other neurochemicals we haven't explored and provide a comprehensive toolkit for studying neural activity and drug effects in living organisms. The text of this chapter is modified from my first-author manuscript published in the *Annual Review of Neuroscience* in 2022.

Despite the essential biological functions that serotonin regulates, as aforementioned, imbalances in the serotonin system have been linked to several psychiatric and neurological disorders, such as depression, anxiety, and obsessive-compulsive disorder. Thus, understanding the underlying mechanisms of serotonin signaling is crucial for developing new treatments for these conditions. In chapters two and three of this dissertation, I expand into engineering two types of GENIs for the NM, serotonin.

To understand the pharmacological mechanisms of drugs on the serotonin system, in chapter two, I present the creation and validation of a GENI, psychLight, based on the 5-HT2A G-protein coupled receptor (GPCR) and circularly permuted green fluorescent protein. After extensive screening and optimization with molecular cloning and live-cell imaging techniques, psychLight was generated. It allows for detecting changes in

serotonin signaling in behaving rodents under aversive stimuli. Additionally, I use psychLight to study the mechanism of action of designer drugs on receptors. By evaluating the biased receptor conformations upon ligand binding, I investigate how to eliminate the side-effect of psychedelic-based antidepressants, i.e., hallucination. I use genetic and viral approaches to develop a cell-based drug screening platform using psychLight (patented), resulting in the synthesis and discovery of novel compounds with both short-term and long-term antidepressant potential but without the hallucination side-effect. Finally, I demonstrate the use of psychLight and other genetic tools to show that psychedelics promote plasticity through intracellular 5-HT2A receptors, and serotonin may not be the natural ligand for those intracellular receptors. This highlights the importance of considering the cellular location of 5-HT2ARs in determining their signaling properties and suggests that intracellular 5-HT2ARs may be a valuable therapeutic target.

In summary, psychLight provides high-spatiotemporal resolution and real-time monitoring of endogenous serotonin in response to behavioral stimuli. The application of psychLight combined with other methods shed light on the mechanisms behind the therapeutic effects of psychedelics and the role of serotonin in promoting brain plasticity. Furthermore, the psychLight drug screening platform demonstrates the potential for conformational indicators in discovering novel treatments for neuropsychiatric and neurodegenerative diseases with fewer side effects. The text of this chapter is modified from my first-author manuscript published in *Cell* in 2021 and my contributions to the manuscript published in *Science* in 2023.

Chapter three presents an innovative method for creating a high-dynamic range serotonin indicator, iSeroSnFR, for better understanding serotonin's role in the brain with a high signal-to-noise ratio (SNR). I use machine learning algorithms to modify an acetylcholine-binding protein, resulting in its ability to bind serotonin selectively. I validated the iSeroSnFR's serotonin selectivity with screenings in mammalian cells and neuronal cultures. Together with others, we use iSeroSnFR to reveal serotonin dynamics during sleep-wakefulness cycles. The text of this chapter is modified from my contributions to the manuscript published in *Cell* in 2020.

In chapter four, I discuss the creation of GENIs to detect neuropeptides (NP), another class of NM. NP has been linked to various brain dysfunctions, including addiction, cognitive disorders, and stress. However, the study of NP signaling is minimal due to the nature of the degradation of peptides over time. Traditional methods that need to extract NP out of the brain for analysis cannot provide detailed enough information on NP signaling. Thus, a direct measurement at the site of release/reception is the key. Of the numerous NP discovered, opioids are clinically the most significant, as they are the primary target of effective pain-relieving treatments. However, these treatments also lead to issues of abuse and overdose. To create a treatment without such adverse side effects, a better understanding of opioid signaling and opioid receptor actions on drugs is necessary.

To fill this knowledge gap, I engineered a set of GENIs based on three opioid receptors to detect endogenous opioids with sub-second temporal precision at the releasing site in real-time. I thoroughly evaluated the binding kinetics of analgesics by

comparing drug screening on the indicators and traditional radio-ligand binding assay on the receptors. By incorporating these indicators with optogenetics, a technology that allows using light to activate specific neuronal projections in the brain, I observed light-induced opioid release on opioid-releasing neurons in behaving animals. Further, I observed different opioid-releasing patterns in the sub-brain regions in rewarding and aversive behaviors with optical imaging. The opioid GENI toolkit is a valuable resource that facilitates new insights into opioid signaling and drug mechanisms that were previously inaccessible. The manuscript of this chapter is finalizing for publication.

Chapter five of the thesis focuses on the future outlook, discussion, and conclusion. I begin the chapter with preliminary data on the optimization of the next generation of gastrin-releasing peptide (GRP), a critical neuropeptide for regulating fear extinction. In this section, I present an ongoing project that aims to optimize the sensitivity from a previous generation GRP sensor, grpLight1.0. Given that we have published the grpLight1.0 in 2021 and used this sensor to reveal that bombesin-like peptide plays a crucial role in enhancing fear memory by recruiting disinhibitory cortical circuits. However, grpLight1.0 is not sensitive enough to detect functionally relevant GRP levels in vivo. The first section of the chapter provides results for the sensitivity optimization of grpLight1.0 with characterizations in vitro and preliminary data for monitoring GRP release in vivo during fear conditioning. This optimized sensor variant, grpLight2.0, will be followed by more detailed ex vivo and in vivo characterizations for further dissecting GRP's role in the brain. In the later sections, I discuss the limitations of GENIs in the field

of neuroscience and present a mathematical model for potential GENI optimization directions. Finally, I summarize my thesis projects and provide a future outlook.

Together, this thesis presents the methodology and applications of GENIs to study the dynamics of selected NM signaling and drug-receptor interaction in the brain. It provided valuable insights into the role of NM in shaping circuit function, both in healthy and diseased conditions. It highlights the need for better indicators of existing and other NM for a broader understanding of brain computation. Optimizing indicators for better SNR and expanding the toolkit for multiplex imaging with indicators on different spectrums is encouraged to perform multi-NM readouts simultaneously. Methods including machine learning and fluorescence-activating cell sorting are also suggested to enhance the indicator optimization process in the future. This thesis presents the significance of GENIs in neuroscience research and their possibilities in furthering our understanding of neural circuits in complex behaviors and pharmacology with precision.

TABLE OF CONTENTS

Chapter 1 – Introduction - from neuronal spikes to neuromodulators

Fluorescence Imaging of Neural Activity, Neurochemical Dynamics, and Drug-Specific Receptor Conformation with Genetically Encoded Sensors

Preface

The text of this chapter is a modified version of a manuscript that was submitted to the Annual Review of Neuroscience on September 10, 2021, and accepted for publication on March 22, 2022 (doi.org/10.1146/annurev-neuro-110520-031137). The layout has been adjusted in accordance with the requirements of a doctoral thesis. The authors on the original manuscript are listed as Chunyang Dong†, Yu Zheng†, Kiran Long-Iyer, Emily C. Wright, Yulong Li, and Lin Tian.

(† authors contributed equally to this work)

Abstract

To study neural circuitry, the action of one cell within a network of others, one would precisely measure and perturb specific neuronal populations and molecules, which are engaged in performing the computation or function of interest in behaving animals. The discovery and heterogeneous expression of green fluorescent protein (GFP) promoted the development of a vast array of genetically encoded sensors that have been created to monitor neurotransmission, synaptic spillover, excitable membrane potential, calcium dynamics, vesicle trafficking, receptor mobilization, and other biochemical events. For example, the development of genetically encoded calcium indicators (GECIs) such as GCaMP and its color variant jRGECO, combined with advanced imaging modalities, has revolutionized systems neuroscience (Chen et al. 2013, Dana et al. 2016, Tian et al. 2009) by permitting mesoscopic recording of intracellular calcium as a proxy for electrical activity (Grienberger & Konnerth 2012). Genetically encoded or hybrid voltage indicators (GEVIs) have also been engineered and significantly improved to directly report spiking patterns and subthreshold voltage activity. In addition, genetically encoded sensors for specific neurochemicals (GENIs) report release dynamics with high spatiotemporal resolutions and molecular specificity. Collectively, the application of these sensors provides new opportunities for in vivo dissection of neural circuits underlying behavior across various species. This chapter outlines a workflow for sensor development and discusses a broad range of applications of GENIs in neuroscience and pharmacology.

Imaging Neuronal Activity in Genetically Defined Populations

The GECIs can be categorized into two types based on Förster resonance energy transfer (FRET) between two fluorescent proteins (FPs) or intensity changes of single FPs (Figure 1.1a). Miyawaki et al. (1997) engineered the very first FRET-based calcium sensor, Cameleon, composed of a calcium-sensitive calmodulin (CaM) and a CaM-binding peptide, M13, sandwiched by two GFP variants (BFP-GFP or CFP-YFP). Calcium binding induces CaM-M13 interaction to increase the FRET efficiency, reflected by changes in the dual emission of donor and acceptor. Further improvements on such FRET-based sensors include chromophore orientation tuning with Venus variants to improve the response dynamic range (Nagai et al. 2004) and CaM-M13 replacement with troponin C (TnC) or structure-guided redesign of the CaM-M13 interface to minimize cellular perturbation (Mank et al. 2008, Palmer et al. 2006). The ratiometric measurement of such FRET sensors confers correction of motion and blood flow artifacts and allows quantification of intracellular calcium concentration. However, FRET sensors often show less sensitivity compared with single FP–based calcium sensors.

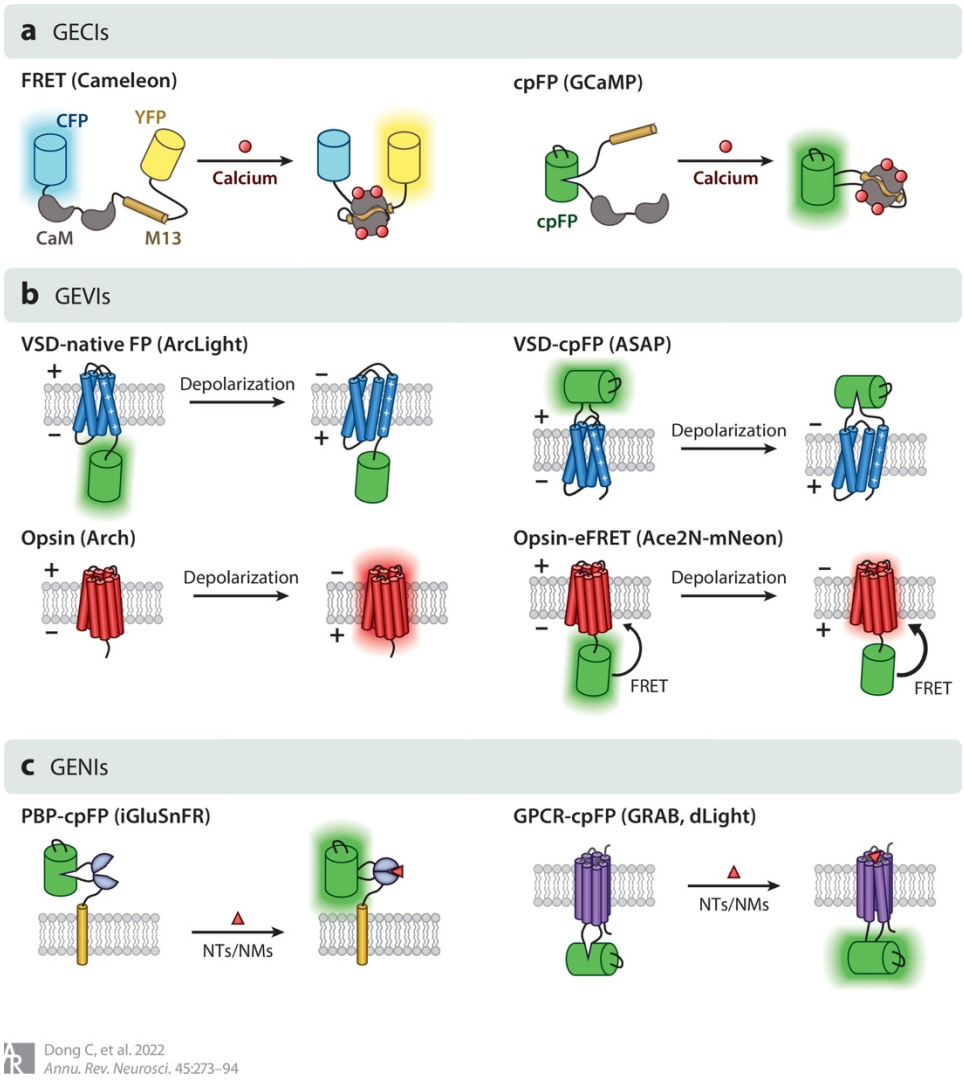

Figure 1.1: Schematic representation of genetically encoded indicators for calcium (GECIs), voltage (GEVIs), and neurochemicals (GENIs).
(a) GECIs are based on Förster resonance energy transfer (FRET) and circularly permuted fluorescent protein (cpFP). The FRET-based calcium sensor is developed by inserting the calmodulin (CaM)-M13 in between donor and acceptor fluorophores such as CFP-YFP or BFP-GFP (e.g., Cameleon). The cpFP-based sensor is intensiometric, in which a cpFP is inserted in between CaM and M13/RS20 (e.g., GCaMP).
(b) GEVIs utilize the voltage-sensitive domain (VSD) or opsin as scaffold. VSD-based sensors are developed by attaching a native fluorescent protein (FP) to the C terminus of VSD (e.g., ArcLight) or inserting a cpFP into the extracellular S3–S4 loop of the VSD (e.g., ASAP series). The light-driven proton pumps (opsin) are functionally reversed to action as a voltage-sensitive optical element (e.g., Arch). A bright FP is attached to the opsin to address the dimness of opsin-based GEVIs via electrochromic FRET (eFRET), as shown in Ace2N-mNeon. The FP is replaced with HaloTag–Janelia Fluor dyes to develop a hybrid voltage sensor, namely Voltron.
(c) Two classes of ligand-binding scaffolds, periplasmic binding proteins (PBPs) and G protein–coupled receptors (GPCRs), are used to develop GENIs. In both cases, a cpFP is inserted into the hinge region of PBPs (e.g., iGluSnFR) or intracellular loop 3 of GPCRs (e.g., GRAB, dLight). Abbreviations: NM, neuromodulator; NT, neurotransmitter. Sources for sensors named in the figure are as follows: Cameleon (Miyawaki et al. 1997), GCaMP (Nagai et al. 2001), ArcLight (Jin et al. 2012), ASAP series (St-Pierre et al. 2014, Villette et al. 2019, Yang et al. 2016), Arch (Kralj et al. 2011), Ace2N-mNeon (Gong et al. 2015), Voltron

(Abdelfattah et al. 2019), iGluSnFR (Marvin et al. 2013), GRAB (Sun et al. 2018), and dLight (Patriarchi et al. 2018).

The emergence of single FP–based calcium sensors originates from the creation of circularly permuted fluorescent protein (cpFP) (Baird et al. 1999). The environment-sensitive cpFP can be modulated by the calcium binding–induced conformational changes of CaM-M13/RS20. Early versions of the cpFP-based calcium sensors include Pericam and GCaMP, both using the CaM and M13, with a circularly permuted yellow fluorescent protein or circularly permuted green fluorescent protein (cpGFP) inserted (Nagai et al. 2001, Nakai et al. 2001). Iterative protein evolution has greatly improved the sensors' sensitivity and pushed them into practical use in vivo. In particular, GCaMP6, a big breakthrough in this field, has been widely used in the neuroscience community for neural activity imaging due to its superior signal-to-noise ratio (SNR) when probing calcium in individual neurons as well as in ensembles in vivo (Chen et al. 2013). Further optimization of GCaMP6 has led to jGCaMP7 and jGCaMP8 series. The jGCaMP7 shows further improved sensitivity and bright basal fluorescence, allowing high-quality calcium imaging in spines and somas (Dana et al. 2019). The latest jGCaMP8 was engineered by swapping the M13 peptide with an endothelial nitric oxide synthase peptide (Zhang et al. 2021). The rational design confers faster kinetics to the sensor, which benefits the tracking of action potentials. A similar strategy was also applied in developing the XCaMP series, in which the M13 was replaced by a ckkap peptide from the neuronal protein CaMKK, which is shown to respond to calcium linearly (Inoue et al. 2019).

Subcellularly targeted GECIs have also been developed to improve the SNR of calcium imaging. Axon-GCaMP6 is a specialized GECI that enriches axonal structures by

fusing growth-associated protein-43 (GAP43) (El-Husseini et al. 2001) at the N terminus of GCaMP6m. Axon-GCaMP enabled the in vivo recording of orientation and direction tuning of axons projecting from L4 V1 neurons across cortical layers without somatodendritic calcium signal contamination (Broussard et al. 2018). The expression of GECIs can also be restricted to neuronal soma to reduce overlapping fluorescence from surrounding neuropil to substantially improve the SNR and specificity of imaging (Chen et al. 2020).

In addition, red-shifted, far-red, and near-infrared (NIR) GECIs have been developed to enable multiplex imaging and to potentially enhance imaging depth, allowing researchers to explore previously unreachable brain regions. R-GECO1 and RCaMP1 were the first red-shifted GECIs designed by replacing cpGFP in GCaMPs with cpmApple and cpmRuby, respectively (Akerboom et al. 2013, Zhao et al. 2011). Further optimization has generated the broadly used jRGECO1a, jRCaMP1a, and jRCaMP1b (Dana et al. 2016). The jRGECO1a is more sensitive but suffers from blue light–induced photoactivation and lysosomal accumulation. A new variant called KGECO1, based on cpFusionRed, was engineered to tackle this issue, while retaining high response (Shen et al. 2018). The color spectrum was further shifted to far red in FR-GECO using the monomeric far-red FP mKelly2 to enable sensitive detection of single action potentials in neurons (Dalangin et al. 2020).

Recent breakthroughs in protein engineering efforts have also led to the development of non-GFP-based NIR GECIs (Shcherbakova et al. 2015). Taking advantage of biliverdin-binding NIR FPs, the first NIR GECI, NIR-GECO1, was designed by

inserting the CaM-RS20 module into the split NIR mIFP (Qian et al. 2019, 2020). A brighter, FRET-based NIR GECI, named iGECI, utilized two bright NIR FPs, miRFP670 and miRFP720, flanking the CaM-RS20 for FRET (Shemetov et al. 2021). Further optimization in the brightness and photostability of these sensors would significantly improve the SNR for in vivo imaging.

GEVIs, based on the voltage-sensing domain of voltage-sensitive phosphatases or light-driven proton pumps (opsin), have been developed to directly resolve firing patterns and coding properties of targeted neurons such as rapid sequential firing, hyperpolarizing, and subthreshold depolarizing (Knopfel & Song 2019). These GEVIs are engineered to measure membrane potential (Vm) changes (Figure 1.1b). Though voltage imaging remains challenging compared to calcium imaging, recent rigorous sensor engineering efforts have enabled spiking imaging in genetically defined neuronal populations in behaving animals.

The development and applications of GEVIs have been reviewed extensively and in great depth elsewhere (Pal & Tian 2020, Panzera & Hoppa 2019, Wang et al. 2019). The current GEVIs are still far from optimal. Inadequate sensitivity, along with the requirement of kilohertz acquisition and very limited imaging duration, has limited their utilization to a few laboratories. We expect a practically useful GEVI, in conjunction with GECIs, to provide more precise dissection of information processing in the brain. Nevertheless, GECIs and GEVIs have paved the way for genetically encoded indicators, providing the foundation for the engineering and application of other sensors, including the neurochemical sensors reviewed below.

Imaging Beyond Spikes with Neurotransmitter and Neuromodulator Sensors

Neurotransmitters (NTs) and neuromodulators (NMs) are essential signaling molecules for information processing in the brain. There are more than 100 known NT and NM molecules (Kovacs 2004), classified as amino acids, monoamines, neuropeptides, purines, and lipids based on their structures. Fast-acting NTs, namely glutamate and gamma-aminobutyric acid (GABA), act through ligand-gated ion channels and G protein–coupled receptors (GPCRs) to modulate firing rate and excitability of postsynaptic cells. In contrast to fast-acting NTs, NMs almost exclusively bind to GPCRs to initiate molecular signaling cascades that modulate synaptic strength, neuronal excitability, and circuit dynamics on timescales of subseconds to hours (Guillaumin & Burdakov 2021, Nadim & Bucher 2014). Altered NT and NM release is central to the pathogenesis of neurological and psychiatric disorders. Although the anatomical characterizations of NT and NM projections and their functional significance are understood at a moderate level, many outstanding questions remain regarding the structural and molecular basis and key computations underlying their release. There is a pressing need to increase experimental capacity to precisely measure the dynamics of these molecules with subsecond and single-cell resolution, high molecular specificity, and cell type specificity, ideally, across the full course of a behavioral paradigm.

Inspired by the design of GECIs, we and others have developed a tool kit of genetically encoded single FP–based indicators to probe various NT and NM systems (Figure 1.1c). To date, two main categories of single FP sensors have been developed,

classified by their ligand-binding scaffolds: bacterial periplasmic binding proteins (PBPs) and GPCRs.

PBP scaffolds are attractive for sensor engineering due to the conserved and large conformational change of PBP upon ligand binding. These proteins usually consist of two domains linked by a hinge region; this structure is conserved across other PBPs (Quiocho & Ledvina 1996). The ligand binding site is located in between the two domains, and the protein typically adopts two distinct conformations: a ligand-free (Apo) and a ligand-bound (Sat) state. These two conformations can interconvert via the hinge region upon ligand binding and releasing. By connecting these PBPs with a cpFP, we can achieve more versatile and intensiometric measurements of the ligand transients in real time. Using this design platform, highly sensitive sensors have been developed for glutamate [iGluSnFR (Helassa et al. 2018; Marvin et al. 2013, 2018)]; acetylcholine [iAChSnFR (Borden et al. 2020)]; GABA [iGABASnFR (Marvin et al. 2019)]; nicotine [iNicSnFR (Shivange et al. 2019)]; ATP [iATPSnFR (Lobas et al. 2019)]; glucose (Hu et al. 2018, Keller et al. 2021, Mita et al. 2019); and, more recently, serotonin [iSeroSnFR (Unger et al. 2020)].

The development of iGluSnFR pioneered the field of NT sensor development and paved the way for developing other NT/NM sensors. For example, the acetylcholine sensor, iAChSnFR, consists of a hyperthermophilic homolog of Bacillus subtilis OpuBC from Thermoanaerobacter sp. X513 and a circularly permuted superfolder green fluorescent protein (cpSFGFP) (Borden et al. 2020). A critical challenge for developing iAChSnFR is the specificity tuning. The X513-OpuBC binds to both choline and acetylcholine, and the affinity for choline (kd = 8 uM) is tighter than that for acetylcholine

(kd = 95 uM). With the guidance of crystal structure modeling and modifications on the binding pockets, hinge region, protein interface between X513 and cpSFGFP, and junctions between the binding protein and cpSFGFP, the specificity and affinity of iAChSnFR have shifted from choline toward acetylcholine, despite the molecular similarity between the two. Expressing iAChSnFR in HEK293T cells yields an apparent kd of 2.9 ± 1.6 uM and a maximum dynamic range of 10 ± 1.4 folds. Furthermore, iAChSnFR has been utilized for in vivo recordings in mice, fish, flies, and worms (Borden et al. 2020).

The recent development of the PBP-based serotonin sensor iSeroSnFR furthered the process of altering specificity and selectivity of the binding protein. By applying a machine learning strategy and computational modeling, the binding pocket of iAChSnFR was radically redesigned to bind serotonin while ablating acetylcholine and choline binding. The finalized iSeroSnFR conveys 19 mutations with an approximately 5,000-fold increase in serotonin binding specificity compared to iAChSnFR. The large dynamic range of this sensor permits in vivo detection of distinct serotonin transients across various brain regions and behaviors, including fear conditioning and sleep-wake cycles (Unger et al. 2020).

Endeavors to create genetically encoded sensors based on GPCRs as a binding module have started to further expand the toolbox (Andreoni et al. 2019, Sabatini & Tian 2020, Wang et al. 2018). Not only are GPCRs the largest and most diverse group of membrane receptors in eukaryotes, but they are also native targets of NTs and NMs in the brain. The readily available binding module for endogenous NTs and NMs of interest,

as well as their highly conserved structures, led to the development of a universal design approach for NM sensors. The existing GPCR structures combined with computational simulation approaches suggest that the largest conformational change upon ligand binding is in the intracellular loop 3 (ICL3), the domain crucial for recruiting G proteins, which lies in between transmembrane (TM) domains TM5 and TM6 (Tikhonova & Costanzi 2009) (for solved GPCR structures, see Zhang et al. 2015).Two major single-FP intensiometric sensors, the Light and GRAB families, have been developed utilizing this conformational change. The general design strategies for GPCR-based sensors are similar to the PBP-based sensors, except they use the binding moiety from GPCRs. For the dLight1 series, based on three dopamine (DA) receptors (DRD1, 2, and 4), ICL3 of various DA receptors was completely removed and the cpGFP was inserted directly onto the TMs with short linkers (Patriarchi et al. 2018), while the GPCR activation–based dopamine sensor (GRABDA) series, based on the DRD2 receptor used different linkers and ICL3 insertion sites (Sun et al. 2018). By systematic site saturation mutagenesis (SSM) on the linker region, GFP, and receptors, dLight1 achieved an affinity range from 4 nM to 2.3 μM, with a dynamic range from 170% to 930%. Similarly, GRABDA has an affinity of 7–130 nM and a dynamic range from 90% to 340%. The high affinity and high specificity of the DA sensors demonstrated excellent fluorescent sensitivity and brightness in response to ligand binding, making them ideally suited for in vivo imaging. This strategy has been successfully expanded to generate more GPCR-based biosensors for detecting other NMs, including acetylcholine (GRABACh), norepinephrine (nLight, GRABNE), serotonin (psychLight, GRAB5-HT), adenosine (GRABAdo), ATP (GRABATP), and

endocannabinoids (GRABeCB) (A. Dong et al. 2021; C. Dong et al. 2021; Feng et al. 2019; Jing et al. 2018, 2020; Peng et al. 2020; Wan et al. 2021; Wu et al. 2022).

Workflow for Development and Optimization of Neurotransmitter and Neuromodulator Sensors

Despite the considerable progress in NT/NM sensors that has been made in recent years, the existing NTs with applicable sensors are still far from adequate. Here, we summarize the workflow of how to develop and optimize NT/NM sensors, with GRABDA as an example, aiming to facilitate the expansion of sensor families (Sun et al. 2018, 2020) (Figure 1.2).

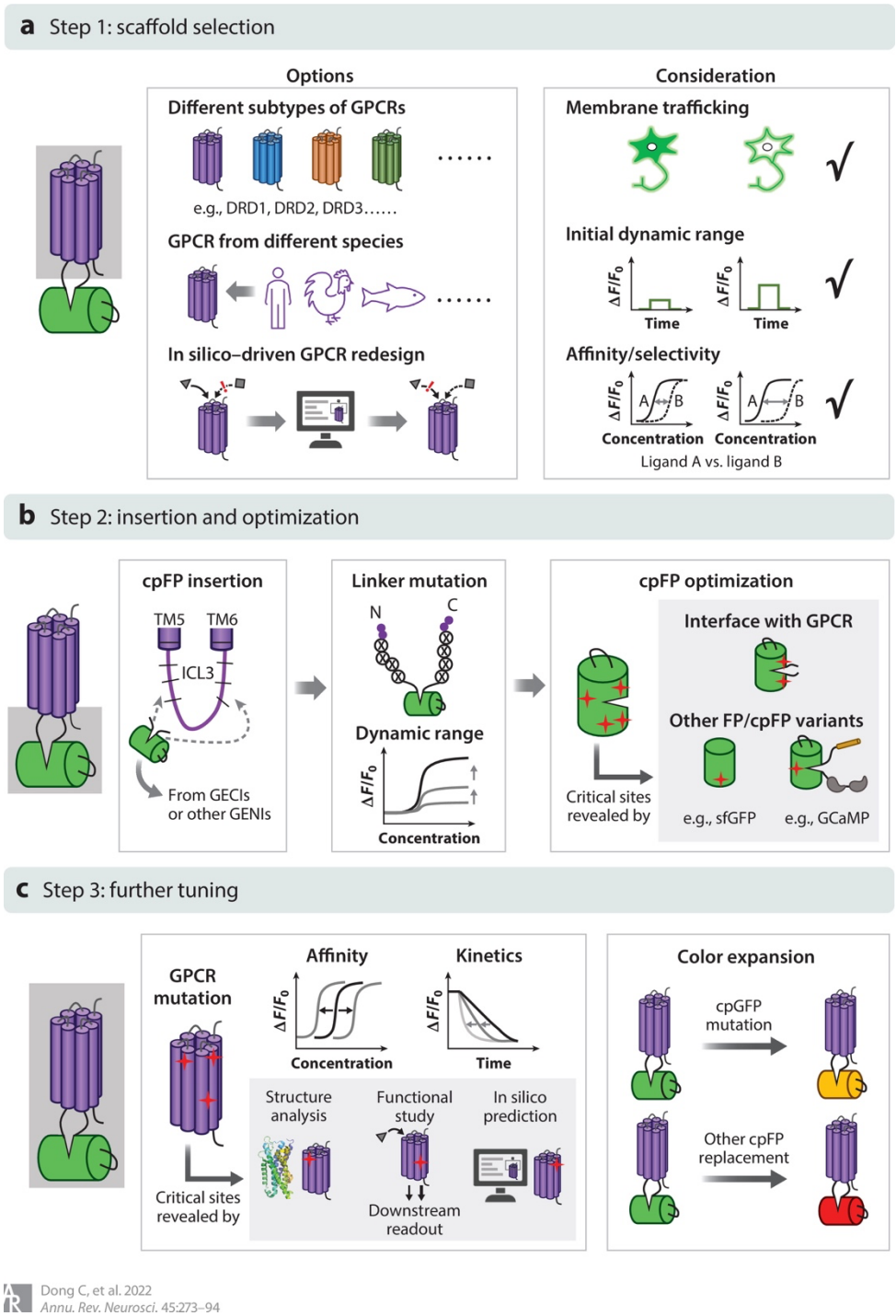

Dong C, et al. 2022
Annu. Rev. Neurosci. 45:273–94

Figure 1.2: A workflow for developing and optimizing GPCR-based neurochemical sensors.
(a) Options and considerations for selecting an appropriate GPCR scaffold. GPCRs can be from different subtypes and species and redesigned in silico. A good scaffold should show good membrane trafficking, high initial dynamic range after cpFP insertion, appropriate affinity, and high selectivity for the neurochemical of interest.
(b) After choosing a good scaffold, cpFP insertion site optimization, linker optimization, and cpFP optimization can be performed sequentially. The critical sites in cpFP optimization are mainly on the interface with the GPCR or learned from other FP or cpFP variants, as highlighted in gray.

(c) Further tuning can be performed by mutating GPCRs to tune the affinity and kinetics. The potential sites in GPCRs can be obtained from the reported GPCR structures, previous functional studies by downstream signaling detection, and in silico prediction, as highlighted in gray. The color can be expanded by introducing several mutations to the cpGFP or by replacing it with other cpFPs (e.g., cpmApple). Abbreviations: cpFP, circularly permuted fluorescent protein; cpGFP, circularly permuted green fluorescent protein; FP, fluorescent protein; GECI, genetically encoded calcium indicator; GENI, genetically encoded neurochemical indicator; GPCR, G protein–coupled receptor; ICL3, intracellular loop-3; sfGFP, superfolder green fluorescent protein; TM, transmembrane.

The first step is choosing a good sensing domain that will determine the overall performance of the sensor (Figure 1.2a). GPCRs are more desirable due to the lack of the corresponding PBPs for most NT/NMs like DA. Moreover, diverse subtypes of GPCRs offer more choices. A potential candidate should be evaluated according to a set of criteria, including membrane trafficking, affinity and selectivity, and the initial dynamic range. During the development of GRABDA sensors, DRD1 and DRD2 showed excellent membrane trafficking when cpGFP was inserted in the preliminary screening of five human DA receptor subtypes. DRD2 was chosen for GRABDA sensors because of its higher affinity than DRD1, while DRD1 was chosen as the scaffold for dLight sensors due to its higher selectivity of DA over norepinephrine (as shown in the dLight1.3b sensor). GPCRs from different species or GPCR redesign by the computational approach also provides additional options.

In order to create an effective sensor with a high SNR, it is imperative to maximize the dynamic range, defined as fluorescent response elicited by ligand binding. One practical approach to amplify the transduction of conformational change to the fluorescent domain is systematic truncation of the ICL3. This strategy helps determine the appropriate position of cpGFP insertion into the GPCRs. After cpGFP insertion, SSM on the linker residues between the FP domain and the receptor scaffold is utilized to generate a library of sensor variants (Figure 1.2b). This method was used to engineer the

GRABDA1m sensor, yielding a maximal dynamic range of about 90%. Further optimization of GRABDA can firstly focus on the cpGFP, especially on the interface with a GPCR. Other potential sites on the cpGFP can be obtained from the differential sites in alignment with brighter GFP variants, such as sfGFP and mClover3, or cpGFP variants from other sensors, including GECIs and GEVIs. A two- to threefold improvement in response was observed in this step for the next-generation GRABDA sensors. These steps are not always sequential. Sometimes, individual optimization of the linker region and cpGFP followed by a combination of beneficial mutations may help to maximize the sensitivity, as presented in the development of GRABACh3.0 (Jing et al. 2020).

Dynamic range and brightness are the priorities for the previous steps. Additional parameters should be considered, including affinity, kinetics, and color expansion, as they also determine the in vivo performance (Figure 1.2c). The affinity can be tuned by rational design on the ligand-binding pocket to match the concentration of NT release in physiological conditions in vivo, in which the resolved structures are of great help. In addition, previous downstream functional analysis also provides potential sites for affinity tuning, especially as some of them are outside of the ligand-binding pocket. For example, in the GRABDA sensor, the T205M mutation on DRD2 that was previously identified by evolution-based computational approaches and validated by downstream signaling detection assay was introduced to generate high-affinity versions (Sung et al. 2016). Fast on and off kinetics are always expected for sensors, but there usually exists a compromise between kinetics and affinity. For example, the high-affinity GRABDA1h and GRABDA2h show a slower off rate than do low-affinity GRABDA1m and

GRABDA2m, respectively. The color of sensors can be slightly yellow-shifted by introducing mutations on cpGFP or further red-shifted by replacing them with other cpFPs such as cpmApple, which is used to develop red GRABDA sensors.

Imaging Neuromodulator Release in Behaving Animals

The fast-growing tool kit of genetically encoded sensors has allowed researchers to study complex neural systems and circuitry across a range of animal models with flexible experimental design. These tools are optimally tuned to answer biological questions about the functionality, pharmacology, and interactions of different molecules involved in chemical neurotransmission. One of the primary advantages is the subsecond temporal resolution. This allows real-time alignment of neural activity across the full course of behaviors. Additionally, the use of spectrally separated sensors permits great flexibility in experimental design, as the sensors can be multiplexed to record and compare transients from different neurochemicals simultaneously (Patriarchi et al. 2020, Sun et al. 2020). For example, researchers can use calcium indicators in conjunction with NM and NT sensors to interrogate the interplay of cellular activity and different neurochemical release phenomena.

Genetically encoded sensors offer the unique advantage of cell type–specific viral strategies for targeting distinct neuronal populations. Researchers can use a host of approaches to narrow the scope of sensor expression. Promoters such as CaMKII and hSyn are often utilized for broad distinction of neurons (Kügler et al. 2003, Nieuwenhuis et al. 2021, Wang et al. 2013). Viral constructs can also be expressed under promoters designed to localize expression to subclasses of neurons, e.g., the GAD67 promoter

selectively expresses in GABAergic neurons (Rasmussen et al. 2007). For additional specificity, researchers can employ transgenic animal models to limit sensor expression. Gene recombination systems, such as Cre/lox, are widely used to constrain sensor expression to specific cell types (Bouabe & Okkenhaug 2013, Kim et al. 2018). These approaches are generally combined with local or systematic viral injections to selectively label and image from region- or projection-specific cell types at scale.

The array of existing sensors combined with various imaging modalities provides an expanded technical arsenal for the interrogation of neural circuits, systems, and behaviors. Fiber photometry combined with genetically encoded sensors enables subsecond recording of calcium and neurochemical dynamics in freely moving, behaving rodents and elucidates neurobiological phenomena underlying innate and learned behaviors, albeit with a lack of single-cell resolution (Sabatini & Tian 2020). Additionally, photometric recording is suitable for targeting deep subcortical nuclei and densely fasciculated projections, which are difficult to access with either one- or multiphoton microscopy. For example, adenosine (GRABAdo) and serotonin (GRAB5-HT and iSeroSnFR) sensors have revealed fluctuating dynamics of extracellular adenosine and serotonin, respectively, over the entire course of the sleep-wake cycle in mouse cortical and subcortical regions (Peng et al. 2020, Unger et al. 2020, Wan et al. 2021) (Figure 1.3a). With fiber photometry, dLight has been used to great effect to understand downstream effects of dopaminergic neuromodulation. Recent work in the field of neural reinforcement learning illustrated a dissociation between dopaminergic ventral tegmental area (VTA) spiking and DA release in the nucleus accumbens (NAc) using

dLight. The authors showed that DA release in the NAc core covaried with reward history and expectations independent of dopaminergic VTA neuron spiking (Mohebi et al. 2019). Other research has revealed that positive and negative DA modulation leads to cell type–specific, asynchronous fluctuations in spiny projection neuron protein kinase A levels (Lee et al. 2021).

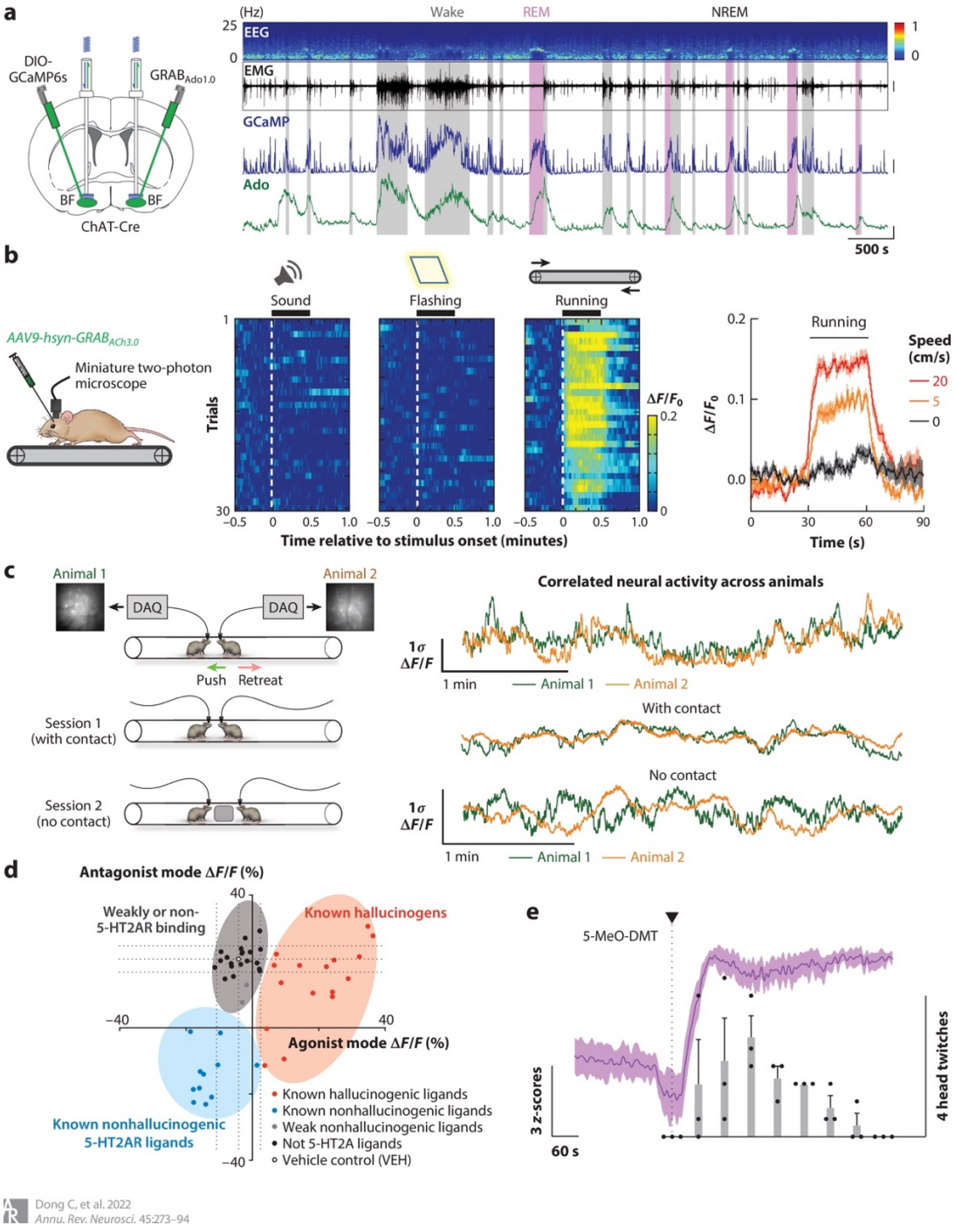

Figure 1.3: Behavioral and pharmacological applications of NT/NM sensors.
(a) Long-term recording of adenosine release in cholinergic neurons using the GRABAdo sensor. Changes in adenosine-dependent fluorescence can be compared to cholinergic calcium activity and EEG/EMG signal across the full time course of the sleep-wake cycle. Panel a adapted from Peng et al. (2020).
(b) Imaging GRABAch3.0 sensor using miniature two-photon microscopy in a treadmill task in mice. Single-cell changes in responses are tractable during different stages of the task and across running speeds. Panel b adapted from Jing et al. (2020).

(c) Simultaneous calcium imaging in dmPFC of two mice during a social interaction test reveals correlations in neural activity during contact versus no contact sessions. Panel c adapted with permission from Kingsbury et al. (2019); copyright 2021 Elsevier.
(d) psychLight-based characterization of compounds based on 5-HT2AR binding and hallucinogenic potential. Panel d adapted from C. Dong et al. (2021).
(e) psychLight tracks in vivo action of 5-MeO-DMT administration over the course of the head-twitch response. Panel e adapted from C. Dong et al. (2021). Abbreviations: 5-MeO-DMT, 5-methoxy-N,N-dimethyltryptamine; DAQ, digital acquisition device; dmPFC, dorsomedial prefrontal cortex; EEG, electroencephalography; EMG, electromyography; NM, neuromodulator; NREM, non-rapid eye movement; NT, neurotransmitter; REM, rapid eye movement.

One- and multiphoton microscopy combined with NM sensors, on the other hand, provide the cellular or subcellular map of distinct release in response to electrical stimuli or behavior. For example, two-photon imaging of DA with the fast DA sensor dLight1.3b revealed the rise and fall of local synaptic release within 200 ms before the postsynaptic current reached plateau (Condon et al. 2021). Two-photon imaging of GRABACh3.0 sensors in the primary somatosensory cortex have led to insights on single-cell cholinergic activity within cortical neuron populations in response to systemic pharmacological manipulation (Jing et al. 2020). Additionally, single- and multiphoton microendoscopy techniques have been adapted and optimized for freely moving behavior (Ziv & Ghosh 2015). These adaptations also permit high-resolution imaging in deep brain regions (Zhang et al. 2019). Miniature two-photon microscopy has been used to demonstrate visual cortex cholinergic response during a treadmill task in mice using the GRABACh3.0 sensor (Figure 1.3b). It is worth mentioning that the intrinsic properties of current NM sensors need to be further optimized for broad application with all microscopies.

What is particularly exciting about the multitude of ways these sensors can be implemented in vivo is the broad range of novel questions and experimental designs to which they can be applied. A prominent topic in neurobehavioral research that will

benefit from the in vivo imaging methods discussed here is social behavior. Social behaviors represent a range of interactions where two or more animals are engaging with each other and relate to a wide array of important and translatable lines of research, including mental health topics (Lim & Young 2006). Researchers have previously encountered roadblocks in measuring neural activity during social behaviors due to the freedom of movement required in many social behavior tests. Recent work has begun to take advantage of recording setups that allow unrestrained movement to investigate circuit-specific activity during behaviors such as neutral interaction (Gunaydin et al. 2014), social defeat (Muir et al. 2018), social isolation (Matthews et al. 2016, Mita et al. 2019), and social reward (Hung et al. 2017). It is even possible to record from multiple animals who are actively interacting and correlate changes in neural activity between animals (Figure 1.3c). All the examples noted thus far utilize calcium imaging with transgenic Cre lines to ensure cell type specificity. However, the advent of NM and NT sensors allows for specific and meaningful observations of dynamic changes in neurocircuitry to be conducted in model species that do not have transgenic options.

Genetically encoded sensors can be modified and used across an array of different species, both vertebrate and invertebrate. GRABACh sensors have been validated in Drosophila and mice, and the GRABDA sensor has been shown to track DA fluctuations in Drosophila, zebrafish, and mice (Jing et al. 2020; Sun et al. 2018, 2020). There are also advantages to using these sensors in wild-type animals, namely that they can serve to better model certain ethology. For example, researchers interested in understanding the neurobiology of paternal behavior may prefer to use mandarin voles as a model, as

mandarin voles are one of the few rodent species to show a high level of paternal infant-directed care (Tai & Wang 2001, Tai et al. 2001). Mandarin vole researchers have used the dLight1 sensor to record DA release into NAc during infant-directed paternal behaviors, allowing for specificity of real-time, unrestrained, region-specific NT recording without a need for transgenics (He et al. 2021). Similarly, the GRABDA was used in zebra finches to monitor DA dynamics in the dopaminergic mesocortical circuit during cultural transmission of vocal behavior (Tanaka et al. 2018). The use of neurochemical sensors in nontraditional models is still in its infancy, but we predict we will see a large increase in popularity. Future studies may see a large increase in the diversity of animal models that allows for the examination of behaviors, conditions, or characteristics not available in inbred lab mice or rats. The California mouse, for example, exhibits high levels of female-female aggression (Trainor et al. 2011) and sex-specific changes in anxiety behavior (Wright et al. 2020), allowing for unique insights into sex differences in anxiety-driven neuromodulation. Forays into sensor application in nonhuman primates have already begun (Sadakane et al. 2015, Seidemann et al. 2016) and represent a future direction of research where sensor neuroimaging could be done in complex cortical regions that do not present in rodents. Neurochemical sensors can be applied in cases like these to probe important questions using the most translatable animal model and ethological experimental design. Spectrally shifted sensors further push the boundaries of in vivo imaging possibilities. Spatiotemporal overlap in neurochemical release, either from synaptic corelease or from converging inputs, is a common phenomenon but one that has been historically difficult to visualize. By using spectrally distinct sensors, researchers

can monitor and correlate activity of multiple neurochemicals without sacrificing spatiotemporal resolution. Red-shifted iGluSnFR (Wu et al. 2018), red- and yellow-shifted dLight (Patriarchi et al. 2020), and red-shifted GRABDA (Sun et al. 2020) sensors have already been engineered. We recognize the importance of continued efforts to produce an expanded palette of neurochemical sensors and the wide-reaching implications that these developments have on the ability to measure interactions and complexities of in vivo neurochemical systems. Additionally, the universally applied sensor engineering methods can also be used to expand the scope of neurochemical sensors. For example, neurolipid indicators have permitted exploration of clinically relevant neurophysiology of endogenous lipid activity. Namely, the GRABeCB2.0 sensor has revealed in vivo endocannabinoid transients across multiple brain regions in response to foot shock, locomotion, and seizure (A. Dong et al. 2021, Farrell et al. 2021).

Application of Neurotransmitter Sensors in Drug Discovery

Besides imaging endogenous NM release dynamics, GPCR-based NM sensors such as psychLight have been recently applied to probe specific ligand-induced conformational changes of the 5-HT2A receptor to predict behavioral outcomes. The cell-based high-throughput assays using 5-HT2A now enable early identification of abusive drugs and the development of 5-HT2AR-dependent nonhallucinogenic therapeutics at scale.

Thirty-five percent of all Food and Drug Administration–approved medications bind to GPCRs (Hauser et al. 2017). The size, shape, and amino acid composition of the orthosteric binding site are very well suited to designing small synthetic molecules

(Shoichet & Kobilka 2012). The ligand-binding-specific conformation of the receptor dictates its function and diverse behavior via different conformation-dependent downstream pathways. It is known that there are multiple signaling pathways for GPCRs, and it is possible to bias the signaling of a given GPCR either through a specific G protein or through β-arrestin induced by designer compounds (Smith et al. 2018), and the biased agonism on GPCRs has been utilized in pharmacology to reduce the side effects of some designer compounds (Whalen et al. 2011). However, the mechanistic action of designer drugs at both molecular and cellular levels is not known. There is a pressing need to develop technologies that can access drugs with addictive potentials at scale in the early stages of drug discovery.

Recently, an open source of 14 optimized bioluminescence resonance energy transfer (BRET)-based sensors, TRUPATH, has facilitated the understanding of drug actions on GPCRs (Olsen et al. 2020). By attaching a RLuc8 on the optimized location of 14 different Gα units and GFP2 on Gγ units—and BRET can happen only when two fluorophores are in the correct proximation and orientation—TRUPATH can specifically indicate the physical association of combinations of Gα, Gβ, and Gγ. Before binding of ligands, the G proteins are in a heterotrimer state. RLuc8 and GFP2 are in proximity so a BRET signal can be observed. Upon binding, Gα subunit exchanges bound guanosine diphosphate with guanosine triphosphate. The disassociation of the Gα unit from the βγ subunit will result in a loss of BRET signal, which indicates when the specific G proteins that are tagged with FP are being engaged. Thus, one can identify specific transducer complexes that are activated by a specific drug in response to a GPCR of interest.

Furthermore, TRUPATH verified that both in wild-type κOR and in chemogenetic κOR Ro1 activated canonical Gαi3 and novel GαGustducin transducers to a similar extent, which was the pathway that was previously reported from in vivo experiments (Mueller et al. 2005).

On the other hand, the use of GPCR-based sensors is a promising strategy to directly monitor the specific receptor conformational changes induced by ligands instead of secondary signaling molecules. The 5-HT2A receptor is the major target of psychedelics, which have shown promising antidepressant, albeit severe hallucinogenic, effects (Chi & Gold 2020). Recent research has shown that the hallucination effect is not necessary for treating depression (Cameron et al. 2021). Thus, it is imperative to screen novel compounds for 5-HT2ARs that do not trigger hallucination but still retain therapeutic effects. To do so, psychLight was engineered by coupling the fluorescence changes of a cpGFP to ligand-binding-induced conformational changes of the 5-HT2AR (C. Dong et al. 2021). PsychLight can categorize compounds into weakly or non-5-HT2AR binding, hallucinogens, and nonhallucinogens by real-time fluorescent readout (Figure 1.3d). The novel compound AAZ-A-154 was discovered by the assay to be a nonhallucinogen. The nonhallucinogenic property of AAZ-A-154 was then validated in vivo with the head-twitch response (HTR) experiment in mice. With the forced swim and glucose preference tests in a genetic model of depression, AAZ-A-154 was shown to be a nonhallucinogenic psychedelic analog that exhibits antidepressant properties.

The genetically encoded approach to designing sensors also has the advantage of being able to study the action of a drug on receptors in vivo. Together with fiber

photometry recording, psychLight signals are able to correlate 5-MeO-DMT action in medial prefrontal cortex (mPFC) during the HTR experiment. An intraperitoneal injection of 5-MeO-DMT takes about a minute to reach mPFC and initiate head twitching (Figure 1.3e). With GPCR-based sensors directly monitoring drug actions in vivo, PBP-based sensors can have a major role in neuropharmacology as well, for example, by monitoring NM release induced by exogeneous drugs.

Author Contributions

C.D. and L.T. generated the models and contributed to the Imaging Beyond Spikes with Neurotransmitter and Neuromodulator Sensors and Application of Neurotransmitter Sensors in Drug Discovery sections. Y.Z., Y.L., L.T., and C.D. contributed to Imaging Neuronal Activity in Genetically Defined Populations, Imaging Beyond Spikes with Neurotransmitter and Neuromodulator Sensors, and Workflow for Development and Optimization of Neurotransmitter and Neuromodulator Sensors sections. K.L.-I., E.C.W., Y.Z., Y.L., and L.T. contributed to the Imaging Neuromodulator Release in Behaving Animals section.

Acknowledgments

The authors would like to thank Dr. Alessio Andreoni for his critiques and helpful comments on modeling, and Dr. Weizhe Hong for providing Figure 4c. This work was supported by the National Institutes of Health BRAIN Initiative (NS1133295, R21EY031858, and NS120824), Human Frontier Research Grant (L.T.), 2R01MH101214-06 (L.T.), T32MH112507 (K.L.-I.), 1F32MMH125597-01A1 (E.C.W.), Beijing Municipal

Science & Technology Commission (Z181100001318002 and Z181100001518004), and the National Science Fund for Distinguished Young Scholars of China (31925017).

Reference

Abdelfattah AS, Kawashima T, Singh A, Novak O, Liu H, et al. 2019. Bright and photostable chemigenetic indicators for extended in vivo voltage imaging. *Science* 365:699–704

Akerboom J, Carreras Calderon N, Tian L, Wabnig S, Prigge M, et al. 2013. Genetically encoded calcium indicators for multi-color neural activity imaging and combination with optogenetics. *Front. Mol. Neurosci.* 6:2

Andreoni A, Davis CMO, Tian L. 2019. Measuring brain chemistry using genetically encoded fluorescent sensors. *Curr. Opin. Biomed. Eng.* 12:59–67

Baird GS, Zacharias DA, Tsien RY. 1999. Circular permutation and receptor insertion within green fluorescent proteins. *PNAS* 96:11241–46

Borden PM, Zhang P, Shivange AV, Marvin JS, Cichon J, et al. 2020. A fast genetically encoded fluorescent sensor for faithful in vivo acetylcholine detection in mice, fish, worms and flies. bioRxiv 2020.02.07.939504. https://doi.org/10.1101/2020.02.07.939504

Bouabe H, Okkenhaug K. 2013. Gene targeting in mice: a review. *Methods Mol. Biol.* 1064:315–36

Broussard GJ, Liang Y, Fridman M, Unger EK, Meng G, et al. 2018. In vivo measurement of afferent activity with axon-specific calcium imaging. *Nat. Neurosci.* 21:1272–80

Cameron LP, Tombari RJ, Lu J, Pell AJ, Hurley ZQ, et al. 2021. A non-hallucinogenic psychedelic analogue with therapeutic potential. *Nature* 589:474–79

Chen T-W, Wardill TJ, Sun Y, Pulver SR, Renninger SL, et al. 2013. Ultrasensitive fluorescent proteins for imaging neuronal activity. *Nature* 499:295–300

Chen Y, Jang H, Spratt P, Kosar S, Taylor DE, et al. 2020. Soma-targeted imaging of neural circuits by ribosome tethering. *Neuron* 107(3):454–69.e6

Chi T, Gold JA. 2020. A review of emerging therapeutic potential of psychedelic drugs in the treatment of psychiatric illnesses. *J. Neurol. Sci.* 411:116715

Condon AF, Robinson BG, Asad N, Dore TM, Tian L, Williams JT. 2021. The residence of synaptically released dopamine on D2 autoreceptors. *Cell Rep.* 36:109465

Dalangin R, Drobizhev M, Molina RS, Aggarwal A, Patel R, et al. 2020. Far-red fluorescent genetically encoded calcium ion indicators. bioRxiv 2020.11.12.380089. https://doi.org/10.1101/2020.11.12.380089

Dana H, Mohar B, Sun Y, Narayan S, Gordus A, et al. 2016. Sensitive red protein calcium indicators for imaging neural activity. *eLife* 5:e12727

Dana H, Sun Y, Mohar B, Hulse BK, Kerlin AM, et al. 2019. High-performance calcium sensors for imaging activity in neuronal populations and microcompartments. *Nat. Methods* 16:649–57

Dong A, He K, Dudok B, Farrell JS, Guan W, et al. 2020. A fluorescent sensor for spatiotemporally resolved endocannabinoid dynamics in vitro and in vivo. bioRxiv 2020.10.08.329169. https://doi.org/10.1101/2020.10.08.329169

Dong C, Ly C, Dunlap LE, Vargas MV, Sun J, et al. 2021. Psychedelic-inspired drug discovery using an engineered biosensor. *Cell* 184:2779–92.e18

El-Husseini AE-D, Craven SE, Brock SC, Bredt DS. 2001. Polarized targeting of peripheral membrane proteins in neurons. *J. Biol. Chem.* 276:44984–92

Erdogan M, Fabritius A, Basquin J, Griesbeck O. 2020. Targeted in situ protein diversification and intra-organelle validation in mammalian cells. *Cell Chem. Biol.* 27:610–21.e5

Farrell JS, Colangeli R, Dong A, George AG, Addo-Osafo K, et al. 2021. In vivo endocannabinoid dynamics at the timescale of physiological and pathological neural activity. *Neuron* 109:2398–403.e4

Feng J, Zhang C, Lischinsky JE, Jing M, Zhou J, et al. 2019. A genetically encoded fluorescent sensor for rapid and specific in vivo detection of norepinephrine. *Neuron* 102:745–61.e8

Gong Y, Huang C, Li JZ, Grewe BF, Zhang Y, et al. 2015. High-speed recording of neural spikes in awake mice and flies with a fluorescent voltage sensor. *Science* 350:1361–66

Grienberger C, Konnerth A. 2012. Imaging calcium in neurons. *Neuron* 73:862–85

Guillaumin MCC, Burdakov D. 2021. Neuropeptides as primary mediators of brain circuit connectivity. *Front. Neurosci.* 15:644313

Gunaydin LA, Grosenick L, Finkelstein JC, Kauvar IV, Fenno LE, et al. 2014. Natural neural projection dynamics underlying social behavior. *Cell* 157:1535–51

Hauser AS, Attwood MM, Rask-Andersen M, Schioth HB, Gloriam DE. 2017. Trends in GPCR drug discovery: new agents, targets and indications. *Nat. Rev. Drug Discov.* 16:829–42

He Z, Zhang L, Hou W, Zhang X, Young LJ, et al. 2021. Paraventricular nucleus oxytocin subsystems promote active paternal behaviors in mandarin voles. *J. Neurosci.* 41:6699–713

Helassa N, Durst CD, Coates C, Kerruth S, Arif U, et al. 2018. Ultrafast glutamate sensors resolve high-frequency release at Schaffer collateral synapses. *PNAS* 115:5594–99

Hu H, Wei Y, Wang D, Su N, Chen X, et al. 2018. Glucose monitoring in living cells with single fluorescent protein-based sensors. *RSC Adv.* 8:2485–89

Hung LW, Neuner S, Polepalli JS, Beier KT, Wright M, et al. 2017. Gating of social reward by oxytocin in the ventral tegmental area. *Science* 357:1406–11

Inoue M, Takeuchi A, Manita S, Horigane SI, Sakamoto M, et al. 2019. Rational engineering of XCaMPs, a multicolor GECI suite for in vivo imaging of complex brain circuit dynamics. *Cell* 177:1346–60.e24

Jin L, Han Z, Platisa J, Wooltorton JRA, Cohen LB, Pieribone VA. 2012. Single action potentials and subthreshold electrical events imaged in neurons with a fluorescent protein voltage probe. *Neuron* 75:779–85

Jing M, Li Y, Zeng J, Huang P, Skirzewski M, et al. 2020. An optimized acetylcholine sensor for monitoring in vivo cholinergic activity. *Nat. Methods* 17:1139–46

Jing M, Zhang P, Wang G, Feng J, Mesik L, et al. 2018. A genetically encoded fluorescent acetylcholine indicator for in vitro and in vivo studies. *Nat. Biotechnol.* 36:726–37

Jumper J, Evans R, Pritzel A, Green T, Figurnov M, et al. 2021. Highly accurate protein structure prediction with AlphaFold. *Nature* 596:583–89

Keller JP, Marvin JS, Lacin H, Lemon WC, Shea J, et al. 2021. In vivo glucose imaging in multiple model organisms with an engineered single-wavelength sensor. *Cell Rep.* 35:109284

Kelly CR, Sharif NA. 2006. Pharmacological evidence for a functional serotonin-2B

receptor in a human uterine smooth muscle cell line. *J. Pharmacol. Exp. Ther.* 317:1254–61

Kim H, Kim M, Im S-K, Fang S. 2018. Mouse Cre-LoxP system: general principles to determine tissue-specific roles of target genes. *Lab Anim. Res.* 34:147–59

Kingsbury L, Huang S, Wang J, Gu K, Golshani P, et al. 2019. Correlated neural activity and encoding of behavior across brains of socially interacting animals. *Cell* 178:429–46.e16

Knopfel T, Song C. 2019. Optical voltage imaging in neurons: moving from technology development to practical tool. *Nat. Rev. Neurosci.* 20:719–27

Kovacs GL. 2004. The endocrine brain: pathophysiological role of neuropeptide-neurotransmitter interactions. *EJIFCC* 15:107–12

Kralj JM, Douglass AD, Hochbaum DR, Maclaurin D, Cohen AE. 2011. Optical recording of action potentials in mammalian neurons using a microbial rhodopsin. *Nat. Methods* 9:90–95

Kügler S, Kilic E, Bähr M. 2003. Human synapsin 1 gene promoter confers highly neuron-specific long-term transgene expression from an adenoviral vector in the adult rat brain depending on the transduced area. *Gene. Ther.* 10:337–47

Lee J, Liu Z, Suzuki PH, Ahrens JF, Lai S, et al. 2020. Versatile phenotype-activated cell sorting. *Sci. Adv.* 6:eabb7438

Lee SJ, Lodder B, Chen Y, Patriarchi T, Tian L, Sabatini BL. 2021. Cell-type-specific asynchronous modulation of PKA by dopamine in learning. *Nature* 590:451–56

Lim MM, Young LJ. 2006. Neuropeptidergic regulation of affiliative behavior and social bonding in animals. *Horm. Behav.* 50:506–17

Lobas MA, Tao R, Nagai J, Kronschlager MT, Borden PM, et al. 2019. A genetically encoded single-wavelength sensor for imaging cytosolic and cell surface ATP. *Nat. Commun.* 10:711

Mank M, Santos AF, Direnberger S, Mrsic-Flogel TD, Hofer SB, et al. 2008. A genetically encoded calcium indicator for chronic in vivo two-photon imaging. *Nat. Methods* 5:805–11

Marvin JS, Borghuis BG, Tian L, Cichon J, Harnett MT, et al. 2013. An optimized fluorescent probe for visualizing glutamate neurotransmission. *Nat. Methods* 10:162–70

Marvin JS, Scholl B, Wilson DE, Podgorski K, Kazemipour A, et al. 2018. Stability, affinity, and chromatic variants of the glutamate sensor iGluSnFR. *Nat. Methods* 15:936–39

Marvin JS, Shimoda Y, Magloire V, Leite M, Kawashima T, et al. 2019. A genetically encoded fluorescent sensor for in vivo imaging of GABA. *Nat. Methods* 16:763–70

Matthews T, Danese A, Wertz J, Odgers CL, Ambler A, et al. 2016. Social isolation, loneliness and depression in young adulthood: a behavioural genetic analysis. *Soc. Psychiatry Psychiatr. Epidemiol.* 51:339–48

Mita M, Ito M, Harada K, Sugawara I, Ueda H, et al. 2019. Green fluorescent protein-based glucose indicators report glucose dynamics in living cells. *Anal. Chem.* 91:4821–30

Miyawaki A, Llopis J, Heim R, McCaffery JM, Adams JA, et al. 1997. Fluorescent indicators for Ca^{2+} based on green fluorescent proteins and calmodulin. *Nature*

388:882–87
Mohebi A, Pettibone JR, Hamid AA, Wong J-MT, Vinson LT, et al. 2019. Dissociable dopamine dynamics for learning and motivation. *Nature* 570:65–70
Motulsky HJ, Neubig RR. 2010. Analyzing binding data. *Curr. Protocols Neurosci.* 52:7.5.1–65
Mueller KL, Hoon MA, Erlenbach I, Chandrashekar J, Zuker CS, Ryba NJP. 2005. The receptors and coding logic for bitter taste. *Nature* 434:225–29
Muir J, Lorsch ZS, Ramakrishnan C, Deisseroth K, Nestler EJ, et al. 2018. In vivo fiber photometry reveals signature of future stress susceptibility in nucleus accumbens. *Neuropsychopharmacology* 43:255–63
Nadim F, Bucher D. 2014. Neuromodulation of neurons and synapses. *Curr. Opin. Neurobiol.* 29:48–56
Nagai T, Sawano A, Park ES, Miyawaki A. 2001. Circularly permuted green fluorescent proteins engineered to sense Ca^{2+}. *PNAS* 98:3197–202
Nagai T, Yamada S, Tominaga T, Ichikawa M, Miyawaki A. 2004. Expanded dynamic range of fluorescent indicators for Ca^{2+} by circularly permuted yellow fluorescent proteins. *PNAS* 101:10554–59
Nakai J, Ohkura M, Imoto K. 2001. A high signal-to-noise Ca^{2+} probe composed of a single green fluorescent protein. *Nat. Biotechnol.* 19:137–41
Nieuwenhuis B, Haenzi B, Hilton S, Carnicer-Lombarte A, Hobo B, et al. 2021. Optimization of adeno-associated viral vector-mediated transduction of the corticospinal tract: comparison of four promoters. *Gene Ther.* 28:56–74
Olsen RHJ, DiBerto JF, English JG, Glaudin AM, Krumm BE, et al. 2020. TRUPATH, an open-source biosensor platform for interrogating the GPCR transducerome. *Nat. Chem. Biol.* 16:841–49
Pal A, Tian L. 2020. Imaging voltage and brain chemistry with genetically encoded sensors and modulators. *Curr. Opin. Chem. Biol.* 57:166–76
Palmer AE, Giacomello M, Kortemme T, Hires SA, Lev-Ram V, et al. 2006. Ca^{2+} indicators based on computationally redesigned calmodulin-peptide pairs. *Chem. Biol.* 13:521–30
Panzera LC, Hoppa MB. 2019. Genetically encoded voltage indicators are illuminating subcellular physiology of the axon. *Front Cell Neurosci* 13:52
Patriarchi T, Cho JR, Merten K, Howe MW, Marley A, et al. 2018. Ultrafast neuronal imaging of dopamine dynamics with designed genetically encoded sensors. *Science* 360:aat4422
Patriarchi T, Mohebi A, Sun J, Marley A, Liang R, et al. 2020. An expanded palette of dopamine sensors for multiplex imaging in vivo. *Nat. Methods* 17:1147–55
Peng W, Wu Z, Song K, Zhang S, Li Y, Xu M. 2020. Regulation of sleep homeostasis mediator adenosine by basal forebrain glutamatergic neurons. *Science* 369:eabb0556
Piatkevich KD, Jung EE, Straub C, Linghu C, Park D, et al. 2018. A robotic multidimensional directed evolution approach applied to fluorescent voltage reporters. *Nat. Chem. Biol.* 14:352–60
Qian Y, Orozco Cosio DM, Piatkevich KD, Aufmkolk S, Su WC, et al. 2020. Improved genetically encoded near-infrared fluorescent calcium ion indicators for in vivo imaging. *PLOS Biol.* 18:e3000965

Qian Y, Piatkevich KD, McLarney B, Abdelfattah AS, Mehta S, et al. 2019. A genetically encoded near-infrared fluorescent calcium ion indicator. *Nat. Methods* 16:171–74

Quiocho FA, Ledvina PS. 1996. Atomic structure and specificity of bacterial periplasmic receptors for active transport and chemotaxis: variation of common themes. *Mol. Microbiol.* 20:17–25

Rasmussen M, Kong L, Zhang G-R, Liu M, Wang X, et al. 2007. Glutamatergic or GABAergic neuron-specific, long-term expression in neocortical neurons from helper virus-free HSV-1 vectors containing the phosphate-activated glutaminase, vesicular glutamate transporter-1, or glutamic acid decarboxylase promoter. *Brain Res.* 1144:19–32

Rózsa M, Bushey D, Zheng J, Reep D, Broussard GJ, et al. 2020. *jGCaMP8 fast genetically encoded calcium indicators*. Inf. Sheet, Janelia, Boston, MA

Sabatini BL, Tian L. 2020. Imaging neurotransmitter and neuromodulator dynamics in vivo with genetically encoded indicators. *Neuron* 108:17–32

Sadakane O, Masamizu Y, Watakabe A, Terada S-I, Ohtsuka M, et al. 2015. Long-term two-photon calcium imaging of neuronal populations with subcellular resolution in adult non-human primates. *Cell Rep.* 13:1989–99

Seidemann E, Chen Y, Bai Y, Chen SC, Mehta P, et al. 2016. Calcium imaging with genetically encoded indicators in behaving primates. *eLife* 5:e16178

Shcherbakova DM, Shemetov AA, Kaberniuk AA, Verkhusha VV. 2015. Natural photoreceptors as a source of fluorescent proteins, biosensors, and optogenetic tools. *Annu. Rev. Biochem.* 84:519–50

Shemetov AA, Monakhov MV, Zhang Q, Canton-Josh JE, Kumar M, et al. 2021. A near-infrared genetically encoded calcium indicator for in vivo imaging. *Nat. Biotechnol.* 39:368–77

Shen Y, Dana H, Abdelfattah AS, Patel R, Shea J, et al. 2018. A genetically encoded Ca^{2+} indicator based on circularly permutated sea anemone red fluorescent protein eqFP578. *BMC Biol.* 16:9

Shivange AV, Borden PM, Muthusamy AK, Nichols AL, Bera K, et al. 2019. Determining the pharmacokinetics of nicotinic drugs in the endoplasmic reticulum using biosensors. *J. Gen. Physiol.* 151:738–57

Shoichet BK, Kobilka BK. 2012. Structure-based drug screening for G-protein-coupled receptors. *Trends Pharmacol. Sci.* 33:268–72

Smith JS, Lefkowitz RJ, Rajagopal S. 2018. Biased signalling: from simple switches to allosteric microprocessors. *Nat. Rev. Drug Discov.* 17:243–60

St-Pierre F, Marshall JD, Yang Y, Gong Y, Schnitzer MJ, Lin MZ. 2014. High-fidelity optical reporting of neuronal electrical activity with an ultrafast fluorescent voltage sensor. *Nat. Neurosci.* 17:884–89

Sun F, Zeng J, Jing M, Zhou J, Feng J, et al. 2018. A genetically encoded fluorescent sensor enables rapid and specific detection of dopamine in flies, fish, and mice. *Cell* 174:481–96.e19

Sun F, Zhou J, Dai B, Qian T, Zeng J, et al. 2020. Next-generation GRAB sensors for monitoring dopaminergic activity in vivo. *Nat. Methods* 17:1156–66

Sung YM, Wilkins AD, Rodriguez GJ, Wensel TG, Lichtarge O. 2016. Intramolecular

allosteric communication in dopamine D2 receptor revealed by evolutionary amino acid covariation. *PNAS* 113(13):3539–44
Tai F, Wang TZ. 2001. Social organization of mandarin voles in burrow system. *Acta Theriol. Sin.* 21:50–56
Tai F, Wang TZ, Zhao YJ. 2001. Mating system of mandarin vole (*Microtus mandarinus*). *Acta Zool. Sin.* 47:260–67
Tanaka M, Sun F, Li Y, Mooney R. 2018. A mesocortical dopamine circuit enables the cultural transmission of vocal behaviour. *Nature* 563:117–20
Tian L, Hires SA, Mao T, Huber D, Chiappe ME, et al. 2009. Imaging neural activity in worms, flies and mice with improved GCaMP calcium indicators. *Nat. Methods* 6:875–81
Tikhonova IG, Costanzi S. 2009. Unraveling the structure and function of G protein-coupled receptors through NMR spectroscopy. *Curr. Pharm. Des.* 15:4003–16
Trainor BC, Pride MC, Landeros RV, Knoblauch NW, Takahashi EY, et al. 2011. Sex differences in social interaction behavior following social defeat stress in the monogamous California mouse (*Peromyscus californicus*). *PLOS ONE* 6:e17405
Tunyasuvunakool K, Adler J, Wu Z, Green T, Zielinski M, et al. 2021. Highly accurate protein structure prediction for the human proteome. *Nature* 596:590–96
Unger EK, Keller JP, Altermatt M, Liang R, Matsui A, et al. 2020. Directed evolution of a selective and sensitive serotonin sensor via machine learning. *Cell* 183:1986–2002.e26
Villette V, Chavarha M, Dimov IK, Bradley J, Pradhan L, et al. 2019. Ultrafast two-photon imaging of a high-gain voltage indicator in awake behaving mice. *Cell* 179:1590–608.e23
Wan J, Peng W, Li X, Qian T, Song K, et al. 2021. A genetically encoded sensor for measuring serotonin dynamics. *Nat. Neurosci.* 24:746–52
Wang H, Jing M, Li Y. 2018. Lighting up the brain: genetically encoded fluorescent sensors for imaging neurotransmitters and neuromodulators. *Curr. Opin. Neurobiol.* 50:171–78
Wang W, Kim CK, Ting AY. 2019. Molecular tools for imaging and recording neuronal activity. *Nat. Chem. Biol.* 15:101–10
Wang X, Zhang C, Szábo G, Sun Q-Q. 2013. Distribution of CaMKIIα expression in the brain in vivo, studied by CaMKIIα-GFP mice. *Brain Res.* 1518:9–25
Whalen EJ, Rajagopal S, Lefkowitz RJ. 2011. Therapeutic potential of β-arrestin- and G protein-biased agonists. *Trends Mol. Med.* 17:126–39
Wright EC, Hostinar CE, Trainor BC. 2020. Anxious to see you: neuroendocrine mechanisms of social vigilance and anxiety during adolescence. *Eur. J. Neurosci.* 52:2516–29
Wu J, Abdelfattah AS, Zhou H, Ruangkittisakul A, Qian Y, et al. 2018. Genetically encoded glutamate indicators with altered color and topology. *ACS Chem. Biol.* 13:1832–37
Wu Z, He K, Chen Y, Li H, Pan S, et al. 2021. An ultrasensitive GRAB sensor for detecting extracellular ATP in vitro and vivo. bioRxiv 2021.02.24.432680. https://doi.org/10.1101/2021.02.24.432680
Yang HH, St-Pierre F, Sun X, Ding X, Lin MZ, Clandinin TR. 2016. Subcellular imaging

of voltage and calcium signals reveals neural processing in vivo. *Cell* 166:245–57
Zhang D, Zhao Q, Wu B. 2015. Structural studies of G protein-coupled receptors. *Mol. Cells* 38:836–42
Zhang L, Liang B, Barbera G, Hawes S, Zhang Y, et al. 2019. Miniscope GRIN lens system for calcium imaging of neuronal activity from deep brain structures in behaving animals. *Curr. Protoc. Neurosci.* 86:e56
Zhao Y, Araki S, Wu J, Teramoto T, Chang YF, et al. 2011. An expanded palette of genetically encoded Ca^{2+} indicators. *Science* 333:1888–91
Ziv Y, Ghosh KK. 2015. Miniature microscopes for large-scale imaging of neuronal activity in freely behaving rodents. *Curr. Opin. Neurobiol.* 32:141–47

Chapter 2 – Monoamine – the serotonin story

2.1 - Psychedelic-Inspired Drug Discovery Using An Engineered Biosensor

Preface

The text of this chapter is a modified version of a manuscript that was submitted to the Cell Press on February 28, 2021 and accepted for publication on April 28, 2021 (doi.org/10.1016/j.cell.2021.03.043). The layout has been adjusted in accordance with the requirements of a doctoral thesis. Authors on the original manuscript are listed as Chunyang Dong†, Calvin Ly†, Lee E. Dunlap†, Maxemiliano V. Vargas, Junqing Sun, In-Wook Hwang, Arya Azinfar, Won Chan Oh, William C. Wetsel, David E. Olson, Lin Tian. († authors contributed equally to this work)

Abstract

Ligands can induce G protein-coupled receptors (GPCRs) to adopt a myriad of conformations, many of which play critical roles in determining the activation of specific signaling cascades associated with distinct functional and behavioral consequences. For example, the 5-hydroxytryptamine 2A receptor (5-HT2AR) is the target of classic hallucinogens, atypical antipsychotics, and psychoplastogens. However, currently available methods are inadequate for directly assessing 5-HT2AR conformation both in vitro and in vivo. Here, we developed psychLight, a genetically encoded fluorescent sensor based on the 5-HT2AR structure. PsychLight detects behaviorally relevant serotonin release and correctly predicts the hallucinogenic behavioral effects of structurally similar 5-HT2AR ligands. We further used psychLight to identify a non-hallucinogenic psychedelic analog, which produced rapid-onset and long-lasting antidepressant-like effects after a single administration. The advent of psychLight will enable in vivo detection of serotonin dynamics, early identification of designer drugs of abuse, and the development of 5-HT2AR-dependent non-hallucinogenic therapeutics.

Introduction

G protein-coupled receptors (GPCRs) represent attractive therapeutic targets with nearly 35% of all Food and Drug Administration (FDA)-approved medications (Hauser et al., 2017) affecting this class of proteins. Ligand-induced changes in GPCR conformation provide a structural basis for initiating intracellular signaling through heterotrimeric G proteins, arrestins, and other effectors (Kenakin and Miller, 2010). Biased ligands are capable of selectively activating or inactivating specific cellular pathways at the expense of others by stabilizing discrete GPCR conformational ensembles, and thus, have the potential to reduce undesirable side effects while maintaining efficacy (Roth et al., 2017; Shonberg et al., 2014).

Ligands for the 5-HT2AR were some of the first small molecules to demonstrate biased agonism (Berg et al., 1998). Since that initial report, 5-HT2AR ligands have been shown to couple to a variety of signal transduction pathways via 5-HT2A monomers and heterodimers leading to distinct transcriptome profiles and behavioral effects (Fribourg et al., 2011; González-Maeso et al., 2003, 2007, 2008; Schmid and Bohn, 2010; Schmid et al., 2008). Furthermore, 5-HT2AR ligands represent some of the most important drugs in neuropsychiatry, including atypical antipsychotics like clozapine, psychedelics such as lysergic acid diethylamide (LSD), and neural plasticity-promoting compounds known as psychoplastogens (Olson, 2018).

Mounting preclinical and clinical evidence suggests that psychedelics may prove useful for treating a variety of neuropsychiatric diseases including depression, post-traumatic stress disorder (PTSD), and substance use disorder (SUD) (Chi and Gold, 2020). However, it is currently unclear if the subjective effects of these drugs are necessary to

ameliorate disease symptoms (Olson, 2020; Yaden and Griffiths, 2020). Like ketamine, psychedelics promote neural plasticity in key circuits relevant to mood, fear, and reward (Ly et al., 2018). Recent rodent studies using sub-hallucinogenic doses (Cameron et al., 2019) and non-hallucinogenic congeners (Cameron et al., 2021) suggest that the hallucinogenic effects of 5-HT2AR ligands may not be necessary to promote neural plasticity and produce therapeutic outcomes. Thus, there is a critical need to develop methods for reliably determining if a novel ligand is likely to induce hallucinogen-specific conformations of the 5-HT2AR.

Recent breakthroughs in the structural determination of ligand-activated GPCRs and GPCR-transducer complexes have significantly increased our understanding of how receptor activation leads to coupling with various signal transducers (Hilger et al., 2018; Kim et al., 2020; Roth et al., 2017). Although traditional methods for assessing GPCR activation have relied on the quantification of downstream signaling molecules (e.g., cyclic AMP [cAMP], Ca2+, etc.), ligand-induced conformational changes are increasingly being exploited to develop fluorescence- and bioluminescence-based assays for measuring the recruitment of various transducers (Olsen et al., 2020; Wan et al., 2018). Although these methods have proven useful for understanding important details of GPCR activation related to kinetics and specific drug responses, the direct measurement of behaviorally relevant GPCR conformations in real time and in vivo is still challenging with current technologies. As a result, there are currently no assays capable of directly measuring hallucinogenic potential across a wide range of structurally diverse 5-HT2AR ligands.

Recently, we reported a modular strategy for creating genetically encoded fluorescent sensors that are activated by ligand-induced conformational changes in GPCRs (Patriarchi et al., 2018). Here, we applied this design strategy to develop psychLight, a 5-HT2AR-based fluorescent biosensor capable of detecting endogenous serotonin (5-HT) release in awake, behaving animals as well as conformations induced by hallucinogenic ligands in vivo and in a medium-throughput functional assay. By screening a small library of compounds, we successfully used psychLight to identify previously unknown hallucinogenic drugs and a non-hallucinogenic psychedelic analog with neural plasticity-promoting and antidepressant properties similar to the state-of-the-art fast-acting antidepressant ketamine (Table S2.1).

Results

(i) Development of Psychlight

To develop a sensor capable of reporting ligand-induced conformations of the human 5-HT2AR, we replaced the third intracellular loop (IL3) of the 5-HT2AR with a circularly permuted green fluorescent protein (cpGFP) inserted between Lys263 and Ser316 (Figure S2.1A). The dynamic range in response to the endogenous ligand 5-HT was maximized by screening linker compositions between cpGFP and 5-HT2AR, optimizing the insertion site of cpGFP, and introducing key point mutations (Figure S2.1B) (Patriarchi et al., 2018). We named the top-performing variant psychLight1 (Figure 2.1A). To further improve membrane localization in neurons, we fused an endoplasmic reticulum (ER) export motif (FCYENEV) (Stockklausner et al., 2001) to the C terminus of psychLight1, yielding a version (i.e., psychLight2) with improved membrane expression in both HEK293T cells and neurons (Figures 2.1B, S2.1C, and S2.1D).

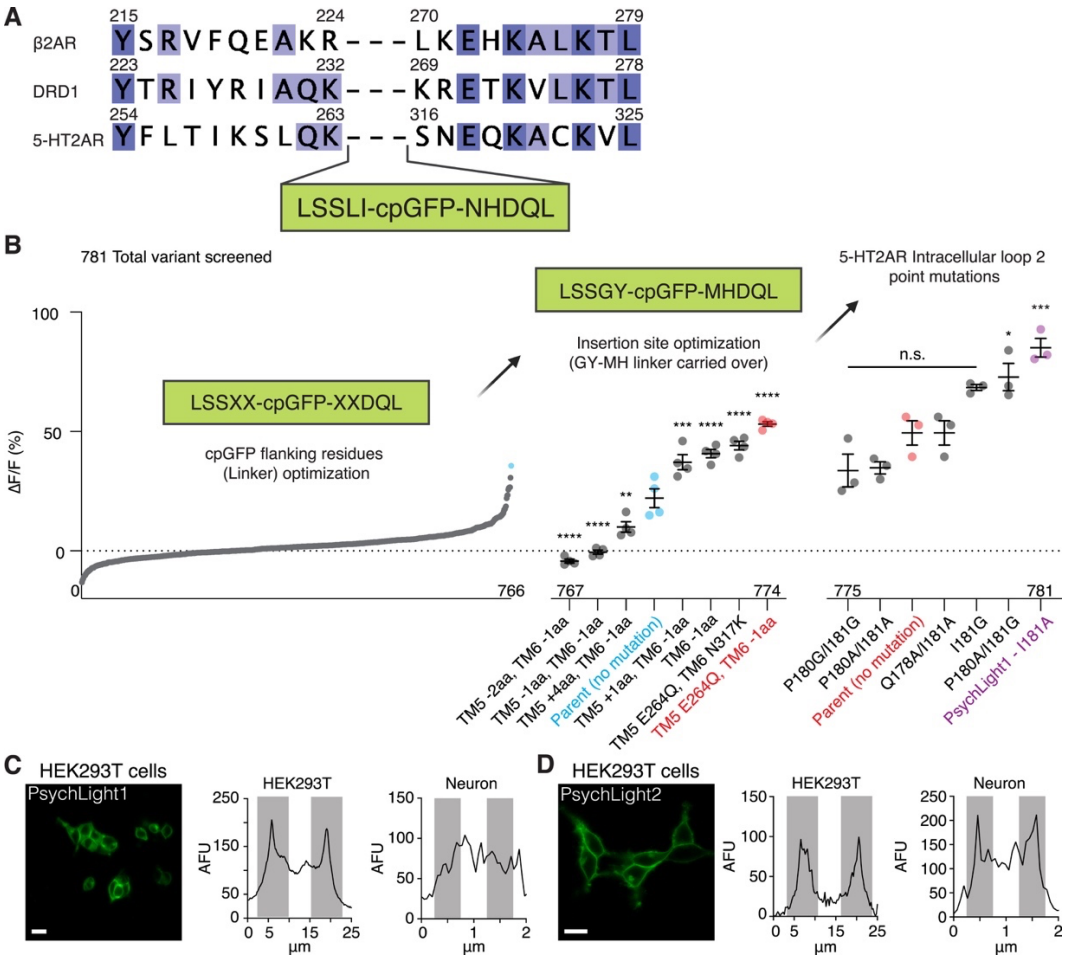

Figure S2.1: Engineering a sensor for hallucinogenic conformations of the 5-HT2A receptor, related to Figure 2.1.

A. Sequence alignment of β2A, DRD1, and 5-HT2A receptors. Initial insertion site of the LSSLI-cpGFP-NHDQL module was between K263 and S316 of the 5-HT2AR. The original cpGFP flanking residues (i.e., LI-cpGFP-NH) were chosen based on the sequence of dLight1.3 (Patriarchi et al., 2018).

B. After the initial insertion site was determined, a total of 781 variants were screened to optimize psychLight. We screened 766 variants related to the aa composition of the linkers. The top performer (i.e., GY-MH, blue) advanced to the next stage of screening. Next, we performed insertion site optimization of the fluorescent module. A point mutation in TM5 (i.e., E264Q) and removal of 1 aa from TM6 yielded a better variant (red). (TM5 −2aa, TM6 −1aa = −4.2 ± 0.8%. TM5 −1aa, TM6 −1aa = −0.5 ± 0.8%. TM5 +4aa, TM6 −1aa = 10.1 ± 2.2%. Parent (no mutation) = 22.1 ± 3.9%. TM5 +1aa, TM6 −1aa = 37.2 ± 3.2%. TM6 −1aa = 40.8 ± 1.7%. TM5 E264Q, TM6 N317K = 44.2 ± 1.8%. TM5 E264Q, TM6 −1aa = 53.2 ± 0.9%. n = 4 replicates from 4 passages of cells). Next, we made point mutations in intracellular loop 2. The top-performing variant was named psychLight1 (magenta) (P180G/I181G = 33.7 ± 6.8%. P180A/I181A = 34.8 ± 2.5%. Parent (no mutation) = 49.4 ± 5.1%. Q178A/I181A = 49.4 ± 5.1%. I181G = 68.5 ± 1.3%. P180A/I181G = 72.9 ± 5.7%. I181A = 85.2 ± 3.9%). n = 3 replicates from 3 passages of cells. Data are represented as mean ± SEM. ****p < 0.0001, ***p < 0.001, **p < 0.01 and *p < 0.05, one-way ANOVA compares to parent variant within the group with Dunnett's test.

C-D. Optimization of psychLight membrane localization. Representative images of HEK293T cells expressing either psychLight1 or psychLight2. Scale bar: 20 μm. Both psychLight1 and psychLight2 are expressed on the cell membranes of HEK293T cells. However, neuronal expression of psychLight1 is primarily intracellular PsychLight2 is expressed on the surface of neurons to a greater extent. AFU = Arbitrary Fluorescence Units.

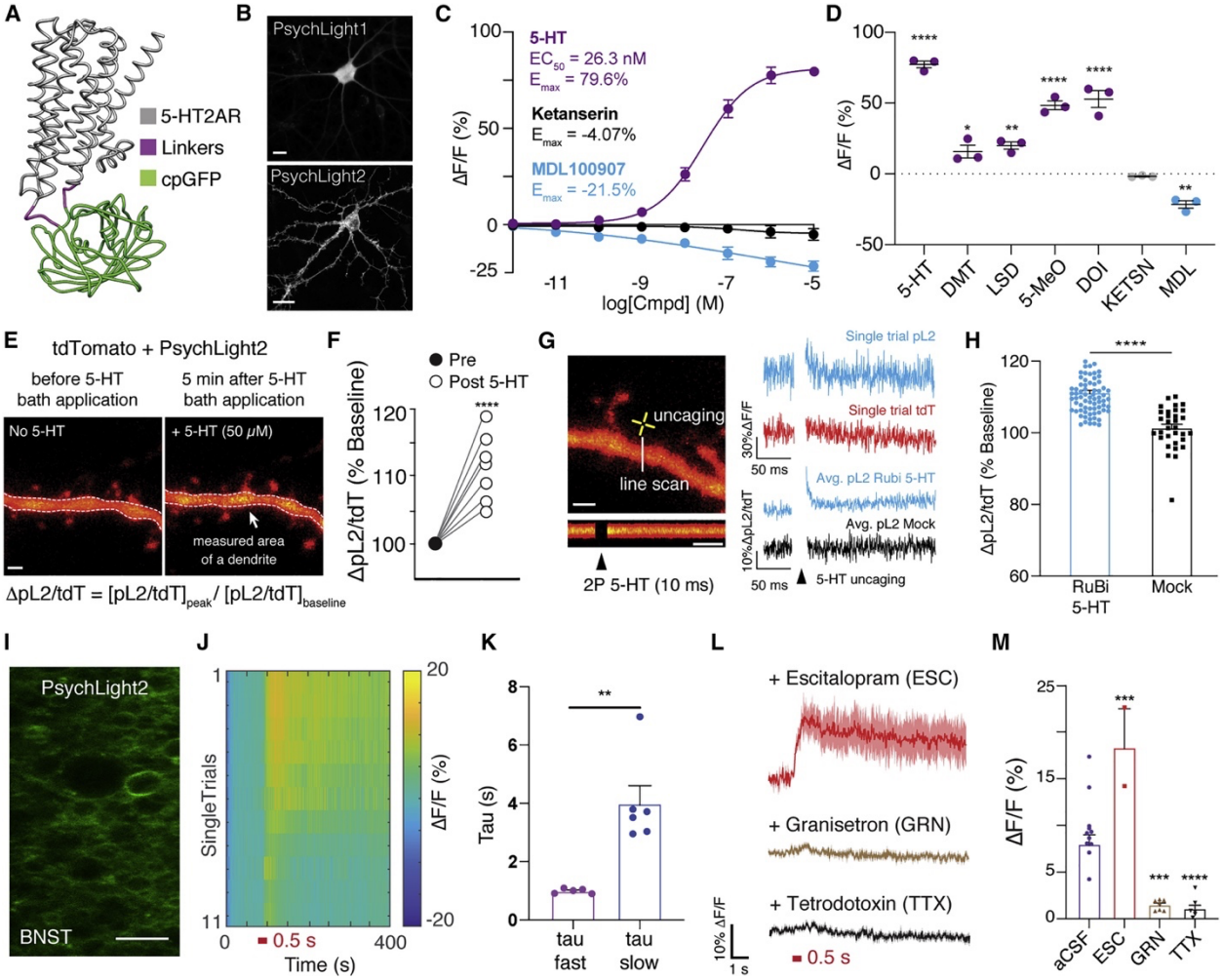

Figure 2.1. Development of a fluorescent sensor based on the 5-HT2A receptor.

(A) Simulated structure of psychLight consisting of 5-HT2AR (gray), a linker (magenta) and a cpGFP (green).

(B) Representative images of cultured dissociated hippocampal neurons transiently expressing psychLight1 and psychLight2. Scale bar, 20 µm.

(C) PsychLight1-expressing HEK293T cells respond to ligands in a concentration-dependent manner.

(D) PsychLight1 is activated by hallucinogenic 5-HT2A ligands, but not non-hallucinogenic compounds when treated at 10 µM. ****p < 0.0001, **p < 0.01 and *p < 0.05, one-way ANOVA compared to KETSN with Dunnett's test.

(E and F) Two-photon imaging of cultured cortical slices expressing psychLight2 (pL2) following bath application of 5-HT.

(E) Representative images of a dendrite expressing psychLight2 (pL2) and tdTomato (tdT) before and after bath application of 50 µM 5-HT (imaged at 920 nm).

(F) Fluorescence intensity changes in pL2 were normalized to the tdT signal, (ΔpL2/tdT = 111.1% ± 1.8%, n = 7 region of interests [ROIs] from 4 cells; ****p < 0.0001, unpaired t test). Scale bar, 1 µm.

(G and H) Two-photon 5-HT uncaging evoked psychLight responses.

(G) Representative apical dendrites imaged during two-photon uncaging of serotonin. Representative single-trial traces of fluorescent intensity changes (ΔF/F%) of pL2 and tdT are shown in response to single pulse uncaging (10 ms). Averaged traces of ΔpL2/tdT in response to uncaging of Rubi-5HT (bottom) and without were shown. Scale bars, 1 µm.

(H) Characterization of peak response of green to red ratio (ΔpL2/tdT) normalized to the baseline for pL2 in response to single-pulse uncaging with and without RuBi-5-HT (ΔpL2/tdT = 111.2% ± 0.7%, n = 76 ROIs from 11 cells (Rubi-5-HT); 101.3% ± 1.0% n = 32 ROIs from 6 cells [mock 2P]), ****p < 0.0001, unpaired t test.
(I–K) Two-photon imaging of endogenous 5-HT release triggered by electrical stimuli in acute slices.
(I) A representative two-photon image of BNST acute slice expressing psychLight2. Scale bar, 50 μm.
(J) Single-trial response of psychLight2 to electrical stimuli (0.5 s, 4 V, 40 Hz, 20 pulses).
(K) The averaged off-kinetics of two groups of ROIs exhibiting fast and slow off rates. (40 pulses: Taufast = 0.997 ± 0.0376 s, n = 5 trials; Tauslow = 3.998 ± 0.6103 s, n = 6 trails), **p < 0.01, unpaired t test.
(L) Averaged-trial traces of psychLight2 in response to electrical stimuli in the presence of escitalopram (ESC, 50 μM), granisetron (GRN, 10 μM), and tetrodotoxin (TTX,1 μM). Shaded area represents SEM.
(M) Peak fluorescence changes in the absence (aCSF, n = 11 trials from 3 mice) and presence of compounds (ESC, n = 2 trials from 3 mice, ***p = 0.0002; GRN, n = 8 trials from 3 mice, ****p < 0.0001; TTX n = 9 trials from 3 mice, 40 pulses, one-way ANOVA compared to aCSF with Sidak's test). Data are represented by mean ± SEM.
See also Figures S2.1 and S2.2A–S2.2D and Tables S2.1 and S2.2.

We next investigated the pharmacological responses of the sensor. When psychLight1 is expressed in HEK293T cells, 5-HT activates the sensor with a half maximal effective concentration comparable to values obtained using assays designed to measure G protein and β-arrestin activation (Wacker et al., 2017) (Figure 2.1C). Moreover, other agonists were able to effectively increase the sensor's fluorescence intensity to varying degrees (Figure 2.1D). In contrast, the traditional 5-HT2AR antagonists ketanserin and MDL100907 either had minimal effect on psychLight1 fluorescence or slightly quenched the sensor (Figures 2.1C and 2.1D), and ketanserin was able to block 5-HT-induced activation of psychLight in HEK293T cells (Figures S2.2A and S2.2B). Taken together, these findings demonstrated that psychLight can convert ligand-induced conformational changes of the 5-HT2AR into fluorescence readouts, suggesting that psychLight may be uniquely suited for detecting specific conformations of the receptor induced by ligands.

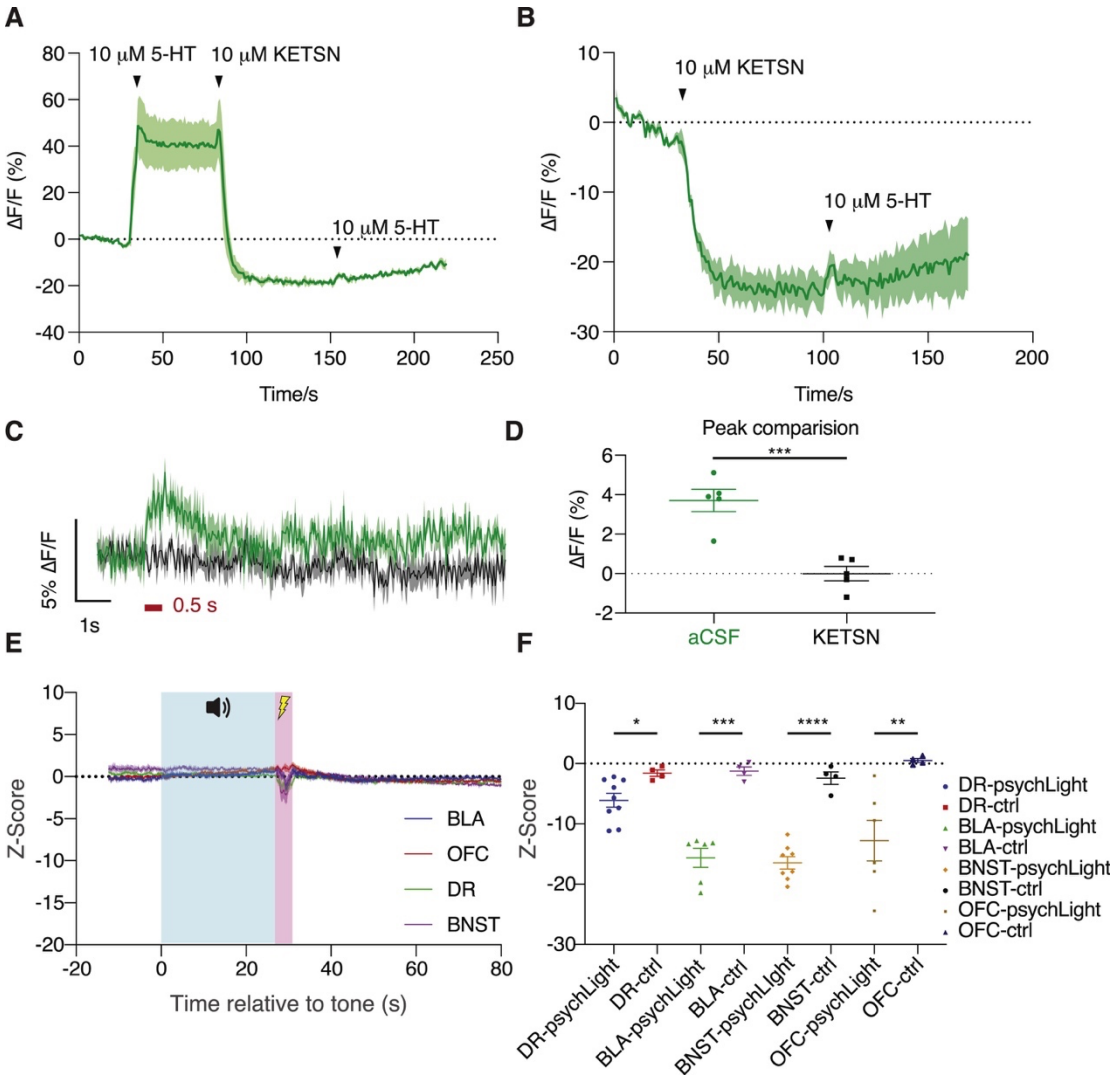

Figure S2.2. Control experiments of psychLight recordings in HEK cells ex-vivo and in vivo, related to Figures 2.1 and 2.2

A–B. Application of 5-HT and KETSN to HEK293T cells in different orders reveals blocking effect of KETSN.

A. The order of addition is 10 μM 5-HT followed by 10 μM KETSN and then 10 μM 5-HT.

B. The order of addition is 10 μM KETSN followed by 10 μM 5-HT.

C. Field stimulation of BNST brain slices followed by two photon imaging of psychLight with either aCSF (green) or a solution of 5-HT2A antagonist KETSN (10 μM, black). The effect of field stimulation was blocked by KETSN. N = 5 slices.

D. Quantification of the peak response in C (aCSF: 3.71 ± 0.57%, KETSN: 0 ± 0.36%, ***p < 0.001, unpaired t test).

E. Fiber photometry recordings of psychLight0—a control sensor that cannot bind to 5-HT due to a key point mutation (D155A).

F. Side by side comparison of psychLight2 and psychLight0 (ctrl) fluorescence during foot shock, indicating psychLight2 is primarily detecting changes in 5-HT concentrations and not simply motion artifacts. DR-psychLight: −6.069 ± 1.165%, DR-ctrl: −1.588 ± 0.5303%, BLA-psychLight: −15.63 ± 1.581%, BLA-ctrl: −1.253 ± 0.7031%, BNST-psychLIght: −16.44 ± 1.034%, BNST ctrl: −2.408 ± 1.033%, OFC-psychLight: −13.79 ± 2.835%, OFC-ctrl: 0.5163 ± 0.3395%, *p < 0.05, **p < 0.01, ***p < 0.001, ****p < 0.0001, unpaired t test compared between each brain region. 5-HT = 5-hydroxytryptamine; KETSN = ketanserin; ctrl = psychLight0; DRN = dorsal raphe nucleus; BNST = bed nucleus of the stria terminalis; BLA = basolateral amygdala; OFC = orbitofrontal cortex.

(ii) Two-Photon Imaging of Endogenous Serotonin Dynamics **Ex-Vivo** *and* **In-Vivo**

To assess the utility of psychLight2 for measuring endogenous serotonin transients, we characterized the sensitivity and kinetics of the sensor using two-photon imaging in cultured and acute brain slices. Approximately 3 weeks after infection with AAV9.hSynapsin1.psychLight2 into organotypic cortical slice cultures and biolistic transfection of a red cell-fill fluorescent protein, tdTomato, we imaged layer 2/3 pyramidal neurons using two-photon time-lapse imaging and line-scan acquisition mode (~3.3 lines/ms). Bath application of 5-HT (50 µM) led to a significant increase in the ratio of green (psychLight2 signal; pL2) to red (tdTomato signal; tdT) fluorescence intensities (Figures 2.1E and 2.1F). Focal uncaging of RuBi-5-HT at apical dendrites (single 10-ms pulse at 810 nm) evoked a rapid increase in psychLight fluorescence that returned to baseline within milliseconds (Tauoff = 5.4 ± 0.9 ms) (Figures 2.1G and 2.1H). In contrast, no increase in fluorescence was observed in response to a mock stimulus.

Next, we examined the ability of psychLight2 to report time-dependent changes in 5-HT dynamics using an acute slice preparation. Three weeks after injection of AAV9.hSynapsin1.psychLight2 into the bed nucleus of the stria terminalis (BNST) (Figure 2.1I), we performed two-photon imaging in frame-scan mode (33 Hz) and triggered endogenous 5-HT release by electrical stimulation. The sensitivity of psychLight2 was sufficient to detect electrically evoked 5-HT release in single trials (d′ = 234.2, see Methods for details) (Figure 2.1J). Interestingly, we noticed two types of responses that differed in their amplitudes and decay rates (ΔF/F = 4.7% ± 1.5%, Tauoff fast = 0.997 ± 0.038 s and ΔF/F = 9.7% ± 1.2%, Tauoff slow = 3.998 ± 0.610 s) (Figures 2.1J

and 2.1K). The amplitude of the psychLight2 response could be enhanced by incubation with 50 μM escitalopram, a blocker of the 5-HT transporter (SERT) ($\Delta F/F = 18.4\% \pm 4.3\%$) (Figure 2.1L). Importantly, application of either the 5-HT3 receptor antagonist granisetron (10 μM) (Ko et al., 2016), the sodium channel blocker tetrodotoxin (1 μM), or ketanserin (10 μM) was sufficient to block psychLight fluorescence in response to electrically-evoked 5-HT transients (Figures 2.1L, 2.1M, S2.2C, and S2.2D).

To determine if psychLight2 could measure 5-HT dynamics in vivo, we employed a fear conditioning paradigm coupled with fiber photometry in freely behaving mice. First, AAV.hSynapsin1.psychLight2 was injected into the BNST, the basolateral amygdala (BLA), the dorsal raphe nucleus (DRN), or the orbitofrontal cortex (OFC) along with implantation of an optical fiber (Figure 2.2A). After 2–3 weeks to allow full expression of the sensor, we measured 5-HT transients during an auditory fear conditioning experiment consisting of 15 presentations of a 30-s tone co-terminating with a 1.5-s foot-shock (0.5 mA) (Figure 2.2B). In the DRN, we observed a robust increase in fluorescence intensity immediately after the onset of foot-shock (Figure 2.2C), followed by a sharp decline during the shock. These results are consistent with Ca2+ transients recorded in the DRN using GCaMP6 during auditory fear conditioning (Ren et al., 2018). In the BNST, we observed an immediate decrease in fluorescence following foot-shock that returned to baseline within 4 s (Figure 2.2D). A similar initial reduction in fluorescence was observed in both the BLA and OFC; however, in these brain regions, the initial decrease in sensor activity was followed by a considerable rise in the fluorescence signal following the shock (Figures 2.2E and 2.2F). Serotonin dynamics were

reliably detected across individual trials of the fear conditioning experiments (d′ = 12.80, 30.38, 26.28, and 32.84 for the DRN, BNST, BLA, and OFC, respectively). To further demonstrate that changes in psychLight fluorescence during fear conditioning are specific to endogenous 5-HT2AR ligands, we injected AAV.hSynapsin1.psychLight0 into all four brain regions. PsychLight0 has a key point mutation (D155A) that completely prevents agonist binding. Unlike experiments using psychLight2, we did not observe significant changes in psychLight0 fluorescence following foot-shock (Figures S**2.**2E and S**2.**2F), indicating that psychLight2 detects endogenous agonists in freely behaving animals.

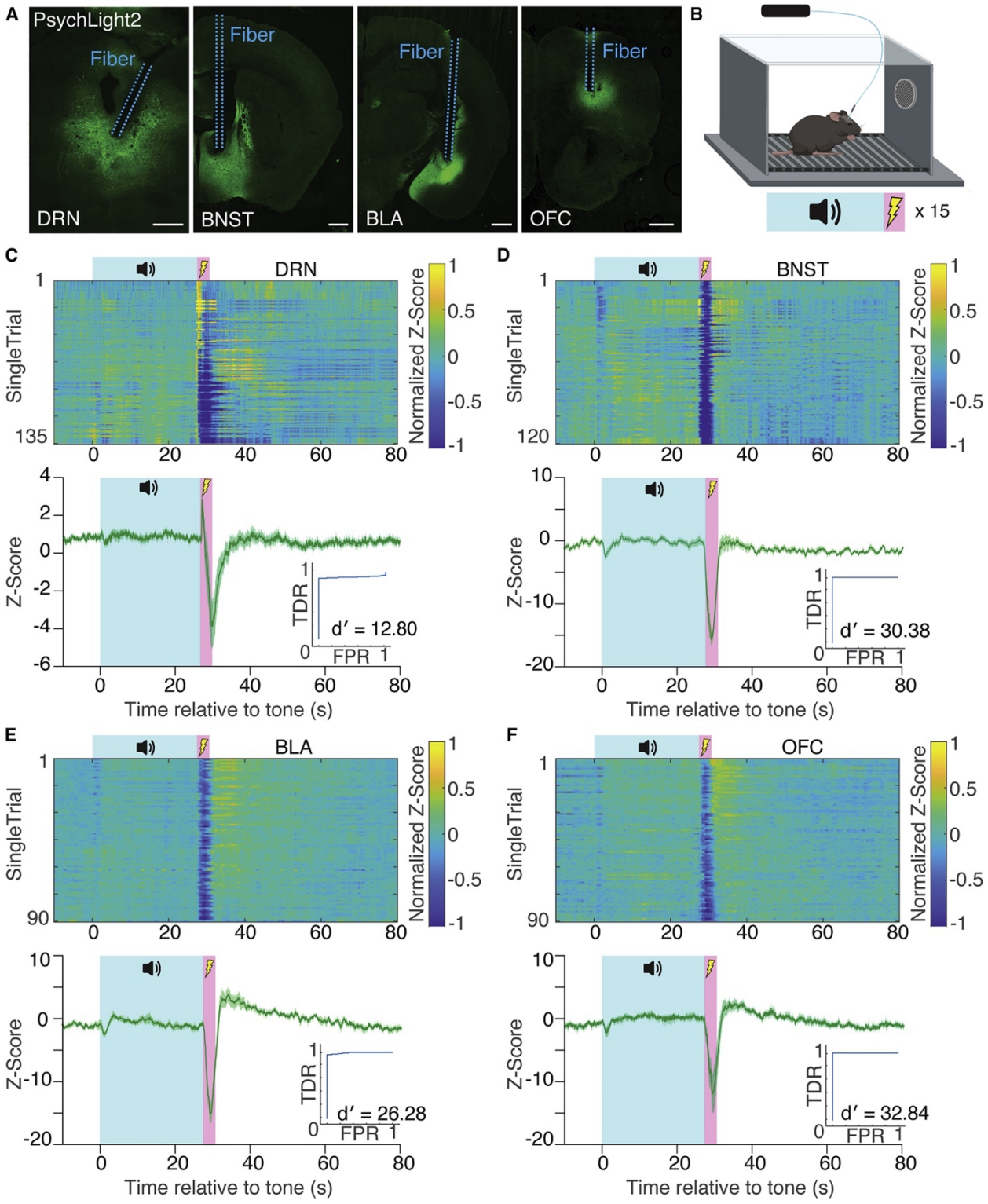

Figure 2.2. PsychLight enables the detection of endogenous serotonin dynamics during fear conditioning using fiber photometry.
(A) Expression of psychLight2 in the DRN, BNST, BLA and OFC near the location of fiber implantation. Scale bars, 500 µm.

(B) Schematic illustrating the design of auditory fear conditioning experiments (30-s tone co-terminating with a 1.5-s foot shock, n = 15 presentations).
(C–F) Single-trial heatmap and averaged-trial traces of serotonin dynamics in DRN (C, n = 135 trials from 9 animals), BNST (D, n = 120 trials from 8 animals), BLA (E, n = 90 trials from 6 animals), and OFC (F, n = 90 trials from 6 animals) in response to a tone (blue) and foot shock (pink). ROC plots indicate true detection rate (TDR) against false-positive rate (FPR), and d′ is calculated by avg(Z scoreshock)/std(Z scorebaseline). Average traces indicated by solid lines; shaded area represents SEM. DRN, dorsal raphe nucleus; BNST, bed nucleus of the stria terminalis; BLA, basolateral amygdala; OFC, orbitofrontal cortex.
See also Figures S2.2E and S2.2F and Tables S2.1 and S2.2.

(iii) Psychlight Activity Differentiates Hallucinogenic and Non-Hallucinogenic Drugs

We next sought to determine if the sensor could faithfully report 5-HT2AR activation in vivo following systemic administration of an exogenous agonist. We chose to use 5-methoxy-N,N-dimethyltryptamine (5-MeO-DMT or 5-MeO), because it produces a robust head-twitch response (HTR) (Dunlap et al., 2020)—a mouse behavior induced by hallucinogenic 5-HT2AR ligands (Halberstadt et al., 2020; Hanks and González-Maeso, 2013). Three weeks after injection of AAV9.hSynapsin1.psychLight2 into the prelimbic cortex, we administered 5-MeO-DMT (50 mg/kg, intraperitoneal [i.p.]) and measured psychLight2 response using fiber photometry (Figures 2.3A and 2.3B). Within 1 min of drug administration, we observed a sharp increase in fluorescence along with a concomitant increase in HTR. After several minutes, the psychLight signal stabilized and remained elevated while head twitch frequency decreased (Figure 2.3B). In contrast, when mice were administered vehicle or the 5-HT2AR antagonist ketanserin (KETSN, 4 mg/kg, i.p.), psychLight fluorescence remained unchanged or decreased, respectively (Figure 2.3C). These data suggest that psychLight is sensitive to both agonist- and antagonist-induced conformational changes in vivo.

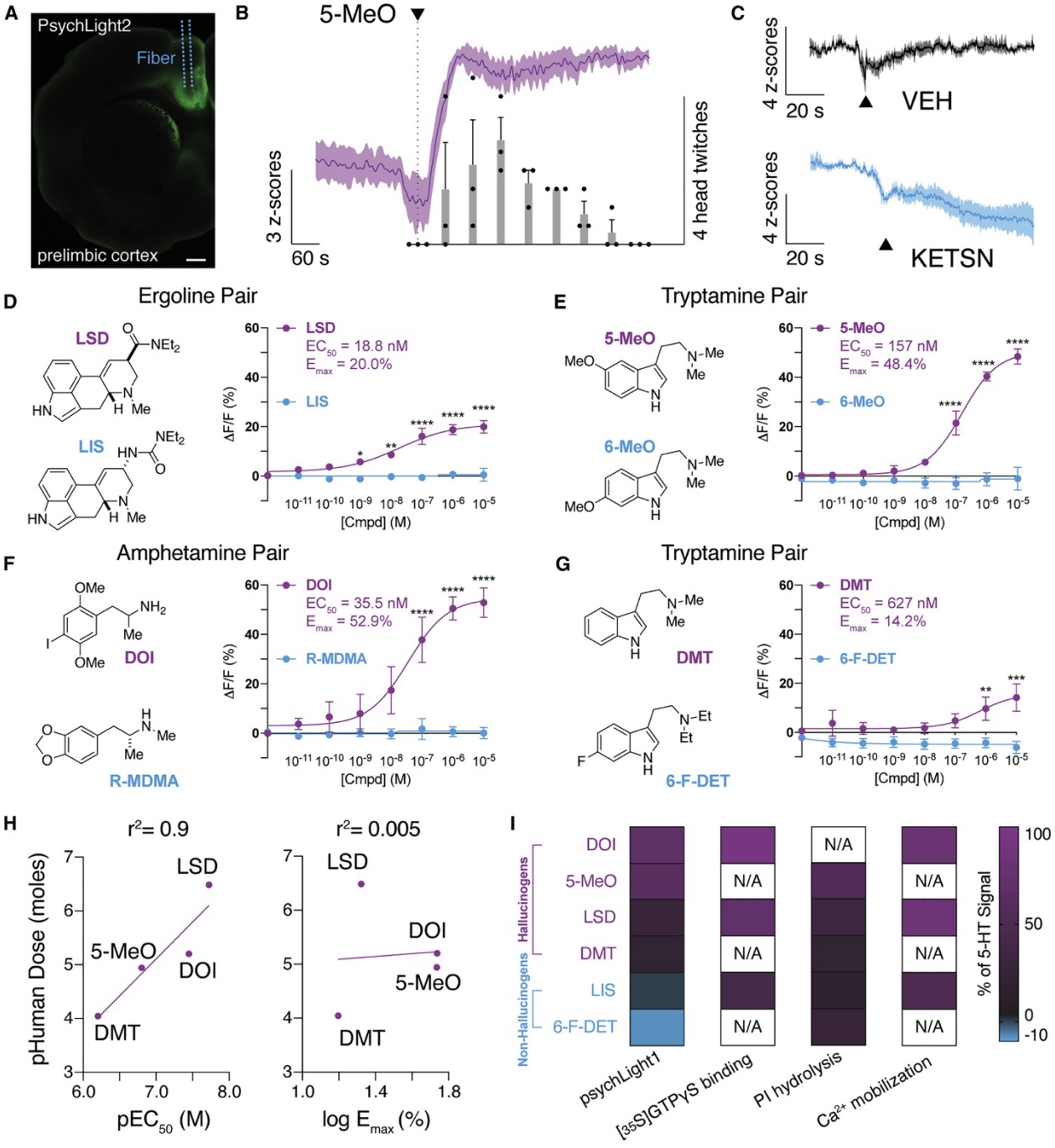

Figure 2.3. PsychLight is activated by hallucinogenic drugs *in-vivo* and *in-vitro*.
(A–C) PsychLight2 in vivo responses to drugs as measured by fiber photometry.
(A) Expression of psychLight2 in the prelimbic cortex near the site of fiber implantation. Scale bar, 500 µm.
(B) Averaged-trial traces of psychLight2 responses shown as Z score following injection of 50 mg/kg 5-MeO (magenta, i.p.). The number of head-twitch responses (bars) were also recorded and binned into 1-min intervals (n = 3 animals).
(C) Averaged-trial traces of psychLight2 responses following the injection either of the saline (VEH; top black) or an antagonist (4 mg/kg KETSN, bottom blue, i.p.) (n = 3 animals). Average traces indicated by solid lines; shaded area represents SEM.

(D–G) Concentration-response studies using HEK293T cells transiently expressing psychLight1. Hallucinogens of the ergoline, tryptamine, and amphetamine classes of psychedelics (magenta) were tested along with their non-hallucinogenic congeners (blue). Hallucinogens activated psychLight1 while their non-hallucinogenic congeners did not. n = 3 cells from 3 different cell passages; Error bars represent SEM, $*p < 0.05$, $**p < 0.01$, $***p < 0.001$, $****p < 0.0001$, compared to the non-psychedelic drug, two-way ANOVA.
(H) PsychLight1 EC50 values, but not Emax values, correlate with hallucinogen potencies in humans.
(I) PsychLight1 Emax values differentiate hallucinogens and non-hallucinogens, but other measures of 5-HT2AR activation (e.g., phosphoinositide [PI] hydrolysis, Ca2+ mobilization, [35S]GTPγS binding) do not. Data represented by the heatmap with a double color gradient from values above 0 (magenta to black) and data below 0 (black to blue). Data are normalized to 5-HT values within each experiment. Data for PI hydrolysis, Ca2+ mobilization, and [35S]GTPγS binding were obtained from previous reports (Cussac et al., 2008; Rabin et al., 2002). PI hydrolysis data for 6-F-DET were estimated based on graphical data presented in Rabin et al. (2002). N/A indicates that the data are not available.
See also Figures S2.3A and S2.3B and Tables S2.1 and S2.2.

We next assessed the sensor's ability to differentiate between known hallucinogenic agonists and structurally similar non-hallucinogenic analogs. We tested several pairs of hallucinogenic and non-hallucinogenic congeners representing the ergoline, tryptamine, and amphetamine classes of psychedelics. We chose these compounds because the propensity of these drugs to produce hallucinations in humans was known (Benes et al., 2006; Dunlap et al., 2018; Halberstadt et al., 2020; Kalir and Szara, 1963) or inferred from data using well-established rodent models of 5-HT2AR-induced hallucinations (Hanks and González-Maeso, 2013), such as rat drug discrimination (DD) (Glennon et al., 1983) and mouse HTR assays (Dunlap et al., 2020), which correlate exceptionally well with hallucinogenic potency in humans (Halberstadt et al., 2020).

All four hallucinogenic compounds activated psychLight1 when expressed in HEK293T cells, with half maximal effective concentrations ranging from 18.8–627 nM (LSD, EC50 = 18.8 nM, Emax = 20.0%; 5-MeO, EC50 = 157 nM, Emax = 48.4%; DOI, EC50 = 35.5 nM, Emax = 52.9%; and DMT, EC50 = 627 nM, Emax = 12.4%). In sharp contrast, none of the non-hallucinogenic congeners were able to increase the sensor's response, even at concentrations as high as 10 μM (Figures 2.3D–2.3G). By running the assay in

antagonist mode, we were able to demonstrate that non-hallucinogenic compounds such as lisuride (LIS) and 6-MeO-DMT (6-MeO) are capable of binding to the receptor despite lacking efficacy (Figures S2.3A and S2.3B). The large Emax differences between the hallucinogenic and non-hallucinogenic compounds within a given pair are remarkable given the extremely high degree of structural similarity between the paired molecules.

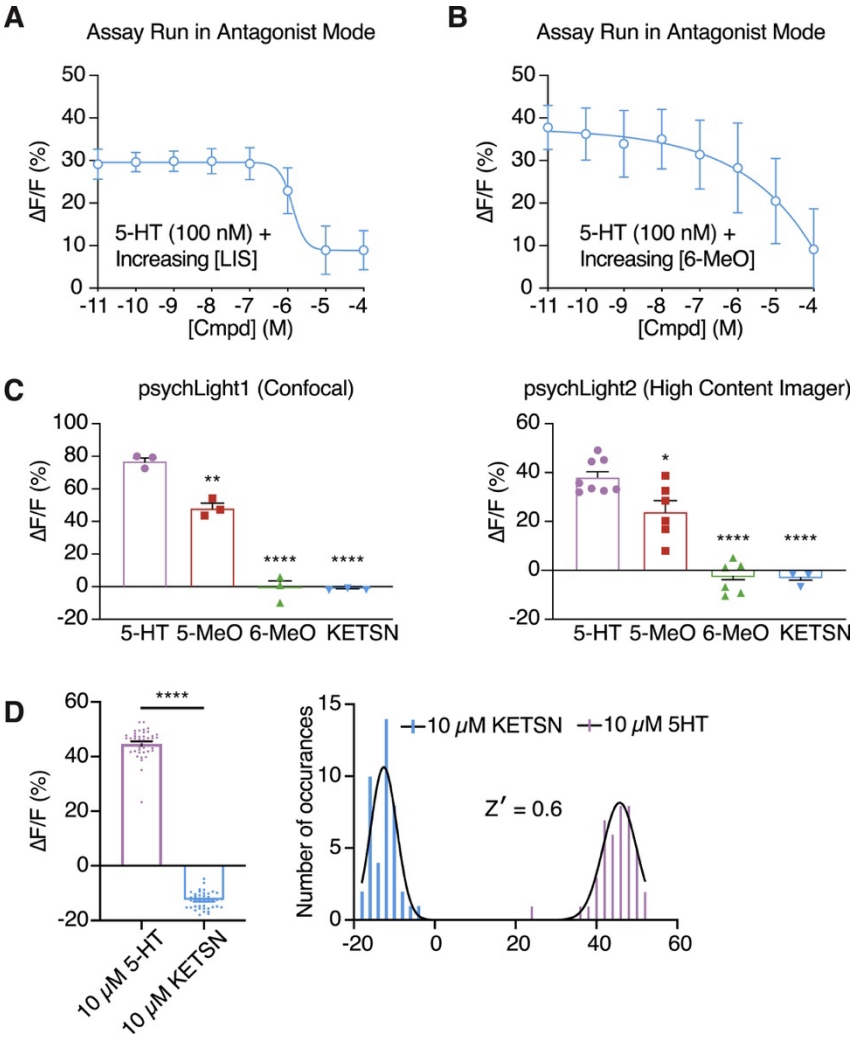

Figure S2.3. Confocal imaging of psychLight1-expressing HEK293T cells after compound treatments and PSYLI2 characterization, related to Figures 2.3 and 2.4.

A–B. The non-hallucinogenic ligands lisuride .(A) and 6-MeO-DMT (B) can compete off 5-HT resulting in a reduction in psychLight fluorescence.

C. PsychLight1 and psychLight2 respond similarly to positive controls (i.e., 5-HT or 5-MeO-DMT at 10 μM) and negative controls (i.e., 6-MeO-DMT or ketanserin at 10 μM). The fluorescence intensities of psychLight1 and psychLight2 were measured using a confocal microscope and a high content imager, respectively (Confocal with psychLight1: psychLight15-HT = 77.3 ± 2.4%, n = 3; psychLight15-MeO = 48.4 ± 3.1%, n = 3;

psychLight16-MeO = −1.1 ± 4.6%, n = 3; psychLight1KETSN = −1.7 ± 0.3%, n = 3. High content imager with psychLight2: psychLight25-HT = 38.2 ± 2.4%, n = 8; psychLight25-MeO = 24.1 ± 4.6% n = 6; psychLight26-MeO = −3.0 ± 2.7%, n = 6; psychLight2KETSN = −3.5 ± 1.6%), n = 3. ****p < 0.0001, **p < 0.01 and *p < 0.05, one-way ANOVA compared to 5-HT with Dunnett's test.
D. Bar graph showing PSYLI2 response to 10 μM 5-HT (44.8 ± 0.8%) and 10 μM KETSN (−12.7 ± 0.5%), and frequency distribution of both positive (magenta, 5-HT) and negative (blue, KETSN) control treatments (Z-factorPSYLI2 = 0.6), n = 42. ****p < 0.0001, unpaired t test.

PsychLight1 potencies, but not efficacies, correlate exceptionally well with hallucinogenic potencies in humans (r2 = 0.9) (Figure 2.3H). This strong correlation is noteworthy considering the error associated with estimating hallucinogenic potencies in humans and the fact that our cellular assay does not account for potential differences in pharmacokinetics. Furthermore, ligand activation of psychLight1 appears to be distinct from other measures of 5-HT2AR activation including phosphoinositide hydrolysis (Cussac et al., 2008), Gq activation (Rabin et al., 2002), and calcium mobilization (Cussac et al., 2008) (Figure 2.3I).

(iv) Development of a Psychlight-Based Medium-Throughput Pharmacological Assay

To enable medium-throughput identification of hallucinogenic designer drugs of abuse as well as non-hallucinogenic therapeutics targeting 5-HT2ARs, we developed a screening platform based on wide-field high content imaging of a HEK293T cell line stably expressing psychLight2 (PSYLI2) under the EF1α promoter (Figures 2.4A and S2.4A). Relative responses were similar using either a confocal microscope or high content imager (Figure S2.3C). A Z-factor (Zhang et al., 1999) was generated using serotonin and ketanserin as positive and negative controls, respectively (Z factor = 0.6, n = 42) (Figure S2.3D).

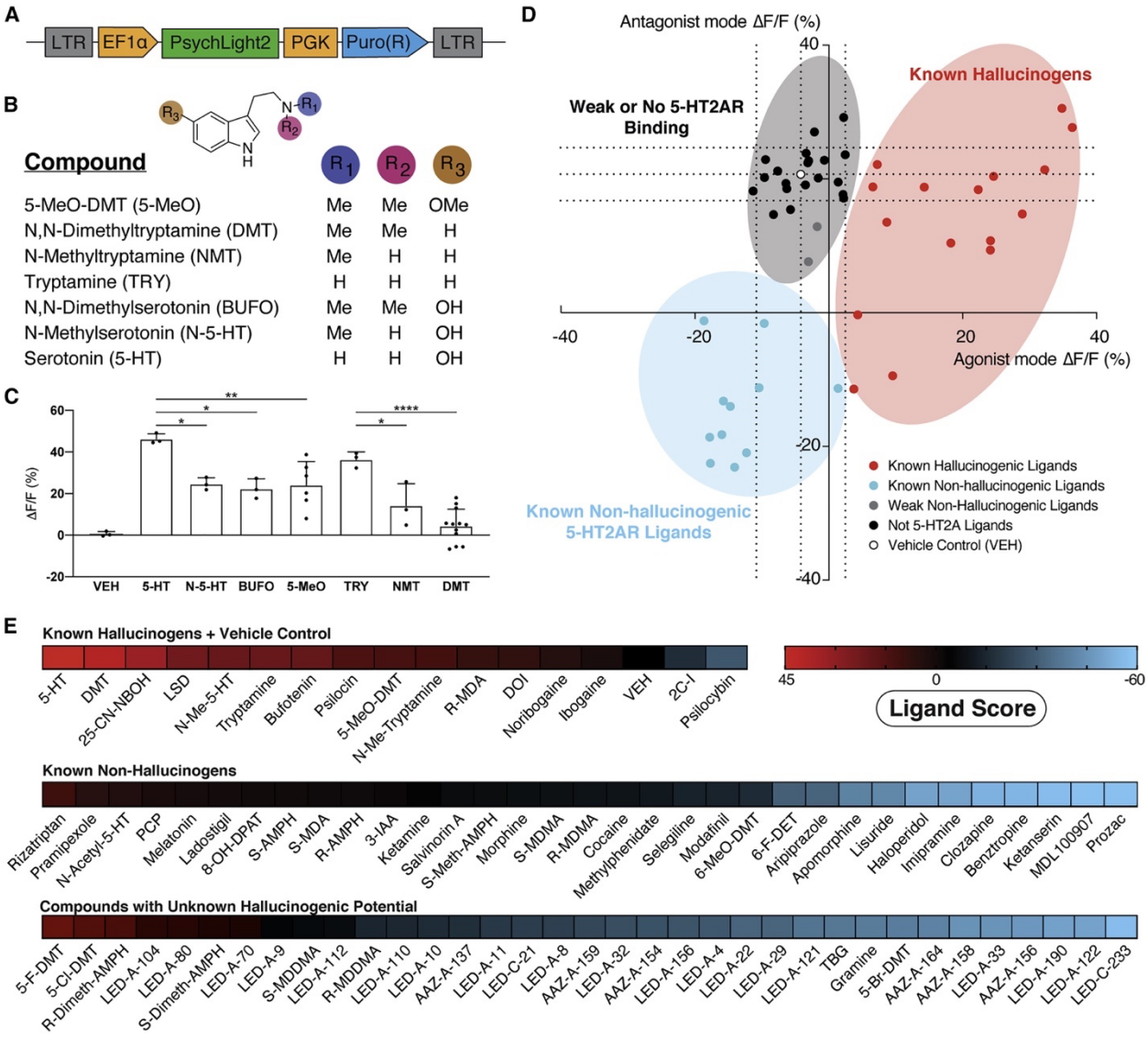

Figure 2.3. Development of a medium-throughput psychLight-based pharmacological assay.
(A) A lentivirus expressing psychLight2 under the EF1α promoter was used to engineer a HEK293T cell line stably expressing psychLight2 (PSYLI2) (see Methods for details).
(B and C) Structure-function studies using a variety of structurally related tryptamines.
(B) Structures of compounds.
(C) PSYLI2 fluorescence in response to compound treatments (10 μM). Data are represented by mean ± SEM, ****$p < 0.0001$, **$p < 0.01$ and *$p < 0.05$, one-way ANOVA multiple comparison with Tukey's test.
(D) A series of hallucinogenic and non-hallucinogenic compounds with known 5-HT2AR affinities were tested in agonist (abscissa) and antagonist (ordinate) modes. Dotted lines represent 1 SD from the VEH control (white). Hallucinogenic and non-hallucinogenic 5-HT2AR ligands are shown in red and blue, respectively. Compounds with weak affinity for the 5-HT2AR (~1–10 μM) are shown in gray, whereas compounds that are known to not bind to the 5-HT2AR are shown in black. Dots indicate averaged ΔF/F values (n = 3 replicates from 3 passages of cells).
(E) Heatmap of ligand scores (see Methods for details). Ligand scores greater than 0 indicate compounds more likely to be hallucinogenic while scores less than 0 indicate compounds that are more likely to be non-hallucinogenic ligands of the 5-HT2AR.
See also Figures S2.3C, S2.3D, S2.4, S2.5, and S2.6A–S2.6D and Tables S2.1 and S2.2.

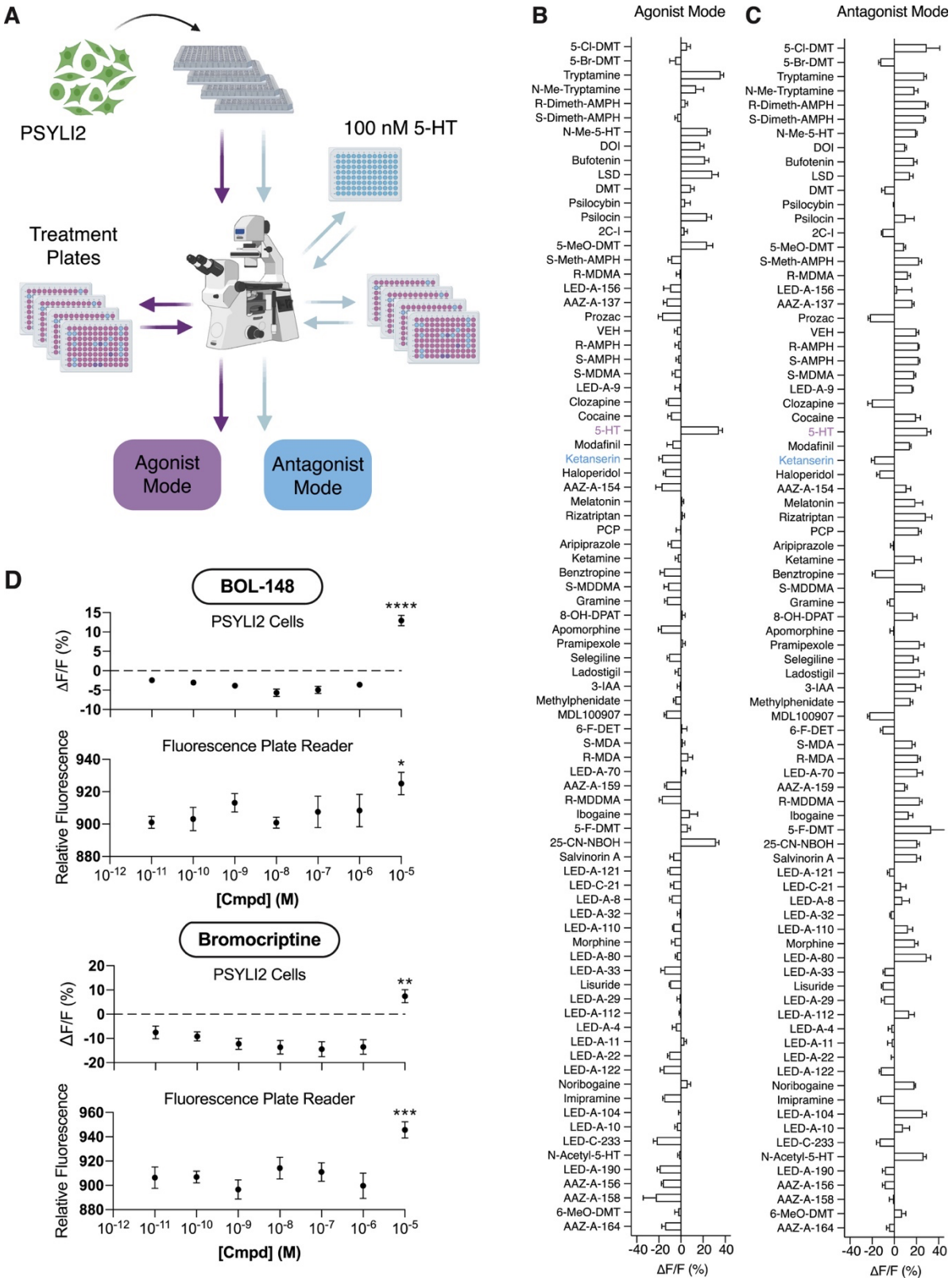

Figure S2.4. Characterization of PSYLI2 cells and their use in high content screening, related to Figure 2.3.

A. Schematic depicting the workflow for a screening campaign using both agonist and antagonist modes.
B. Agonist mode screen of a compound library using PSYLI2 cells.
C. Antagonist mode screen of a compound library using PSYLI2 cells.
D. Concentration-response studies using PSYL2 cells (top) and a cell free wells (bottom) reveal that BOL-148 and bromocriptine produce fluorescence artifacts at 10 μM (****$p < 0.0001$, ***$p < 0.001$, **$p < 0.01$ and *$p < 0.05$, one-way ANOVA compares to parent variant within the group with Dunnett's test). Data are represented as mean ± SEM 5-HT = 5-hydroxytryptamine; KETSN = ketanserin; BOL-148 = 2-bromolysergic acid diethylamide.

To assess the sensitivity of this assay, we first tested a panel of ligands with similar molecular structures to 5-HT (Figure 2.3B). We observed that subtle differences in ligand structure can significantly modulate the fluorescence signal generated by PSYLI2 cells (Figure 2.3C). Most notably, increasing N-methylation tends to reduce the magnitude of the sensor response (e.g., 5-HT: $\Delta F/F = 46.3\% \pm 1.4\%$; N-methylserotonin, N-5-HT: $\Delta F/F = 24.6\% \pm 1.7\%$; and N,N-dimethylserotonin, BUFO: $\Delta F/F = 22.3\% \pm 2.8\%$), which is consistent with a structure-activity relationship previously reported for 5-HT2AR-induced accumulation of [3H]inositol phosphates (Ebersole et al., 2003). Surprisingly, the hydroxyl substituent of 5-HT does not appear to be necessary for achieving full agonism as tryptamine produces a robust response (Figure 2.3C).

Next, we screened a library of eighty-three compounds consisting of known hallucinogens (as defined by human data or predicted based on the mouse HTR and/or DD assays), known non-hallucinogenic 5-HT2AR ligands, psychoactive drugs with unknown 5-HT2AR affinity, and compounds from our medicinal chemistry program (Figures S2.4B, S2.4C, and S2.5; see Methods for details). When the assay was performed in agonist mode (Figure 2.3D, abscissa), serotonergic hallucinogens reliably gave a response of greater than +1 SD from the vehicle control (Figures 2.4D and S2.4B). Non-hallucinogenic 5-HT2AR ligands did not activate the sensor in agonist mode but

decreased fluorescence in antagonist mode (Figure 2.3D, ordinate). Compounds that do not bind to the 5-HT2AR did not produce a response in either agonist or antagonist mode.

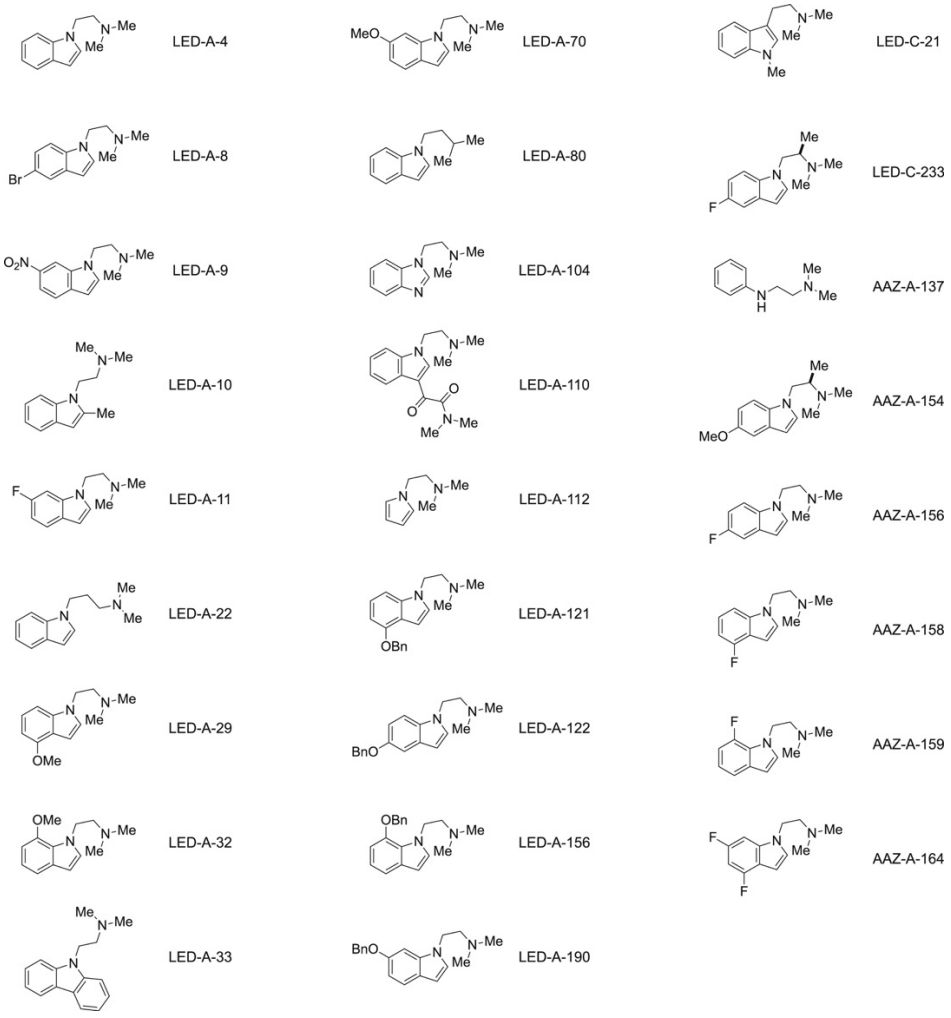

Figure S2.5. Chemical structures of compounds synthesized in house, related to Figure 2.3.
Syntheses and characterization data for compounds are shown in the supporting information.

When screened at 10 μM using PSYLI2 cells, 2-bromolysergic acid diethylamide (BOL-148) and bromocriptine produced unexpected fluorescence signals, because these compounds are widely believed to be non-hallucinogenic. Given that both compounds contain a two-bromoindole structural motif, we suspected that the inherent fluorescence of these molecules was resulting in false-positive signals. Therefore, we performed concentration-response experiments in PSYLI2 cells using a high content imager and

under cell-free conditions using a fluorescence plate reader (Figure S2.4D). The results confirmed our hypothesis that the signal from BOL-148 and bromocriptine at 10 μM was due to the inherent fluorescence of these compounds, and not due to activation of the sensor.

By running the assay in both agonist and antagonist mode (i.e., 100 nM 5-HT with 10 μM test compound), we were able to distinguish between non-hallucinogenic ligands of the 5-HT2AR and compounds that do not bind to the receptor (Figures 2.4D, 2.4E, and S2.4C). We combined data from agonist and antagonist modes to define a "ligand score" (see Methods for details); positive and negative ligand scores indicated likely hallucinogenic and non-hallucinogenic ligands of the 5-HT2AR, respectively, whereas values close to zero indicated compounds that were unlikely to be 5-HT2AR ligands (Figure 2.3E). For example, the ligand scores for LSD and lisuride were 23.0 and −42.3, respectively. In contrast, non-serotonergic hallucinogens/dissociatives such as salvinorin A, ketamine, and phencyclidine displayed ligand scores close to 0 (Figure 2.3E).

Finally, to further characterize the pharmacological profiles of non-hallucinogenic ligands, we performed Schild regression analysis for several compounds with negative ligand scores (Figures S2.6A–S2.6D). The pA2 values indicate that LIS, apomorphine, and benztropine are potent psychLight competitive antagonists, whereas 6-MeO is significantly less potent (Figures S2.6A–S2.6D).

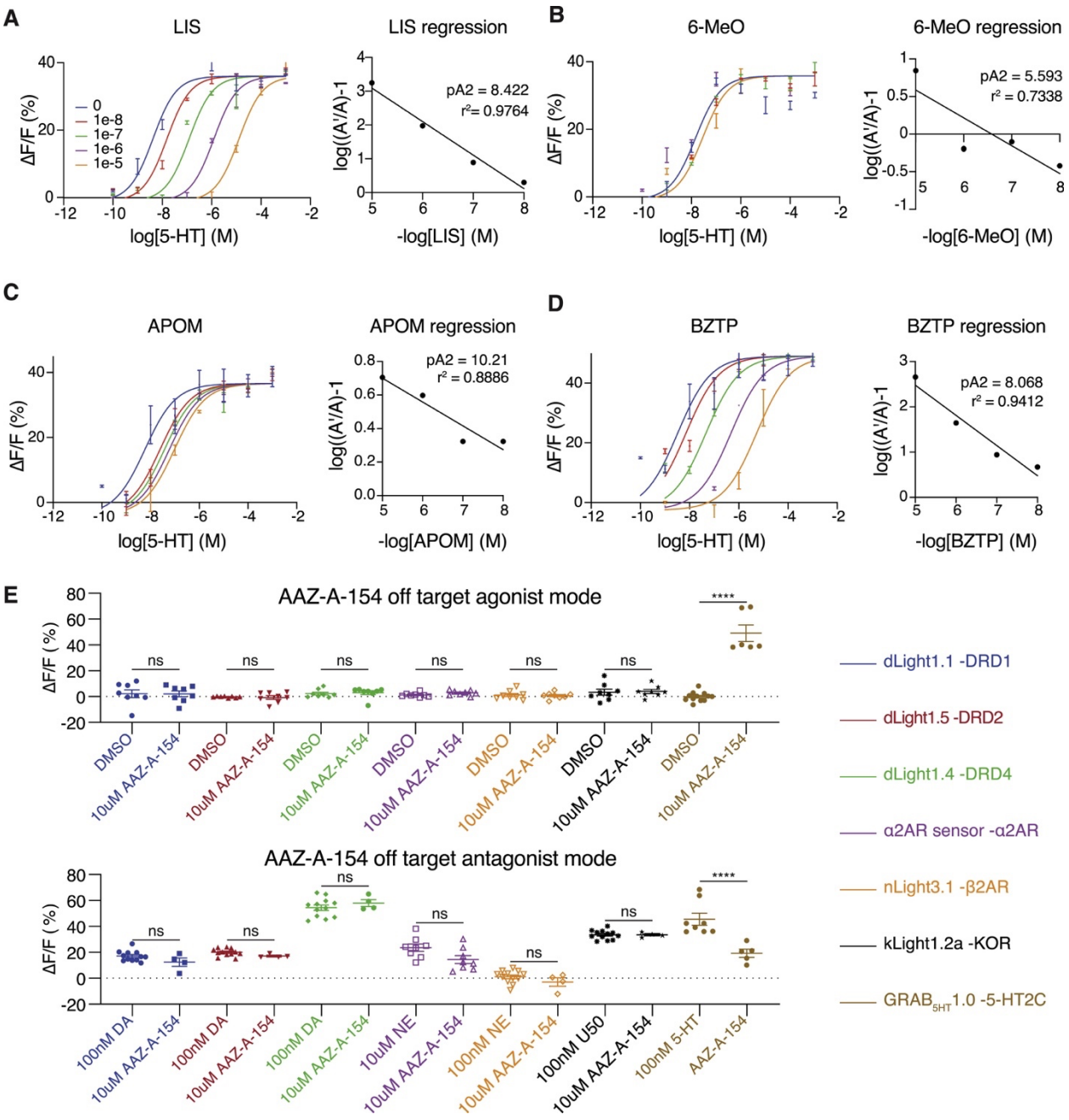

Figure S2.6. Schild regression analysis for non-hallucinogenic 5-HT2AR ligands and off target characterization for AAZ-A-154, related to Figures 2.4 and 2.5.

A–D. Schild analysis using 5-HT (100 nM) as the agonist and 4 concentrations of non-hallucinogenic compounds (i.e., LIS, 6-MeO, apomorphine, benztropine). LIS = lisuride, 6-MeO = 6-MeO-DMT, APOM = apomorphine, BZTP = benztropine.

E. Data from agonist and antagonist mode of 7 receptor-based sensors (Agonist mode: 0.1% DMSO or 10 μM AAZ-A-154 was added; Antagonist mode: 0.1% DMSO or 10uM AAZ-A-154 was added in the presence of 100 nM dopamine (DA), norepinephrine (NE), U-50488 (U50) or serotonin(5-HT)). ****$p < 0.0001$, ns $p > 0.05$. One-way ANOVA. Tukey's multiple comparisons test.

(v) Psychlight Accurately Predicts the Hallucinogenic Potentials of Designer Drugs

We next screened a small library consisting of thirty-four compounds with unknown hallucinogenic potentials (Figure 2.3E). By assessing ligand scores, we predicted that the smaller 5-F-DMT and 5-Cl-DMT would be hallucinogenic, while the larger 5-Br-DMT would not (Figures 2.4E and 2.5A). To confirm this prediction in vivo, we performed a three-point dose-response study measuring HTR (Figure 2.5B). As expected, both 5-F-DMT and 5-Cl-DMT produced robust HTRs, while 5-Br-DMT failed to induce HTRs at any dose (Figure 2.5B). Interestingly, the effects of the compounds on locomotion and the HTR were not correlated (Figure 2.5C). The 5-halo-DMT series really highlights the power of psychLight for detecting profound functional differences between compounds that share a high degree of structural similarity.

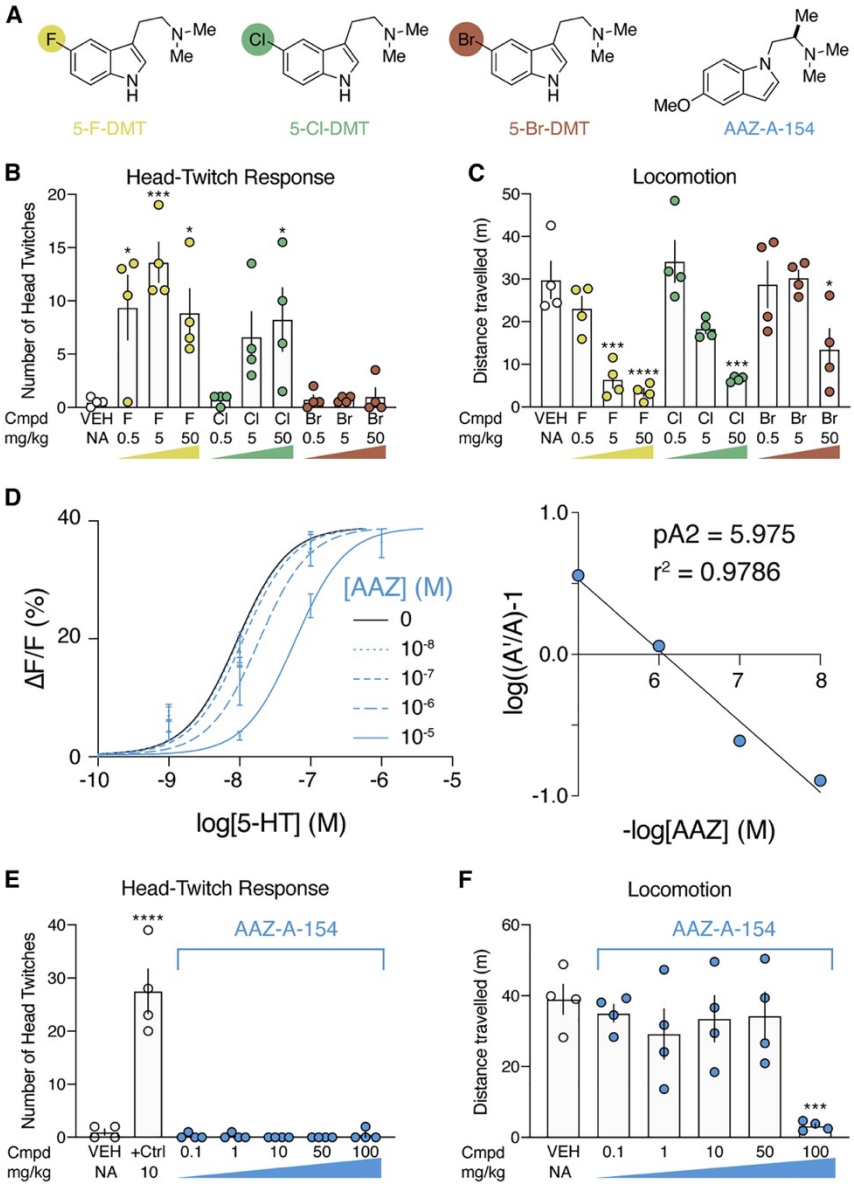

Figure 2.5. PsychLight accurately predicts hallucinogenic potentials of previously untested compounds.
(A) Structures of 5-halo-DMT derivatives and AAZ-A-154. Colored circles indicate the relative size of the halogen atom compared to each other
(B) Both 5-F-DMT and 5-Cl-DMT produce positive ligand scores and induce head-twitches in mice. In contrast, 5-Br-DMT produces a negative ligand score and does not induce a HTR (n = 4 mice).
(C) All 5-halo-DMTs produce dose-dependent decreases in locomotion (n = 4 mice).
(D) Schild regression analysis reveals that AAZ-A-154 is a psychLight competitive antagonist (n = 3 replicates from 1 passage of cells).
(E) AAZ-A-154 does not trigger a HTR at any dose compared to that triggered by 5-MeO-DMT (n = 4 mice).
(F) AAZ-A-154 only decreases locomotion at a very high dose (100 mg/kg) (n = 4 mice). Data are represented as mean ± SEM. ****p < 0.0001, ***p < 0.001, and *p < 0.05, versus the vehicle control, one-way ANOVA with Dunnett's test.
See also Figure S2.6E and Tables S2.1 and S2.2.

Next, we sought to use psychLight to identify non-hallucinogenic 5-HT2AR ligands occupying previously unknown chemical space. Because AAZ-A-154 (Figure 2.5A) had never been reported in the literature and exhibited a favorable ligand score, we subjected it to further testing. Schild regression analysis revealed that AAZ-A-154 functions as a psychLight competitive antagonist (Figure 2.5D). Using a panel of GPCR-based sensors (e.g., dopamine, adrenergic, opioid, and serotonin receptors) (Patriarchi et al., 2018; Wan et al., 2021) in both agonist and antagonist mode, we observed that AAZ-A-154 exhibits high selectivity for 5-HT2 receptors (Figure S2.6E). To assess the hallucinogenic potential of AAZ-A-154 in vivo, we performed HTR experiments across multiple doses in mice. As expected, AAZ-A-154 failed to produce any head-twitches, even up to doses as high as 100 mg/kg (Figure 2.5E). However, a high dose of AAZ-A-154 decreased locomotion (Figure 2.5F), indicating that this compound can still impact behavior without producing hallucinogenic effects.

(vi) Characterizing the Antidepressant-Like Effects of AAZ-A-154

Given its similar structure to several known psychoplastogens (Ly et al., 2018), we tested the ability of AAZ-A-154 to promote dendritic outgrowth in cultured rat embryonic cortical neurons (Cameron et al., 2021; Dunlap et al., 2020). Treatment with AAZ-A-154 increases dendritic arbor complexity to a comparable extent as the fast-acting antidepressant ketamine (KET) (Figures 2.6A and 2.6B). This psychoplastogenic effect was abolished by the 5-HT2R antagonist ketanserin (KETSN) (Figure 2.6C), suggesting

that AAZ-A-154 triggers dendritic growth through activation of 5-HT2Rs.

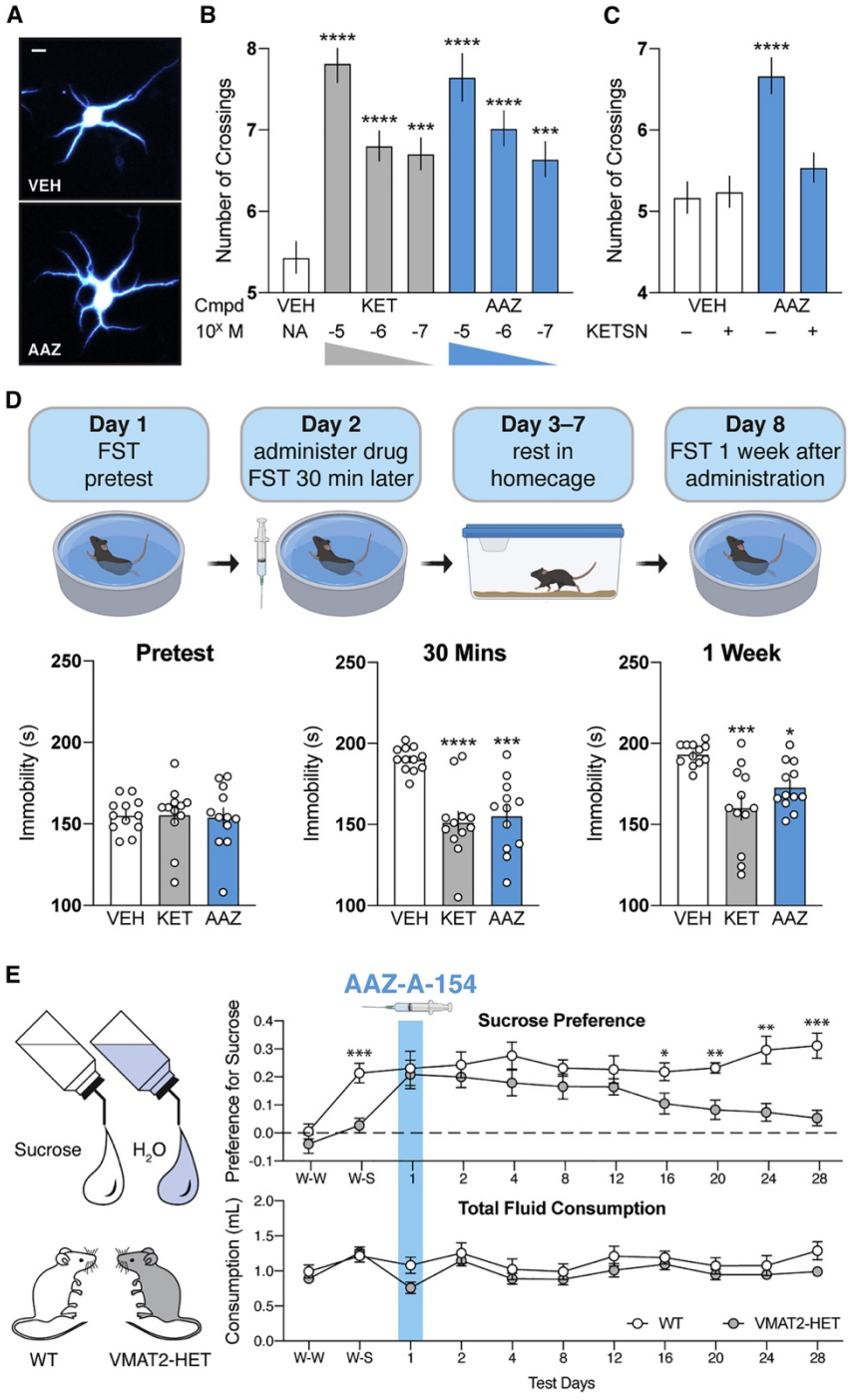

Figure 2.6. A predicted non-hallucinogenic compound with antidepressant potential.
(A) Representative images demonstrating that AAZ-A-154 promotes dendritic branching. Scale bar, 20 µm.
(B) Maximal number of crossings (Nmax) from Sholl plots (n = 51–60 neurons). ****p < 0.0001, ***p < 0.001, one-way ANOVA with Dunnett's test.
(C) The effects of AAZ (100 nM) on dendritic growth can be blocked by the 5-HT2R antagonist ketanserin (KETSN, 1 µM, n = 39–58 neurons). ****p < 0.0001, one-way ANOVA with Dunnett's test.

(D) Schematic depicting the forced swim test design. AAZ-A-154 (20 mg/kg) produces fast (30 min) and long-lasting (1 week) antidepressant-like effects in the FST comparable to ketamine (KET) (n = 12). ∗∗∗∗p < 0.0001, ∗∗∗p < 0.001, and ∗p < 0.05, one-way ANOVA with Dunnett's test
(E) Sucrose preference test reveals that AAZ (15 mg/kg) reduces anhedonia in VMAT2-HET mice for at least 12 days. W-W, water-water pairing; W-S, water-sucrose (1%) pairing. When given the choice between water and a 1% sucrose solution (W-S), only WT mice displayed a sucrose preference. Total fluid consumption was not different between genotypes at any time point. n = 11 mice/genotype; data are represented as means and SEMs, ∗∗p < 0.01 and ∗p < 0.05, WT versus VMAT2-HET, repeated-measures ANOVA with Bonferroni corrected pairwise comparisons.
See also Tables S2.1 and S2.2.

Hallucinogenic and dissociative psychoplastogens, are known to produce both rapid and sustained antidepressant effects (Olson, 2018). Because AAZ-A-154 is not predicted to produce hallucinations (Figures 2.4E and 2.5E), we were interested in assessing its antidepressant potential in vivo using behavioral assays relevant to active stress-coping strategies (i.e., forced swim test) and anhedonia (i.e., sucrose preference).

AAZ-A-154 decreased immobility in the forced swim test (FST) (Figure 2.6D)—an effortful behavioral response commonly produced by other known psychoplastogens (Cameron et al., 2018) and antidepressants such as ketamine (Li et al., 2010). In these studies, we utilized C57BL/6J mice, because this strain does not respond robustly to traditional antidepressants such as selective serotonin reuptake inhibitors (SSRIs) or tricyclics (Hascoët and Bourin, 2009), thus highlighting the similarity between AAZ-A-154 and next-generation antidepressants like ketamine. AAZ-A-154 produced both rapid (30 min) and long-lasting (1 week) antidepressant-like effects after a single administration (Figure 2.6D).

To determine if AAZ-A-154 could ameliorate anhedonia, we used VMAT2 heterozygous (VMAT2-HET) mice. We chose this animal model of depression because pharmacological inhibition of VMAT2 precipitates depressive-like behaviors in humans, and VMAT2-HET mice display several depressive phenotypes including a reduced

preference for a 1% sucrose solution over water alone (Fukui et al., 2007). At baseline, the wild-type (WT) animals displayed a strong preference for the sucrose solution whereas the VMAT2-HET mice did not (Figure 2.6E). However, immediately following a single administration of AAZ-A-154, the VMAT2-HET mice exhibited a sucrose preference that was indistinguishable from WT controls. This anti-anhedonic effect persisted for at least 12 days before the treated VMAT2-HET animals began to display reduced sucrose preference (Figure 2.6E). Notably, the change in sucrose preference observed for the VMAT2-HET mice cannot be attributed to differential fluid consumption because both genotypes drank similar volumes of liquids across the entire experiment (Figure 2.6E). Moreover, the effects of AAZ-A-154 cannot be ascribed to increasing sucrose palatability, because AAZ-A-154 did not modify sucrose preference in the WT animals (Figure 2.6E). Taken together, these results suggest that psychLight can be used to identify both hallucinogenic and non-hallucinogenic ligands of the 5-HT2AR.

Discussion

We developed psychLight as a 5-HT2AR-based fluorescent sensor capable of measuring endogenous 5-HT dynamics and detecting hallucinogenic conformations of the receptor. PsychLight exhibits millisecond off kinetics, which enabled us to detect time-dependent release/reuptake of 5-HT ex vivo and in vivo. Interestingly, we observed both fast and slow decaying 5-HT signals in acute BNST slices following electrical stimulation. However, it is unclear what causes the differential 5-HT time courses, although an SSRI can increase the amplitude of the response and slow reuptake. Compared to iSeroSnFR (Unger et al., 2020), psychLight displayed a much higher

apparent affinity even with a relatively smaller dynamic range. These intrinsic properties may make psychLight extremely useful for reporting low concentration events, although psychLight is likely to become fully saturated following a massive release of 5-HT. Together with existing genetically encoded indicators (Unger et al., 2020; Wan et al., 2021), we anticipate that psychLight will prove essential for fully understanding the effects of endogenous 5-HT on brain function. Future side-by-side comparisons of the sensors' properties under identical experimental conditions across various species will provide useful information to guide which sensor to choose for a particular in vivo application.

Unlike existing serotonin sensors, psychLight is based on the 5-HT2AR, which plays an essential role in the hallucinogenic effects of psychedelics. Thus, the fluorescence changes of psychLight correlate with ligand-induced conformational changes specific to serotonergic hallucinogens. This is a unique feature of psychLight compared to other 5-HT sensors. In fact, iSeroSnFR exhibits low affinity for many hallucinogenic 5-HT2AR ligands (Unger et al., 2020). In principle, extensive binding pocket engineering of iSeroSnFR could produce a sensor specific for a single hallucinogenic compound, but such a sensor would not be generalizable to the broad class of structurally diverse serotonergic hallucinogens. PsychLight solves this issue by directly measuring conformational changes of the 5-HT2AR—a receptor that is activated by a wide range of diverse serotonergic hallucinogens including tryptamines, ergolines, and amphetamines. This direct measurement of 5-HT2AR conformational change overcomes the limitations of existing methods, which either provide a snap-shot view of the interaction or depend on slow, indirect secondary signaling (González-Maeso et al., 2007). However, to fully

understand the action of biased 5-HT2AR ligands at the molecular level, the structures of psychLight bound to activating and inactivating ligands will be essential. Determining the spatial and temporal kinetics of ligand-receptor interactions and correlating this information to downstream signaling will provide additional insight into ligands' molecular and cellular mechanisms of action.

PsychLight fills the gap between in vitro testing of novel compounds and in vivo behavioral studies. To date, labor-intensive and costly rodent HTR and DD assays have been the most commonly used methods to assess the hallucinogenic potentials of novel compounds (Halberstadt et al., 2020). González-Maeso et al. (2007) have demonstrated that hallucinogenic and non-hallucinogenic 5-HT2AR ligands induce distinct immediate early gene expression patterns and may differentially activate 5-HT2AR-mGluR2 heterodimers (González-Maeso et al., 2007, 2008). However, these results have yet to be developed into a reliable cellular assay capable of differentiating between hallucinogenic and non-hallucinogenic congeners across a wide range of chemical structures. Using psychLight, hallucinogenic potential can be rapidly assessed in cells through direct fluorescence readout, enabling the identification of potential hallucinogens at an early stage in the drug discovery process. We predict that this assay will be easily adapted to a 384-well format and will complement additional orthogonal GPCR assays (e.g., Ca2+ flux, G protein activation, β-arrestin activation, cAMP production, etc.).

PsychLight can be used to identify non-hallucinogenic 5-HT2AR antagonists (e.g., antipsychotics like clozapine) or non-hallucinogenic biased agonists (e.g., LIS). Non-hallucinogenic psychoplastogens have emerged as an incredibly exciting class of 5-

HT2AR ligands given the broad implications that neural plasticity-promoting compounds have for treating a variety of brain disorders (Cameron et al., 2021; Dunlap et al., 2020). We used psychLight to identify AAZ-A-154—a non-hallucinogenic analog of a psychedelic compound occupying previously unknown chemical space that promotes neuronal growth and produces long-lasting (>2-week) beneficial behavioral effects in rodents following a single administration. Tabernanthalog (TBG) is the only other known non-hallucinogenic psychoplastogen with antidepressant-like properties (Cameron et al., 2021), and TBG has a similar ligand score as AAZ-A-154 (Figure 2.3E). In vivo, it appears that AAZ-A-154 may be more potent than TBG while producing more sustained antidepressant effects.

To date, the precise mechanisms of action of hallucinogens at molecular and circuit levels remain largely unknown (Aghajanian and Marek, 1999; Preller et al., 2018). Genetic tools including reporters, sensors, and effectors that enable the monitoring and manipulation of neuronal activity will be useful for dissecting the circuits involved in hallucinogenic versus antidepressant effects. Furthermore, the identification of functionally selective GPCR ligands will be key to the advancement of future therapeutics targeting this class of receptors. The development of psychLight outlines a general strategy for achieving this goal by directly measuring distinct, behaviorally relevant, ligand-induced conformational changes.

Author Contributions

D.E.O. and L.T. conceived the project, supervised its execution, and assisted with data analysis. C.D. developed psychLight1 and psychLigth2 and engineered PSYLI2. C.D.

and C.L. designed the assay and screened the compounds. L.E.D. and A.A. synthesized the compounds in the medicinal chemistry library. C.D., C.L., and L.E.D. performed the HTR experiments for the halo-DMTs. M.V.V. performed the FST and HTR experiments for AAZ-A-154. W.C.W. supervised the sucrose preference experiments in the VMAT2-HET mice and the statistical analyses. W.C.O. and I.-W.H. performed the two-photon uncaging experiments. J.S. performed ex vivo recording. CD performed the fiber photometry experiments. C.D., C.L., L.E.D., D.E.O., and L.T. wrote the manuscript with input from W.C.O. and W.C.W.

Acknowledgments

We thank Dr. Yiyang Gong (Duke University) for helping out with d′ analysis. We also thank Mr. Christopher Means and Dr. Ramona Rodriguiz for conducting and analyzing the sucrose preference experiment (Duke University). We also thank Kyle Puhger (UC Davis) and Dr. Brian Wiltgen (UC Davis) for providing critical suggestions on fiber-photometry data analysis. We thank Drs. Michael Bruchas (University of Washington), Henry Lester (CalTech), and Bruce Cohen (CalTech) for providing critical suggestions on pA2 analysis. Some graphic components were created with BioRender.com. This project used the Biological Analysis Core of the UC Davis MIND Institute Intellectual and Development Disabilities Research Center (U54 HD079125). Several of the drugs used in this study were provided by the NIDA Drug Supply Program. This work was supported by funds from the National Insitute of Health (R01GM128997 to D.E.O.; DP2MH107056, U01NS090604, U01NS013522, U01NS103571, and R01MH101214 to L.T.; and R01MH12478 and R21MH126073 to W.C.O.), a Hellman

Fellowship (to D.E.O.), Human Frontier Fellowship (to L.T.), Rita Allen Investigator Award (to L.T.), UC Davis STAIR and STAIR Plus grants (to D.E.O. and L.T.), two National Institute Healthy training grants (T32GM113770 to C.L. and 5T32GM099608 to M.V.V.), Brain and Behavior Research Foundation NARSAD Young Investigator Award (to W.C.O.), and a Brain Research Foundation Seed Grant (to W.C.O.).

Inclusion And Diversity

We worked to ensure sex balance in the selection of non-human subjects. One or more of the authors of this paper self-identifies as an underrepresented ethnic minority in science. The author list of this paper includes contributors from the location where the research was conducted who participated in the data collection, design, analysis, and/or interpretation of the work.

Method Details

Materials Availability

The following plasmids have been deposited in Addgene:

163910	pCMV_psychLight2
163909	pAAV_hSynapsin_psychLight2

AAV Viruses are available through Addgene and the Canadian Neurophotonics Centre. PSYLI2 cell line will be available upon request via MTA with UCD.

Data And Code Availability

The full sequence of psychLight has been deposited in GenBank:MW285156 (psychLight1), GeneBank: MW285157 (psychLight2). All source data present in this manuscript are available from https://github.com/lintianlab/psychLight. Custom MATLAB code is available via https://github.com/lintianlab/psychLight.

Experimental Model and Subject Details

All experimental procedures involving animals were approved by the Institutional Animal Care and Use Committee (IACUC) at the University of California, Davis, the University of Colorado School of Medicine, or Duke University, and adhered to principles described in the National Institutes of Health Guide for the Care and Use of Laboratory Animals. The University of California, Davis, the University of Colorado School of Medicine, and Duke University are accredited by the Association for Assessment and Accreditation of Laboratory Animal Care International (AAALAC).

Abbreviations (In alphabetical order)

β2AR = beta-2 adrenergic receptor; (S)-Meth-AMPH = (S)-methamphetamine; +Ctrl = positive control; μm = micrometer; 25-CN-NBOH = 4-(2-(2-Hydroxybenzylamino)ethyl)-2,5-dimethoxybenzonitrile hydrochloride; 2C-I = 2-(4-Iodo-2,5-dimethoxyphenyl)ethan-1-amine; 2p = 2-photon; 3-IAA = indole-3-acetic acid; 5-Br-DMT = 5-bromo-N,N-dimethyltryptamine; 5-Cl−DMT = 5-chloro-N,N-dimethyltryptamine; 5-F-DMT = 5-flouo-N,N-dimethyltryptamine; 5-HT = serotonin; 5-HT2AR = serotonin 2A receptor; 5-MeO = 5-methoxy-N,N-dimethyltrytamine; 6-F-DET = 6-flouro-N,N-diethyltrytamine; 6-MeO = 6-methoxy-N,N-dimethyltryptamine; 8-OH-DPAT = (±)-8-hydroxy-2-(dipropylamino)tetralin; AAV = adeno-associated virus; AAZ = AAZ-A-154; aCSF = artificial cerebrospinal fluid; BLA = basolateral amygdala; BNST = bed nucleus of the stria terminalis; BOL-148 = 2-bromo- lysergic acid diethylamide; BUFO = bufotenin, N,N-dimethyltryptamine; cpGFP = circularly permuted green fluorescent protein; CPMD = compound; D1R = dopamine receptor D1; DA = dopamine; DMSO = dimethyl sulfoxide; DMT = N,N-dimethyltrytamine; DOI = 2,5-dimethoxy-4-iodoamphetamine; DRN = dorsal raphe nucleus; EC50 = half maximal effective concentration; EF1α = human elongation factor-1 alpha; Emax = maximum efficacy; ESC = escitalopram oxalate; FST = forced swim test; GABA = γ-aminobutyric acid; GLU = glutamate; HEK293T = human embryonic kidney 293 cells with SV40 T-antigen; HTR = head-twitch response; IL3 = third intracellular loop; KET = ketamine; KETSN = ketanserin; LIS = lisuride; LSD = lysergic acid diethylamide; LTR = long terminal repeat; MDL = MDL 100907; N-5-HT = N-methylserotonin; N-acetyl-5-HT = N-acetylserotonin;

NA = not available; NE = norepinephrine; NMT = N-methyltryptamine; OFC = orbitofrontal cortex; PCP = Phencyclidine; PCP = phencyclidine; PGK = phosphoglycerate kinase; Puro(R) = puromycin resistance; R-AMPH = (R)-amphetamine; R-dimeth-AMPH = (R)-dimethamphetamine; R-MDA = (R)-3,4-methylenedioxyamphetamine; R-MDDMA = (R)-3,4-methylenedioxydimethylamphetamine; R-MDMA = (R)-3,4-methylenedioxy-methamphetamine; ROI = region of interest; S-AMPH = (S)-amphetamine; S-dimeth-AMPH = (S)-dimethamphetamine; S-MDA = (S)-3,4-methylenedioxyamphetamine; S-MDDMA = (S)-3,4-methylenedioxydimethylamphetamine; S-MDMA = (S)-3,4-methylenedioxy-methamphetamine; SEM = standard error mean; STD = standard deviation; TRY = tryptamine; TTX = tetrodotoxin citrate; U50 = U50488; VEH = vehicle; VMAT2-HET = vesicular monoamine transporter 2 heterozygous; W-S = water and 1% sucrose solution; W-W = water and water; WT = wild-type; TBG = Tabernanthalog; $\Delta F/F$ = change in fluorescence over initial fluorescence.

Compounds

The NIH Drug Supply Program provided lysergic acid diethylamide hemitartrate, psilocin, psilocybin, 2-(4-Iodo-2,5-dimethoxyphenyl)ethan-1-amine hydrochloride (2C-I), 2-bromo-lysergic acid diethylamide tartrate (BOL-148), ibogaine hydrochloride, noribogaine, cocaine hydrochloride, salvinorin A, and phencyclidine hydrochloride (PCP). Other chemicals were purchased from commercial sources such as serotonin hydrochloride (5-HT, Fisher, 50-120-7920), ketanserin (KETSN, ApexBio, 50-190-5332), ketamine hydrochloride (KET, Fagron, 803647), morphine sulfate (Mallinckrodt, Inc.,

0406-1521-53), lisuride maleate (LIS, Tocris, 40-5210), bromocriptine mesylate (Tocris, 04-275-0), (±)-2,5-dimethoxy-4-iodoamphetamine hydrochloride (DOI, Cayman, 13885), imipramine hydrochloride (Cayman, 15890), modafinil (Cayman, 15417), (±)-threo-methylphenidate hydrochloride (Cayman, 11639), indole 3-aceitic acid (3-IAA, ACROS, AC12216-0250), gramine (ACROS, AC12018-0100), N-acetylserotonin (ACROS, AC22693-1000), melatonin (ACROS, AC12536-2500), tryptamine (TRY, ACROS, AC15798-0050), N-methyltryptamine (NMT, ACROS, AC151751000), MDL 100907 (MDL, Sigma, M3324-5MG), haloperidol (Sigma, H1512), clozapine (Sigma, C6305), aripiprazole (Sigma, SML0935), fluoxetine hydrochloride (Sigma, F132-10MG), rizatriptan benzoate (Sigma, SML0247-10MG), benztropine mesylate (Sigma, SML0847-500MG), (±)-8-hydroxy-2-(dipropylamino)tetralin hydrobromide (8-OH-DPAT, Sigma, H8520-25MG), R-(-)-apomorphine hydrochloride hemihydrate (Sigma, A4393-100MG), pramipexole hydrochloride (Sigma, PHR1598-500MG), selegiline hydrochloride (Sigma, M003-250MG), ladostigil tartrate (Sigma, SML2263-5MG), RuBi-5-HT (Tocris, 3856) escitalopram oxalate (ESC, Tocris, 4796), L-glutamic acid (GLU, Sigma, G1251-500G), γ-aminobutyric acid (GABA, A5835-25G), dopamine hydrochloride (DA, Sigma, H8502-25G), and norepinephrine bitartrate (NE, 1468501). For cellular experiments, the VEH is dimethyl sulfoxide (DMSO, ACROS, AC327182500). For in vivo experiments, VEH = USP grade saline (0.9%, VWR, 68099-103). The remaining compounds used in these studies were synthesized in house and judged to be pure based on NMR and UHPLC-MS. Compounds of the DMT, IsoDMT families (LED-A-4 − LED-C-21) and Tabernanthalog (TBG) were prepared as described previously (Cameron et al., 2021; Dunlap et al., 2020).

All enantiopure amphetamines (i.e., amphetamine, methamphetamine, dimethamphetamine) and methylenedioxymethamphetamines (i.e., MDA, MDMA, MDDMA) were prepared using methodology described by Nenajdenko (Huot et al., 2011; Nenajdenko et al., 2001). The key step involved the regioselective ring opening of enantiopure Boc-protected aziridines derived from R- and S-alaninol, respectively. The Boc-protected amphetamines and methylenedioxymethamphetamines were determined to be enantiomerically pure (> 99 % ee) by chiral HPLC. The methylated amphetamines and methylated methylenedioxyamphetamines were readily prepared using known methods (Dunlap et al., 2020; Talluri and Sudalai, 2007). All amphetamine and methylenedioxyamphetamine derivatives were prepared as the 1:1 fumarate salts with the exception of R- and S-MDMA, which were prepared as the 2:1 fumarate salts (i.e., hemifumarates). Lastly, N-Me-5-HT, N-Me-5-MeO-tryptamine hemifumarate, 6-fluorodiethyltryptamine (6-F-DET hemifumarate), 5-bromo-DMT hemifumarate, 5-chloro-DMT hemifumarate, 5-fluoro-DMT hemifumarate, and AAZ-A-137 hemifumarate were prepared using previously reported methods (Blair et al., 2000; Marzaro et al., 2009; Somei et al., 2001; Tombari et al., 2019). Synthetic procedures and characterization data for AAZ-A-154 and LED-C-233 are reported below.

PsychLight Development and Characterization

Development of PsychLight1 and PsychLight2

All constructs were designed using circular polymerase extension cloning (CPEC), restriction cloning, and gBlock gene fragments (Integrated DNA Technologies) (Quan and Tian, 2011). Sequences coding for a FLAG epitope were placed at the 5′ end of the

construct as previously described (Irannejad et al., 2013). HindIII and NotI cut sites were placed at the 5′- and 3′ ends, respectively, for cloning into pCMV (Addgene) to generate all pCMV constructs. BamHI and HindIII sites were introduced via PCR for final subcloning onto pAAV.hSynapsin1 vectors (Addgene). To maximize coupling between conformational changes and chromophore fluorescence, we chose to use a cpGFP module (LSS-LE-cpGFP-LP-DQL) from GCaMP6 (Chen et al., 2013) for insertion into the human 5-HT2AR using circular polymerase extension cloning (CPEC).

For screening linker variants, we generated linker libraries by first creating an insert DNA carrying a randomized 2 amino acid linker on each side of cpGFP (LSS-xx-cpGFP-xx-DQL). Cloned constructs were amplified and purified with the QIAGEN PCR purification kit prior to NEB® 5-α competent E. coli transformation. Competent cells were plated onto kanamycin-containing agar plates. After allowing for 24-hour of growth at 37°C, single colonies were manually picked and grown overnight as described previously (Tian et al., 2009). Plasmids from the colonies were with purified using the QIAGEN miniprep kit. Top variants were sequenced by Genewiz. For conversion of psychLight1 to psychLight2, an ER2 tag was added to the C terminus of the protein, as described previously (Stockklausner et al., 2001), and the two original amino acids from the cpGFP sequence (i.e., F511 and N512, numbering based on psychLight2) were inserted into the N-terminal side of linker 2 to increase the baseline fluorescence. NEB® stable competent cells were transformed with PAAV_hSynapsin_psychLight2. After growth on an agar plate at 30°C, a single colony was selected. After sequencing confirmed the presence of the psychLight2 gene, the cells were expanded at 30°C in 100 mL of growth medium

(2xYT), and purified with a QIAGEN Endo-free Plasmid Maxi kit and send to the UC DAVIS Virus Packaging Core for virus production. Sequence information for psychLight1 and psychLight2, see Data S2.1.

Tissue Culture

HEK293T cells were grown in DMEM, supplemented with fetal bovine serum (FBS) and penicillin-streptomycin. Cells were transfected with Effectene according to the manufacturer's instructions. Prior to imaging, cells were washed with Hank's Balanced Salt Solution (HBSS) supplemented with 2 mM MgCl2 and 2 mM CaCl2. All images were collected in HBSS containing Mg2+ and Ca2+.

Transient Transfection of PsychLight1

HEK293T cells were plated and transfected concurrently 24 h prior to each experiment using the QIAGEN Effectene Transfection Reagent kit according to the manufacture's protocol.

Confocal Microscopy Experiments

Dose-response experiments were performed using an Automate Perfusion System. Cells (HEK293T) were grown on 12 mm coverslips and transfected with psychLight1. The coverslips were then placed into a coverslip holder and washed with 5 mL of HBSS containing 2 mM MgCl2 and 2 mM CaCl2. Cells were perfused first with 5 mL of 0.1% DMSO, then drugs in ascending concentrations from 1 pM to 10 µM were added, with

the concentration of DMSO being held constant at 0.1%. Images were recorded using a 465 nm laser and a 40x oil objection (0.55 N.A.) on a Zeiss 710 confocal microscope. For the competition studies described in Figure S2.3, HEK293T cells were prepared as described above; however, the cells were first exposed to 5 mL of 0.2% DMSO. Next, 100 nM 5-HT in 0.2% DMSO was introduced to the cells followed by ascending concentrations of the drug (from 1 pM to 10 µM) in a solution of 100 nM 5-HT, with the concentration of DMSO kept constant at 0.2%. Analysis was performed by taking 3 ROIs on the cell membrane using ImageJ and calculating the mean intensity for each ROI across the time-points. Finally, the ΔF/F was calculated using the average of the baseline (0.1 or 0.2% DMSO) and the average intensity between each dosage over the average of the baseline.

Two-Photon Uncaging Experiments

Organotypic slice cultures from the frontal cortex were prepared from postnatal day 2–3 (P2–P3) C57BL/6J mice, as described previously (Stoppini et al., 1991). Slices were infected 19–20 days prior to imaging by adding a drop of a solution containing 1 µL of concentrated psychLight2 virus (AAV_hSyn_psychLight2) and 4 µL of slice culture media (pre-warmed to 37°C) to the top of the cortical layers. Slices were transfected with tdTomato 17–18 days prior to imaging using biolistic gene transfer (180 psi). Gold particles (6–7 mg) were coated with 12 µg of the tdTomato plasmid (Kwon et al., 2012). Two-photon imaging and uncaging were performed after 21–23 days in vitro (DIV) on transfected layer 2/3 pyramidal neurons within 40 µm of the slice surface at 30°C in

recirculating artificial cerebrospinal fluid (aCSF; in mM: 127 NaCl, 25 NaHCO3, 1.25 NaH2PO4, 2.5 KCl, 25 D-glucose, aerated with 95%O2/5%CO2) with 2 mM CaCl2, 1 mM MgCl2, 0.1 mM RuBi-5-HT, and 0.001 mM tetrodotoxin. For each neuron, image stacks (512 × 512 pixels; 0.047 µm / pixel) with 1 µm z-steps were collected from one segment of secondary or tertiary apical dendrites 50–80 µm from the soma using a two-photon microscope (Bruker) with a pulsed Ti::sapphire laser (Mai Tai, Spectra Physics) tuned to 920 nm (4–5 mW at the sample). All images shown are maximum projections of 3D image stacks after applying a median filter (2 × 2) to the raw image data. Two-photon uncaging was achieved, as previously described (Oh et al., 2016), except that RuBi-5-HT was used. In brief, the 5-HT uncaging stimulus (1 pulse of 10-ms duration; 17–20 mW at the sample, 810 nm) was delivered by parking the beam at a point ~0.5 µm from the edge of a dendrite with a pulsed Ti::sapphire laser (MaiTai HP, Spectra-Physics). The mock stimulus was identical in parameters to the uncaging stimulus, except carried out in the absence of RuBi-5-HT. Line-scan recording of fluorescence transients was performed simultaneous with 5-HT uncaging on layer 2/3 pyramidal neurons using two pulsed Ti::sapphire lasers for imaging and uncaging at wavelengths of 920 nm and 810 nm, respectively. The fluorescent measurements of psychLight transients were represented as ΔpL2/tdT = [(pL2/tdT) peak / (pL2/tdT) baseline], where pL2 and tdT represent the fluorescence from psychLight2 and tdTomato, respectively. After measuring baseline fluorescences (50 ms), 5-HT uncaging (1 pulse of 10-ms duration, 17–20 mW) was delivered at the target region and peak fluorescences were averaged over 10 ms around the peak. Only cells that showed stable 5-HT-insensitive (Red) signals (< ± 5% fluctuation) were included in our

analysis (Oh et al., 2016). To measure changes in psychLight fluorescence intensities following 5-HT bath application (50 µM), fluorescence intensities were calculated from bleed-through-corrected and background subtracted green (psychLight) and red (tdTomato) fluorescence intensities using the integrated pixel intensity of a boxed region surrounding a dendrite and were represented as ΔpL2/tdT = [(pL2/tdT) peak / (pL2/tdT) baseline] (Oh et al., 2016). All statistics were performed across regions of interest (ROIs).

Slice Experiments

Viral Injections

Injection procedures were performed as previously described (Broussard et al., 2018). Briefly, animals were anesthetized using 0.5%–2.5% isoflurane and mounted on a stereotaxic apparatus (Model 900). For injections into the BNST (AP: 0.3 mm, ML: 1 mm, DV: −4.35 mm from the skull), a small craniotomy (1–2 mm diameter) was performed on top of BNST injection site. The virus injection was performed using a Sub-Microliter Injection System with nanofil needles. Three hundred nL of AAV9.hSynapsin1.psychLight2 was injected into C57/BL6J mice. Mice were allowed to recover > 2 weeks to allow for sensor expression.

Brain Slices for Two-Photon Imaging

Two to 4 weeks after viral injection, mice were anesthetized with 2.5% avertin and decapitated. The heads were placed into a high-sucrose artificial cerebrospinal fluid (aCSF) solution that contained (in mM): 73 NaCl, 2.5 KCl, 2 MgCl2, 1.25 NaH2PO4, 25 NaHCO3, 24 dextrose, 0.5 CaCl2 and 75 sucrose, saturated with 95% O2 and 5% CO2.

The brains were removed from skull and cut (400 µm) with a vibratome (V1200s, Leica) in ice-cold high sucrose aCSF. Brain slices were incubated at 32°C for 30 min before imaging in normal aCSF that contained (in mM): 128 NaCl, 2.5 KCl, 1 MgCl2, 1.25 NaH2PO4, 25 NaHCO3, 10 dextrose and 2 CaCl2, saturated with 95% O2 and 5% CO2. Imaging was carried out at room temperature using a 2-photon microscope. The sensor was excited at 920 nm with a Ti: sapphire laser (Ultra II, Coherent) that was focused by an Olympus 40 ×, 0.8NA water immersion objective. Emitted fluorescence was separated by a 525/50 nm filter set, and detected by a photomultiplier (H7422PA-40, Hamamatsu). Data were acquired and collected with ScanImage5 software. Electrical stimulation was performed with a tungsten concentric bipolar microelectrode (TM33CCINS-B, World Precision Instruments).

The area within approximately 20 µm of the electrode was imaged. Rectangular voltage pulses were applied though a 9-channel programmable pulse stimulator (Master-9, A.M.P. Instruments LTD) and a stimulus isolation unit (ISO-Flex, A.M.P. Instruments LTD). Imaging and electrical stimulation were controlled by an Axon Digidata 1550B. Field potentials were applied at 20 pulses with a duration of 0.5 s. Experiments were carried out at a scan rate of 30 (512 × 512 pixels) Hz. Image analysis was performed with ImageJ, data analyses were calculated using MATLAB and SigmaPlot 12.0. Drugs were dissolved as a stock solution in imaging HBSS buffer and diluted at 1:1000 prior to application in the perfusion system.

In vivo PsychLight Recordings

General

At the beginning of surgery, mice were anesthetized with 5% isoflurane for induction and later 1% isoflurane was used for maintenance. After induction of anesthesia, Carprofen (5 mg/kg) and Buprenorphine (1 mg/kg) were subcutaneously injected. The mouse was mounted on a stereotaxic frame. During surgery, body temperature was maintained with a heating pad. Before a sterile scalpel was used to make an incision, the hair covering the skin above the skull was removed. To have consistent horizontal alignment of the skull, bregma and lambda were leveled to be on the same z axis while two points on the surface of the skull 1.5 mm to either side of lambda were used to level the skull with regard to the y axis. Following viral injection, optical fiber was implanted and secured with metabond and dental cement. Mice were monitored up to 14 days after surgery.

Viral Injection

To inject virus and implant optical fibers for fiber photometry experiments, craniotomy holes were made over the DRN, BNST, BLA, and OFC (DRN, inject with 20° angle, AP: −4.3 mm, ML: 1.1, DV: −2.85 mm; BNST, AP: 0.3 mm, ML: 1 mm, DV: −4.35 mm; BLA, AP: −1.35 mm, ML: 3mm, DV: −4.5 mm; and OFC, AP: 2.5 mm, ML: 1.5 mm, DV: −2.5 mm). Mice were injected with 300 nL of AAV9.hSynapsin1.psychLight2 (BNST, BLA, OFC) or AAV8.hSynapsin1.psychLight2 (DRN). Virus was injected using the Sub-Microliter Injection System with nanofil needles. The injection needle was lowered into the brain regions indicated above and infused per site at a rate of 100 nL per min. The injection volume was controlled by a microsyringe pump, which was connected to a

controller. Following injection, the virus was allowed to diffuse into the tissue for an additional 10 min before the needle was withdrawn.

Optical Fiber Implantation

After viral injection, optical fibers were mounted into a stereotaxic holder and inserted into tissue targeting 50 µm above the brain regions mentioned above. A layer of Metabond was applied to the surface of the skull around the optical fiber followed by a layer of dental cement to secure the optical fiber.

Auditory Fear Conditioning

Mice were placed into a fear conditioning chamber (Med Associates) with a patch cord connected for photometric recordings. A Doric fiber photometry system was used in this study with 465 nm and 405 nm light (LED, ~30 µW) used for generating the signal and as an isosbestic control, respectively. Each animal received 15 presentations of a 27 s tone (3000 Hz) co-terminating with a foot-shock (0.5 mA for 1.5 s) delivered at 2 min intervals. Each animal received 15 tone/foot-shock pairings over the course of 40 min, and the responses for these trials were averaged to create a single trace per animal. Data analysis was performed with custom-written script in MATLAB. In brief, 405 nm traces were fit with a bi-exponential curve, and then the fit was subtracted from the signal to correct for baseline drift. ΔF/F% was calculated as [100∗(465 signal - fitted signal) / fitted signal)]. Traces were then z-scored. A heatmap was plotted using a custom MATLAB script by plotting normalized single trials of traces from all animals tested per brain region.

ROC analysis was done by a custom MATLAB script. We first calculated the baseline response from a defined a period of time (fixed measurement time point) before the shock and the sensor response from a defined period of time after the shock from the single trial data. We then calculated the probability distributions for the baseline and response periods by binning the single trial data into two histograms. We then applied a range of thresholds to the two distributions and calculated the true detection rate and false positive rate, which resulted in the ROC curve. Finally, we integrated the area under the ROC curve and approximated the d' of the sensor as the discriminability index that had equal area under the ROC curve.

Head-twitch Response with Fiber Photometry

Three animals were used for experiments measuring sensor activity in the prelimbic cortex. A 10 min baseline was recorded prior to compound administration (50 mg/kg 5-MeO or 4 mg/kg KETSN, i.p.) in a 5 mL/kg volume using 0.9% saline as the vehicle. To calculate the ΔF/F time series, a linear fit was applied to the 405 nm signals and aligned to the 465 nm signals. The fitted 405 nm signal was subtracted from 465 nm channels, and then divided by the fitted 405 nm signal to yield ΔF/F values. The number of head twitches were counted in 1 min intervals by 2 observers blinded to the treatment conditions and the results were averaged (interpersonnel kappas, Pearson's correlation coefficient = 0.96)

Perfusion and Histology

Stock Avertin was self-made by mixing 10 g of 2,2,2-tribromoethyl alcohol and 10 mL of tert-amyl alcohol. The working stock was diluted to 1.2% (v/v) with water and shielded from light. Animals were euthanized with 125 mg/kg 1.2% Avertin (i.p.) followed by transcardial perfusion with ice-cold 1x phosphate buffered saline (PBS) and subsequently perfused with ice-cold 4% paraformaldehyde (PFA) in 1x PBS. After extraction of the mouse brains, samples were post-fixed in 4% PFA at 4°C overnight. The mouse brains were cryo-protected by immersion in 10% sucrose in a 1x PBS solution overnight. Samples were next placed in 30% sucrose in a 1x PBS solution for > 1 day, before embedding the samples in O.C.T. Samples were then transferred to a −80°C freezer for long-term storage or were sliced into 50 µm sections on a cryostat (Leica Biosystems) for histology. Histology samples were imaged on Zeiss LSM 710 confocal microscope.

High Content Screening with PSYLI2 Cells

Creation of PSYLI2 Cell Line Stably Expressing PsychLight2

The psychLight2 gene was cloned into a pLVX plasmid with the EF1α promotor. The plasmid was transfected into HEK293T cells together with pCMV_delta8.2 and pCMV_VSV_G in a ratio of 10:7:3 using the QIAGEN Effectene Transfection kit. After 14 h of incubation, the medium was exchanged for fresh DMEM. After an additional 48 h of incubation, the lentivirus-containing medium was collected, filtered through a 0.45 µm Durapore low-protein binding filter, concentrated using a Centricon-70 ultra filtration unit at 3,500 g for 50 min, and stored at −80°C. Next, confluent HEK293T cells that had been grown in 24-well plates were infected with 20 µL of concentrated lentivirus for 48 h.

Puromycin selection was performed as described by Tandon and co-workers (Tandon et al., 2018). Expression was assessed via fluorescence microscopy, and a single cell was selected for expansion. The new cell line, named PSYLI2, was frozen in 10% DMSO at −80°C and then transferred to a liquid nitrogen dewar.

High-Content Imaging Experiments

Glass bottom 96-well plates (P96-1.5H-N, Cellvis) were coated with 50 µg/mL of poly-D-lysine (Sigma, P6407-5MG) and 10 µg/mL of laminin (Sigma, L2020) overnight in an incubator (37°C, 5% CO2). Plates were washed with Dulbecco's PBS (ThermoFisher, 14190-250) and PSYLI2 cells were suspended in DMEM (Fisher, 11995073) containing 10% FBS (Fisher, 26-140-079) with 5% penicillin-streptomycin (Fisher, 15140-163) and plated at a density of 40,000 cells/well 24 h prior to each experiment. Immediately prior to an experiment, stock solutions of drugs in DMSO (10 mM) were diluted 1:100 in imaging media distributed across an empty 96-well plate (treatment plate) in triplicate following a randomized plate map. The imaging media consisted of 1 x HBSS (Fisher, 14175103) containing 0.5 M MgCl2 (Sigma, M8266-1KG) and 0.5 M CaCl2 (Sigma, C5670-50G). Cells grown in a separate 96-well plate (assay plate) were gently washed 3x with imaging media, and the wells were filled with an appropriate volume of imaging media for the respective experiment (vide infra).

Agonist Mode

For agonist mode experiments, 180 µL of imaging media were added to each well of the assay plate. Wells were then imaged on a Lecia DMi8 using Leica Application Suite X (V3.6.0.20104) at 40x (N.A. = 0.6) with 5 regions of interest (ROI) taken per well using

the default 5 ROI pattern for each well with no bias to location and no overlap of the ROIs (exposure = 350 ms, LED power = 80%). Next, 20 µL from the treatment plate was transferred to the assay plate containing a 1:1000 dilution of drug (10 µM as the final concentration in 0.1% DMSO). As positive, negative, and neutral controls, 5-HT (10 µM), ketanserin (10 µM), and DMSO (0.1%) were used, respectively. All final concentrations of drugs were 10 µM (0.1% DMSO) in agonist mode unless stated otherwise. After 5 min of incubation, the same sites were re-imaged using the same settings.

Once imaging was complete, the images were exported, and analyzed using self-written MATLAB script. Script will be deposit on to Github. In short, segmentation was performed on individual images and a mask highlighting the membrane of the HEK293T cells was generated. Pixel intensities were obtained from the mask-highlighted area and exported into Excel. The ΔF/F values for each well were calculated using the following equation:

$$\frac{(average\ after\ drug - average\ before\ drug)}{average\ before\ drug\ (baseline)}$$

These values were then used to obtain the triplicate mean (N = 3).

Antagonist Mode

For antagonist mode experiments, 160 µL of imaging media was added to each well of the assay plate. Wells were imaged on a Lecia DMi8 using Leica Application Suite X (V3.6.0.20104) at 40x (N.A. = 0.6) with 5 regions of interest (ROI) taken per well using the default 5 ROI pattern for each well with no bias to location and no overlap of the ROIs

(exposure = 350 ms, LED power = 80%). A 100 µM 5-HT stock solution in DMSO was diluted 1:100 in imaging buffer. Next, 20 µL of this solution was added to the assay plate for a final concentration of 111 nM 5-HT (0.1% DMSO). The same 5 ROIs were imaged after 5 min of incubation. Next, 20 µL from the treatment plate was transferred to the assay plate for a final 1:1000 dilution of drug (10 µM drug, 100 nM 5-HT, 0.2% DMSO). All final concentrations of drugs were 10 µM with 100 nM 5-HT (0.2% DMSO) in antagonist mode unless stated otherwise. After 5 min of incubation, the same sites were re-imaged using the same settings.

Once imaging was complete, the images were exported, and analyzed using self-written MATLAB script. Script will be deposit on to Github. In short, segmentation was performed on individual images and a mask highlighting the membrane of the HEK293T cells was generated. Pixel intensities were obtained from the mask highlighted area and exported into Excel. Then the ΔF/F values for each well were calculated using the following equation:

$$\frac{(average\ after\ drug - average\ after\ 5-HT\ )}{average\ after\ 5-HT\ (baseline)}$$

These values were then used to obtain the triplicate average (N = 3). All imaging and incubation (both agonist and antagonist mode) were performed at ambient atmosphere and temperature.

Calculation of the Ligand Score

Compounds unlikely to bind to the sensor should produce minimal to no response in either agonist or antagonist mode. Therefore, a ligand score was calculated as:

$\Delta(F/F)_{\text{Compound Agonist Mode}} - [(\Delta F/F)_{\text{VEH Antagonist Mode}} - (\Delta F/F)_{\text{Compound Antagonist Mode}}]$

The black heatmap value indicating no effect was set to the value calculated for the vehicle control (i.e., −4.2). The maximal red and blue values were set to those calculated for a prototypical agonist (i.e., LSD, Ligand Score = 21) and antagonist (i.e., MDL100907, Ligand Score = −58), respectively.

Schild Regression Analysis

A treatment plate was prepared by pre-mixing various concentrations of a non-hallucinogenic compound with increasing concentrations of 5-HT. During imaging, 180 µL of imaging media were added to each well of the assay plate. Wells were then imaged on a Lecia DMi8 using Leica Application Suite X (V3.6.0.20104) at 40x (N.A. = 0.6) with 5 regions of interest (ROI) taken per well using the default 5 ROI pattern for each well with no bias to location and no overlap of the ROIs (exposure = 350 ms, LED power = 80%). Next, 20 µL from the treatment plate was transferred to the assay plate for a final 1:1000 dilution of drug. All final drug treatments contained 0.1% DMSO. After 5 min of incubation, the same sites were re-imaged using the same settings. The data analysis method was the same as in agonist and antagonist mode.

Plate reader screening for compound fluorescence

A 96-well plate (UV transparent) was prepared with 100 µL of increasing concentration of BOL-148 and bromocriptine from 10−12 to 10−5 M together with vehicle control. The plate was read by Tecan Microplate Reader Spark® with excitation wavelength 465 nm (bandwidth 20 nm), emission wavelength 518 nm (bandwidth 20 nm),

gain of 120, 5 ROI per well, total 30 flashes per well, and read at z-position 30000 µm from bottom of the plate. All settings controlled by SparkControl software, V2.3.

Antidepressant and Hallucination Related Behavior

Dendritogenesis Experiments

For the dendritogenesis experiments conducted using cultured E18 cortical neurons, timed-pregnant Sprague Dawley rats were obtained from Charles River Laboratories (Wilmington, MA). Full culturing, staining, and analysis details were performed as previously described (Dunlap et al., 2020).

Forced Swim Test (FST)

Male and female C57BL/6J mice (9–10 weeks old at time of experiment, n = 6 of each sex per condition) were obtained from The Jackson Laboratory and housed 4–5 mice of the same sex/cage in a UCD vivarium following an IACUC approved protocol. After 1 week in the vivarium, each mouse was handled for approximately 1 min by a male experimenter for 3 consecutive days prior to the first FST. All experiments were conducted by the same male experimenter who performed the initial handling. During the FST, mice underwent a 6 min swim session in a clear Plexiglas cylinder (40 cm tall, 20 cm in diameter) filled with 30 cm of 24 ± 1°C water. Fresh water was used for every mouse. After handling and habituation to the experimenter, drug-naive mice first underwent a pretest swim to more reliably induce a depressive-like phenotype in subsequent FST sessions. Immobility scores for all mice were determined after the pre-test and mice were assigned to treatment groups to generate groups with similar mean immobility scores

used in the following two FST sessions. The next day, the animals received injections (i.p.) of AAZ-A-154 (20 mg/kg), ketamine (3 mg/kg) as the positive control, or vehicle (saline). After 30 min, the animals were subjected to the FST, dried with a towel, and then returned to their home cages. One week later, the FST was performed to assess the sustained effects of the drugs. All FSTs were performed between the hours of 0800 and 1300 h. The experiments were divided into two cohorts either of all males or females and conducted on different days. Experiments were video-recorded and manually scored offline by an experimenter blinded to treatment conditions. Immobility time—defined as passive floating or remaining motionless with no activity other than that needed to keep the mouse's head above water—was scored for the last 4 min of the 6 min trial.

Head-Twitch Response (HTR) and Locomotion Assays

The HTR assay was performed as described previously (Dunlap et al., 2020) using both male and female C57BL/6J mice (2 male and 2 female = 4 total per treatment). The mice were obtained from The Jackson Laboratory (Sacramento, C.A.) and were approximately 8-weeks old at the time of the experiments. Compounds were administered (5 mL/kg, i.p.) using 0.9% saline as the vehicle. After injection, animals were placed into an empty cage (8" x 13" x 5") and HTRs were videotaped, scored later by two blinded observers, and the results were averaged (interpersonnel kappas, Pearson correlation coefficient > 0.91). Locomotion was assessed using AnyMaze automated tracking software.

Sucrose Preference

Adult male and female wild-type (WT) and VMAT2 heterozygous (VMAT2-HET) mice were used for these experiments (Fukui et al., 2007), and they were housed in a humidity- and temperature-controlled room on a 14:10 h light:dark cycle. Mice were housed individually 48 h prior to the experiment with ad libitum access to chow and water. For each day's experiment, bottles were prepared with water or a 1% sucrose solution and these were weighed just prior to the test. Two h prior to the beginning of the dark cycle, the home-cage water bottle was removed. One h after onset of the dark cycle, a pair of bottles was placed into the home-cage. The mouse was given 2 h to drink, after which the bottles were removed and weighed immediately. Approximately 1 h later, the home-cage water bottle was returned. This procedure was repeated daily with the water-water (W-W) pairing until the mouse showed stable drinking volumes over 3 consecutive days without any side-bias. Once criterion was achieved, the mouse was presented with the water-sucrose (W-S) pairing. The next day (day 1), mice were administered an acute injection of AAZ-A-154 (15 mg/kg, i.p.) and 5 min later were given the W-S pairing (i.e., day 1). Subsequent W-S pairings were presented on days 2 and 4, and then at 4-day intervals. Preference for the sucrose bottle was calculated as the volume of sucrose consumed minus the volume of water consumed, divided by the total volume of liquid consumed. Preference scores approaching "0" indicated no preference for sucrose or water, whereas positive scores signified a preference for sucrose and negative scores denoted a preference for water.

Compound Synthesis

Synthesis of Previously Uncharacterized Compounds

The syntheses and characterization of most compounds used in this study have been reported previously. Here, we provide synthetic procedures and characterization data (Data S2.2) for AAZ-A-154 and LED-C-233, as they have not been previously described.

(R)-2-(dimethylamino)propan-1-ol

To an ice-cold solution of R-alaninol (4.93 g, 65.6 mmol) and glacial acetic acid (18.9 mL, 328 mmol, 5.0 equiv) in MeOH (328 mL) was added sodium cyanoborohydride (9.075 g, 144 mmol, 2.2 equiv) followed by 37% formaldehyde(aq) (13.8 mL, 171 mmol, 2.6 equiv). The reaction was stirred at room temperature for 12 h before being concentrated under reduced pressure. The residue was diluted with glycerol (100 mL) and distilled under reduced pressure to yield the pure compound as a colorless oil (6.5 g, 96%), which was used without further purification.

(R)-1-chloro-N,N-dimethylpropan-2-amine hydrochloride

To an ice-cold solution of SOCl2 (2.1 mL, 29 mmol, 1.1 equiv) was added (R)-2-(dimethylamino)propan-1-ol (2.7 g, 26 mmol). The mixture was heated to reflux for 4 h before being concentrated under reduced pressure to yield the desired product as a white solid (3.92 g, 95%), which was used without further purification.

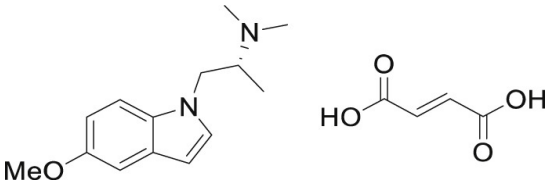

AAZ-A-154

To a solution of 5-methoxyindole (441 mg, 3.00 mmol) in DMSO (7.5 mL) was added (R)-1-chloro-N,N-dimethylpropan-2-amine hydrochloride (664 mg, 4.20 mmol, 1.4 equiv), potassium iodide (697 mg, 4.2 mmol, 1.4 equiv), and potassium tert-butoxide (0943 mg, 8.40 mmol, 2.8 equiv). The reaction mixture was stirred for 24 h, before being diluted with 1.0 M NaOH(aq) (750 mL). The aqueous phase was extracted with DCM (3 × 100mL). The organic extracts were combined, dried over Na2SO4, filtered, and concentrated under reduced pressure to yield a colorless oil, which was purified by flash chromatography (9:1 DCM/MeOH with 1% ammonium hydroxide(aq)). The purified oil was dissolved in CHCl3 (3 mL) and added dropwise to a boiling solution of fumaric acid (253 mg, 2.18 mmol, 1.0 equiv) in THF (10 mL). The mixture was concentrated under reduced pressure to yield the desired product as the 1:1 fumarate salt (758 mg, 73%). 1H NMR (600 MHz, DMSO-d6) δ 7.37 (d, 1H, J = 8.8 Hz), 7.30 (s, 1H), 7.03 (s, 1H, J = 3.1 Hz), 6.76 (d, 1H, J = 8.8 Hz), 6.61 (s, 2H), 6.32 (s, 1H), 4.25 (dd, 1H J = 6.3, 7.8 Hz), 4.02 (dd, 1H, J = 6.3, 7.8 Hz), 3.74 (s, 3H,) 3.11 (q, 1H, J = 6.3, 6.6, Hz), 2.30 (s, 6H), 0.84 (d, 3H, J = 6.6 Hz). 13C NMR (100 MHz, CD3OD) δ 171.0, 155.8, 136.1, 132.8, 130.9, 129.7, 113.3, 111.2, 103.8, 103.3, 61.6, 56.2, 47.5, 39.9, 11.7 ppm.

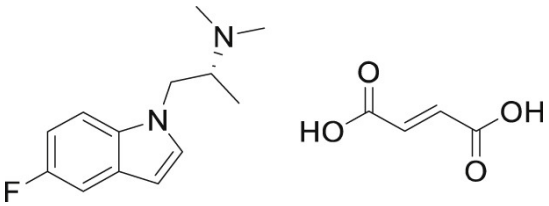

LED-C-233

To a solution of 5-fluoroindole (100 mg, 0.739 mmol) in DMSO (1.90 mL) was added (R)-1-chloro-N,N-dimethylpropan-2-amine hydrochloride (128 mg, 0.814 mmol, 1.1 equiv), potassium iodide (135 mg, 0.814 mmol, 1.1 equiv), and potassium hydroxide (166 mg, 15.8 mmol, 5.0 equiv). The reaction mixture was stirred for 24 h, before being diluted with 1.0 M NaOH(aq) (100mL). The aqueous phase was extracted with DCM (3 × 25 mL). The organic extracts were combined, dried over Na2SO4, filtered, and concentrated under reduced pressure to yield a colorless oil, which was purified by flash chromatography (9:1 DCM/MeOH with 1% ammonium hydroxide(aq)). The purified oil was dissolved in acetone (2 mL) and added dropwise to a boiling solution of fumaric acid (48.1 mg, 0.409 mmol, 1.0 equiv) in acetone (5 mL). The mixture was concentrated under reduced pressure to yield the desired product as the 1:1 fumarate salt (111 mg, 54%). 1H NMR (600 MHz, CD3OD) δ 7.49 (m, 1H,), 7.34 (d, 1H, J = 3.2 Hz), 7.25 (dd, 1H, J = 2.5, 9.3 Hz), 6.98 (td, 1H, J = 2.5. 9.3 Hz), 6.72 (s, 2H), 6.53 (d, 1H, J = 3.2 Hz), 4.63 (dd, 1H J = 5.7, 8.9 Hz), 4.35 (dd, 1H, J = 5.7, 8.9 Hz), 3.86 (m, 1H,) 2.84 (s, 6H), 1.21 (d, 3H, J = 6.7 Hz). 13C NMR (100 MHz, CD3OD) δ 171.0, 160.2, 158.7, 136.1, 134.2, 131.1, 130.8, 130.7, 111.5, 111.4, 111.3, 111.1, 106.7, 106.5, 103.6, 103.5, 61.5, 47.6, 40.0, 11.6ppm.

Quantification and Statistical Analysis

Treatments were randomized, and the data were analyzed by experimenters blinded to the treatment conditions. Statistical analyses were performed using GraphPad Prism (version 8.1.2) unless noted otherwise. All comparisons were planned prior to performing each experiment. The sucrose preference and the volume of liquid consumed in the anhedonia test were analyzed separately by repeated-measures ANOVA using a

within subjects' effects of days and a between subjects' effects of genotype with SPSS 27 programs (IBM SPSS Statistics, Chicago, IL). Post hoc analyses were by Bonferroni corrected pairwise comparisons. A $p < 0.05$ was considered significant. Data are represented as mean ± SEM, unless otherwise noted, with asterisks indicating $*p < 0.05$, $**p < 0.01$, $***p < 0.001$, and $****p < 0.0001$. Details of the statistical tests are displayed in Table S2.2.

Data S2.1: psychLight1 sequence

psychLight1.prot (695 aa)

```
MKTIIALSYIFCLVFADYKDDDDAMDILCEENTSLSSTTNSLMQLNDDTRLYSND
1        10        20        30        40        50

FNSGEANTSDAFNWTVDSENRTNLSCEGCLSPSCLSLLHLQEKNWSALLTAVVII
60        70        80        90        100       110

LTIAGNILVIMAVSLEKKLQNATNYFLMSLAIADMLLGFLVMPVSMLTILYGYRW
120       130       140       150       160

PLPSKLCAVWIYLDVLFSTASIMHLCAISLDRYVAIQNPAHHSRFNSRTKAFLKI
170       180       190       200       210       220

IAVWTISVGISMPIPVFGLQDDSKVFKEGSCLLADDNFVLIGSFVSFFIPLTIMV
230       240       250       260       270

ITYFLTIKSLQKQLSSGYNVYIKADKQKNGIKANFKIRHNIEDGGVQLAYHYQQN
280       290       300       310       320       330

TPIGDGPVLLPDNHYLSVQSKLSKDPNEKRDHMVLLEFVTAAGITLGMDELYKGG
340       350       360       370       380

TGGSMVSKGEELFTGVVPILVELDGDVNGHKFSVSGEGEGDATYGKLTLKFICTT
390       400       410       420       430       440

GKLPVPWPTLVTTLTYGVQCFSRYPDHMKQHDFFKSAMPEGYIQERTIFFKDDGN
450       460       470       480       490

YKTRAEVKFEGDTLVNRIELKGIDFKEDGNILGHKLEYNMHDQLNEQKACKVLGI
500       510       520       530       540       550

VFFLFVVMWCPFFITNIMAVICKESCNEDVIGALLNVFVWIGYLSSAVNPLVYTL
560       570       580       590       600

FNKTYRSAFSRYIQCQYKENKKPLQLILVNTIPALAYKSSQLQMGQKKNSKQDAK
610       620       630       640       650       660

TTDNDCSMVALGKQHSEEASKDNSDGVNEKVSCV*
670       680       690       695
```

Data S2.1: psychLight2 sequence

psychLight2.prot (704 aa)

```
MKTIIALSYIFCLVFADYKDDDDAMDILCEENTSLSSTTNSLMQLNDDTRLYSND
1|        10|        20|        30|        40|        50|

FNSGEANTSDAFNWTVDSENRTNLSCEGCLSPSCLSLLHLQEKNWSALLTAVVII
60|        70|        80|        90|       100|       110|

LTIAGNILVIMAVSLEKKLQNATNYFLMSLAIADMLLGFLVMPVSMLTILYGYRW
       120|       130|       140|       150|       160|

PLPSKLCAVWIYLDVLFSTASIMHLCAISLDRYVAIQNPKHHSRFNSRTKAFLKI
170|       180|       190|       200|       210|       220|

IAVWTISVGISMPIPVFGLQDDSKVFKEGSCLLADDNFVLIGSFVSFFIPLTIMV
       230|       240|       250|       260|       270|

ITYFLTIKSLQKQLSSGYNVYIKADKQKNGIKANFKIRHNIEDGGVQLAYHYQQN
280|       290|       300|       310|       320|       330|

TPIGDGPVLLPDNHYLSVQSKLSKDPNEKRDHMVLLEFVTAAGITLGMDELYKGG
       340|       350|       360|       370|       380|

TGGSMVSKGEELFTGVVPILVELDGDVNGHKFSVSGEGEGDATYGKLTLKFICTT
390|       400|       410|       420|       430|       440|

GKLPVPWPTLVTTLTYGVQCFSRYPDHMKQHDFFKSAMPEGYIQERTIFFKDDGN
       450|       460|       470|       480|       490|

YKTRAEVKFEGDTLVNRIELKGIDFKEDGNILGHKLEYNFNMHDQLNEQKACKVL
500|       510|       520|       530|       540|       550|

GIVFFLFVVMWCPFFITNIMAVICKESCNEDVIGALLNVFVWIGYLSSAVNPLVY
       560|       570|       580|       590|       600|

TLFNKTYRSAFSRYIQCQYKENKKPLQLILVNTIPALAYKSSQLQMGQKKNSKQD
610|       620|       630|       640|       650|       660|

AKTTDNDCSMVALGKQHSEEASKDNSDGVNEKVSCVFCYENEV*
       670|       680|       690|       700|  704|
```

Data S2.2: AAZ-A-A154 mass spectrum

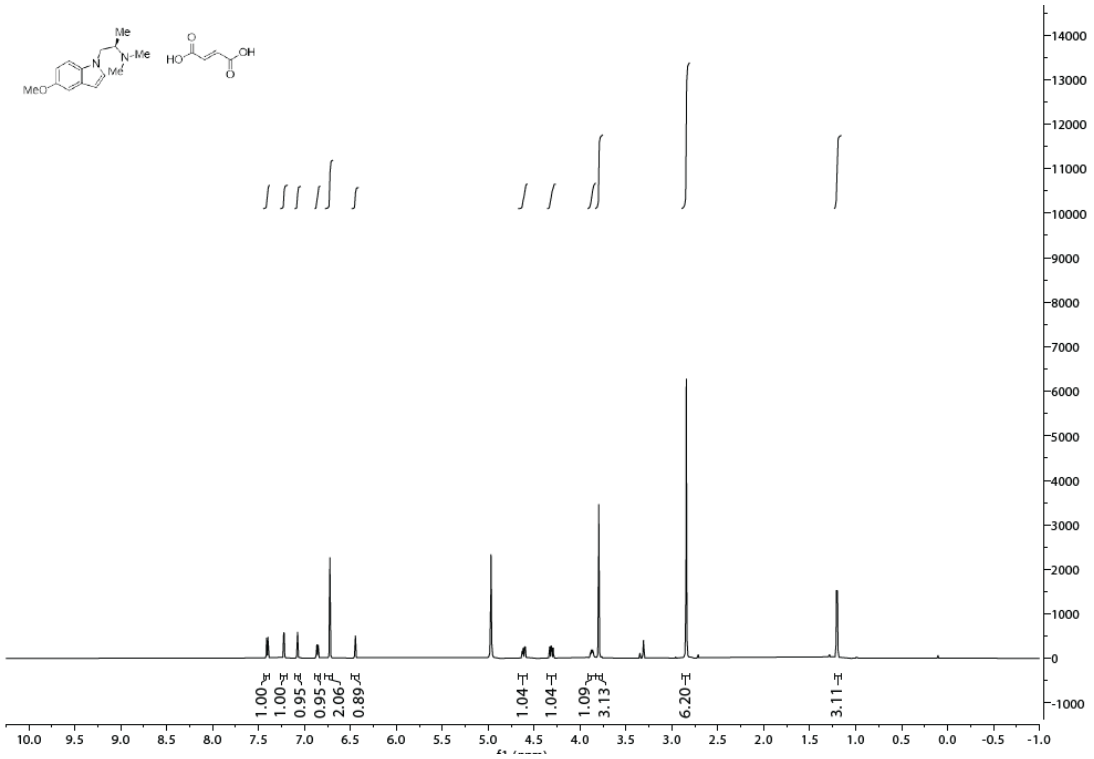

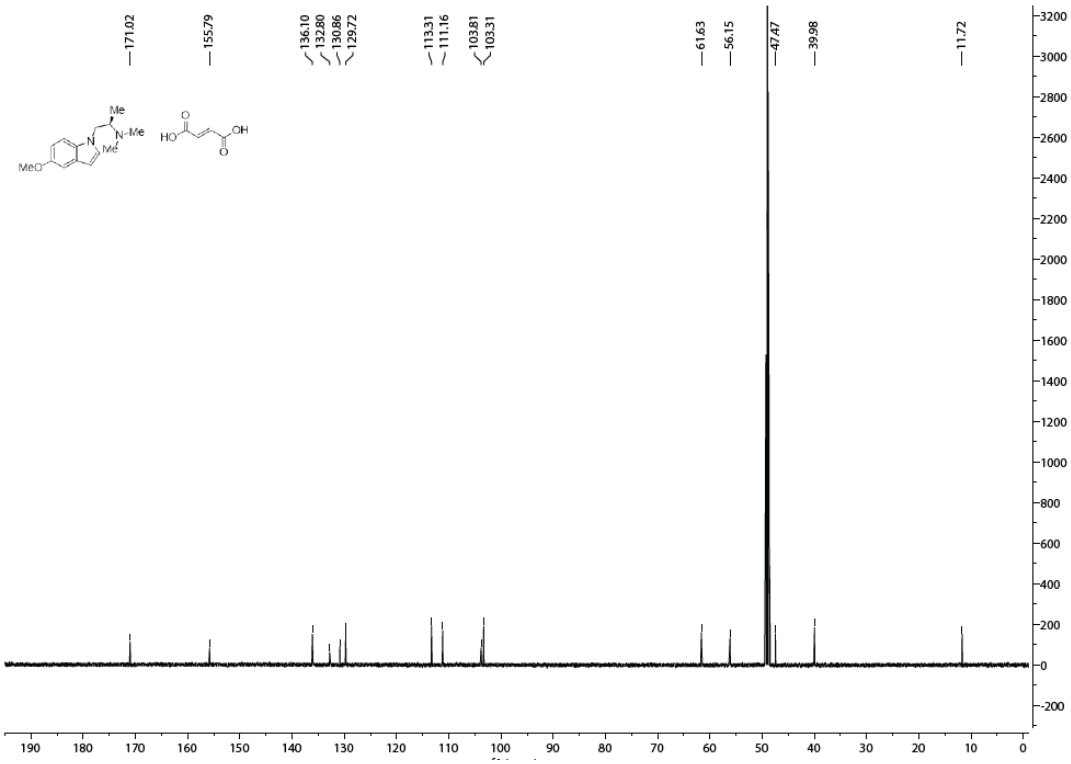

Data S2.2: LED-C-233 mass spectrum

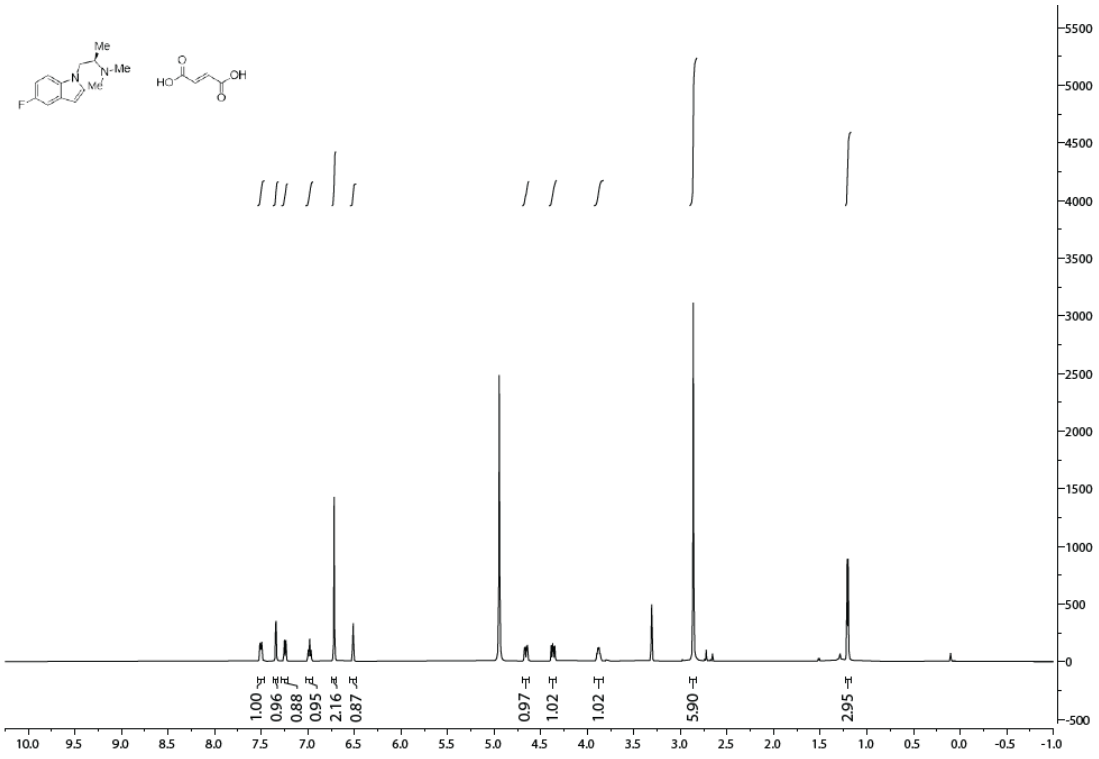

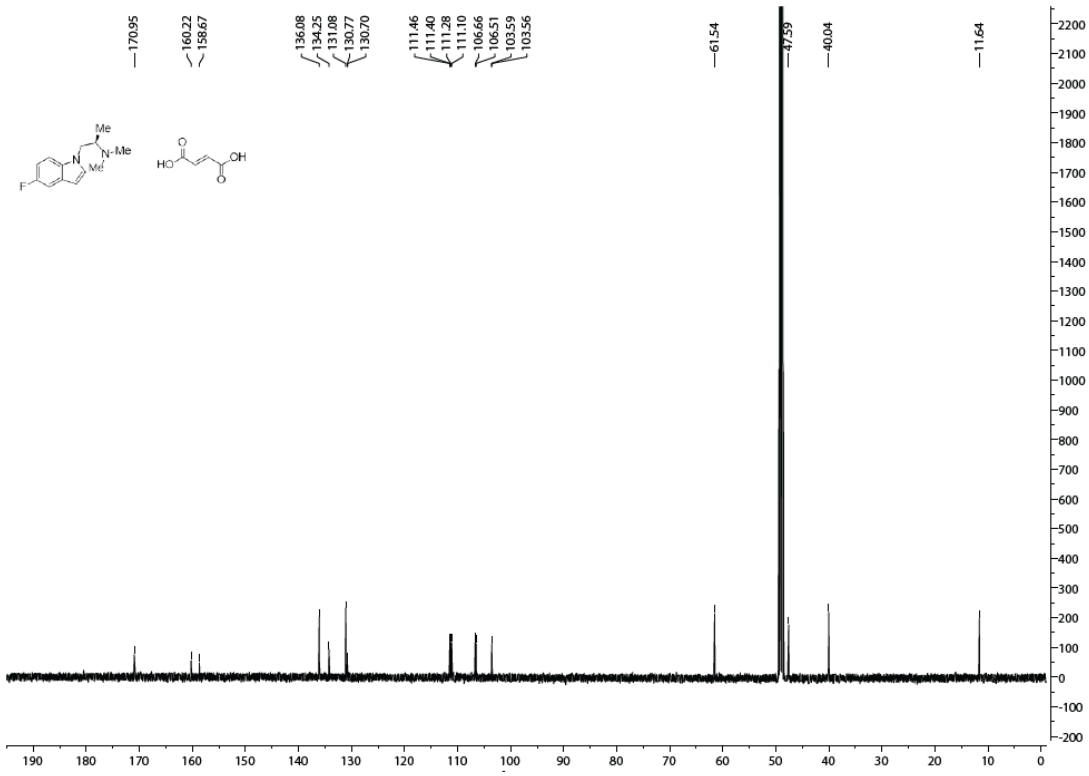

Table S2.1: Summary of the paper

Question	Approach	Results	Figures
Development of psychLight for imaging serotonin and hallucinogens			
Can we design a sensor to probe ligand-induced conformational changes of 5-HT2A receptor?	We replaced the third intracellular loop of the 5-HT2A receptor with cpGFP followed by linker screening and membrane localization optimization	psychLight responded to serotonin, but not to 5-HT2AR antagonists. Serotonin displayed an EC_{50} = 26.3 nM	Figure 1A–D
What is the sensitivity and kinetics of psychLight?	Two-photon uncaging and imaging of serotonin in cultured cortical slices	psychLight displayed fast off kinetics (5.4 ms) in response to single pulse uncaging (10ms)	Figure 1E–H
	Two-photon imaging of serotonin release triggered by electrical stimuli in acute slices	psychLight was able to detect electrically-evoked serotonin release in BNST acute slices. The fluorescence response can be modulated by a SSRI and abolished by a sodium channel blocker TTX and a serotonin receptor antagonist granisetron	Figure 1I–M
In vivo imaging of serotonin release in multiple brain regions with fiber photometry			
Can psychLight detect behaviorally relevant serotonin release?	We applied fiber photometry to study endogenous serotonin release in DRN, BNST, BLA, and OFC triggered by auditory fear conditioning	psychLight can faithfully detect the serotonin dynamics across the full-course of fear-learning in single trials (d'>12).	Figure 2
Imaging hallucinogenic conformations of 5-HT2AR			
Can psychLight be used to detect activation of 5-HT2AR by hallucinogens in vivo?	In vivo fiber-photometry recording in mPFC	Fluorescence increased upon administration of 5-MeO-DMT and the onset of increase correlated with the head-twitch response	Figure 3A–C
How effectively do hallucinogenic compounds activate psychLight?	Concentration-response curve in 293T cells	Determined EC_{50} values for a panel of hallucinogens	Figure 3D–G
		PsychLight EC_{50} values correlate with human hallucinogenic potency	Figure 3H
		PsychLight response is not equivalent to other measures of 5-HT2AR activation	Figure 3I
Medium-throughput pharmacological assay based on psychLight			
Can we use psychLight to establish a cell-based assay for determining hallucinogenic potentials of library compounds?		Z-score of the assay is 0.6	Figure S3D
	Engineered HEK293T cell line stably expressing psychLight2	The assay is sensitive to compounds with similar molecular structures	Figure 4B–C
	Screened a library consisting of hallucinogens, non-hallucinogens, and a panel of compounds with unknown hallucinogenic potentials	Defined a ligand score to predict the pahrmacological features of compounds: Ligand score >0: 5-HT2AR-activating hallucinogens Ligand score <0: non-hallucinogenic 5-HT2AR ligands Ligand score ~0: not 5HT2AR ligands	Figure 4D–E
		Schild regression analysis defined non-hallucinogenic ligands as competative antagonists	Figure 5D Figure S6
Identification of new hallucinogenic and non-hallucinogenic compounds			
Will predicted hallucinogens produce hallucinogenic behaviors?	Performed a three-point dose-response study of 5-halo-DMT family measuring head-twitch response and locomotion	5-F-DMT and 5-Cl-DMT produce robust HTR as predicted by psychLight 5-Br-DMT did not produce a HTR as predicted by psychLight	Figure 5A–C
What are the pharmacological features and behavioral effects of predicted non-hallucinogens, such as AAZ-A-154 ?	Performed Schild regression analysis Performed a three-point dose-response study measuring head-twitch response and locomotion	AAZ-A-154 is a competative 5-HT2AR ligand that did not produce a HTR as predicted by psychLight	Figure 5D–F
Characterizing antidepressant-like effects of a novel non-hallucinogenic compound			
Can AAZ-A-154 promote dendritic growth in cultured neurons? If yes, is the effect 5-HT2R dependent?	Performed Sholl analysis in cultured cortical neurons treated with AAZ-A-154 or vehicle in the presence and absence of 5HT2R antagonist ketanserin.	AAZ-A-154 promoted dendritic growth. This effect can be blocked by ketanserin, implicating 5-HT2Rs in the mechanism of action	Figure 6A–C
Does AAZ-A-154 have antidepressant potential? If yes, is the effect comparable to Ketamine?	Performed forced swim test	AAZ-A-154 produces both rapid (30 min) and long-lasting (1 week) antidepressant-like effects after a single administration comparable to ketamine	Figure 6D
	Measured anhedonia in a genetic animal model relevant to depression	VMAT2-HET mutants exhibited a sucrose preference that was indistinguishable from WT controls after a single-administration and the effect was long-lasting (12-days)	Figure 6E

Reference

Aghajanian, G.K., and Marek, G.J. (1999). Serotonin and Hallucinogens. Neuropsychopharmacology 21, 16-23.

Benes, H., Deissler, A., Rodenbeck, A., Engfer, A., and Kohnen, R. (2006). Lisuride treatment of restless legs syndrome: first studies with monotherapy in de novo patients and in combination with levodopa in advanced disease. J Neural Transm (Vienna) 113, 87-92.

Berg, K.A., Maayani, S., Goldfarb, J., Scaramellini, C., Leff, P., and Clarke, W.P. (1998). Effector pathway-dependent relative efficacy at serotonin type 2A and 2C receptors: evidence for agonist-directed trafficking of receptor stimulus. Mol Pharmacol 54, 94-104.

Blair, J.B., Kurrasch-Orbaugh, D., Marona-Lewicka, D., Cumbay, M.G., Watts, V.J., Barker, E.L., and Nichols, D.E. (2000). Effect of ring fluorination on the pharmacology of hallucinogenic tryptamines. J Med Chem 43, 4701-4710.

Broussard, G.J., Unger, E.K., Liang, R., McGrew, B.P., and Tian, L. (2018). Imaging Glutamate with Genetically Encoded Fluorescent Sensors. In Biochemical Approaches for Glutamatergic Neurotransmission, S. Parrot, and L. Denoroy, eds. (New York, NY: Springer New York), pp. 117-153.

Cameron, L.P., Benson, C.J., DeFelice, B.C., Fiehn, O., and Olson, D.E. (2019). Chronic, Intermittent Microdoses of the Psychedelic N,N-Dimethyltryptamine (DMT) Produce Positive Effects on Mood and Anxiety in Rodents. ACS Chem Neurosci 10, 3261-3270.

Cameron, L.P., Benson, C.J., Dunlap, L.E., and Olson, D.E. (2018). Effects of N, N-Dimethyltryptamine on Rat Behaviors Relevant to Anxiety and Depression. ACS Chem Neurosci 9, 1582-1590.

Cameron, L.P., Tombari, R.J., Lu, J., Pell, A.J., Hurley, Z.Q., Ehinger, Y., Vargas, M.V., McCarroll, M.N., Taylor, J.C., Myers-Turnbull, D., et al. (2021). A non-hallucinogenic psychedelic analogue with therapeutic potential. Nature 589, 474-479.

Chen, T.W., Wardill, T.J., Sun, Y., Pulver, S.R., Renninger, S.L., Baohan, A., Schreiter, E.R., Kerr, R.A., Orger, M.B., Jayaraman, V., et al. (2013). Ultrasensitive fluorescent proteins for imaging neuronal activity. Nature 499, 295-300.

Chi, T., and Gold, J.A. (2020). A review of emerging therapeutic potential of psychedelic drugs in the treatment of psychiatric illnesses. J Neurol Sci 411, 116715.

Cussac, D., Boutet-Robinet, E., Ailhaud, M.C., Newman-Tancredi, A., Martel, J.C., Danty, N., and Rauly-Lestienne, I. (2008). Agonist-directed trafficking of signalling at serotonin 5-HT2A, 5-HT2B and 5-HT2C-VSV receptors mediated Gq/11 activation and calcium mobilisation in CHO cells. Eur J Pharmacol 594, 32-38.

Dunlap, L.E., Andrews, A.M., and Olson, D.E. (2018). Dark Classics in Chemical Neuroscience: 3,4-Methylenedioxymethamphetamine. ACS Chem Neurosci 9, 2408-2427.

Dunlap, L.E., Azinfar, A., Ly, C., Cameron, L.P., Viswanathan, J., Tombari, R.J., Myers-Turnbull, D., Taylor, J.C., Grodzki, A.C., Lein, P.J., et al. (2020). Identification of Psychoplastogenic N,N-Dimethylaminoisotryptamine (isoDMT) Analogues through Structure–Activity Relationship Studies. Journal of Medicinal Chemistry 63, 1142-1155.

Ebersole, B.J., Visiers, I., Weinstein, H., and Sealfon, S.C. (2003). Molecular Basis of Partial Agonism: Orientation of Indoleamine Ligands in the Binding Pocket of the Human Serotonin 5-HT2A Receptor Determines Relative Efficacy. Molecular Pharmacology 63, 36.

Fribourg, M., Moreno, J.L., Holloway, T., Provasi, D., Baki, L., Mahajan, R., Park, G., Adney, S.K., Hatcher, C., Eltit, J.M., et al. (2011). Decoding the signaling of a GPCR heteromeric complex reveals a unifying mechanism of action of antipsychotic drugs. Cell 147, 1011-1023.

Fukui, M., Rodriguiz, R.M., Zhou, J., Jiang, S.X., Phillips, L.E., Caron, M.G., and Wetsel, W.C. (2007). Vmat2 heterozygous mutant mice display a depressive-like phenotype. The Journal of neuroscience : the official journal of the Society for Neuroscience 27, 10520-10529.

Glennon, R.A., Young, R., Jacyno, J.M., Slusher, M., and Rosecrans, J.A. (1983). DOM-stimulus generalization to LSD and other hallucinogenic indolealkylamines. European Journal of Pharmacology 86, 453-459.

González-Maeso, J., Ang, R.L., Yuen, T., Chan, P., Weisstaub, N.V., López-Giménez, J.F., Zhou, M., Okawa, Y., Callado, L.F., Milligan, G., et al. (2008). Identification of a serotonin/glutamate receptor complex implicated in psychosis. Nature 452, 93-97.

Gonzalez-Maeso, J., Weisstaub, N.V., Zhou, M., Chan, P., Ivic, L., Ang, R., Lira, A., Bradley-Moore, M., Ge, Y., Zhou, Q., et al. (2007). Hallucinogens recruit specific cortical 5-HT(2A) receptor-mediated signaling pathways to affect behavior. Neuron 53, 439-452.

González-Maeso, J., Yuen, T., Ebersole, B.J., Wurmbach, E., Lira, A., Zhou, M., Weisstaub, N., Hen, R., Gingrich, J.A., and Sealfon, S.C. (2003). Transcriptome fingerprints distinguish hallucinogenic and nonhallucinogenic 5-hydroxytryptamine 2A receptor agonist effects in mouse somatosensory cortex. J Neurosci 23, 8836-8843.

Halberstadt, A.L., Chatha, M., Klein, A.K., Wallach, J., and Brandt, S.D. (2020). Correlation between the potency of hallucinogens in the mouse head-twitch response assay and their behavioral and subjective effects in other species. Neuropharmacology 167, 107933.

Hanks, J.B., and Gonzalez-Maeso, J. (2013). Animal models of serotonergic psychedelics. ACS Chem Neurosci 4, 33-42.

Hascoët, M., and Bourin, M. (2009). The Forced Swimming Test in Mice: A Suitable Model to Study Antidepressants. In, pp. 85-118.

Hauser, A.S., Attwood, M.M., Rask-Andersen, M., Schioth, H.B., and Gloriam, D.E. (2017). Trends in GPCR drug discovery: new agents, targets and indications. Nat Rev Drug Discov 16, 829-842.

Hilger, D., Masureel, M., and Kobilka, B.K. (2018). Structure and dynamics of GPCR signaling complexes. Nature Structural & Molecular Biology 25, 4-12.

Huot, P., Johnston, T.H., Lewis, K.D., Koprich, J.B., Reyes, M.G., Fox, S.H., Piggott, M.J., and Brotchie, J.M. (2011). Characterization of 3,4-methylenedioxymethamphetamine (MDMA) enantiomers in vitro and in the MPTP-lesioned primate: R-MDMA reduces severity of dyskinesia, whereas S-MDMA extends duration of ON-time. The Journal of neuroscience : the official journal of the Society for Neuroscience 31, 7190-7198.

Irannejad, R., Tomshine, J.C., Tomshine, J.R., Chevalier, M., Mahoney, J.P., Steyaert, J., Rasmussen, S.G., Sunahara, R.K., El-Samad, H., Huang, B., et al. (2013). Conformational biosensors reveal GPCR signalling from endosomes. Nature 495, 534-538.

Kalir, A., and Szara, S. (1963). Synthesis and Pharmacological Activity of Fluorinated Tryptamine Derivatives. Journal of Medicinal Chemistry 6, 716-719.

Kenakin, T., and Miller, L.J. (2010). Seven transmembrane receptors as shapeshifting proteins: the impact of allosteric modulation and functional selectivity on new drug discovery. Pharmacol Rev 62, 265-304.

Kim, K., Che, T., Panova, O., DiBerto, J.F., Lyu, J., Krumm, B.E., Wacker, D., Robertson, M.J., Seven, A.B., Nichols, D.E., et al. (2020). Structure of a Hallucinogen-Activated Gq-Coupled 5-HT2A Serotonin Receptor. Cell 182, 1574-1588 e1519.

Ko, K.W., Rasband, M.N., Meseguer, V., Kramer, R.H., and Golding, N.L. (2016). Serotonin modulates spike probability in the axon initial segment through HCN channels. Nat Neurosci 19, 826-834.

Kwon, H.B., Kozorovitskiy, Y., Oh, W.J., Peixoto, R.T., Akhtar, N., Saulnier, J.L., Gu, C., and Sabatini, B.L. (2012). Neuroligin-1-dependent competition regulates cortical synaptogenesis and synapse number. Nat Neurosci 15, 1667-1674.

Li, N., Lee, B., Liu, R.J., Banasr, M., Dwyer, J.M., Iwata, M., Li, X.Y., Aghajanian, G., and Duman, R.S. (2010). mTOR-dependent synapse formation underlies the rapid antidepressant effects of NMDA antagonists. Science 329, 959-964.

Ly, C., Greb, A.C., Cameron, L.P., Wong, J.M., Barragan, E.V., Wilson, P.C., Burbach, K.F., Soltanzadeh Zarandi, S., Sood, A., Paddy, M.R., et al. (2018). Psychedelics Promote Structural and Functional Neural Plasticity. Cell Reports 23, 3170-3182.

Marzaro, G., Guiotto, A., and Chilin, A. (2009). Microwave-promoted mono-N-alkylation of aromatic amines in water: A new efficient and green method for an old and problematic reaction. Green Chemistry - GREEN CHEM 11.

Nenajdenko, V.G., Karpov, A.S., and Balenkova, E.S. (2001). A new convenient approach to chiral β-aryl(heteroaryl)alkylamines. Tetrahedron: Asymmetry 12, 2517-2527.

Oh, W.C., Lutzu, S., Castillo, P.E., and Kwon, H.-B. (2016). De novo synaptogenesis induced by GABA in the developing mouse cortex. Science 353, 1037.

Olsen, R.H.J., DiBerto, J.F., English, J.G., Glaudin, A.M., Krumm, B.E., Slocum, S.T., Che, T., Gavin, A.C., McCorvy, J.D., Roth, B.L., et al. (2020). TRUPATH, an open-source biosensor platform for interrogating the GPCR transducerome. Nat Chem Biol 16, 841-849.

Olson, D.E. (2018). Psychoplastogens: A Promising Class of Plasticity-Promoting Neurotherapeutics. J Exp Neurosci 12, 1179069518800508-1179069518800508.

Olson, D.E. (2020). The Subjective Effects of Psychedelics May Not Be Necessary for Their Enduring Therapeutic Effects. ACS Pharmacology & Translational Science.

Patriarchi, T., Cho, J.R., Merten, K., Howe, M.W., Marley, A., Xiong, W.H., Folk, R.W., Broussard, G.J., Liang, R., Jang, M.J., et al. (2018). Ultrafast neuronal imaging of dopamine dynamics with designed genetically encoded sensors. Science 360.

Preller, K.H., Burt, J.B., Ji, J.L., Schleifer, C.H., Adkinson, B.D., Stämpfli, P., Seifritz, E., Repovs, G., Krystal, J.H., Murray, J.D., et al. (2018). Changes in global and thalamic

brain connectivity in LSD-induced altered states of consciousness are attributable to the 5-HT2A receptor. eLife 7, e35082.
Quan, J., and Tian, J. (2011). Circular polymerase extension cloning for high-throughput cloning of complex and combinatorial DNA libraries. Nat Protoc 6, 242-251.
Rabin, R.A., Regina, M., Doat, M., and Winter, J.C. (2002). 5-HT2A receptor-stimulated phosphoinositide hydrolysis in the stimulus effects of hallucinogens. Pharmacol Biochem Behav 72, 29-37.
Ren, J., Friedmann, D., Xiong, J., Liu, C.D., Ferguson, B.R., Weerakkody, T., DeLoach, K.E., Ran, C., Pun, A., Sun, Y., et al. (2018). Anatomically Defined and Functionally Distinct Dorsal Raphe Serotonin Sub-systems. Cell 175, 472-487 e420.
Roth, B.L., Irwin, J.J., and Shoichet, B.K. (2017). Discovery of new GPCR ligands to illuminate new biology. Nat Chem Biol 13, 1143-1151.
Schmid, C.L., and Bohn, L.M. (2010). Serotonin, but not N-methyltryptamines, activates the serotonin 2A receptor via a ss-arrestin2/Src/Akt signaling complex in vivo. J Neurosci 30, 13513-13524.
Schmid, C.L., Raehal, K.M., and Bohn, L.M. (2008). Agonist-directed signaling of the serotonin 2A receptor depends on beta-arrestin-2 interactions in vivo. Proc Natl Acad Sci U S A 105, 1079-1084.
Shonberg, J., Lopez, L., Scammells, P.J., Christopoulos, A., Capuano, B., and Lane, J.R. (2014). Biased agonism at G protein-coupled receptors: the promise and the challenges--a medicinal chemistry perspective. Med Res Rev 34, 1286-1330.
Somei, M., Yamada, F., Kurauchi, T., Nagahama, Y., Hasegawa, M., Yamada, K., Teranishi, S., Sato, H., and Kaneko, C. (2001). The chemistry of indoles. CIII. Simple syntheses of serotonin, N-methylserotonin, bufotenine, 5-methoxy-N-methyltryptamine, bufobutanoic acid, N-(indol-3-yl)methyl-5-methoxy-N-methyltryptamine, and lespedamine based on 1-hydroxyindole chemistry. Chem Pharm Bull (Tokyo) 49, 87-96.
Stockklausner, C., Ludwig, J., Ruppersberg, J., and Klˆcker, N. (2001). A sequence motif responsible for ER export and surface expression of Kir2.0 inward rectifier K+ channels. FEBS Letters 493.
Stoppini, L., Buchs, P.A., and Muller, D. (1991). A simple method for organotypic cultures of nervous tissue. J Neurosci Methods 37, 173-182.
Talluri, S.K., and Sudalai, A. (2007). An organo-catalytic approach to the enantioselective synthesis of (R)-selegiline. Tetrahedron 63, 9758-9763.
Tandon, N., Thakkar, K.N., LaGory, E.L., Liu, Y., and Giaccia, A.J. (2018). Generation of Stable Expression Mammalian Cell Lines Using Lentivirus. Bio Protoc 8, e3073.
Tian, L., Hires, S.A., Mao, T., Huber, D., Chiappe, M.E., Chalasani, S.H., Petreanu, L., Akerboom, J., McKinney, S.A., Schreiter, E.R., et al. (2009). Imaging neural activity in worms, flies and mice with improved GCaMP calcium indicators. Nat Methods 6, 875-881.
Tombari, R.J., Saunders, C.M., Wu, C.-Y., Dunlap, L.E., Tantillo, D.J., and Olson, D.E. (2019). Ex Vivo Analysis of Tryptophan Metabolism Using 19F NMR. ACS Chemical Biology 14, 1866-1873.

Unger, E.K., Keller, J.P., Altermatt, M., Liang, R., Matsui, A., Dong, C., Hon, O.J., Yao, Z., Sun, J., Banala, S., et al. (2020). Directed Evolution of a Selective and Sensitive Serotonin Sensor via Machine Learning. Cell 183, 1986-2002.e1926.

Wacker, D., Wang, S., McCorvy, J.D., Betz, R.M., Venkatakrishnan, A.J., Levit, A., Lansu, K., Schools, Z.L., Che, T., Nichols, D.E., et al. (2017). Crystal Structure of an LSD-Bound Human Serotonin Receptor. Cell 168, 377-389 e312.

Wan, J., Peng, W., Li, X., Qian, T., Song, K., Zeng, J., Deng, F., Hao, S., Feng, J., Zhang, P., et al. (2020). A genetically encoded GRAB sensor for measuring serotonin dynamics in vivo. BioRxiv.

Wan, Q., Okashah, N., Inoue, A., Nehme, R., Carpenter, B., Tate, C.G., and Lambert, N.A. (2018). Mini G protein probes for active G protein-coupled receptors (GPCRs) in live cells. J Biol Chem 293, 7466-7473.

Yaden, D.B., and Griffiths, R.R. (2020). The Subjective Effects of Psychedelics Are Necessary for Their Enduring Therapeutic Effects. ACS Pharmacology & Translational Science.

Zhang, J.H., Chung, T.D., and Oldenburg, K.R. (1999). A Simple Statistical Parameter for Use in Evaluation and Validation of High Throughput Screening Assays. J Biomol Screen 4, 67-73.

2.2 - Psychedelics Promote Neuroplasticity Through the Activation of Intracellular 5-HT2A Receptors

Preface

The text of this chapter is a modified version of a manuscript that was submitted to the Science Magazine on September 27, 2022, and accepted for publication on January 9, 2023 (http://doi.org/10.1126/science.adf0435). The content of this chapter includes my original work contributing to the project and experiments done by the first author under my mentorship. The layout has been adjusted in accordance with the requirements of a doctoral thesis. Authors on the original manuscript are listed as Maxemiliano V. Vargas, Lee E. Dunlap†, Chunyang Dong†, Samuel J. Carter, Robert J. Tombari, Shekib A. Jami, Lindsay P. Cameron, Seona D. Patel, Joseph J. Hennessey, Hannah N. Saeger, John D. McCorvy, John A. Gray, Lin Tian, David E. Olson.

(† authors contributed equally to this work)

Abstract

Decreased dendritic spine density in the cortex is a hallmark of several neuropsychiatric diseases, and the ability to promote cortical neuron growth has been hypothesized to underlie the rapid and sustained therapeutic effects of psychedelics. Activation of 5-hydroxytryptamine (serotonin) 2A receptors (5-HT2ARs) is essential for psychedelic-induced cortical plasticity, but it is currently unclear why some 5-HT2AR agonists promote neuroplasticity, whereas others do not. We used molecular and genetic tools to demonstrate that intracellular 5-HT2ARs mediate the plasticity-promoting properties of psychedelics; these results explain why serotonin does not engage similar plasticity mechanisms. This work emphasizes the role of location bias in 5-HT2AR signaling, identifies intracellular 5-HT2ARs as a therapeutic target, and raises the intriguing possibility that serotonin might not be the endogenous ligand for intracellular 5-HT2ARs in the cortex.

Introduction

Dysregulation of the cortex has been hypothesized to play an important role in the pathophysiology of mental illnesses such as depression and often manifests as structural changes, including decreased dendritic arbor complexity and reduced dendritic spine density (1–3). Traditional antidepressants, such as selective serotonin reuptake inhibitors (SSRIs), can rescue these deficits after chronic treatment, although it seems that their effects may be independent of serotonin and perhaps involve the activation of tropomyosin receptor kinase B (TrkB) signaling (4, 5). A class of therapeutic compounds known as psychoplastogens (6) is differentiated from SSRIs by their ability to produce both rapid and sustained effects on structural plasticity and behavior after a single administration (7). Psychoplastogens include both ketamine and serotonergic psychedelics, although their primary targets are distinct (7).

Psychedelics are 5-hydroxytryptamine (serotonin) 2A receptor (5-HT2AR) agonists that can lead to profound changes in perception, cognition, and mood (8). Recent evidence suggests that they promote cortical structural and functional neuroplasticity through activation of 5-HT2ARs (9, 10). The mechanism by which 5-HT2AR activation leads to changes in neuronal growth is still poorly defined, although it appears to involve TrkB, mechanistic target of rapamycin (mTOR), and AMPA receptor signaling (11). It is currently unclear why some 5-HT2AR ligands can promote neuroplasticity and produce sustained therapeutic behavioral responses in the absence of hallucinogenic effects, whereas other 5-HT2AR agonists do not promote plasticity at all (12–15). Indeed, serotonin itself does not produce psychedelic-like effects on neuronal growth when administered to cortical cultures (9). This enigmatic finding cannot be easily explained

by traditional biased agonism because serotonin is a balanced agonist of the 5-HT2AR that exhibits high potency and efficacy for activating both heteromeric guanine nucleotide–binding protein (G protein) and β-arrestin pathways (16, 17).

Unlike psychedelics, the physicochemical properties of serotonin prevent it from entering cells by passively diffusing across nonpolar membranes (8). Thus, we reasoned that another form of functional selectivity, known as location bias, might explain the difference in cellular signaling elicited by serotonin and psychedelics (18, 19). Here, we leveraged both chemical design and genetic manipulation to test the hypothesis that activation of an intracellular population of 5-HT2ARs is necessary for 5-HT2AR ligands to induce cortical structural plasticity and produce antidepressant-like behavioral responses.

Results

(vii) Lipophilicity Correlates with Psychoplastogenicity

To firmly establish the role of 5-HT2AR activation in psychedelic-induced spinogenesis, we administered 5-methoxy-N,N-dimethyltryptamine (5-MeO) to wild-type (WT) and 5-HT2AR knockout (KO) mice (20) and assessed structural and functional changes in layer 5 pyramidal neurons of the prefrontal cortex (PFC) 24 hours later (Figure S2.7A to C). Golgi-Cox staining revealed that 5-MeO increased spine density in both male and female animals, and this effect was absent in 5-HT2AR KO mice (Figure S2.7A and B). Furthermore, ex vivo electrophysiology confirmed that 5-HT2AR activation is necessary for 5-MeO to produce sustained increases in both the frequency and amplitude of spontaneous excitatory postsynaptic currents (sEPSCs) (Figure S2.7C).

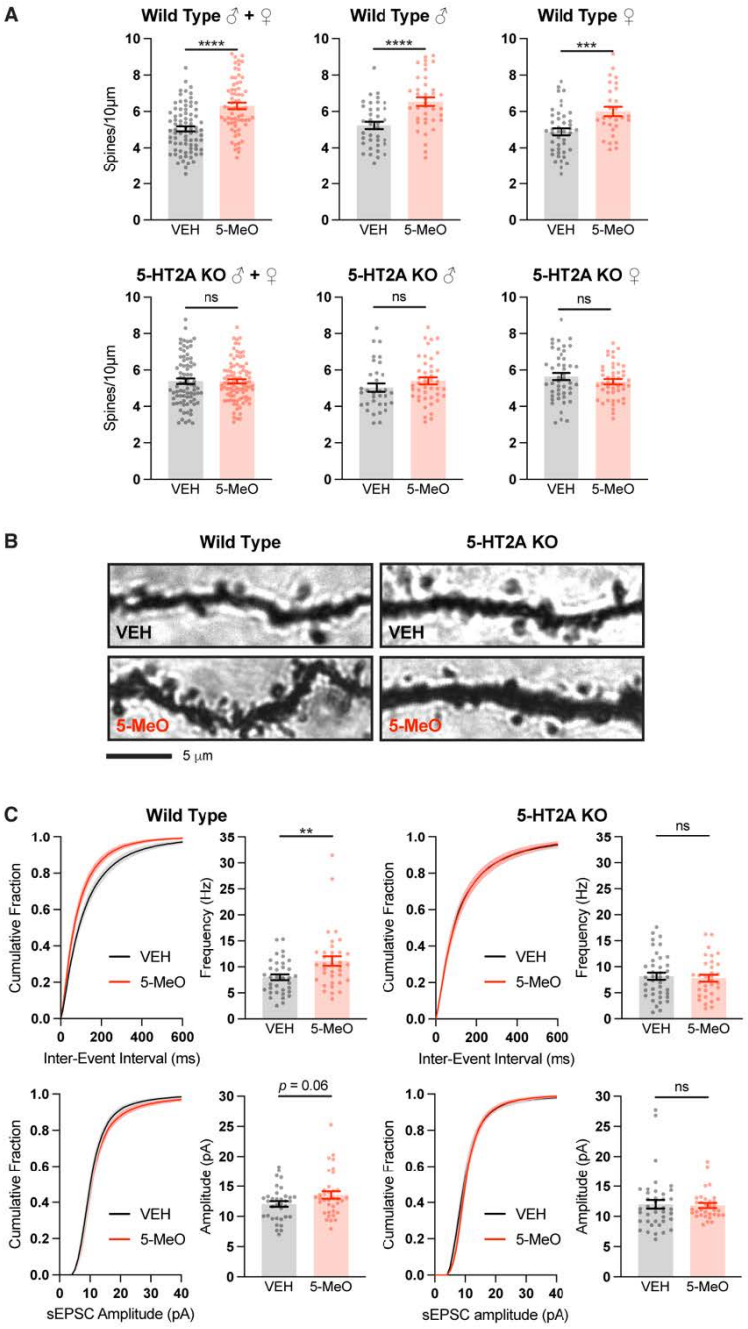

Figure S2.7. 5-MeO-DMT promotes cortical plasticity through activation of 5-HT2A receptors.
(A) Dendritic spine density is increased in the PFC of WT, but not 5-HT2AR KO mice, 24 h after a single dose of 5-MeO-MT (50 mg/kg, IP).
(B) Representative images of dendritic spines
following treatment with 5-MeO.
(C) Frequency and amplitude of sEPSCs is increased in the PFC of WT, but not 5-HT2AR KO mice, 24 h after a single dose of 5-MeO-DMT (50 mg/kg, IP).
Data represent mean Å} SEM. *p < 0.05, **p < 0.01, ***p < 0.001, ****p < 0.0001 (two-tailed unpaired Student's t test).

Next, we determined how the structures of 5-HT2AR ligands affect their abilities to promote neuronal growth by treating embryonic rat cortical neurons with serotonin, tryptamine (TRY), 5-methoxytryptamine (5-MeO–TRY), and their corresponding N-methyl and N,N-dimethyl congeners (Figure 2.7A) before assessing neuronal morphology by means of Sholl analysis (21). Ketamine was used as a positive control because of its known ability to induce structural plasticity in this assay (9). These structure-activity relationship (SAR) studies revealed that increasing N-methylation led to an enhanced ability to promote neuronal growth, with the N,N-dimethyl compounds increasing dendritic arbor complexity to the greatest extent (Figure 2.7B to D).

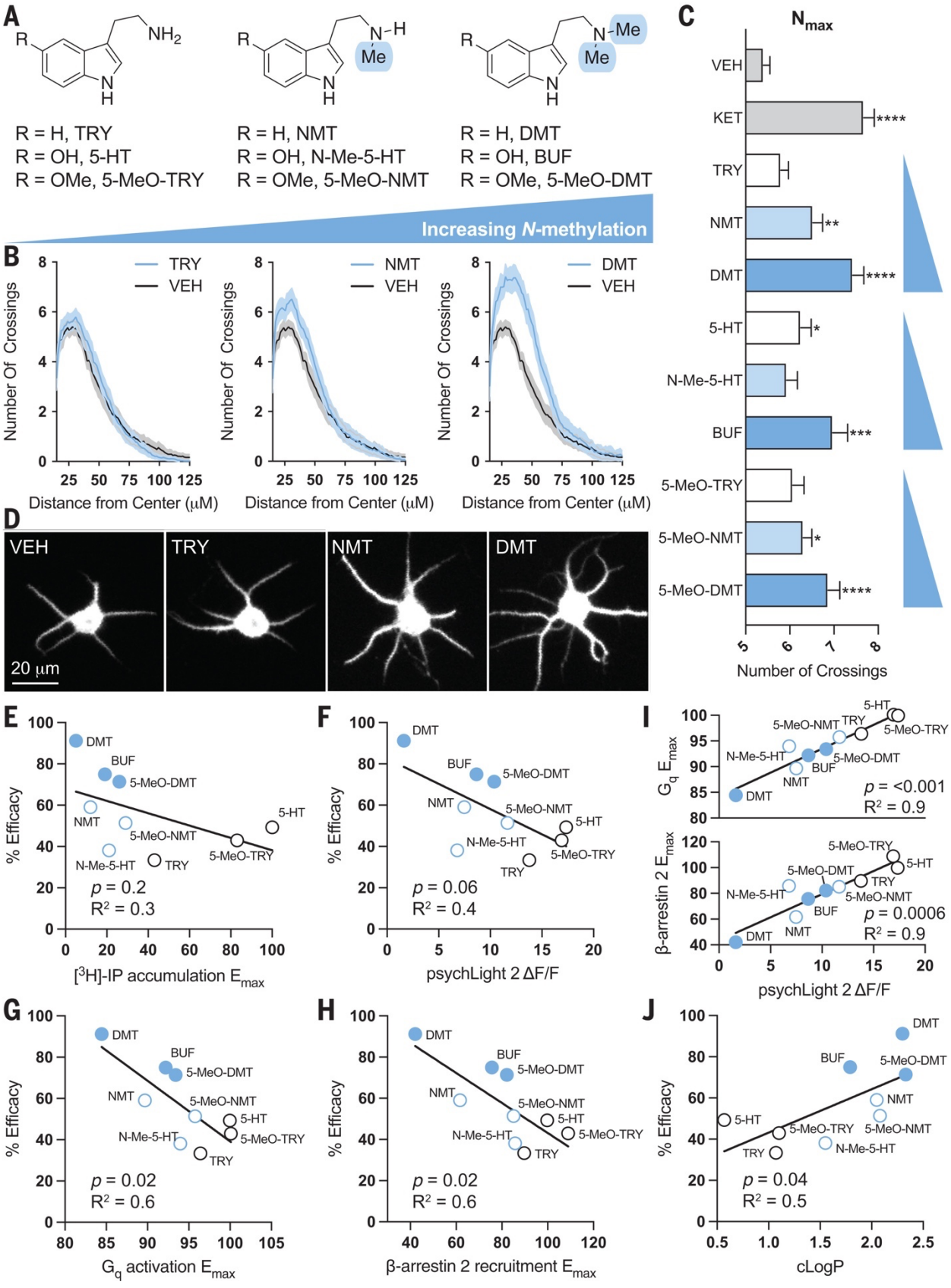
A
R = H, TRY
R = OH, 5-HT
R = OMe, 5-MeO-TRY
R = H, NMT
R = OH, N-Me-5-HT
R = OMe, 5-MeO-NMT
R = H, DMT
R = OH, BUF
R = OMe, 5-MeO-DMT
Increasing N-methylation
B
TRY
VEH
NMT
DMT
Number Of Crossings
Distance from Center (μM)
C
Nmax
VEH
KET
TRY
NMT
DMT
5-HT
N-Me-5-HT
BUF
5-MeO-TRY
5-MeO-NMT
5-MeO-DMT
Number of Crossings
D
VEH
TRY
NMT
DMT
20 μm
E
% Efficacy
[3H]-IP accumulation Emax
p = 0.2
R2 = 0.3
F
psychLight 2 ΔF/F
p = 0.06
R2 = 0.4
I
Gq Emax
p = <0.001
R2 = 0.9
β-arrestin 2 Emax
p = 0.0006
R2 = 0.9
G
Gq activation Emax
p = 0.02
R2 = 0.6
H
β-arrestin 2 recruitment Emax
p = 0.02
R2 = 0.6
J
cLogP
p = 0.04
R2 = 0.5

Figure 2.7. Compound-induced neuronal growth correlates with ligand lipophilicity.
(A) Chemical structures of serotonin, TRY, and 5-MeO–TRY as well as their corresponding N-methyl and N,N-dimethyl analogs. 5-HT, serotonin; BUF, bufotenin; Me, methyl; N-Me-5-HT, N-methylserotonin; NMT, N-methyltryptamine.
(B) Sholl analysis demonstrates that increasing N-methylation leads to a concomitant increase in dendritic arbor complexity. The shaded area represents 95% confidence intervals. Sholl plots were generated from rat embryonic cortical neurons (DIV6) treated with compounds (10 μM). VEH, vehicle.
(C) Maximum numbers of crossings (Nmax) of the Sholl plots in (B) (N = 45 to 64 neurons per treatment). Error bars represent standard error of the mean. KET, ketamine.
(D) Widefield images of rat embryonic cortical neurons (DIV6) treated with compounds (10 μM).
(E to J) Correlation plots of Sholl analysis percent efficacy (Nmax values relative to 10 μM ketamine as the positive control) versus [3H]-IP accumulation (E), activation of psychLight2 (F), Gq activation (G), β-arrestin recruitment (H), or calculated LogP (J). PsychLight2 activation correlates well with both Gq activation and β-arrestin recruitment (I).
Compounds were treated at 10 μM. Data for [3H]-IP accumulation were obtained from literature values (22). *$p < 0.05$, **$p < 0.01$, ***$p < 0.001$, and ****$p < 0.0001$, as compared with VEH controls [one-way analysis of variance (ANOVA) followed by Dunnett's multiple comparisons test]. R2 values were calculated through simple liner regression. $\Delta F/F$, change in fluorescence intensity relative to the baseline fluorescence intensity; Emax, maximum effect.

Increasing N-methylation is known to affect the efficacy of 5-HT2AR signaling, so we attempted to correlate psychoplastogenic efficacy across a range of 5-HT2AR ligands with efficacy in a traditional [3H]–inositol phosphates (IP) accumulation assay (Figure 2.7E) (22). Notably, we did not observe a positive correlation between psychoplastogenic effects and ligand efficacy. Indeed, there seemed to be a nonsignificant inverse correlation between [3H]-IP accumulation and dendritogenesis efficacy (Figure 2.7E). To avoid potential issues associated with the amplification of secondary messengers, we used psychLight2, a fluorescent biosensor that is capable of directly detecting changes in 5-HT2AR conformation (14). PsychLight2 efficacy closely mirrored that observed by using [3H]-IP accumulation assays, although psychLight2 efficacy exhibited an even stronger anticorrelation with dendritogenesis efficacy ($P = 0.06$) (Figure 2.7F). Lastly, we used bioluminescence resonance energy transfer (BRET) assays to directly measure Gq activation or β-arrestin-2 recruitment (Figure S2.8) (23). Both measures of 5-HT2AR

efficacy exhibited a strong negative correlation with psychoplastogenicity (Figure 2.7G and H). Moreover, both Gq activation and β-arrestin recruitment correlated well with psychLight efficacy [coefficient of determination (R2) = 0.9; $P < 0.0001$ and $P = 0.0006$, respectively] (Figure 2.7I). Negative correlation between 5-HT2AR efficacy and psychoplastogenicity should be interpreted with caution because this relationship may only apply to tryptamine-based ligands or compounds that exhibit a threshold level of 5-HT2AR activation.

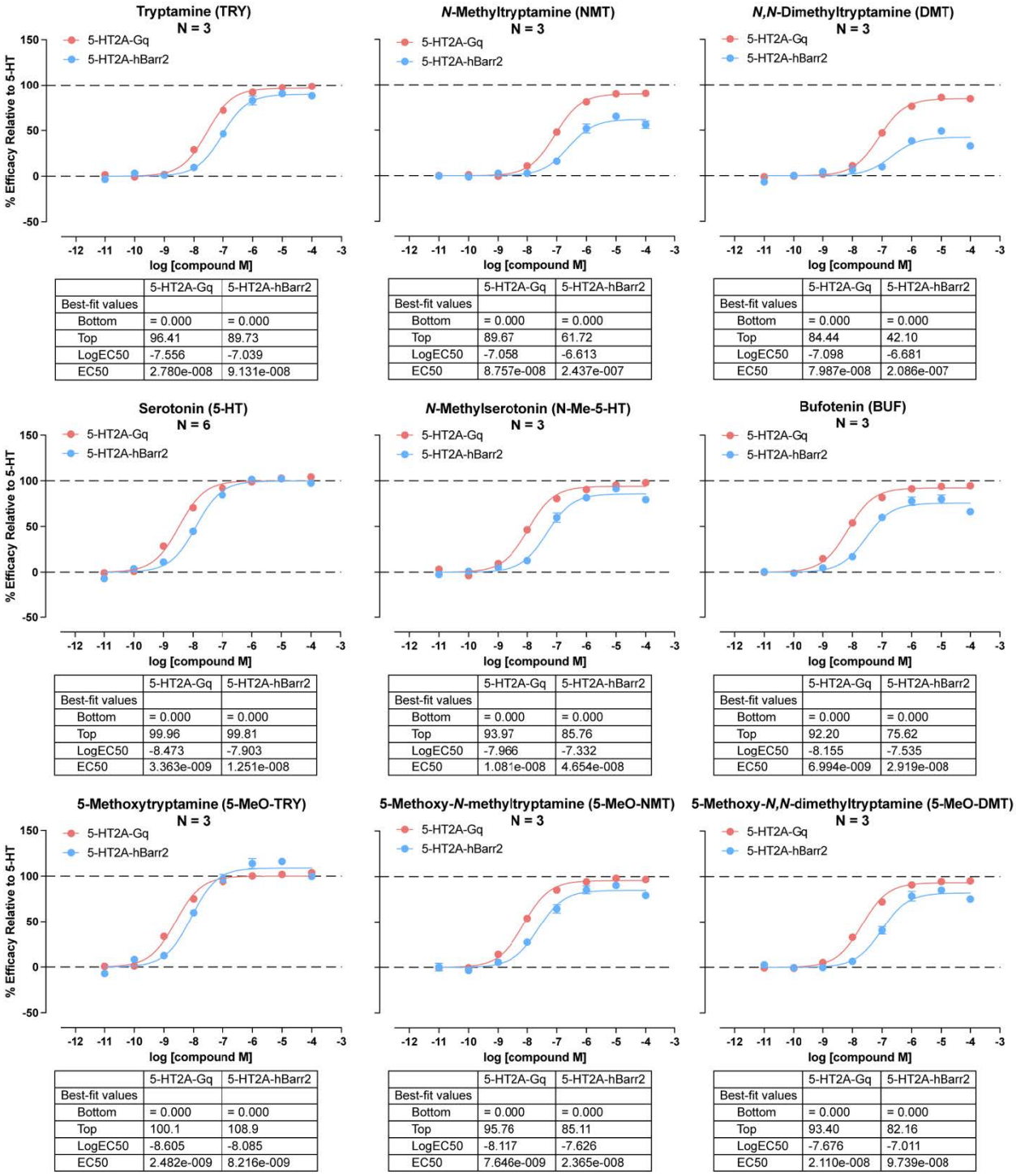

	5-HT2A-Gq	5-HT2A-hBarr2
Best-fit values		
Bottom	= 0.000	= 0.000
Top	96.41	89.73
LogEC50	-7.556	-7.039
EC50	2.780e-008	9.131e-008

	5-HT2A-Gq	5-HT2A-hBarr2
Best-fit values		
Bottom	= 0.000	= 0.000
Top	89.67	61.72
LogEC50	-7.058	-6.613
EC50	8.757e-008	2.437e-007

	5-HT2A-Gq	5-HT2A-hBarr2
Best-fit values		
Bottom	= 0.000	= 0.000
Top	84.44	42.10
LogEC50	-7.098	-6.681
EC50	7.987e-008	2.086e-007

	5-HT2A-Gq	5-HT2A-hBarr2
Best-fit values		
Bottom	= 0.000	= 0.000
Top	99.96	99.81
LogEC50	-8.473	-7.903
EC50	3.363e-009	1.251e-008

	5-HT2A-Gq	5-HT2A-hBarr2
Best-fit values		
Bottom	= 0.000	= 0.000
Top	93.97	85.76
LogEC50	-7.966	-7.332
EC50	1.081e-008	4.654e-008

	5-HT2A-Gq	5-HT2A-hBarr2
Best-fit values		
Bottom	= 0.000	= 0.000
Top	92.20	75.62
LogEC50	-8.155	-7.535
EC50	6.994e-009	2.919e-008

	5-HT2A-Gq	5-HT2A-hBarr2
Best-fit values		
Bottom	= 0.000	= 0.000
Top	100.1	108.9
LogEC50	-8.605	-8.085
EC50	2.482e-009	8.216e-009

	5-HT2A-Gq	5-HT2A-hBarr2
Best-fit values		
Bottom	= 0.000	= 0.000
Top	95.76	85.11
LogEC50	-8.117	-7.626
EC50	7.646e-009	2.365e-008

	5-HT2A-Gq	5-HT2A-hBarr2
Best-fit values		
Bottom	= 0.000	= 0.000
Top	93.40	82.16
LogEC50	-7.676	-7.011
EC50	2.110e-008	9.739e-008

Figure S2.8. Tryptamines are agonists of 5-HT2ARs.
Bioluminescence resonance energy transfer (BRET) assays were conducted to directly measure Gq dissociation or β-arrestin-2 recruitment following stimulation of 5-HT2Ars in HEK293T cells.
Data represent mean and standard error of the mean (SEM) performed in duplicate in the assay plates, and data are from three independent experiments.

Nitrogen methylation of 5-HT2AR ligands structurally related to serotonin is known to result in partial agonism (22), but it also has a profound effect on their physicochemical properties. These compounds display a wide range of lipophilicities that ranged from highly polar molecules such as serotonin to relatively nonpolar compounds such as N,N-dimethyltryptamine (DMT). Using calculated LogP (cLogP) values, we observed a significant positive correlation with psychoplastogenic effects—more lipophilic agonists exhibited greater abilities to promote structural plasticity than polar compounds (Figure 2.7J). This relationship was evident within the TRY, serotonin, and 5-MeO–TRY scaffolds. The finding that lipophilicity was a better predictor of psychoplastogenicity than 5-HT2AR activation led us to hypothesize that an intracellular pool of 5-HT2ARs in cortical neurons might be responsible for psychedelic-induced neuronal growth.

(viii) Primary Localization of 5-HT2ARs in Cortical Neurons is Intracellular

Although most G protein–coupled receptors (GPCRs) are believed to be localized primarily to the plasma membrane, several exhibit substantial intracellular localizations (24–27). In vitro and ex vivo experiments have also established the existence of large intracellular pools of 5-HT2ARs in various cell types in the absence of a ligand (28–31). To compare 5-HT2AR localization patterns between cell types, we expressed a Myc–5-HT2AR–enhanced cyan fluorescent protein (ECFP) construct in both human embryonic kidney 293T (HEK293T) cells and cortical neurons, performed live-cell imaging, and assessed colocalization with a membrane dye (Cellbrite Steady) that labels the extracellular side of the plasma membrane. Because overexpression of tagged receptor constructs might alter trafficking and localization, we included several controls. We used

a β2 adrenergic receptor tagged with ECFP (β2AR-ECFP) as a GPCR that is canonically described as being plasma membrane bound, and we used an ECFP construct to establish the localization of a fluorescent protein that is not tagged to a GPCR (32, 33).

When expressed in HEK293T cells that were cultured in the absence of serum, 5-HT2ARs and β2ARs exhibited similar cellular expression patterns (Figure 2.8A) and possessed correlation coefficients with the plasma membrane marker that were not statistically different (Figure 2.8B). However, these two GPCRs displayed distinct localization patterns in neurons. In cortical neurons, β2AR expression was more highly correlated with the plasma membrane marker than was 5-HT2AR expression (Figure 2.8B), which demonstrates that overexpression of a GPCR in cortical neurons does not necessarily lead to intracellular localization. The extent of overexpression was similar for 5-HT2ARs and β2ARs in both HEK293T cells and cortical neurons (Figure S2.9A). We performed these localization experiments without serum in the culturing media because serum contains serotonin, which can lead to agonist-induced changes in trafficking and localization (Figure S2.93, B and C). In both neurons and HEK293T cells, the expression patterns of the tagged GPCRs were markedly distinct from ECFP, which confirms that the GPCR component of the constructs dictates cellular localization. Expression of a FLAG–5-HT2AR construct in rat cortical neurons produced a similar intracellular localization pattern, which suggests that these tags do not substantially alter the localization patterns of the 5-HT2AR (34).

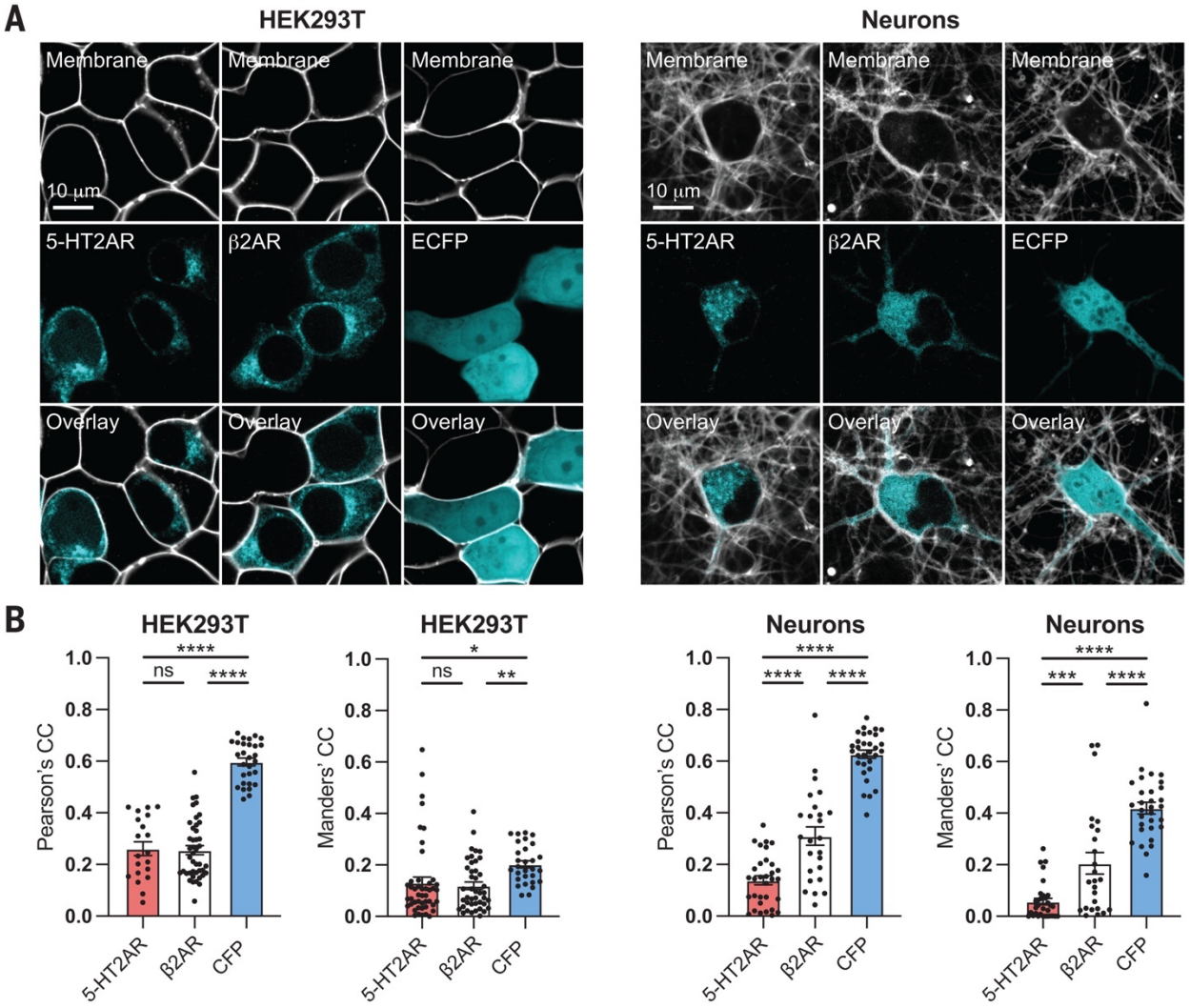

Figure 2.8. Cortical neurons express intracellular 5-HT2A receptors.
(A) Live-cell images of HEK293T cells and rat embryonic cortical neurons (DIV6) expressing Myc–5-HT2AR–CFP, β2AR-ECFP, or ECFP. Signals from the fluorescent protein and fluorescent plasma membrane marker (Cellbrite Steady) are shown in cyan and white, respectively. The expression patterns of 5-HT2ARs and β2ARs are comparable in HEK293T cells. However, in neurons, β2ARs exhibit higher expression on the plasma membrane than 5-HT2ARs. The expression of ECFP is diffuse in both HEK293T cells and cortical neurons.
(B) Pearson's correlation coefficients (Pearson's CCs) and Manders' colocalization coefficients (Manders' CCs) quantify the extent of colocalization between MYC–5-HT2AR–CFP, β2AR-ECFP, or ECFP and the fluorescent plasma membrane marker (N = 20 to 43 cells per group). Error bars represent standard error of the mean. ns is not significant, *$p < 0.05$, **$p < 0.01$, ***$p < 0.001$, and ****$p < 0.0001$; bars indicate comparisons between data (one-way ANOVA followed by Tukey's multiple comparisons test).

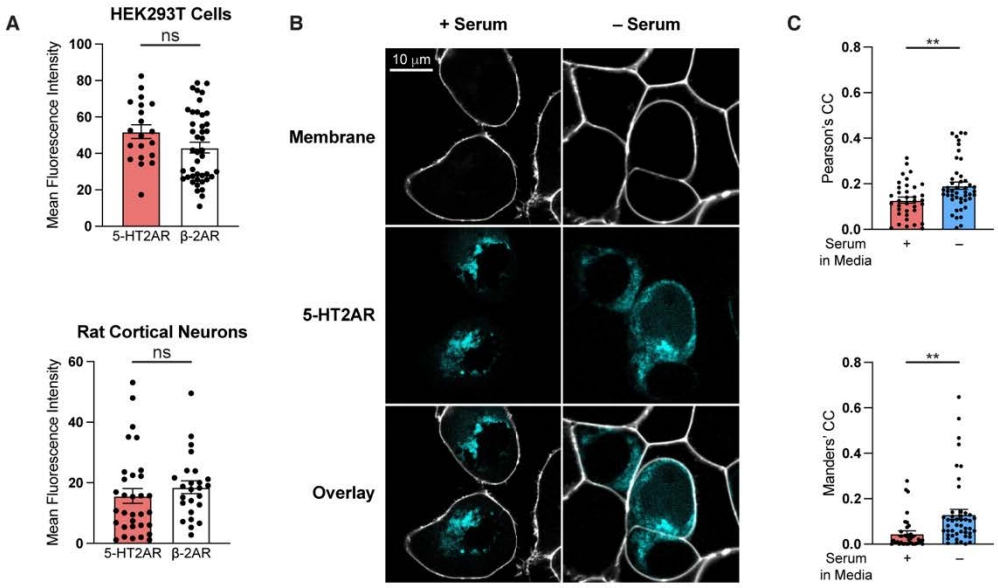

Figure S2.9. The presence of serum in the media impacts the cellular localization of 5-HT2ARs.
(A) Expression levels of 5-HT2ARs and b-2ARs tagged with CFP and ECFP, respectively, are comparable in both HEK293T cells and rat cortical neurons.
(B) Representative live cell images of HEK293T cells expressing MYC-5-HT2AR-CFP grown in the presence (+) and absence (–) of serum. Cellbrite® Steady was used to mark the plasma membrane.
(C) Pearson's Correlation Coefficient (PCC) and Manders' Colocalization Coefficient (MCC) quantify the extent of colocalization between Myc-5-HT2AR-CFP and Cellbrite® Steady (N = 36–46 HEK293T cells per treatment). Data represent mean ± SEM. *p < 0.05, **p < 0.01, ***p < 0.001, ****p < 0.0001 (two-tailed unpaired Student's t test).

Bright punctate staining within neurons suggested that 5-HT2ARs were localized within intracellular compartments (Figure 2.8A), so we performed additional immunocytochemistry experiments to assess the overlap with markers of various subcellular organelles (Figure S2.10). We observed a high level of 5-HT2AR colocalization with Rab5 and Rab7 in both HEK293T cells and neurons. Ras-related guanosine triphosphatases (GTPases) of the Rab family are known to regulate intracellular transport of GPCRs (35). We observed a very large difference in 5-HT2AR colocalization with the Golgi apparatus between neurons and HEK293T cells, with the former exhibiting substantially higher correlation coefficients (Figure S2.10). The Golgi apparatus is a key regulator of GPCR signaling, and ligands can either passively diffuse into Golgi-localized

receptor pools or gain access by facilitated transmembrane transport (18, 36, 37). Signaling from within the Golgi can be distinct, as is the case for opioid receptors (38).

To ensure that high 5-HT2AR colocalization with the Golgi was not an artifact of overexpression, we assessed native 5-HT2AR expression in neurons using one of the few validated 5-HT2AR antibodies (30). To confirm the antibody's specificity, we performed in-house validation by overexpressing 5-HT2ARs in HEK293T cells (Figure S2.11A) and we used mouse 5-HT2AR KO cortical neurons (Figure S2.11B). Next, we imaged rat embryonic cortical neurons that expressed only native 5-HT2ARs or overexpressed a Myc–5-HT2AR–ECFP construct. Longitudinal and transverse line scans indicated that Myc–5-HT2AR–ECFP expression closely mirrored the native localization pattern of 5-HT2ARs (Figure S2.11C and D).

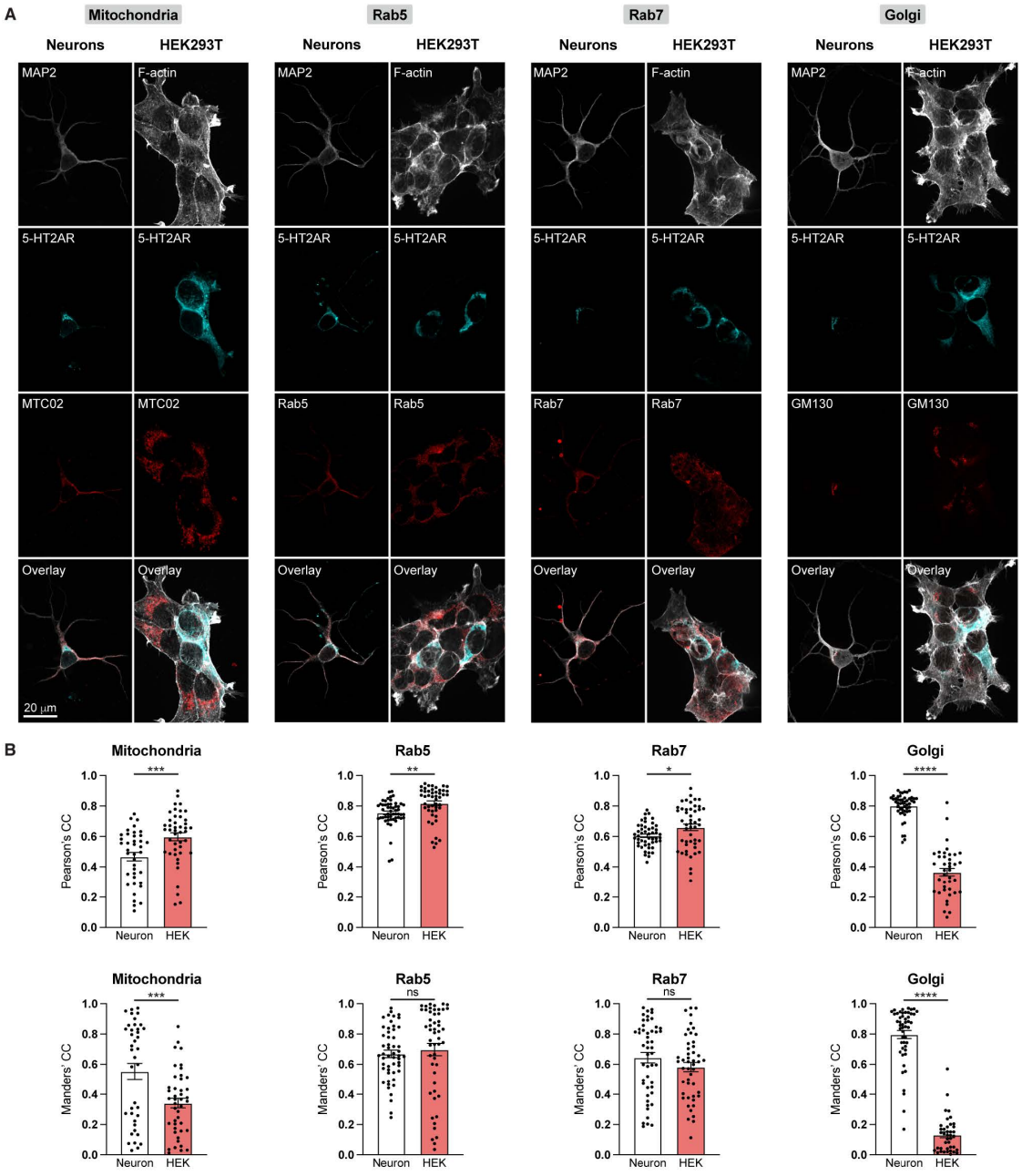

Figure S2.10. Subcellular localization of 5-HT2ARs in fixed HEK293T cells and cortical neurons.
(A) Representative images of HEK293T cells or embryonic rat cortical neurons (DIV6) expressing Myc-5-HT2AR-CFP (anti-CFP Ab) and co-stained for various markers of subcellular organelles (mitochondria, anti-MTC02; early endosomes, anti-Rab5; late endosomes, anti-Rab7; Golgi apparatus, anti-GM130). An anti-MAP2 antibody or a fluorescent phalloidin conjugate was used to visualize the morphology of neurons and HEK293T cells, respectively.
(B) Pearson's Correlation Coefficient (PCC) and Manders' Colocalization Coefficient (MCC) quantify the extent of colocalization between MYC-5-HT2AR-CFP and various subcellular markers (N = 39–52 cells per group). Data represent mean ± SEM. *p < 0.05, **p < 0.01, ***p < 0.001, ****p < 0.0001 (two-tailed unpaired Student's t test).

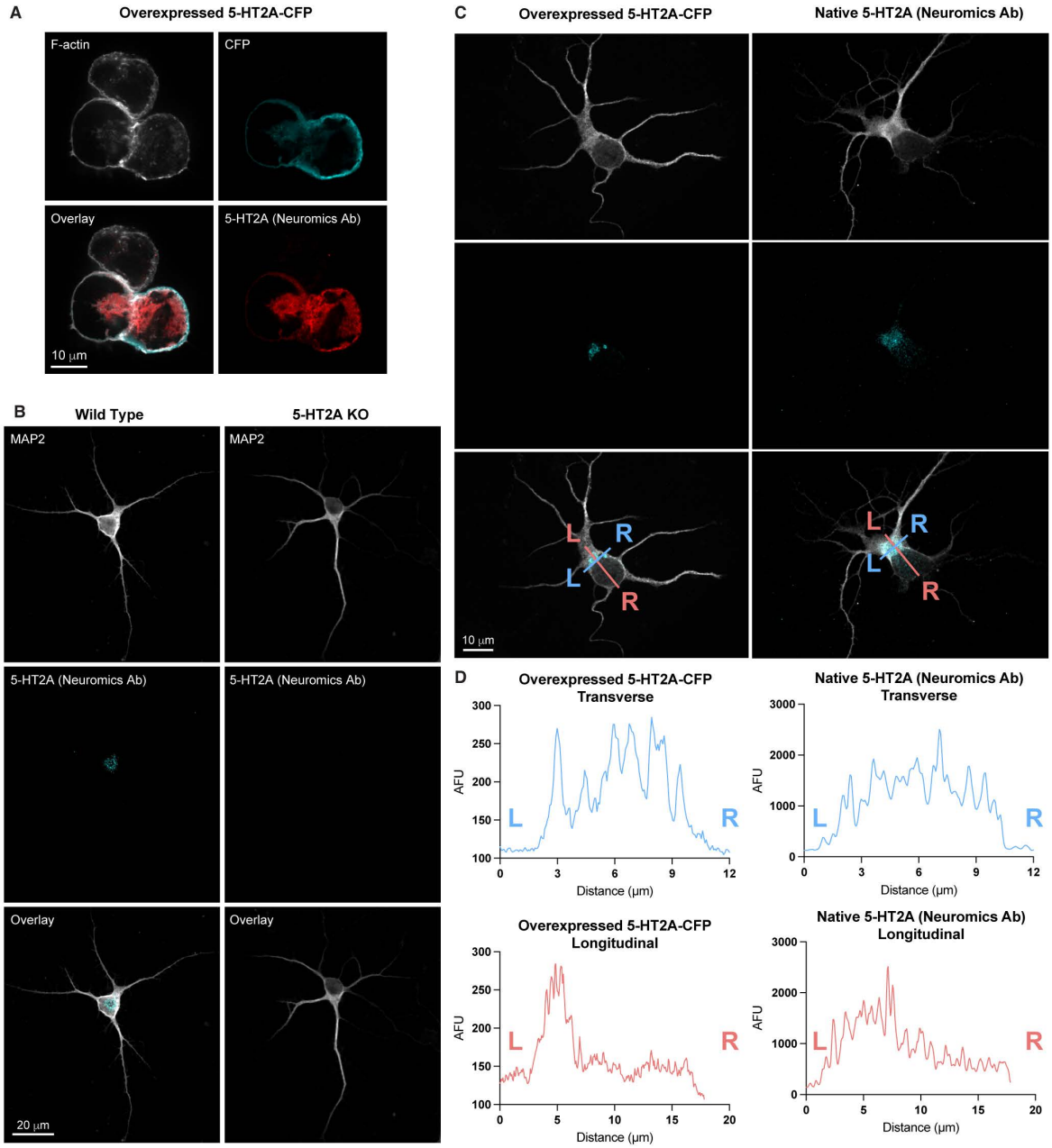

Figure S2.11. Validation of an antibody for the 5-HT2AR.

(A) HEK293T cells were transfected with MYC-5-HT2AR-CFP. The cells were fixed and stained for f-actin (fluorescent phalloidin conjugate), CFP (anti-CFP Ab) and 5-HT2ARs (Neuromics anti-5-HT2B Ab). Excellent overlap between the 5-HT2AR and CFP signals were observed. Moreover, 5-HT2AR staining was absent in the cell that did not express the plasmid (top cell).

(B) Signal from the Neuromics anti-5-HT2AR Ab is observed in wild type but not 5-HT2AR knockout embryonic mouse neurons (DIV7).

(C) Representative images comparing native expression of 5- HT2ARs (Neuromics Ab) to overexpression of a Myc-5-HT2AR-CFP construct (CFP) in embryonic rat cortical neurons (DIV7).

(D) Longitudinal (red) and transverse (blue) line scans from images in C demonstrate similar localization of native 5-HT2ARs and overexpressed 5-HT2ARs in rat cortical neurons. Line scans are shown from left (L) to right (R).

(ix) Membrane Permeability is Required for Psychedelic-Induced Neuroplasticity

Given that cortical neurons have a large pool of intracellular 5-HT2ARs, we next used chemical tools to determine whether activation of this intracellular population was essential for psychedelics to promote structural neuroplasticity. Chemical modification of the membrane-permeable ligands DMT, psilocin (PSI), and ketanserin (KTSN) converted them into highly charged membrane-impermeable congeners N,N,N-trimethyltryptamine (TMT), psilocybin (PSY), and methylated ketanserin (MKTSN), respectively (Figure 2.9A). All of the charged species exhibited negative cLogP scores (Figure S2.12A) but retained affinity for 5-HT2ARs, as determined by radioligand competition binding experiments (Figure S2.12B). In psychLight2 assays, the membrane-impermeable analogs displayed comparable efficacies to their uncharged parent molecules with reduced potencies (Figure S2.12, C and D).

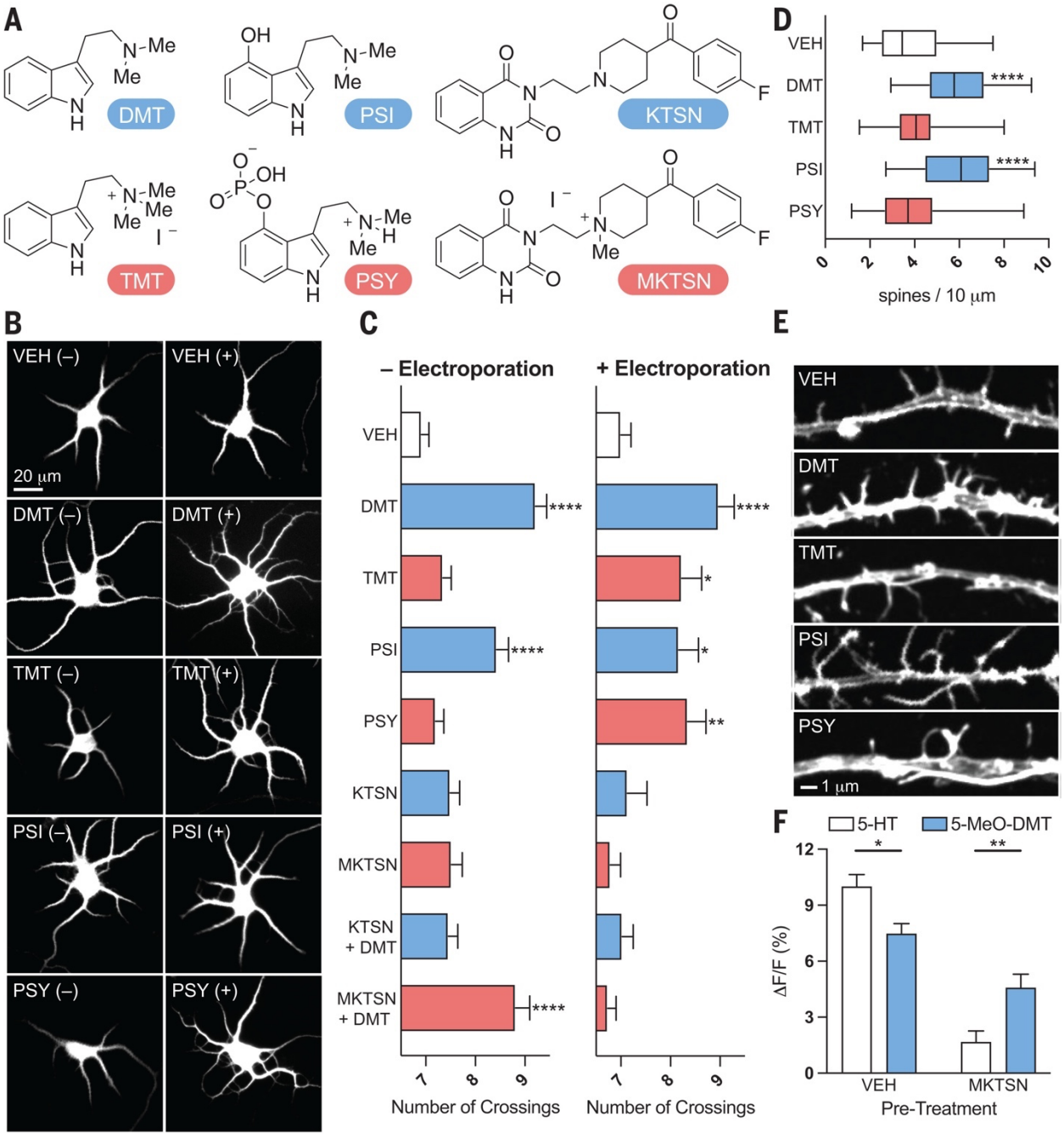

Figure 2.9. Intracellular 5-HT2ARs mediate structural plasticity induced by serotonergic psychoplastogens.
(A) Structures of membrane-permeable (blue) and impermeable (red) compounds.
(B) Widefield images of rat embryonic cortical neurons (DIV6) that were administered compounds with (+) and without (−) electroporation.
(C) Nmax values obtained from Sholl plots. Membrane-impermeable analogs of psychedelics (1 µM) only promote growth when administered with electroporation (N = 35 to 110 neurons per treatment). Unlike KTSN (10 µM), MKTSN (10 µM) only blocks psychedelic-induced plasticity when administered with electroporation (N = 45 to 109 neurons per treatment).
(D) Membrane-impermeable agonists of 5-HT2ARs (1 µM) cannot promote spinogenesis in cultured embryonic rat cortical neurons (DIV15) (N = 30 to 34 neurons per treatment).

(E) Confocal images of treated cortical neurons (DIV15).
(F) HEK293T cells that expressed psychLight1 were pretreated with VEH or MKTSN (10 μM) before the administration of serotonin (10 μM) or 5-MeO–DMT (10 μM) (N = 41 to 54 cells per treatment).
Error bars in (C) and (F) represent standard error of the mean. *p < 0.05, **p < 0.01, and ****p < 0.0001, as compared with VEH controls in (D) and (C) (one-way ANOVA followed by Dunnett's multiple comparisons test) or between indicated pairs of data in (F) (two-way ANOVA followed by Šídák's multiple comparisons test). For box-and-whisker plots in (D), the center line represents the median, box limits are upper and lower quartiles, and whiskers are minimum and maximum values.

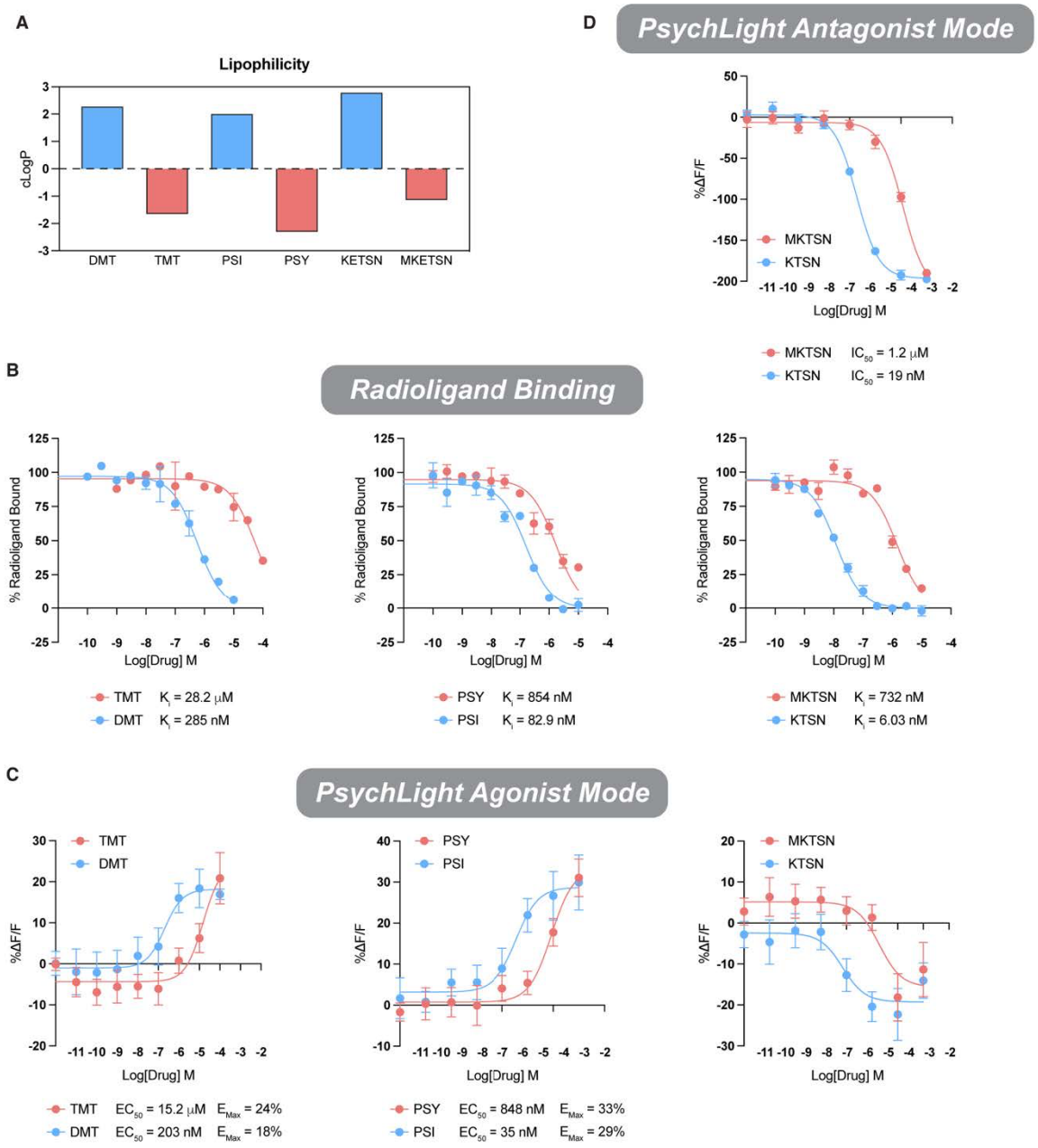

Figure S2.12. Membrane impermeable analogs of 5-HT2AR ligands retain efficacy but exhibit. reduced potency.
(A) Individual cLogP values were calculated using Molinspiration. Membrane permeable (blue) and impermeable (red) compounds exhibited positive and negative cLogP values, respectively.

(B) Competition radioligand binding studies demonstrate that membrane impermeable ligands (red) are 5-HT2AR ligands, but they are less potent than their membrane permeable congeners (blue). The percentage of [3H]-LSD bound is shown on the y-axis (N = 2–4 wells per concentration).
(C) PsychLight assays performed in agonist mode demonstrate that membrane impermeable ligands (red) retain the same efficacy as their membrane permeable congeners (blue). While DMT, TMT, PSI, and PSY are agonists, both KTSN and MKTSN act as inverse agonists (N = 5–6 wells per 21 concentration).
(D) PsychLight assays performed in antagonist mode demonstrate that both KTSN and MKTSN are antagonists (N = 5–6 wells per concentration). DMT = N,N-dimethyltryptamine; TMT = N,N,N-trimethyltryptamine; PSI = psilocin; PSY = psilocybin; KETSN = ketanserin, MKETSN = methylated ketanserin. Data represent mean ± SEM.

Next, we treated freshly dissected rat embryonic cortical neurons with DMT (1 μM) and PSI (1 μM) as well as their membrane-impermeable congeners in the presence and absence of electroporation. Electroporation creates temporary openings in the plasma membrane, which enables highly charged molecules to pass through and access the intracellular space. Although the membrane-permeable 5-HT2AR agonists were able to promote dendritogenesis regardless of whether electroporation was applied, the membrane-impermeable compounds could only promote neuronal growth when applied with electroporation (Figure 2.9B and C). Similarly, the membrane-permeable 5-HT2AR antagonist KTSN (treated in 10-fold excess at 10 μM) blocked DMT-induced plasticity both with and without electroporation; however, the membrane-impermeable antagonist MKTSN (10 μM) could only block DMT-induced neuronal growth when it was applied with electroporation (Figure 2.9B and C). By using more mature neurons (DIV15), we demonstrated that the membrane-permeable 5-HT2AR agonists increased dendritic spine density—another measure of structural neural plasticity—whereas the membrane-impermeable agonists did not (Figure 2.9D and E). KTSN was able to inhibit the effects

of DMT and PSI on dendritic spine density, whereas MKTSN was not (Figure S2.13).

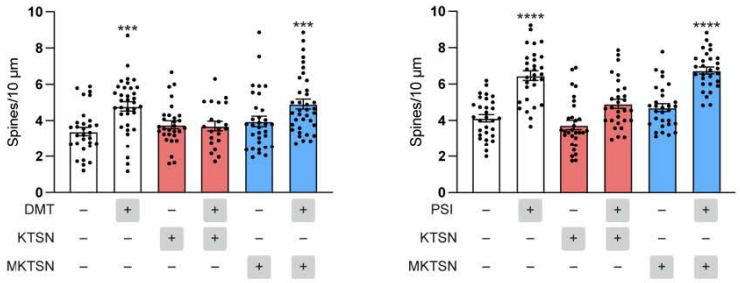

Figure S2.13. Pretreatment with KTSN, but not the membrane impermeable MKTSN, blocks the spinogenic effects of DMT and PSI.
Embryonic rat cortical neurons (DIV15) were pre-treated for 30 min with VEH (white), KTSN (10µM, red), or MKTSN (10 µM, blue) prior to the administration of VEH, DMT (1 µM), or PSI (1µM). Spine density was assessed 24 h later using a fluorescent phalloidin conjugate to label Factin-rich spines (N = 27–37 neurons per treatment). VEH = vehicle; KETSN = ketanserin; MKTSN = methylated ketanserin. Data represent mean ± SEM. *p < 0.05, **p < 0.01, ***p < 0.001, ****p < 0.0001 as compared to VEH controls (one-way ANOVA followed by Dunnet's multiple comparisons test).

To further establish that membrane-permeable and -impermeable ligands target different populations of 5-HT2ARs, we performed an experiment in HEK293T cells that express psychLight1. The psychLight1 construct was chosen over psychLight2 because the former lacks an endoplasmic reticulum (ER) export sequence, which results in greater intracellular localization (14). PsychLight1-expressing HEK293T cells were pretreated with either vehicle or MKTSN to selectively antagonize the population of 5-HT2ARs that were expressed on the plasma membrane. Next, changes in psychLight1 fluorescence were measured after administration of the membrane-impermeable ligand serotonin or its membrane-permeable congener 5-MeO–DMT. Because serotonin is a full agonist, it induced a stronger response in the absence of antagonist compared with the partial agonist 5-MeO–DMT. Pretreatment with MKTSN resulted in a much larger reduction in the serotonin-induced psychLight1 signal compared with that induced by 5-MeO–DMT (Figure 2.9F). Pretreatment with MKTSN could nearly fully antagonize the effect of

serotonin. In sharp contrast, MKTSN only partially blocked the ability of 5-MeO–DMT to turn on psychLight1 fluorescence.

Because serotonin and 5-MeO–DMT exhibit different lipophilicities (cLogP values of 0.57 and 2.33, respectively), we reasoned that their abilities to displace [3H]–d-lysergic acid diethylamide (LSD) bound to the 5-HT2AR would depend on whether those receptors were exposed to the extracellular environment. Thus, we performed radioligand competition binding experiments using intact HEK293T cells that expressed Myc–5-HT2AR or psychLight2 as well as membrane preparations obtained from these systems. The inhibition constant (Ki) values for serotonin and 5-MeO–DMT were nearly identical when using membrane preparations or intact PSYLI2 cells, with HEK293T cells that stably expressed a 5-HT2AR construct with an ER export sequence resulting in a large proportion of the 5-HT2ARs being exposed to the extracellular environment (Figure S2.14). However, 5-MeO–DMT was an order of magnitude more potent than serotonin when using intact HEK293T cells that expressed large populations of both plasma membrane–bound and intracellular 5-HT2ARs (Figure S2.14).

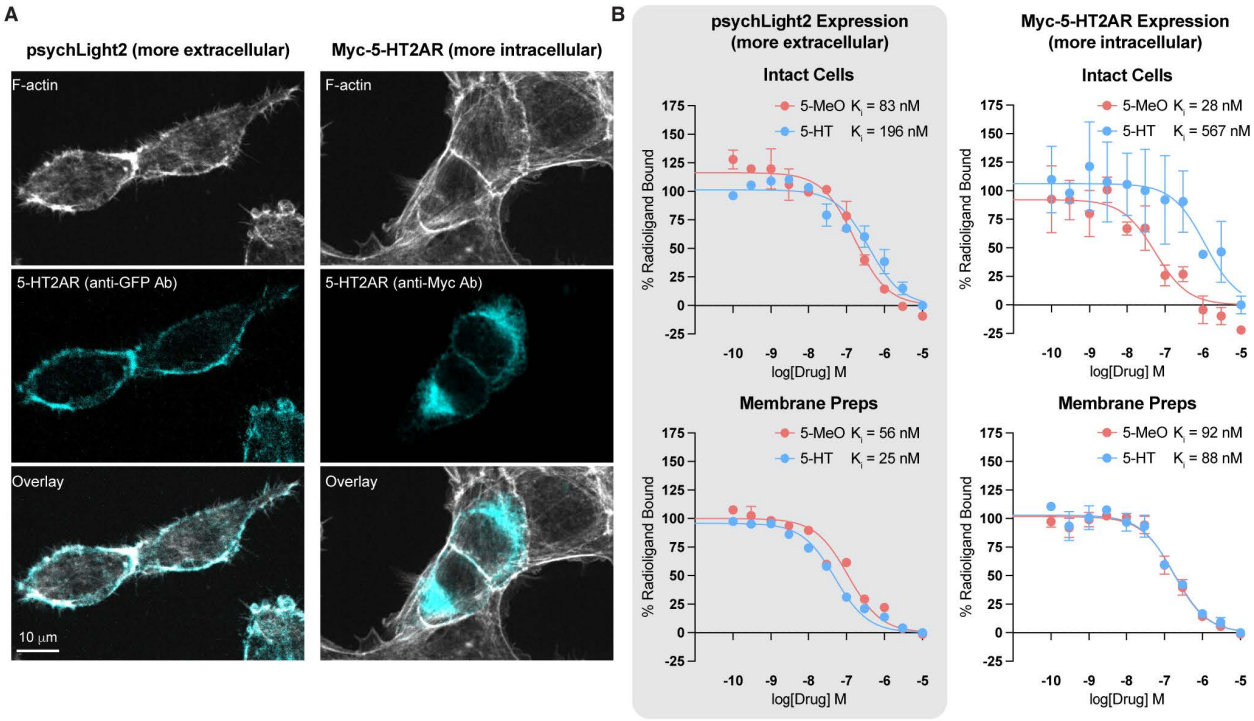

Figure S2.14. Serotonin exhibits lower potency than 5-MeO-DMT for outcompeting radioligands from intracellular 5-HT2AR binding pockets.
(A) Representative images of PSYLI2 and HEK293T cell lines expressing psychLight2 and Myc-5-HT2AR, respectively. PsychLight2 has an ER export tag, and thus, exhibits higher expression on the plasma membrane.
(B) Competition radioligand binding experiments using intact cells or membrane preparations generated from PSYLI2 cells stably expressing psychLight2 or HEK293T cells overexpressing Myc-5-HT2AR. The percentage of [3H]-LSD bound is shown on the y-axis (N = 2–3 wells per concentration). Data represent mean ± SEM.

To confirm that serotonin and 5-MeO–DMT can target distinct populations of 5-HT2ARs, we performed inositol monophosphate (IP1) assays in cortical neurons and HEK293T cells that expressed the Myc–5-HT2AR–ECFP construct. When the assay was performed in HEK293T cells that expressed Myc–5-HT2AR–ECFP, which display a large proportion of plasma membrane–bound 5-HT2ARs, serotonin and 5-MeO–DMT had comparable potencies and efficacies (Figure S2.15A). When the same experiment was performed in rat cortical neurons, serotonin failed to elicit an agonist response, although

5-MeO–DMT remained a potent agonist (Figure S2.15B).

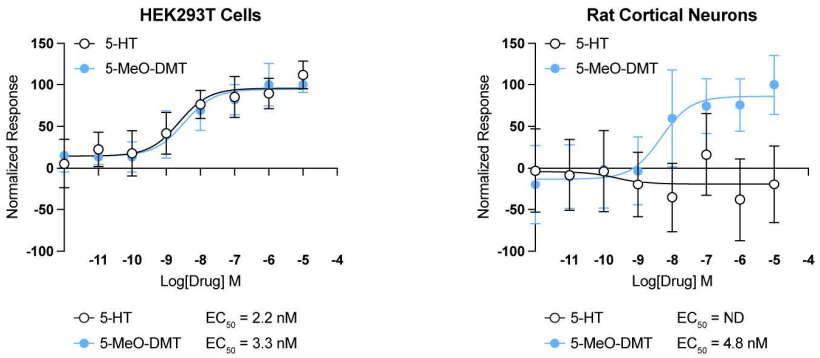

Figure S2.15. 5-HT increases IP1 accumulation in 5-HT2AR-expressing HEK293T cells, but not cortical neurons.
A FRET assay was used to assess IP1 accumulation following 5-HT2AR activation in HEK293T cells transfected with Myc-5-HT2A-ECFP or embryonic rat cortical neurons (DIV6) natively expressing 5-HT2ARs (N =11–12 wells per concentration). Data represent mean ± SEM, ND = not determined.

(x) Cellular Import of Serotonin Leads to Structural Plasticity and Antidepressant-Like Effects

If activation of intracellular 5-HT2ARs in cortical neurons is sufficient to promote structural plasticity, we hypothesized that serotonin should be able to promote cortical neuron growth if given access to the intracellular space. To test this hypothesis, we first treated cortical neurons with serotonin (1 µM) in the presence and absence of electroporation. Unlike ketamine (1 µM), serotonin was only able to promote cortical neuron growth when applied with electroporation (Figure 2.10A). Next, we took advantage of the serotonin transporter (SERT), which can import serotonin from the extracellular environment (39). Endogenous expression of SERT is typically restricted to presynaptic terminals of neurons that emanate from the raphe, and thus, rat cortical neurons do not express appreciable levels of the transporter (40, 41). Embryonic rat cortical neurons were electroporated with an enhanced yellow fluorescent protein (EYFP)–tagged SERT construct under the control of the calcium/calmodulin-dependent

protein kinase II (CaMKII) promoter to restrict expression to excitatory pyramidal neurons. Sparse transfection resulted in cultures that expressed both SERT-positive and SERT-negative neurons (Figure 2.10B), which enabled us to compare the effects of serotonin on neurons capable of importing the monoamine with those that could not within the same cultures.

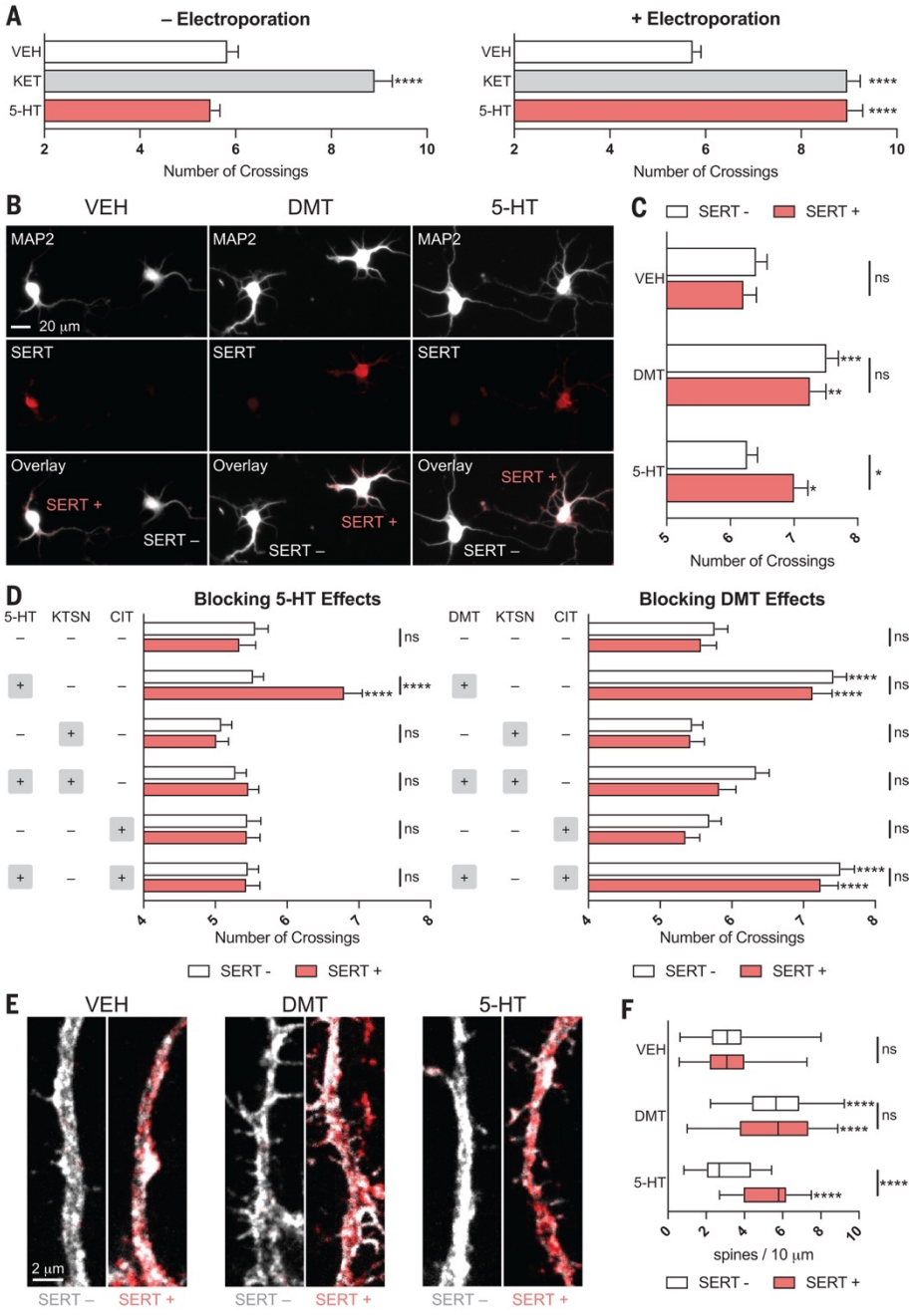

Figure 2.10. Cellular uptake of serotonin induces structural plasticity in vitro.
(A) Rat embryonic cortical neurons were administered compounds (1 µM) with (+) and without (−) electroporation. Nmax values obtained from Sholl plots (DIV6) demonstrates that unlike ketamine, serotonin only promotes growth when administered with electroporation (N = 49 to 59 neurons per treatment).
(B) Widefield images of embryonic rat cortical cultures (DIV6) sparsely transfected with CaMKII-SERT-EYFP and treated with compounds.
(C) Nmax values obtained from Sholl plots demonstrate that serotonin (10 µM) can only increase the dendritic arbor complexity of SERT-positive neurons, whereas DMT (10 µM) can promote the growth of both SERT-positive and SERT-negative neurons (N = 69 to 93 neurons per treatment).
(D) KTSN pretreatment (10 µM) blocks the plasticity-promoting effects of serotonin (1 µM) in SERT-positive neurons and DMT (1 µM) in both SERT-positive and SERT-negative neurons. CIT (10 µM) only blocks the plasticity-promoting effects of serotonin (1 µM) in SERT-positive neurons (N = 59 to 100 neurons per treatment).
(E) Confocal images of CaMKII-SERT-EYFP positive and negative dendrites (DIV15) treated with compounds (10 µM).
(F) Serotonin only promotes spine growth in SERT-positive neurons (N = 11 to 35 neurons per treatment). Error bars in (A), (C), and (D) represent standard error of the mean. ns is not significant, *$p < 0.05$, **$p < 0.01$, ***$p < 0.001$, and ****$p < 0.0001$, as compared with VEH controls in (A) (one-way ANOVA followed by Dunnett's multiple comparisons test) or compared with VEH controls from the same genotype in (C), (D), and (F) (two-way ANOVA followed by Tukey's multiple comparisons test). For box-and-whisker plots in (F), the center line represents the median, box limits are upper and lower quartiles, and whiskers are minimum and maximum values.

Treatment with the membrane-permeable psychedelic DMT (10 µM) resulted in greater dendritic arbor complexity and increased spine density in both SERT-positive and SERT-negative neurons (Figure 2.10B to F). Only SERT-positive neurons treated with serotonin (10 µM) displayed increased dendritogenesis and spinogenesis (Figure 2.10B to F). To ensure that serotonin-induced changes in structural neural plasticity were due to the engagement of intracellular 5-HT2Rs through serotonin importation from SERT, we performed similar experiments in the presence of the selective SERT inhibitor citalopram (CIT) and KTSN. When these experiments were performed in the presence of CIT (10 µM), the plasticity-promoting effects of serotonin (1 µM) on SERT-positive neurons were blocked (Figure 2.10D). By contrast, CIT had no effect on the ability of DMT (1 µM) to promote the growth of SERT-positive or SERT-negative cortical neurons (Figure 2.10D). In the presence of KTSN (10 µM), neither serotonin nor DMT could promote neuronal

growth, which confirms that DMT and intracellular serotonin promote plasticity by means of 5-HT2AR receptors in vitro (Figure 2.10D).

To determine whether intracellular serotonin could promote the growth of cortical neurons in vivo, we injected the medial PFC (mPFC) of Thy1–enhanced green fluorescent protein (EGFP) mice with either CaMKII-SERT-mCherry or CaMKII-mCherry. The mPFC was chosen as the injection site because it exhibits high levels of 5-HT2AR expression (28) and has been implicated in the antidepressant-like effects of psychoplastogens (42). After 3 weeks to enable construct expression (Figure 2.11A and B), both groups were administered (±)-para-chloroamphetamine [PCA, 5 mg/kg intraperitoneally (ip)], a selective serotonin-releasing agent (43). Dendritic spine density on mPFC pyramidal neurons was assessed 24 hours later. Animals that expressed SERT in the mPFC displayed significantly higher densities of dendritic spines after PCA administration as compared with mCherry controls (Figure 2.11C and D). Notably, PCA is not a 5-HT2AR agonist (Figure S2.16A), does not directly promote the growth of SERT-positive or SERT-negative cortical neurons in culture (Figure S2.16B), and does not induce a head-twitch response (HTR) in WT mice (Figure S2.16C).

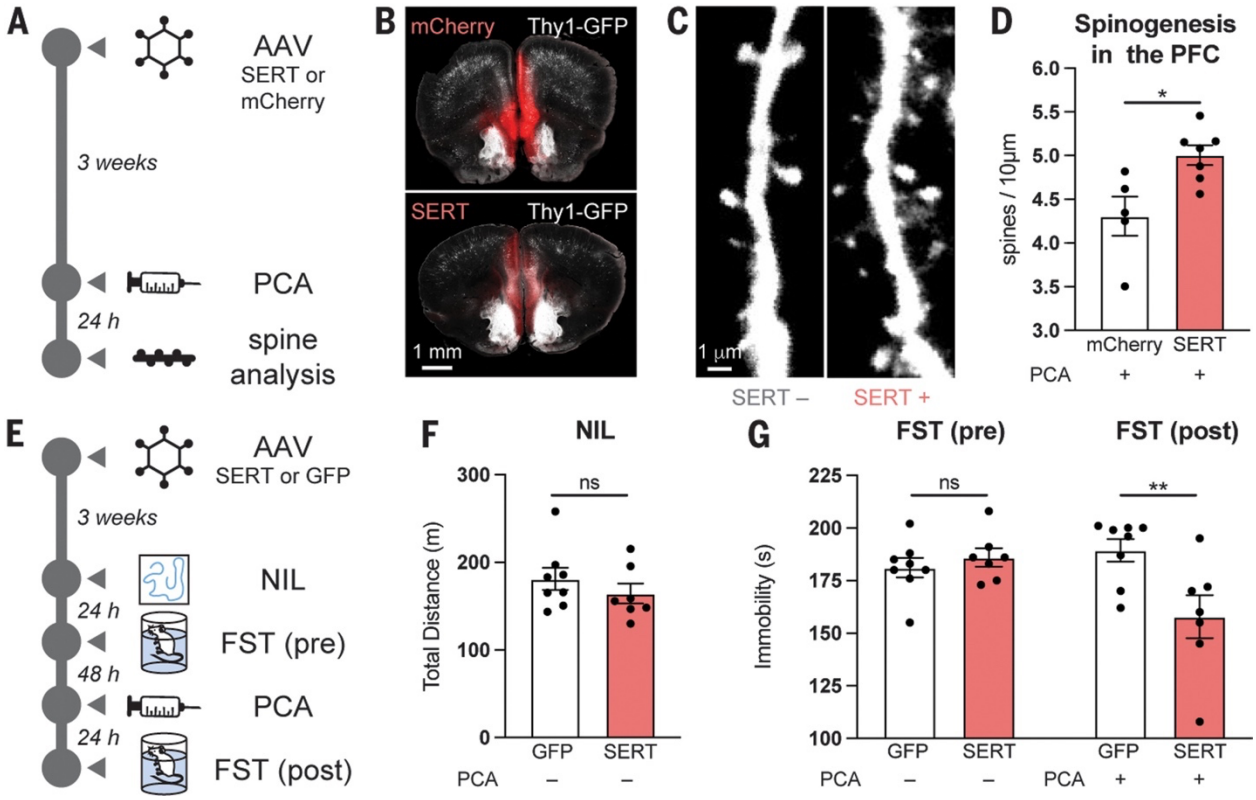

Figure 2.11. Cellular uptake of serotonin produces antidepressant-like effects in vivo.
(A) Schematic that displays experimental design for measuring spine density in Thy1-EGFP mice after administration of a serotonin-releasing agent.
(B) Histology images of the mPFC of Thy1-EGFP mice that express CaMKII-mCherry or CaMKII-SERT-mCherry.
(C) Confocal images of dendritic spines in the mPFC of mice treated with PCA (5 mg/kg ip).
(D) Mice that express CaMKII-SERT-mCherry display increased dendritic spine density after PCA treatment.
(E) Schematic that displays experimental design for determining the sustained antidepressant-like effects of serotonin in mice that express SERT in the mPFC.
(F) NIL demonstrates no difference between CaMKII-SERT-EYFP– and CaMKII-GFP–expressing mice.
(G) CaMKII-SERT-EYFP– and CaMKII-GFP–expressing mice exhibit no differences in the FST. After PCA (5 mg/kg ip) administration, CaMKII-SERT-EYFP–expressing mice display a sustained antidepressant-like effect.
ns is not significant, *$p < 0.05$, and **$p < 0.01$, as compared between indicated pairs of data in (D) and (F) (two-tailed unpaired Student's t test) or (G) (two-way repeated measures ANOVA followed by Šídák's multiple comparisons test). Error bars in (D), (F), and (G) represent the standard error of the mean.

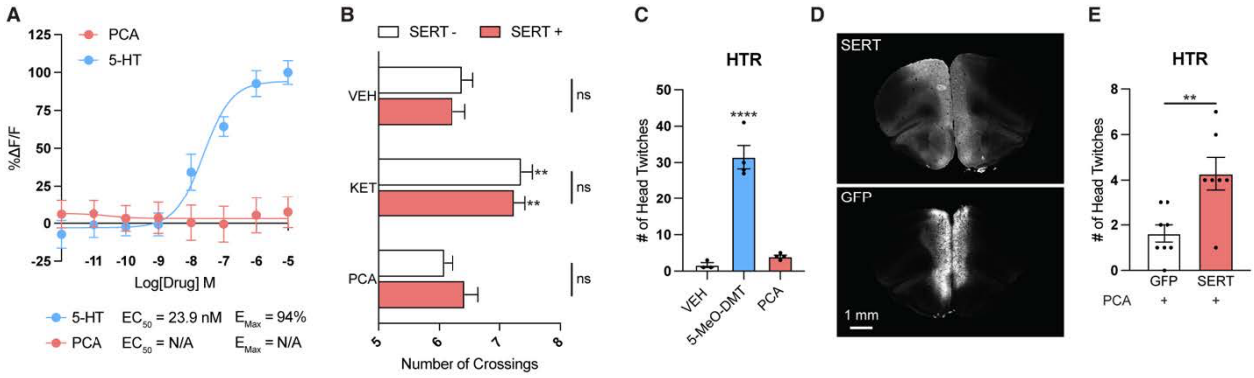

Figure S2.16. PCA is not a 5-HT2AR agonist and does not promote structural plasticity in cortical cultures.
(A) Assays using PSYLI2 cells demonstrate that PCA is not a psychLight2 agonist (N = 5–6 wells per concentration).
(B) Nmax values obtained from Sholl plots demonstrate that PCA (10 μM) cannot increase the dendritic arbor complexity of SERT+ or SERT– neurons, while ketamine (KET, 10 μM) can promote the growth of both SERT+ and SERT– neurons (DIV6, N = 57–93 neurons per treatment).
(C) PCA (5 mg/kg) does not induce a HTR in WT animals.
(D) Histology images of mice expressing CaMKII-SERT-EYFP and CaMKII-GFP in the mPFC.
(E) PCA (5 mg/kg) induces a HTR in mice expression SERT in the the mPFC immediately after administration.
*p < 0.05, **p < 0.01, ***p < 0.001, ****p < 0.0001, as compared to VEH controls of the same genotype in (B) (two-way ANOVA followed by Tukey's multiple comparisons test), VEH controls in (C) (one-way ANOVA followed by Dunnett's multiple comparisons test), or the GFP controls in (E) (unpaired two-tailed Student's t test)

Evidence suggests that psychoplastogen-induced structural plasticity in the mPFC might be related to sustained antidepressant-like effects in rodents (44). To probe for an antidepressant-like response that might be linked to neuroplasticity, we injected an adeno-associated virus (AAV) that contained a CaMKII-SERT-EYFP or CaMKII–green fluorescent protein (GFP) construct into the mPFC of WT C57BL/6J mice (Figure 2.11E and Figure S2.16D). After 3 weeks to allow for construct expression, both groups of mice underwent a novelty induced locomotion (NIL) test, and no differences in locomotion were observed (Figure 2.11F). After 24 hours, mice were subjected to a forced swim test (FST) (7, 45). Again, we observed no differences between the mice that expressed SERT and those that expressed the GFP control (Figure 2.11G). Two days later, we administered

PCA (5 mg/kg ip), waited 24 hours, and then performed a second FST (Figure 2.11G). The SERT-expressing mice exhibited a statistically significant HTR immediately after the administration of PCA as compared with the GFP control mice (Figure S2.16E), and they also displayed a significant reduction in immobility in the FST 24 hours after administration (Figure 2.11G).

Discussion

Although GPCRs are traditionally viewed as initiators of signal transduction that originates at the plasma membrane, increasing evidence suggests that GPCR signaling from intracellular compartments can play important roles in cellular responses to drugs. Recently, location bias has been proposed to explain signaling differences between endogenous membrane-impermeable peptide ligands and membrane-permeable ligands of opioid receptors (38). Moreover, distinct ligand-induced signaling has been observed for plasma membrane–localized and intracellular populations of δ-opioid receptors (46). Here, we extend the concept of location bias to ligands of the 5-HT2AR.

A substantial proportion of 5-HT2ARs in cortical neurons are localized to the Golgi, and intracellular compartments such as the Golgi are slightly acidic compared with the cytosol and extracellular space. Thus, it is possible that protonation of psychedelics within the Golgi leads to retention and sustained signaling, which results in neuronal growth, even after transient stimulation (47). Persistent growth after the drugs have been removed from the extracellular space is a hallmark of serotonergic psychoplastogens (47, 48). Although the mechanistic details that link intracellular 5-HT2AR activation to cortical neuron growth have not been fully elucidated, they are likely to involve AMPA

receptor, TrkB, and mTOR signaling, as previously established (9). Future studies should examine the detailed signaling interplay between these proteins.

In addition to promoting psychedelic-induced structural neuroplasticity, the intracellular population of 5-HT2ARs might also contribute to the hallucinogenic effects of psychedelics. When we administered a serotonin-releasing agent to WT mice, we did not observe a HTR. However, the same drug was able to induce a HTR in mice that expressed SERT on cortical neurons of the mPFC, a brain region that is known to be essential for the HTR (49). Thus, activation of intracellular cortical 5-HT2ARs may play a role in the subjective effects of psychedelics. This hypothesis is further supported by previous work that demonstrates that a high dose of the serotonin precursor 5-hydroxytryptophan (5-HTP) induces a HTR in WT mice, which can be blocked by an N-methyltransferase inhibitor that prevents the metabolism of 5-HTP to N-methyltryptamines (50). Inhibition of N-methyltransferase failed to block the HTR induced by 5-MeO–DMT (50). Taken together, this work emphasizes that accessing intracellular 5-HT2ARs is important for 5-HT2AR agonists to produce a HTR.

Our results demonstrate that membrane permeability is essential for a ligand to activate 5-HT2ARs in cortical neurons; however, our experiments did not distinguish between intracellular signaling or the possibility of psychedelics acting as pharmacological chaperones. Others have hypothesized that GPCR ligands may act as pharmacological chaperones, which facilitates their export to the plasma membrane where they could presumably engage in canonical signaling (51). Thus, future studies

should determine whether intracellular 5-HT2AR signaling is distinct from 5-HT2AR signaling at the plasma membrane.

Although intracellular expression of 5-HT2ARs within cortical pyramidal neurons has been known for some time, it is unclear at present why the subcellular localization of these receptors differs greatly between neurons and HEK293T cells (28, 29, 31). One possibility is that 5-HT2ARs form heterodimeric complexes that affect cellular trafficking (31). Thus, by dictating 5-HT2AR localization, cellular context could influence responses to endogenous neuromodulators and/or exogenous drugs, which potentially results in circuit-specific effects of 5-HT2AR ligands.

Intracellular signaling has been hypothesized to contribute to the pharmacological properties of a diverse range of compounds that includes nicotine, ketamine, and SSRIs (51–53). Like psychedelics, these compounds are weak bases with pKa (where Ka is the acid dissociation constant) values ranging from 7 to 10. Given that the antidepressant mechanisms of ketamine and SSRIs have not been definitively established, it is intriguing to speculate that they also might promote cortical neuron growth by binding to intracellular targets. Perhaps other antidepressants affect the function of scaffolding proteins within the cell interior to modulate neuronal growth phenotypes.

Without facilitated transport across the plasma membrane, serotonin cannot induce psychedelic-like effects on neuronal morphology. Although it is possible that serotonin could alter cortical neuron physiology by activating cell-surface 5-HT2ARs, this receptor pool does not seem to be involved in 5-HT2AR–induced structural plasticity. Our results raise the intriguing possibility that serotonin may not be the endogenous

ligand for the population of 5-HT2ARs expressed inside cortical neurons. Alternative ligands could include methylated congeners of serotonin or TRY because these compounds have greater abilities to cross nonpolar membranes. Endogenous psychedelics such as DMT, 5-MeO–DMT, and bufotenin have been identified in a variety of species, including humans, and have long been hypothesized to play roles in diseases such as schizophrenia (54). However, they are rapidly degraded in vivo, which makes their detection by classic analytical methods quite challenging. The use of more modern analytical techniques has improved detection of these analytes (55), with a recent study demonstrating that the concentration of DMT in the cortex was comparable to that of serotonin (56). The possibility that endogenous psychedelics play a role in health or disease should therefore be thoroughly investigated.

Author Contributions

M.V.V. performed most of the in vitro experiments, including the dendritogenesis, spinogenesis, subcellular colocalization, IP1, neuromics antibody validation, and psychLight assays. C.D. cloned and validated key reagents for the in vivo experiments, performed the surgeries, and the perfusions. M.V.V. performed the small-molecule electroporation experiments, key pilot experiments imaging HEK293T cells and neurons, and brain-slice imaging with assistance from C.D., and M.V.V. performed the behavioral experiments. L.E.D. performed the N-methylation SAR dendritogenesis experiments, calculated cLogP values, and synthesized TMT and MKTSN. R.J.T. and S.J.C. performed the radioligand binding studies. H.N.S. performed culturing of 5-HT2AR KO cultures. L.P.C. and S.D.P. performed the Golgi staining experiments. S.A.J. performed the

electrophysiology experiments. J.J.H. performed BRET assays of 5-HT2AR activation. J.D.M., J.A.G., L.T., and D.E.O. supervised various aspects of this project and assisted with data analysis. D.E.O. conceived the project and wrote the manuscript with input from all authors.

Acknowledgments

We thank C. Ly, A. C. Greb, L. P. Cameron, and W. C. Duim for performing early pilot studies; A. Avanes for assistance with radioligand binding studies; K. Zito for providing Thy1-GFP breeders; J. González-Maeso for providing the Myc–5-HT2AR–ECFP plasmid; R. Iyer for performing high-resolution mass spectrometry analysis; and P. Beal for use of his CLARIOStar plate reader. We also thank C. Nichols for advice about the radioligand binding experiments.

Funding: This work was supported by funds from the National Institutes of Health (NIH) (R01GM128997 to D.E.O., R35GM133421 to J.D.M., and U01NS120820, U01NS115579, and 2R01MH101214-06 to L.T.), three NIH training grants (T32GM099608 to M.V.V., T32GM113770 to R.J.T., and T32MH112507 to H.N.S.), Human Frontier (L.T.), the Camille and Henry Dreyfus Foundation (D.E.O.), a sponsored research agreement with Delix Therapeutics (D.E.O.), and a University of California (UC) Davis Provost's Undergraduate Fellowship (S.J.C.). This project used the Biological Analysis Core of the UC Davis MIND Institute Intellectual and Development Disabilities Research Center (U54 HD079125). The Nikon High Content Analysis Spinning Disk Confocal microscope used in this study was purchased using NIH Shared Instrumentation Grant 1S10OD019980-01A1. We thank the MCB Light Microscopy Imaging Facility, which is a

UC Davis Campus Core Research Facility, for the use of this microscope. Funding for the nuclear magnetic resonance spectrometers was provided by the National Science Foundation (NSF CHE-04-43516) and NIH (08P0ES 05707C). Analysis for this project was performed in the UC Davis Campus Mass Spectrometry Facilities, with instrument funding provided by the NIH (1S10OD025271-01A1). Several of the drugs used in this study were provided by the National Institute on Drug Abuse (NIDA) Drug Supply Program.

Method Details

Data Analysis and Statistics. Treatments were randomized, and data were analyzed by experimenters blinded to treatment conditions. Statistical analyses were performed using GraphPad Prism (version 9.3.1) unless noted otherwise. All comparisons were planned prior to performing each experiment.

Drugs. Many of the drugs used in these studies were purchased from commercial sources including ketamine hydrochloride (KET, Fagron), ketanserin (KTSN, ApexBio), mianserin hydrochloride (TCI),(±)-para-chloroamphetamine (PCA, Sigma-Aldrich), and 5-hydroxytryptamine (5-HT, Sigma-Aldrich), 5-hydroxy-N-mehtyltryptamine (N-Me-5-HT, Sigma-Aldrich), tryptamine (TRY, ACROS), N-methyltryptamine (NMT, ACROS), and 5-MeO-tryptamine (5-MeO-TRY, ACROS). The psilocybin (PSY) and psilocin (PSI) used in these studies was generously provided by the NIDA Drug Supply Program. N,N-dimethyltryptamine (DMT) 5-methoxy-N,N-dimethyltryptamine (5-MeO-DMT), 5-MeO-N-Methyl-tryptamine (5-MeO-NMT), and bufotenin (BUF) were synthesized in-house as previously described (14). Methylated ketanserin (MKTSN) and N,N,N-trimethyltryptamine (TMT) were synthesized according to the procedures outlined in the supporting information. All compounds synthesized in-house were judged to be analytically pure based on NMR and LC-MS data. For cell culture experiments, VEH = 0.1% (agonist studies) or 0.2% (antagonist studies) molecular biology grade dimethyl sulfoxide (DMSO, Sigma-Aldrich). For in vivo experiments, the vehicle was USP grade saline (0.9%). Free bases were used for all cellular experiments with the exception of PCA hydrochloride, which was used for both in vitro and in vivo studies.

N,N,N-trimethyltryptamine Iodide. To a solution of tryptamine (100 mg, 0.6 mmol) in THF/IPA (6.2 mL, 1:1) was added sodium bicarbonate (115 mg, 1.9 mmol, 3.0 equiv) and methyl iodide (0.19 mL, 3.1 mmol, 5.0 equiv). The reaction was stirred at room temperature for 12 h before being filtered and rinsed with several portions of ice-cold IPA (3 mL) to yield the desired product as a white crystalline solid. Yield = 146 mg, 71%. 1H NMR (400 MHz, CD3OD) δ 7.64 (d, 1H, J = 7.9 Hz), 7.38 (d, 1H, J = 7.9 Hz), 7.23 (s, 1H), 7.14 (t, 1H, J = 7.5, Hz), 7.06 (t, 1H, J = 2.9 Hz), 3.64 (m, 2H), 3.33–3.27 (m, 2H), 3.25 (s, 9H) ppm; 13C NMR (101 MHz, CD3OD) δ 138.2, 128.0, 124.3, 122.8, 120.2, 118.6, 112.6, 109.3, 67.8, 53.7, 20.36 ppm; HRMS (ES+) calcd for C13H19N2+ 203.1543 found 203.1544 (M+).

N-Me-Ketanserin Iodide. To a solution of ketanserin (100 mg, 0.25 mmol) was added methyl iodide (2.5 mL) and the reaction was stirred at 50°C for 24 h before being filtered and rinsed with several portions of ice cold EtOAc (1 mL) to yield the desired product as a white crystalline solid. Yield = 56 mg, 41%. 1H NMR (400 MHz, DMSO-d6) δ 11.65 (s, 1H), 8.08 (dd, 2H, J = 6.8, 2.4 Hz), 7.96 (d, 1H, J = 8.3 Hz), 7.71 (t, 1H, J = 7.3 Hz), 7.42 (t, 2H, J = 8.3, Hz), 7.24 (m, 2H), 4.38 (t, 2H, J = 7.0 Hz), 3.77 (quint, 1H, J = 7.3 Hz), 3.63 (m, 6H), 3.17 (s, 3H), 2.05 (m, 4H) ppm. HRMS (ES+) calcd for C23H25FN3O3 + 410.1874, found 410.1875 (M+).

Animals. All in vivo experimental procedures involving animals were approved by the University of California, Davis Institutional Animal Care and Use Committee (IACUC) and adhered to the principles described in the NIH Guide for the Care and Use of Laboratory Animals. Timed pregnant Sprague Dawley rats were obtained from

Charles River Laboratories (Wilmington, MA, USA). Thy1-GFP line M (Tg(Thy1-EGFP)MJrs/J, Stock No.007788) transgenic mice were obtained as a gift from Karen Zito's lab at UC Davis and C57BL/6J (Stock No. 000664) mice were obtained from Jackson Laboratory. All behavior and Thy1-EGFP imaging experiments were performed using both males and females. Animals were randomly assigned to genotype groups. At the time of experiments mice were 11–12 weeks old. Mice were group housed (2–5 mice per cage) under controlled temperature in a 12 h light/dark cycle (7:00 AM to 7:00 PM) with access to food and water ad libitum. UC Davis is accredited by the Association for Assessment and Accreditation of Laboratory Animal Care International (AAALAC).

Dendritogenesis experiments. Culturing, immunostaining, and data analysis was performed as previously described with the exception that there was no media change after treatments (12). DMSO and ketamine (10 □M) were used as vehicle and positive controls, respectively. For blocking experiments, antagonists were added 30 min prior to addition of agonists in 10-fold excess. Experiments were performed in duplicate with plates prepared using neurons obtained from independent pregnant dams.

Spinogenesis experiments. Spinogenesis experiments were performed as previously described with the exception that cells were treated at DIV14 and fixed 24 h after treatment on DIV15 (8). The images were taken on a Nikon HCA confocal microscope a with a 100x/NA 1.45 oil objective. DMSO and ketamine (10 μM) were used as vehicle and positive controls, respectively. For blocking experiments, antagonists were added 30 min prior to addition of agonists in 10-fold excess. Experiments were performed

in duplicate with plates prepared using neurons obtained from independent pregnant dams.

Electroporation Experiments. For experiments employing electroporation with drugs, freshly dissected E18 rat cortical neurons in suspension were centrifuged at 250 g for 10 min. The cell pellet was re-suspended in Lonza P3 Primary Cell Nucleofector Solution containing supplement 1 at a concentration of 2.5 x 105 cells per 18 µL. Next, 18 µL/well of cell suspension was transferred into a P3 Primary Cell 96-well Nucleofector plate (Lonza, #V4SP-3096) and plates were inserted into the Lonza 4D-Nucleofector® 96-well Unit (Lonza, #AAF-1003S). Separately, 10 mM drug stocks in DMSO were diluted to 100 µM in sterile water, and 2 µL of the 100 µM drug solution was added into each well to achieve a final concentration of 10 µM (total dilution = 1:1000). For antagonist experiments, 1 µL of a 20 µM agonist solution and a 1 µL 200 µM antagonist solution diluted in sterile water to achieve final concentrations of 1 µM agonist and 10 µM antagonist (total dilution = 1:1000 for each drug). Neurons were electroporated using the neuron rat brain high efficiency setting. After the electroporation, cells were allowed to sit at room temperature for 10 min. During this time, prewarmed plating media was added to the wells of a poly-D-lysine coated 96-well plate. Cells were then plated into the inner 60 wells at a density of 1.5 x 104 cells/well. Cells were placed back in the incubator and cultured until DIV6, at which time they were fixed, immunostained for MAP2 (1:10,000; EnCor, CPCA-MAP2), and analyzed as for changes in dendritic arborization as previously described (12).

For experiments employing electroporation with plasmid DNA, Lonza 100 µL Nucleocuvette vessels (Lonza, #V4XP-3024) were utilized. Freshly dissected E18 rat cortical neurons (5 x 106 cells per Nucleocuvette) were centrifuged at 250 g for 10 min in a 15 mL conical tube. The cell pellet was re-suspended in 100 µL of Lonza P3 Primary Cell Nucleofector Solution containing supplement 1 and then transferred to the Nucleocuvette. Next, 5 µg of CaMKII-SERT-N1-pEYFP (Subcloned from RRID:Addgene_70105) or Myc-5-HT2AR-ECFP plasmid DNA (described in ref 53), was added (volume of plasmid DNA was ≤ 10 µL) and the Nucleocuvettes were gently flicked to mix the solution. Nucleocuvettes were electroporated using the 4D-Nucleofector® X Unit (Lonza, #AAF-1003X) using the DR114 electroporation code (54). Nucleocuvettes were then removed and allowed to sit at room temperature for 10 min before adding 500 µL of prewarmed plating media. The provided single use pipettes were used to mix and transfer the cell solution into plating media.

For experiments in Figure 2.10B,C and S2.15B using poly-D-lysine coated 96 well plates, the full 600 µL solution was diluted into 12.4 mL of plating media and plated at 200 µL/well into the inner 60-wells. Cells were returned to the incubator and then treated as previously described at DIV3 and fixed 72 h later on DIV6 to be stained for MAP2 and the EYFP tag on the SERT construct (Invitrogen, # A-21311, 1:1000 dilution) (12).

For experiments in Figure 2.10E using poly-D-lysine coated 24-well plates containing glass coverslips (No. 1.5) the full 600 µL solution was diluted into 4.9mL of plating media and plated at 500 µL/well into the inner 8-wells. Cells were returned to the incubator and then treated as previously described at DIV14 and fixed 24 h later on

DIV15 to be stained for MAP2, EYFP, and F-actin using phalloidin conjugated to Alexa Fluor 555 (Invitrogen, #A34055, 1:40) (8).

As a consequence of sparse electroporation, there were both SERT-positive and SERT-negative cortical neurons in the same well; SERT-positive and SERT-negative neurons were chosen for analysis based on the presence or absence of the EYFP signal, respectively. This was done by applying the same brightness/contrast setting to all images and manually sorting SERT positive and negative neurons for Sholl analysis. Experiments were performed in duplicate with plates prepared using neurons obtained from independent pregnant dams.

Lipofection. Freshly dissected E18 rat cortical neurons were plated into poly-D-lysine coated 35 mm live cell dishes (MatTek, P35G-1.5-14-C) at 1.5 x 105 cells/well and cultured as previously described (12). On DIV5, neurons were transfected with Myc-5-HT2A-ECFP, β2-adrenergic receptor-ECFP (RRID:Addgene_55794), or pCAG-ECFP (RRID:Addgene_32597) using Lipofectamine™ 3000 Transfection Reagent (Invitrogen catalog # L3000001) according to manufacturer protocol with slight modifications. Culture media was switched for prewarmed Opti-MEM (Invitrogen, #11058021) 30 min prior to addition of the transfection mixture. Transfection reagents were mixed in Opti-MEM using 1 µg DNA/well, 2 µL P3000 reagent/well, and 0.75 µL Lipofectamine 3000/well and then added dropwise. After addition of the transfection mixture, cells were returned to the incubator for 4–6 h, and then the media was replaced with fresh culture media. HEK293T cells (ATCCCRL-11268; mycoplasma free) were cultured in complete media consisting of DMEM-high glucose-pyruvate (Gibco, #11995065), 1%

Penicillin-Streptomycin (Giboco, # 5140122), and 10% fetal bovine serum (Gibco # 26140079). On the day of transfection, cells were suspended in DMEM prior to the addition of transfection reagents. After addition of transfection reagents, cells were plated at a density of 1.5 x 105 cells/well. The plate was placed into the incubator and the media was not changed. To compare the effects of media lacking serum versus media containing serum, a separate dish of HEK293T cells were transfected in complete media. Both neurons and HEK293T cells were imaged 24 h after transfection in a live cell chamber connected to a Nikon HCA confocal microscope.

Colocalization Experiments. Freshly dissected E18 rat cortical neurons were electroporated with Myc-5-HT2A-ECFP or HEK293T (ATCCCRL-11268; mycoplasma free) cells were lipofected with Myc-5-HT2A-ECFP. Both cell types were cultured in the inner 8 wells of poly-D-lysine coated 24-well plates containing glass coverslips (No. 1.5) at a density of 3.5 x 104 cells/well and fixed on DIV6 as previously described (12). Neurons were immunostained for subcellular markers, MAP2, and CFP (note: anti-GFP antibodies cross react with CFP): anti-GFP (Invitrogen, #MA5-15256, 1:1000, used for co-labeling with antibodies from rabbits); anti-GFP (Rockland, #600-401-215, 1:1000, used for co-labeling with antibodies from mice); anti-GM130 (Invitrogen, #703794, 1:100); anti-RAB5 (Invitrogen, #PA5-29022, 1:100); anti-RAB7 (Invitrogen, #PA5-52369, 1:100); anti-MTC02 (Invitrogen, #MA5-12017, 1:100); anti-MAP2 (1:10,000; EnCor, CPCA-MAP2). MAP2 was labeled with an anti-chicken secondary antibody conjugated to Alexa Fluor 568 (Invitrogen, #A-11041, 1:500), CFP was labeled with an anti-mouse or anti-rabbit secondary antibody conjugated to Alexa Fluor 405 (Invitrogen, #A31553 and #A48258,

1:500), and subcellular markers were labeled with an anti-mouse or anti-rabbit secondary antibody conjugated to Alexa Fluor 488 (Invitrogen, #A-11001 and #A-11008, 1:500). HEK293T cells expressing Myc-5-HT2A-ECFP were prepared in the same fashion with the exception that instead of immunostaining for MAP2, the morphology of the cell was established by labeling F-actin with phalloidin conjugated to Alexa Fluor 555 (Invitrogen, #A34055, 1:40). Coverslips were mounted onto microscope slides using ProLong Gold (Invitrogen # P36930) and imaged on a Nikon HCA confocal microscope with a 100x/NA 1.45 oil objective imaging in the following order: 568 nm (25% laser power), 488 nm (25% laser power), and 405 nm (25% laser power). For each image, stacks (0.065 µm / 1 pixel) with 13x 0.25 µm z-steps were acquired for all three wavelengths. All images shown are maximum projections of the 7th and 8th stack where the outline of the cell body and processes are most prominent. Regions of interest (ROIs) were drawn around the cell using the MAP2 or phalloidin channel, and all signal was cleared from the outside of the ROI for all wavelengths. Using the ImageJ Just Another Colocalization Plugin (JACoP), the cleaned images of the Myc-5-HT2A-ECFP and the subcellular marker were analyzed to determine the Pearson's correlation coefficient and Manders' colocalization coefficient. Brightness/contrast and thresholding were kept consistent for each experiment. Experiments were performed in duplicate with plates prepared using neurons obtained from independent pregnant dams or independent HEK293T cultures.

Live Cell Membrane Imaging. Following the manufacturer's protocols, CelllBrite® Steady 550 Membrane Staining Kit (Biotium, #30107) was added to live DIV6 rat cortical neurons or HEK293T cells (ATCCCRL-11268; mycoplasma free) lipofected

with Myc-5-HT2A-ECFP, Beta-2-adrenergic receptor-ECFP, or pCAG-ECFP cultured in poly-D-lysine coated 35 mm live cell dishes at 1.5 x 105 cells/well. Briefly, media was aspirated from the dishes and cells were washed three times with warm HBSS supplemented with 2 mM MgCl2 and 2 mM CaCl2 (Thermo Fisher, 14025092). Next, 1.5 mL of a 1x dye and enhancer solution diluted in HBSS was added and the dish placed in the incubator for 10 min. The media was aspirated and replaced with 1 mL of warm HBSS. Cells were imaged in a live cell chamber connected to a Nikon HCA confocal microscope a with a 60x/NA 1.40 oil objective imaging in the following order: 568 nm (25% laser power) and 405 nm (35% laser power). All other imaging and analysis parameters were kept consistent with the other subcellular imaging experiments with the exception that the membrane channel was used to draw the ROI around the cell.

5-HT2AR Antibody Validation and Native 5-HT2A Immunostaining. The Neuromics 5-HT2A antibody was validated in-house by lipofecting HEK293T cells (ATCCCRL-11268; mycoplasma free) with Myc-5-HT2A-ECFP and then plating cells in poly-D-lysine coated 24-well plates containing glass coverslips (No. 1.5) at 3.5 x 104 cells/well as described above. The next day, cells were fixed and immunostained for CFP (Invitrogen, #MA5-15256, 1:1000) and the 5-HT2AR (Neuromics, RA24288, 1:50) following previously described methods with slight modifications (12). The cells were incubated with primary antibody for 48 h at 4 ^{o}C. Following primary antibody incubation, CFP was labeled with an anti-mouse secondary antibody conjugated to Alexa Fluor 405 (Invitrogen, #A31553, 1:500), the 5-HT2AR was labeled with an anti-rabbit conjugated to

Alexa Fluor 488 (Invitrogen, #A-11008, 1:500), and the actin-cytoskeleton was labeled using phalloidin conjugated to Alexa Fluor 555 (Invitrogen, #A34055, 1:40).

For antibody validation in 5-HT2AR knock out embryonic mouse cortical neurons and wild type controls, P1 pups were sacrificed by decapitation, and their cortices were removed and stored in Hibernate E (Invitrogen catalog # A12476-01) supplemented with 2% B-27 Plus (Invitrogen catalog # 17504-044) and 1% Pen/Strep (Invitrogen catalog # 15140-122) for 5 days while genotypes were confirmed via PCR. Next, cortices were pooled, dissociated, and plated at a density of 7.5 x 104 cells/well into the inner 8 wells of poly-D-lysine coated 24-well plates containing glass coverslips (No. 1.5). Plating media consisted of MEM (Invitrogen catalog # 51200-038) supplemented with 10% heat-inactivated horse serum (Invitrogen catalog # 26050-088), 0.4% glucose (Sigma Aldrich catalog # G7528), 1 mM sodium pyruvate (Invitrogen catalog # 11360-070), and 10 mM HEPES (Invitrogen catalog # 15630-106). After 3 hours, the plating media was exchanged for maintenance media consisting of Neurobasal (Invitrogen catalog # 21103-049), 2% B-27 Plus (Invitrogen catalog # 17504-044), 1% Pen/Strep (Invitrogen catalog # 15140-122), 0.3125% Glutamax (Invitrogen catalog # 35050-061), 1 mM sodium pyruvate (Invitrogen catalog # 11360-070), and 10 mM HEPES (Invitrogen catalog # 15630-106). The neurons were cultured until DIV6, at which time they were fixed and stained for MAP2 and 5-HT2ARs (Neuromics, RA24288, 1:50) as described above.

Coverslips were mounted onto microscope slides using ProLong Gold and imaged on a Nikon HCA confocal with a 60x/NA 1.40 oil objective imaging in the following order: 568 nm (25% laser power), 488 nm (25% laser power), and 405 nm (25%) to image F-actin,

MAP2, and the CFP tag, respectively. All other imaging and analysis parameters were kept consistent. Due to the sparse lipofection in HEK293T cells, there were 5-HT2AR-positive and -negative cells within the same well to determine the specificity of the 5-HT2AR antibody. For mouse cortical neurons, separate wells containing knockout or wild type neurons were used.

To compare localization of native 5-HT2AR expression to overexpression of 5-HT2AR in cultures of embryonic rat cortical neurons, a line scan was performed on images of DIV7 cultures immunostained for native 5-HT2AR (Neuromics, RA24288, 1:50) or rat cortical neurons lipofected with Myc-5-HT2A-ECFP and stained for CFP . Transverse (perpendicular to the apical dendrite) and longitudinal (parallel to the apical dendrite) line scans were performed to quantify 5-HT2A fluorescence intensity across the cell membrane and intracellular space.

IP1 Experiments. Freshly dissected E18 rat cortical neurons or Myc-5-HT2A-ECFP lipofected HEK293T cells (ATCCCRL-11268; mycoplasma free) were plated onto poly-D-lysine coated HTRF 96-well low volume white plates with clear bottoms (cisbio, 66PL96) at 2.0 x 105 cells/well. The HTRF IP-One Gq kit (cisbio, 62IPAPEB) was used to assess Gq activation in response to treatment with 5-HT2AR agonists according to the manufacturer's protocol. Briefly, neurons were cultured to DIV6 and Myc-5-HT2A-ECFP expressing HEK293T cells were cultured overnight. On the day of the experiment, plates were washed three times with ultrapure water (Thermo Fisher, 10977015). Next, 20 µL of 1x stimulation buffer diluted in ultrapure water was added to the wells. Separately,10

mM drug stocks in DMSO were diluted to 35 µM in 1x stimulation buffer. Then, 8 µL of the 35 µM agonist solution was added to the wells to achieve a final concentration of 10 µM (total dilution = 1:1000). Serial dilutions (1:10) were performed in an empty treatment plate to generate a concentration response and added following a randomized plate map. The plate was sealed and placed in the incubator for 1 h. Next, 12 µL of a 6x IP1 d2 reagent and 6x IP1 Tb cryptate antibody reagent solution diluted in the provided lysis buffer was added to each well. The plate was sealed and placed on a shaker set to low for 1 h at room temperature. The plate was then imaged using the CLARIOStar plate reader (BMG LABTECH) using an excitation wavelength of 340 nm and recording emissions at 620 nm and 665 nm. Optimal gain and focal height settings were determined to observe the largest delta between the vehicle control and 10 µM 5-MeO-DMT treatment. The HTRF ratio was calculated according to the manufacturing protocol: (Signal 665nm)/(Signal 620)×10^4

Both 5-HT and 5-MeO-DMT were assayed as 8-point concentration responses and experiments were performed in quadruplicate with plates prepared using neurons obtained from independent pregnant dams or independent HEK293T cultures with a total of N = 11–12 wells per concentration. Raw HTRF ratios were normalized to the vehicle control set as 0% and the 10 µM 5-MeO-DMT response set as 100%.

Radioligand Binding Experiments. Binding buffer consisted of 50 mM Tris HCl, 10 mM MgCl2, 0.1 mM EDTA disodium dihydrate in autoclaved deionized water. The solution was adjusted to pH 7.4 with 10 M NaOH(aq) and stored at 4 °C. This solution

was used for membrane preparation generation as well as in saturation and competition binding assays.

For the generation of membrane preparations, 15-cm plates of PSYLI2 cells (HEK293T cell line stably expressing psychLight2; mycoplasma free) or HEK293T cells (ATCCCRL-11268; mycoplasma free) lipofected with Myc-5-HT2AR (RRID:Addgene_67944) were grown in Dulbecco's Modified Eagle Media (DMEM) containing 10% fetal bovine serum and 1% penicillin/streptomycin. When the cells were >90% confluent, the media was removed, and the cells were washed with Dulbecco's Phosphate Buffered Saline (DPBS, 15 mL). Next, DMEM (15 mL) lacking fetal bovine serum and penicillin/streptomycin was added, and the cells were serum-starved for 4–12 h. All but ~5 mL of the media was removed from the plates before placing them on ice. After 1 min on ice, the contents of the plates were scraped and transferred to a pre-chilled 50 mL Falcon tube and then centrifuged (2,000 g, 10 min, 4 °C). The supernatant was discared, and the pellet was resuspended in ice-cold binding buffer (2 mL per 15-cm plate). The cells in the pellet were lysed by 60 s of repeated pipetting of the suspension with a 10 mL serological pipet, and then the mixture was centrifuged (2,000 g, 10 min, 4 °C). The supernatant was discarded, removing endogenous ligands from the lysed cells, and the pellet was resuspended in ice-cold binding buffer (2 mL per 15-cm plate). The suspension was transferred to 2.0 mL Eppendorf tubes in 1.0 mL aliquots, saving a single aliquot of 0.25 mL suspension to use for quantification of protein concentration via a Bradford assay (55). All aliquots were then centrifuged (20,000 g, 20 min, 4 °C). The supernatant was removed, and the aliquots were stored at -80 °C for later use.

For intact cell experiments, PSYLI2 cells or HEK293T cells transiently expressing Myc-5-HT2AR were cultured in 15-cm plates in DMEM containing 10% fetal bovine serum and 1% penicillin/streptomycin. Approximately 16–28 h prior to the experiment, the cells were plated in 24-well plates (2x105 cells/well) pre-coated with poly-D-lysine and grown in DMEM containing 10% fetal bovine serum and 1% penicillin/streptomycin. Prior to experiments, plated cells were washed three times at room temperature with 500 µL/well of DPBS (with calcium and magnesium). All compounds and radioligands were diluted in DMEM. For saturation binding experiments, after wash steps, DMEM (450 µL) was added to each well. A 1:1 mixture of various concentrations of [3H]-LSD and either vehicle (1% DMSO) or 1 mM mianserin hydrochloride (1% DMSO, 50 µL) was added to each well, bringing the final well volume to 500 µL comprised of [3H]-LSD and either vehicle (0.1% DMSO) or 100 µM mianserin hydrochloride (0.1% DMSO). PSYLI2 cells were incubated with 0–80 nM [3H]-LSD and HEK293T cells transiently expressing Myc-5-HT2AR were incubated with 0–40 nM [3H]-LSD for 60 min at 37°C. For competition binding experiments, after wash steps, DMEM (450 µL) was added to each well. A (1:1) mixture of [3H]-LSD (23.3 nM for PSYLI2 cells and 29.3 nM for HEK293T cells transiently expressing Myc-5-HT2AR) and either 5-HT (1% DMSO) or 5-MeO-DMT (1% DMSO) at various concentrations was added to each well, bringing the final well volume to 500 µL comprised of [3H]-LSD (2.33 nM for PSYLI2 cells and 2.93 nM for HEK293T cells transiently expressing Myc-5-HT2AR) and either 5-HT or 5-MeO-DMT at various concentrations. Cells were incubated with 0–10 µM 5-HT or 5-MeO-DMT for 60 min at 37°C. At the end of intact cell saturation and competition binding experiments, the cells

were washed three times with DPBS (with calcium and magnesium). Cells were solubilized by the addition of 0.1 M NaOH and 0.5% Triton X-100 (500 µL/well) at ambient temperature, and after 30 min the lysates were transferred to 7 mL scintillation vials containing 3 mL Ultima Gold liquid scintillation cocktail.

For membrane preparation experiments, saturation binding assays to determine the Kd values of [3H]-LSD and competition binding assays to determine the Ki values of unlabeled compounds were carried out using Millipore MultiScreen HTS FB filter plates that had been pre-soaked with 0.3% polyethylenimine(aq) (PEI) for at least 30 min on a Millipore Multiscreen HTS vacuum manifold. All compounds and radioligands were diluted in binding buffer. For PSYLI2 cell membrane preparation saturation binding experiments, binding buffer (0.21% DMSO, 47.5 µL) was added to half of the wells to determine total binding, while mianserin hydrochloride (0.21% DMSO, 210.5 µM, 47.5 µL) was added to the other wells to determine nonspecific binding. [3H]-LSD (20X solution in binding buffer, 5 µL, 0–5.76 µM) was then added to the wells. Membrane preparations were thawed on ice before resuspension in binding buffer. The membrane preparation suspension (47.5 µL, 0.211 µg/µL, 10 µg) was added as the final component in each well, bringing the final volume in each well to 100 µL, comprised of either vehicle (0.1% DMSO) or 100 µM mianserin hydrochloride (0.1% DMSO), [3H]-LSD ranging in concentrations from 0–288 nM, and a suspension of membrane preparation protein (10 µg). For HEK293T cells transiently expressing Myc-5-HT2AR membrane preparation saturation binding experiments, binding buffer (0.25% DMSO, 50 µL) was added to half of the wells to determine total binding, while mianserin hydrochloride (0.25% DMSO, 250 µM, 50 µL)

was added to the other wells to determine nonspecific binding. [3H]-LSD (5X solution in binding buffer, 25 µL, 0–480 nM) was then added to the wells. Membrane preparations were thawed on ice before resuspension in binding buffer. The membrane preparation suspension (50 uL, 0.50 µg/µL, 25 µg) was added as the final component in each well, bringing the final volume in each well to 125 □L comprised of either vehicle (0.1% DMSO) or 100 µM mianserin hydrochloride (0.1% DMSO), [3H]-LSD ranging in concentrations from 0–96.0 nM, and a suspension of membrane preparation protein (25 µg). For PSYLI2 cell membrane preparation competition binding experiments, [3H]-LSD (2.5X solution in binding buffer, 50 uL, 12.5 nM) and various concentrations of unlabeled compounds (5X solution in binding buffer, 25 uL, 0.5% DMSO, 0–500 µM) were added to the wells. Membrane preparations were thawed on ice before being resuspended in binding buffer. The membrane preparation suspension (50 µL, 0.2 µg/uL, 10 µg) was added as the final component in each well, bringing the final volume in each well to 125 µL comprised of [3H]-LSD (5.00 nM), unlabeled compounds (0–100 µM), and a suspension of membrane preparation protein (10 µg). For HEK293T cells transiently expressing Myc-5-HT2AR membrane preparation competition binding experiments, [3H]-LSD (2.5X solution in binding buffer, 50 uL, 9.23 nM) and various concentrations of unlabeled compounds (5X solution in binding buffer, 25 uL, 0.5% DMSO, 0–50 µM) were added to the wells. Membrane preparations were thawed on ice before resuspension in binding buffer. The membrane preparation suspension (50 µL, 0.5 µg/uL, 25 µg) was added as the final component in each well, bringing the final volume in each well to 125 µL comprised of [3H]-LSD (3.69 nM), unlabeled compounds (0–10 µM), and a suspension of membrane

preparation protein (25 µg). All incubations were carried out at ambient temperature for 60 min before separation of bound and free radioligand was conducted via rapid vacuum filtration followed by washing with ice-cold binding buffer (3 x 200 µL). Dried filter screens from the plates were transferred to 7 mL scintillation vials containing 1 mL PerkinElmer Ultima Gold liquid scintillation cocktail.

Analysis of the radioactivity was conducted using a Beckman LS 6000 liquid scintillation counter. Saturation binding data were analyzed in counts per minute (CPM) using the One site – Total and nonspecific binding nonlinear regression on GraphPad Prism version 9.3.1. Competition binding experiment data were normalized to the radioactivity in disintegrations per minute (DPM) observed in the presence of vehicle (100% [3H]-LSD bound) and 10 µM 5-HT (0% [3H]-LSD bound). Competition binding data were analyzed using the One site – Fit Ki nonlinear regression on GraphPad Prism version 9.3.1, constraining HotKdNM to the Kd value of the radioligand determined in saturation binding assays, HotNM to the concentration of radioligand employed in the assays, and the bottom plateau to 0%. To analyze the data using this method, the 0.1% DMSO vehicle condition was set to an arbitrarily dilute concentration of 10-25 M to be included on the logarithmic scale of the X-axis.

PsychLight1 Experiments. HEK293T cells (ATCCCRL-11268; mycoplasma free) lipofected with pCMV_PsychLight1 (described in ref 14) were plated at 1.5 x 105 cells/well in poly-D-lysine coated 35 mm live cell dishes. After 24 h, the cells were washed three times with HBSS supplemented with 2 mM MgCl2 and 2 mM CaCl2. A 10 mM methylated ketanserin stock in DMSO was diluted in 1 mL of HBSS to achieve a

concentration of 10 µM, added to the empty dishes, and placed back in the incubator for 10 min. Cells were then imaged in a live cell chamber connected to a Nikon HCA confocal microscope a with a 60 x /NA 1.40 oil objective at 488 nm (35% laser power). Baseline images of cells were manually captured, and the coordinates were saved. Next, 10 mM 5-HT or 5-MeO-DMT drug stocks in DMSO were diluted to 20 µM in 1 mL of HBSS and added dropwise to the dish to achieve a final concentration of 10 µM (total dilution = 1:1000). The dish was incubated for 5 min before re-imaging at the saved positions. Using ImageJ, ROIs were drawn around individual cells to determine fluorescence intensity on a per cell basis. The same ROI was applied to the baseline and post treatment images to quantify the change in fluorescence (ΔF/F). The ΔF/F values for each image were calculated using the following equation:

(fluorescence intensity after drug- fluorescence intensity before drug)/(fluorescence intensity before drug)

Individual cell ΔF/F values were averaged to determine the mean ΔF/F for each treatment. Experiments were performed in duplicate using dishes from independent HEK293T cultures with a total of N = 41–54 cells per treatment.

PsychLight2 Experiments. For experiments using PSYLI2 cells (HEK293T cell line stably expressing psychLight2; mycoplasma free) cells were plated at 8.0 x 104 cells/well in poly-D-lysine coated glass bottom 96-well plates (P96-1.5H-N, Cellvis) in complete media and returned to the incubator. The next day, plates were washed three times with warm HBSS supplemented with 2 mM MgCl2 and 2 mM CaCl2. Next, 50 µL HBSS was added to the wells of the assay plate and a baseline scan was performed using a

CellInsight CX7 HCA Platform (ThermoFisher, CX7A1110) connected to an onstage incubator for live cell imaging (ThermoFisher, NX7LIVE001) at 40x with nine ROIs taken per well using an arbitrary ROI pattern for each well with no bias to location and no overlap of the ROIs (exposure = 400 ms, LED power = 100%). Immediately prior to re-imaging, 10 mM stock solutions of drugs in DMSO were diluted in HBSS to 20 µM and distributed across an empty 96-well treatment plate in triplicate following a randomized plate map. Serial 1:10 dilutions were performed in the treatment plate to generate a concentration response. For agonist mode, 50 µL from the treatment plate was transferred to the assay plate resulting in a final 10 µM concentration (total dilution = 1:1000). After a 5 min incubation, the same sites were re-imaged using the same settings. For antagonist mode, a 100 µM 5-HT stock in DMSO was diluted in HBSS to a 200 nM solution, 50 µL of 200 nM 5-HT was added to the wells to achieve a final concentration of 100 nM 5-HT (total dilution = 1:1,000). After a 5-minute incubation the plate was scanned. Following this, a 10 mM antagonist stock in DMSO was diluted in HBSS to a 20 µM solution, and 100 µL of the 20 µM antagonist was added to the wells to achieve a final concentration of 10 µM (total dilution = 1:1000). After a 5 min incubation, the plate was re-scanned. Once imaging was complete, the images were exported and processed through a custom Python script to obtain average ΔF/F values for each treatment (https://github.com/moagonzalez/OlsonLab/blob/main/PsychLightV3_Clean.txt).

Next, ΔF/F values for each treatment were fitted to a nonlinear regression of agonist vs response (three parameter) for agonist mode and inhibitor vs response (three parameter) for antagonist mode using Prism (version 9.3.1). Responses were normalized to the

positive control (10 µM 5-HT) set as 100% and the average of the 1 pM concentration response between both treatments on each graph set as 0%. An 8-point concentration response was performed for each compound except for DMT and TMT where a 9-point concentration responses were used, adding an additional 100 µM treatment due to the low potency of each compound. Experiments were performed in duplicate with plates prepared using independent PSYLI2 cultures with a total of N = 5–6 wells per concentration.

Surgery and Viral Injections for in vivo Experiments Involving SERT Expression in the PFC. Male and female C57/BL6J or Thy1-EGFP mice (8-weeks-old) were anesthetized using 5% isoflurane for induction and 1% isoflurane for maintenance. After induction of anesthesia, Carprofen (5 mg/kg) and Buprenorphine (1 mg/kg) were administered subcutaneously. Mice were mounted on a stereotaxic apparatus (Kopf, model 900). During surgery, body temperature was maintained with a heating pad. Petrolatum ophthalmic ointment was used to cover the animal's eyes. Before a sterile scalpel was used to make an incision, the hair covering the skin above the skull was removed and then disinfected with an ethanol pad and betadine. To have consistent horizontal alignment of the skull, bregma and lambda were leveled to be on the same z axis while two points on the surface of the skull 1.5 mm to either side of lambda were used to level the skull with respect to the y axis. For bilateral injections into the infralimbic cortex (AP: + 1.94 mm, ML: +/- 0.25 mm, DV: −3 mm from the skull), a small craniotomy (1–2 mm diameter) was performed on top of each hemisphere over the injection site. The virus injection was performed using a Sub-Microliter Injection System with nanofil

needles (WPI, NF35BV-2). The injection needle was lowered into the brain regions indicated and infused per site at a rate of 100 nL per min. The injection volume was controlled by a microsyringe pump, which was connected to a controller. Following injection, the virus was allowed to diffuse into the tissue for an additional 10 min before the needle was withdrawn. For FST experiments, 300 nL of AAV1-CaMKII-SERT-EYFP (subcloned from RRID:Addgene_70105) or AAV1-CaMKII-GFP (RRID:Addgene_64545) was injected into C57/BL6J mice. For dendritic spine imaging experiments, 300 nL of AAV1-CaMKII-SERT-mCherry (subcloned from RRID:Addgene_70105 and RRID:Addgene_114469) or AAV5-CaMKIIa-mCherry (RRID:Addgene_114469) was injected into Thy1-EGFP mice. Mice were allowed to recover for 3 weeks in the vivarium to allow for construct expression before beginning experiments.

Behavioral Experiments Using Mice Expressing SERT in the PFC. At 3-weeks post-surgery, each mouse was handled for approximately 1 min by a male experimenter for three consecutive days leading up to the first day of behavioral testing. All experiments were carried out by the same male experimenter. Mice were allowed to habituate to the behavior room for 1 h before beginning the experiment. For multi-day experiments, mice were returned to their home cages and placed back in the vivarium after each test. All behavior was performed between the hours of 8:00 and 13:00. On day 1, mice were placed in a 40 cm x 40 cm arena for 60 min and baseline locomotor activity was assessed using AnyMaze automated tracking software. On day 2, a pre-test FST was performed. During the FST, mice underwent a 6 min swim session in a clear Plexiglas cylinder (40 cm tall, 20 cm in diameter) filled with 30 cm of 24 ± 1 °C water. Fresh water

was used for each mouse. Mice were dried and returned to their home cages following each FST session.. On day 3, the mice were allowed to rest and remained in the vivarium. On day 4, mice were administered PCA (5 mg/kg; IP) and were returned to their home cages and vivarium. On day 5, mice were subjected to a FST to determine the sustained effects of serotonin release between the two groups. Experiments were video-recorded and manually scored offline by a blinded experimenter. Immobility time—defined as passive floating or remaining motionless with no activity other than that needed to keep the head above water—was scored for the last 4 min of the 6 min trial.

Perfusion and Histology for in vivo Experiments Involving SERT Expression in the PFC. Mice were deeply anesthetized with avertin and transcardially perfused with paraformaldehyde (PFA, 4% in PBS, 7.4 pH). After extraction of the mouse brains, samples were fixed in 4% PFA at 4°C overnight. The mouse brains were cryo-protected by immersion in 10% sucrose in a 1x PBS solution overnight. Next, samples were placed in 30% sucrose in a 1x PBS solution for at least 1 day. Samples were then embedded in O.C.T, sliced into 50 µm coronal brain slices using a cryostat (Leica Biosystems), and mounted on slides for staining. Slides were left in the dark at room temperature overnight to dry before staining the next day. A barrier around the slides was drawn using a PAP Pen (Biotium, 22006). Brain slices were permeabilized using 0.2% Triton X-100 (ThermoFisher) in DPBS for 20 min at room temperature without shaking. Brain slices were blocked with antibody diluting buffer (ADB) containing 2% bovine serum albumin (BSA) in DPBS for 1 h at room temperature. Then, slides were incubated overnight at 4 ^{o}C in ADB containing rabbit anti-GFP antibody (Invitrogen, #MA5-15256, 1:1000) to

immunostain constructs with GFP like tags or enhance the Thy1-GFP signal or anti-RFP antibody (Rockland, #600-401-379, 1:1000) to immunostain constructs with an mCherry tag. The next day, slides were washed three times with DPBS. Following washes, slides were incubated for 1 h at room temperature in ADB containing an anti-mouse secondary antibody conjugated to Alexa Fluor 488 (Invitrogen, #A-11001, 1:500) and an anti-rabbit secondary antibody conjugated to Alexa Fluor 568 (Invitrogen, #A-11011, 1:500). Slides washed three times with DPBS, and after the final wash, slides were allowed to dry for 10 min before coverslips were mounted onto microscope slides using ProLong Gold. Slides were imaged on a Zeiss LSM 710 confocal microscope equipped with a Plan-Apochromat 63x/1.40 N.A. oil objective for dendritic spine imaging and a Plan-Apochromat 20x/0.8 N.A. objective for stitching images of an entire brain slice.

Experiments Assessing Dendritic Spine Density in Mice Expressing SERT in the PFC. Thy1-GFP mice expressing either AAV1-CaMKII-SERT-mCherry or AAV5-CaMKIIa-mCherry were administered PCA (5 mg/kg; IP). After 24 h, the mice were perfused and brain slices prepared as described above. Slices were mounted and immunostained for anti-GFP to label Thy1-EFGP and anti-RFP to label the mCherry constructs. Immunostained slides were imaged on a Zeiss LSM 710 confocal microscope using a Plan-Apochromat 63x/1.40 oil objective imaging in the following order: 561 nm (20% laser power), and 458 nm (25% laser power). Images of apical dendrites and their dendritic spines within the infralimbic cortex were captured and manually counted by a trained experimenter blinded to treatment conditions.

Reference

1. R. S. Duman, G. K. Aghajanian, G. Sanacora, J. H. Krystal, Synaptic plasticity and depression: New insights from stress and rapid-acting antidepressants. Nat. Med. 22, 238–249 (2016). doi:10.1038/nm.4050 Medline

2. H. Qiao, M.-X. Li, C. Xu, H.-B. Chen, S.-C. An, X.-M. Ma, Dendritic spines in depression: What we learned from animal models. Neural Plast. 2016, 8056370 (2016). doi:10.1155/2016/8056370 Medline

3. R. M. Shansky, C. Hamo, P. R. Hof, B. S. McEwen, J. H. Morrison, Stress-induced dendritic remodeling in the prefrontal cortex is circuit specific. Cereb. Cortex 19, 2479–2484 (2009). doi:10.1093/cercor/bhp003 Medline

4. T. Rantamäki, P. Hendolin, A. Kankaanpää, J. Mijatovic, P. Piepponen, E. Domenici, M. V. Chao, P. T. Männistö, E. Castrén, Pharmacologically diverse antidepressants rapidly activate brain-derived neurotrophic factor receptor TrkB and induce phospholipase-Cγ signaling pathways in mouse brain. Neuropsychopharmacology 32, 2152–2162 (2007). doi:10.1038/sj.npp.1301345 Medline

5. P. C. Casarotto, M. Girych, S. M. Fred, V. Kovaleva, R. Moliner, G. Enkavi, C. Biojone, C. Cannarozzo, M. P. Sahu, K. Kaurinkoski, C. A. Brunello, A. Steinzeig, F. Winkel, S. Patil, S. Vestring, T. Serchov, C. R. A. F. Diniz, L. Laukkanen, I. Cardon, H. Antila, T. Rog, T. P. Piepponen, C. R. Bramham, C. Normann, S. E. Lauri, M. Saarma, I. Vattulainen, E. Castrén, Antidepressant drugs act by directly binding to TRKB neurotrophin receptors. Cell 184, 1299–1313.e19 (2021). doi:10.1016/j.cell.2021.01.034 Medline

6. D. E. Olson, Psychoplastogens: A promising class of plasticity-promoting neurotherapeutics. J. Exp. Neurosci. 12, 1179069518800508 (2018). doi:10.1177/1179069518800508 Medline

7. M. V. Vargas, R. Meyer, A. A. Avanes, M. Rus, D. E. Olson, Psychedelics and other psychoplastogens for treating mental illness. Front. Psychiatry 12, 727117 (2021). doi:10.3389/fpsyt.2021.727117 Medline

8. A. C. Kwan, D. E. Olson, K. H. Preller, B. L. Roth, The neural basis of psychedelic action. Nat. Neurosci. 25, 1407–1419 (2022). doi:10.1038/s41593-022-01177-4 Medline

9. C. Ly, A. C. Greb, L. P. Cameron, J. M. Wong, E. V. Barragan, P. C. Wilson, K. F. Burbach, S. Soltanzadeh Zarandi, A. Sood, M. R. Paddy, W. C. Duim, M. Y. Dennis, A. K. McAllister, K. M. Ori-McKenney, J. A. Gray, D. E. Olson, Psychedelics promote structural and functional neural plasticity. Cell Rep. 23, 3170–3182 (2018). doi:10.1016/j.celrep.2018.05.022 Medline

10. M. de la Fuente Revenga, B. Zhu, C. A. Guevara, L. B. Naler, J. M. Saunders, Z. Zhou, R. Toneatti, S. Sierra, J. T. Wolstenholme, P. M. Beardsley, G. W. Huntley, C. Lu, J.

González-Maeso, Prolonged epigenomic and synaptic plasticity alterations following single exposure to a psychedelic in mice. Cell Rep. 37, 109836 (2021). doi:10.1016/j.celrep.2021.109836 Medline

11. D. E. Olson, Biochemical mechanisms underlying psychedelic-induced neuroplasticity. Biochemistry 61, 127–136 (2021). doi:10.1021/acs.biochem.1c00812 Medline

12. L. E. Dunlap, A. Azinfar, C. Ly, L. P. Cameron, J. Viswanathan, R. J. Tombari, D. MyersTurnbull, J. C. Taylor, A. C. Grodzki, P. J. Lein, D. Kokel, D. E. Olson, Identification of psychoplastogenic N,N-dimethylaminoisotryptamine (isoDMT) analogues through structure-activity relationship studies. J. Med. Chem. 63, 1142–1155 (2020). doi:10.1021/acs.jmedchem.9b01404 Medline

13. L. P. Cameron, R. J. Tombari, J. Lu, A. J. Pell, Z. Q. Hurley, Y. Ehinger, M. V. Vargas, M. N. McCarroll, J. C. Taylor, D. Myers-Turnbull, T. Liu, B. Yaghoobi, L. J. Laskowski, E. I. Anderson, G. Zhang, J. Viswanathan, B. M. Brown, M. Tjia, L. E. Dunlap, Z. T. Rabow, O. Fiehn, H. Wulff, J. D. McCorvy, P. J. Lein, D. Kokel, D. Ron, J. Peters, Y. Zuo, D. E. Olson, A non-hallucinogenic psychedelic analogue with therapeutic potential. Nature 589, 474–479 (2021). doi:10.1038/s41586-020-3008-z Medline

14. C. Dong, C. Ly, L. E. Dunlap, M. V. Vargas, J. Sun, I.-W. Hwang, A. Azinfar, W. C. Oh, W. C. Wetsel, D. E. Olson, L. Tian, Psychedelic-inspired drug discovery using an engineered biosensor. Cell 184, 2779–2792.e18 (2021). doi:10.1016/j.cell.2021.03.043 Medline

15. D. Cao, J. Yu, H. Wang, Z. Luo, X. Liu, L. He, J. Qi, L. Fan, L. Tang, Z. Chen, J. Li, J. Cheng, S. Wang, Structure-based discovery of nonhallucinogenic psychedelic analogs. Science 375, 403–411 (2022). doi:10.1126/science.abl8615 Medline

16. L. M. Luttrell, S. Maudsley, L. M. Bohn, Fulfilling the promise of “biased” G proteincoupled receptor agonism. Mol. Pharmacol. 88, 579–588 (2015). doi:10.1124/mol.115.099630 Medline

17. K. Kim, T. Che, O. Panova, J. F. DiBerto, J. Lyu, B. E. Krumm, D. Wacker, M. J. Robertson, A. B. Seven, D. E. Nichols, B. K. Shoichet, G. Skiniotis, B. L. Roth, Structure of a hallucinogen-activated Gq-coupled 5-HT2A serotonin receptor. Cell 182, 1574–1588.e19 (2020). doi:10.1016/j.cell.2020.08.024 Medline

18. R. Irannejad, V. Pessino, D. Mika, B. Huang, P. B. Wedegaertner, M. Conti, M. von Zastrow, Functional selectivity of GPCR-directed drug action through location bias. Nat. Chem. Biol. 13, 799–806 (2017). doi:10.1038/nchembio.2389 Medline

19. M. A. Mohammad Nexhady, J. C. Nezhady, S. Chemtob, Location bias as emerging paradigm in GPCR biology and drug discovery. iScience 23, 101643 (2020). doi:10.1016/j.isci.2020.101643 Medline

20. N. V. Weisstaub, M. Zhou, A. Lira, E. Lambe, J. González-Maeso, J.-P. Hornung, E. Sibille, M. Underwood, S. Itohara, W. T. Dauer, M. S. Ansorge, E. Morelli, J. J. Mann, M. Toth, G. Aghajanian, S. C. Sealfon, R. Hen, J. A. Gingrich, Cortical 5-HT2A receptor signaling modulates anxiety-like behaviors in mice. Science 313, 536–540 (2006). doi:10.1126/science.1123432 Medline

21. D. Ristanović, N. T. Milosević, V. Stulić, Application of modified Sholl analysis to neuronal dendritic arborization of the cat spinal cord. J. Neurosci. Methods 158, 212–218 (2006). doi:10.1016/j.jneumeth.2006.05.030 Medline

22. B. J. Ebersole, I. Visiers, H. Weinstein, S. C. Sealfon, Molecular basis of partial agonism: Orientation of indoleamine ligands in the binding pocket of the human serotonin 5-HT2A receptor determines relative efficacy. Mol. Pharmacol. 63, 36–43 (2003). doi:10.1124/mol.63.1.36 Medline

23. R. H. J. Olsen, J. F. DiBerto, J. G. English, A. M. Glaudin, B. E. Krumm, S. T. Slocum, T. Che, A. C. Gavin, J. D. McCorvy, B. L. Roth, R. T. Strachan, TRUPATH, an opensource biosensor platform for interrogating the GPCR transducerome. Nat. Chem. Biol. 16, 841–849 (2020). doi:10.1038/s41589-020-0535-8 Medline

24. J. C. Bermak, M. Li, C. Bullock, Q. Y. Zhou, Regulation of transport of the dopamine D1 receptor by a new membrane-associated ER protein. Nat. Cell Biol. 3, 492–498 (2001). doi:10.1038/35074561 Medline

25. U. E. Petäjä-Repo, M. Hogue, A. Laperriere, P. Walker, M. Bouvier, Export from the endoplasmic reticulum represents the limiting step in the maturation and cell surface expression of the human δ opioid receptor. J. Biol. Chem. 275, 13727–13736 (2000). doi:10.1074/jbc.275.18.13727 Medline

26. S. E. Jacobsen, I. Ammendrup-Johnsen, A. M. Jansen, U. Gether, K. L. Madsen, H. BräunerOsborne, The GPRC6A receptor displays constitutive internalization and sorting to the slow recycling pathway. J. Biol. Chem. 292, 6910–6926 (2017). doi:10.1074/jbc.M116.762385 Medline

27. C. A. Purgert, Y. Izumi, Y.-J. I. Jong, V. Kumar, C. F. Zorumski, K. L. O'Malley, Intracellular mGluR5 can mediate synaptic plasticity in the hippocampus. J. Neurosci. 34, 4589–4598 (2014). doi:10.1523/JNEUROSCI.3451-13.2014 Medline

28. V. Cornea-Hébert, M. Riad, C. Wu, S. K. Singh, L. Descarries, Cellular and subcellular distribution of the serotonin 5-HT2A receptor in the central nervous

system of adult rat. J. Comp. Neurol. 409, 187–209 (1999). doi:10.1002/(SICI)1096-9861(19990628)409:2<187:AID-CNE2>3.0.CO;2-P Medline

29. V. Cornea-Hébert, K. C. Watkins, B. L. Roth, W. K. Kroeze, P. Gaudreau, N. Leclerc, L. Descarries, Similar ultrastructural distribution of the 5-HT2A serotonin receptor and microtubule-associated protein MAP1A in cortical dendrites of adult rat. Neuroscience 113, 23–35 (2002). doi:10.1016/S0306-4522(02)00146-X Medline

30. C. L. Schmid, K. M. Raehal, L. M. Bohn, Agonist-directed signaling of the serotonin 2A receptor depends on β-arrestin-2 interactions in vivo. Proc. Natl. Acad. Sci. U.S.A. 105, 1079–1084 (2008). doi:10.1073/pnas.0708862105 Medline

31. R. Toneatti, J. M. Shin, U. H. Shah, C. R. Mayer, J. M. Saunders, M. Fribourg, P. T. Arsenovic, W. G. Janssen, S. C. Sealfon, J. F. López-Giménez, D. L. Benson, D. E. Conway, J. González-Maeso, Interclass GPCR heteromerization affects localization and trafficking. Sci. Signal. 13, eaaw3122 (2020). doi:10.1126/scisignal.aaw3122 Medline

32. J. E. Saffitz, S. B. Liggett, Subcellular distribution of β2-adrenergic receptors delineated with quantitative ultrastructural autoradiography of radioligand binding sites. Circ. Res. 70, 1320–1325 (1992). doi:10.1161/01.RES.70.6.1320 Medline

33. Q. Fu, Y. K. Xiang, Trafficking of β-adrenergic receptors: Implications in intracellular receptor signaling. Prog. Mol. Biol. Transl. Sci. 132, 151–188 (2015). doi:10.1016/bs.pmbts.2015.03.008 Medline

34 A. C. Magalhaes, K. D. Holmes, L. B. Dale, L. Comps-Agrar, D. Lee, P. N. Yadav, L. Drysdale, M. O. Poulter, B. L. Roth, J.-P. Pin, H. Anisman, S. S. G. Ferguson, CRF receptor 1 regulates anxiety behavior via sensitization of 5-HT2 receptor signaling. Nat. Neurosci. 13, 622–629 (2010). doi:10.1038/nn.2529 Medline

35. J. L. Seachrist, S. S. Ferguson, Regulation of G protein-coupled receptor endocytosis and trafficking by Rab GTPases. Life Sci. 74, 225–235 (2003). doi:10.1016/j.lfs.2003.09.009 Medline

36. C. A. Nash, W. Wei, R. Irannejad, A. V. Smrcka, Golgi localized β1-adrenergic receptors stimulate Golgi PI4P hydrolysis by PLCε to regulate cardiac hypertrophy. eLife 8, e48167 (2019). doi:10.7554/eLife.48167 Medline

37. R. Irannejad, J. C. Tomshine, J. R. Tomshine, M. Chevalier, J. P. Mahoney, J. Steyaert, S. G. F. Rasmussen, R. K. Sunahara, H. El-Samad, B. Huang, M. von Zastrow, Conformational biosensors reveal GPCR signalling from endosomes. Nature 495, 534–538 (2013). doi:10.1038/nature12000 Medline

38. M. Stoeber, D. Jullié, B. T. Lobingier, T. Laeremans, J. Steyaert, P. W. Schiller, A. Manglik, M. von Zastrow, A genetically encoded biosensor reveals location bias of

opioid drug action. Neuron 98, 963–976.e5 (2018). doi:10.1016/j.neuron.2018.04.021 Medline

39. S. Aggarwal, O. V. Mortensen, Overview of monoamine transporters. Curr. Protocols Pharmacol. 79, 12.16.1–12.16.17 (2017). doi:10.1002/cpph.32 Medline

40. F. C. Zhou, Y. Sari, J. K. Zhang, Expression of serotonin transporter protein in developing rat brain. Brain Res. Dev. Brain Res. 119, 33–45 (2000). doi:10.1016/S01653806(99)00152-2 Medline

41. C. Lebrand, O. Cases, R. Wehrlé, R. D. Blakely, R. H. Edwards, P. Gaspar, Transient developmental expression of monoamine transporters in the rodent forebrain. J. Comp. Neurol. 401, 506–524 (1998). doi:10.1002/(SICI)1096-9861(19981130)401:4<506:AIDCNE5>3.0.CO;2-# Medline

42. M. Fuchikami, A. Thomas, R. Liu, E. S. Wohleb, B. B. Land, R. J. DiLeone, G. K. Aghajanian, R. S. Duman, Optogenetic stimulation of infralimbic PFC reproduces ketamine's rapid and sustained antidepressant actions. Proc. Natl. Acad. Sci. U.S.A. 112, 8106–8111 (2015). doi:10.1073/pnas.1414728112 Medline

43. T. Sharp, T. Zetterström, L. Christmanson, U. Ungerstedt, p-Chloroamphetamine releases both serotonin and dopamine into rat brain dialysates in vivo. Neurosci. Lett. 72, 320–324 (1986). doi:10.1016/0304-3940(86)90534-3 Medline

44. R. N. Moda-Sava, M. H. Murdock, P. K. Parekh, R. N. Fetcho, B. S. Huang, T. N. Huynh, J. Witztum, D. C. Shaver, D. L. Rosenthal, E. J. Alway, K. Lopez, Y. Meng, L. Nellissen, L. Grosenick, T. A. Milner, K. Deisseroth, H. Bito, H. Kasai, C. Liston, Sustained rescue of prefrontal circuit dysfunction by antidepressant-induced spine formation. Science 364, eaat8078 (2019). doi:10.1126/science.aat8078 Medline

45. D. A. Slattery, J. F. Cryan, Using the rat forced swim test to assess antidepressant-like activity in rodents. Nat. Protoc. 7, 1009–1014 (2012). doi:10.1038/nprot.2012.044 Medline

46. S. E. Crilly, W. Ko, Z. Y. Weinberg, M. A. Puthenveedu, Conformational specificity of opioid receptors is determined by subcellular location irrespective of agonist. eLife 10, e67478 (2021). doi:10.7554/eLife.67478 Medline

47. C. Ly, A. C. Greb, M. V. Vargas, W. C. Duim, A. C. G. Grodzki, P. J. Lein, D. E. Olson, Transient stimulation with psychoplastogens is sufficient to initiate neuronal growth. ACS Pharmacol. Transl. Sci. 4, 452–460 (2020). doi:10.1021/acsptsci.0c00065 Medline

48. L. X. Shao, C. Liao, I. Gregg, P. A. Davoudian, N. K. Savalia, K. Delagarza, A. C. Kwan, Psilocybin induces rapid and persistent growth of dendritic spines in frontal

cortex in vivo. Neuron 109, 2535–2544.e4 (2021). doi:10.1016/j.neuron.2021.06.008 Medline

49. J. González-Maeso, N. V. Weisstaub, M. Zhou, P. Chan, L. Ivic, R. Ang, A. Lira, M. Bradley-Moore, Y. Ge, Q. Zhou, S. C. Sealfon, J. A. Gingrich, Hallucinogens recruit specific cortical 5-HT2A receptor-mediated signaling pathways to affect behavior. Neuron 53, 439–452 (2007). doi:10.1016/j.neuron.2007.01.008 Medline

50. C. L. Schmid, L. M. Bohn, Serotonin, but not N-methyltryptamines, activates the serotonin 2A receptor via a ß-arrestin2/Src/Akt signaling complex in vivo. J. Neurosci. 30, 13513–13524 (2010). doi:10.1523/JNEUROSCI.1665-10.2010 Medline

51. H. A. Lester, J. M. Miwa, R. Srinivasan, Psychiatric drugs bind to classical targets within early exocytotic pathways: Therapeutic effects. Biol. Psychiatry 72, 907–915 (2012). doi:10.1016/j.biopsych.2012.05.020 Medline

52. B. J. Henderson, H. A. Lester, Inside-out neuropharmacology of nicotinic drugs. Neuropharmacology 96, 178–193 (2015). doi:10.1016/j.neuropharm.2015.01.022 Medline

53. H. A. Lester, L. D. Lavis, D. A. Dougherty, Ketamine inside neurons? Am. J. Psychiatry 172, 1064–1066 (2015). doi:10.1176/appi.ajp.2015.14121537 Medline

54. S. A. Barker, E. H. McIlhenny, R. Strassman, A critical review of reports of endogenous psychedelic N,N-dimethyltryptamines in humans: 1955-2010. Drug Test. Anal. 4, 617– 635 (2012). doi:10.1002/dta.422 Medline

55. S. A. Barker, J. Borjigin, I. Lomnicka, R. Strassman, LC/MS/MS analysis of the endogenous dimethyltryptamine hallucinogens, their precursors, and major metabolites in rat pineal gland microdialysate. Biomed. Chromatogr. 27, 1690–1700 (2013). doi:10.1002/bmc.2981 Medline

56. J. G. Dean, T. Liu, S. Huff, B. Sheler, S. A. Barker, R. J. Strassman, M. M. Wang, J. Borjigin, Biosynthesis and extracellular concentrations of N,N-dimethyltryptamine (DMT) in mammalian brain. Sci. Rep. 9, 9333 (2019). doi:10.1038/s41598-019-45812-w Medline

57. M. V. Vargas, L. E. Dunlap, C. Dong, S. J. Carter, R. J. Tombari, S. A. Jami, L. P. Cameron, S. D. Patel, J. J. Hennessey, H. N. Saeger, J. D. McCorvy, J. A. Gray, L. Tian, D. E. Olson, Data set for Intracellular 5-HT2A Paper, Figshare (2022); https://doi.org/10.6084/m9.figshare.21669635.

58. J. McCall, L. Nicholson, N. Weidner, A. Blesch, Optimization of adult sensory neuron electroporation to study mechanisms of neurite growth. Front. Mol. Neurosci. 5, 11 (2012). Medline

59. M. M. Bradford, A rapid and sensitive method for the quantitation of microgram quantities of protein utilizing the principle of protein-dye binding. Anal. Biochem. 72, 248–254 (1976). doi:10.1016/0003-2697(76)90527-3 Medline

Chapter 3 – Exploration of New Methods – machine learning

Directed Evolution of a Selective and Sensitive Serotonin Sensor via Machine Learning

Preface

The text of this chapter is a modified version of a manuscript that was submitted to the Cell Press on November 23, 2019, and accepted for publication on December 16, 2020 (doi.org/10.1016/j.cell.2020.11.040). The content of this chapter is selected from a portion of the full manuscript based on my original work contributing to the project. The layout has been adjusted in accordance with the requirements of a doctoral thesis. The authors on the original manuscript are listed as Elizabeth K Unger†, Jacob P Keller†, Michael Altermatt†, Ruqiang Liang, Aya Matsui, Chunyang Dong, Olivia J Hon, Zi Yao, Junqing Sun, Samba Banala, Meghan E Flanigan, David A Jaffe, Samantha Hartanto, Jane Carlen, Grace O Mizuno, Phillip M Borden, Amol V Shivange, Lindsay P Cameron, Steffen Sinning, Suzanne M Underhill, David E Olson, Susan G Amara, Duncan Temple Lang, Gary Rudnick, Jonathan S Marvin, Luke D Lavis, Henry A Lester, Veronica A Alvarez, Andrew J Fisher, Jennifer A Prescher, Thomas L Kash, Vladimir Yarov-Yarovoy, Viviana Gradinaru, Loren L Looger, Lin Tian.

(† authors contributed equally to this work)

Abstract

Serotonin plays a central role in cognition and is the target of most pharmaceuticals for psychiatric disorders. Existing drugs have limited efficacy; creation of improved versions will require better understanding of serotonergic circuitry, which has been hampered by our inability to monitor serotonin release and transport with high spatial and temporal resolution. We developed and applied a binding-pocket redesign strategy, guided by machine learning, to create a high-performance, soluble, fluorescent serotonin sensor (iSeroSnFR), enabling optical detection of millisecond-scale serotonin transients. We demonstrate that iSeroSnFR can be used to detect serotonin release in freely behaving mice during fear conditioning, social interaction, and sleep/wake transitions. We also developed a robust assay of serotonin transporter function and modulation by drugs. We expect that both machine-learning-guided binding-pocket redesign and iSeroSnFR will have broad utility for the development of other sensors and in vitro and in vivo serotonin detection, respectively.

Introduction

Serotonergic systems profoundly modulate diverse behaviors (Berger et al., 2009; Charnay and Léger, 2010). Serotonin (5-HT) dysregulation has been implicated in mental disorders, including depression and anxiety (Belmaker and Agam, 2008; Calhoon and Tye, 2015). Most antidepressants target some aspect of the serotonergic system; selective serotonin reuptake inhibitors (SSRIs) specifically target the 5-HT transporter (SERT) (Bos et al., 2012; Cipriani et al., 2018). Despite the critical importance of 5-HT, development of novel and more effective therapies has been challenging due to poor understanding of 5-HT dynamics, specifically the inability to measure 5-HT with high spatiotemporal resolution. Existing methods for measuring 5-HT, including microdialysis and fast-scan cyclic voltammetry (FSCV) (Abdalla et al., 2017; Jaquins-Gerstl and Michael, 2015; Peñalva et al., 2003; Schultz and Kennedy, 2008), as well as transporter assays relying primarily on radiolabeled 5-HT or analogs (Clarke and Khalid, 2015), lack the spatial or temporal resolution to adequately probe 5-HT dynamics and targetability.

A genetically encoded 5-HT sensor could potentially overcome these technical challenges (for review, see Broussard et al., 2014; Lin and Schnitzer, 2016; Looger and Griesbeck, 2012). We and others have recently produced single-fluorescent protein (FP)-based sensors for neurotransmitters and neuromodulators based on either microbial periplasmic binding proteins (PBPs) or G-protein-coupled-receptors (GPCRs). Combined with modern microscopy, these sensors enable direct and specific measurements of diverse neurotransmitters and neuromodulators including glutamate (Marvin et al., 2013), GABA (Marvin et al., 2019), ATP (Lobas et al., 2019), dopamine (Patriarchi et al., 2018; Sun et al., 2018), acetylcholine (ACh) (Borden et al., 2020; Jing et al., 2020), and

norepinephrine (Feng et al., 2019) with the necessary resolution for use in behaving animals (Corre et al., 2018; Madisen et al., 2015).

Although GPCR-based sensors can yield sensitive indicators, their response to pharmaceutical manipulations makes them problematic for use in any studies involving drug administration. Furthermore, it is difficult to target GPCR-based sensors to intracellular locations (e.g., to study 5-HT transport). PBP-based sensors are soluble and can therefore readily be targeted to subcellular locations, are amenable to high-throughput screening in bacteria, and easily allow detailed characterization in purified protein (Marvin et al., 2011). Naturally evolved PBPs typically bind few, if any, drugs targeting host proteins. In addition, microbial PBPs are bio-orthogonal to pathways in model organisms, promising minimal interference with endogenous signaling, a particular concern following long-term expression. Importantly, ligand binding in PBPs induces large conformational changes, resulting in very large dynamic ranges (Marvin et al., 2011, Marvin et al., 2013, Marvin et al., 2018). However, with no annotated PBPs for 5-HT, we opted to redesign the binding pocket of an existing PBP-based sensor to selectively bind 5-HT.

There are several complementary approaches available for binding-site redesign (Baker, 2019; Khoury et al., 2014). Site-saturated mutagenesis (SSM) combined with rational design can optimize sensor properties such as brightness, dynamic range, kinetics, and affinity (Cobb et al., 2013; Packer and Liu, 2015). However, SSM, while sufficient to convert our ACh sensor to one binding the cholinergic agonist nicotine (Shivange et al., 2019), cannot plausibly cover sufficient sequence space to radically

change binding specificity to the structurally very different 5-HT. Computational design (Rosetta) can successfully predict proteins with high affinity and selectivity for a given small molecule (Richter et al., 2011), but has never been used for sensors. Recently, machine-learning approaches of varying complexity have been applied to optimize protein function (Bedbrook et al., 2019; Biswas et al., 2018; Ehren et al., 2008; Liao et al., 2007; Saito and Nakatsuji, 2001; Wu et al., 2019). Our approach combined computational design and machine learning to guide an SSM pipeline. Using this method, we developed the first PBP-based 5-HT sensor (iSeroSnFR) by redesigning the binding pocket of the ACh sensor iAChSnFR0.6 (Borden et al., 2020). iSeroSnFR contains 19 mutations relative to iAChSnFR0.6; these conferred >5,000-fold improvement in 5-HT affinity while eliminating choline and ACh binding. We demonstrate that iSeroSnFR enables imaging of 5-HT dynamics in brain slices and freely moving mice. In addition, we highlight the clinical relevance of iSeroSnFR for pharmacological assays.

Results

(xi) Sensor Design

Before redesigning a binding pocket for structurally disparate molecules, we established our machine learning pipeline on structurally similar molecules (Figure S3.1; Table S3.1; Data S3.1; Methods). As a starting scaffold for our sensor, we chose an early version of iAChSnFR, based on a choline-binding PBP, OpuBC, from the hyperthermophile Thermoanaerobacter sp. X513 (Miller et al., 2011). In addition, this variant displayed detectable binding to 5-HT (apparent Kd >1 mM) (Figure S3.2A), making it a good starting template. We used a multi-stage pipeline to iteratively improve 5-HT binding and sensor response (Figure 3.1A). We first performed computational binding-pocket redesign using Rosetta, then iterative rounds of SSM guided by machine learning.

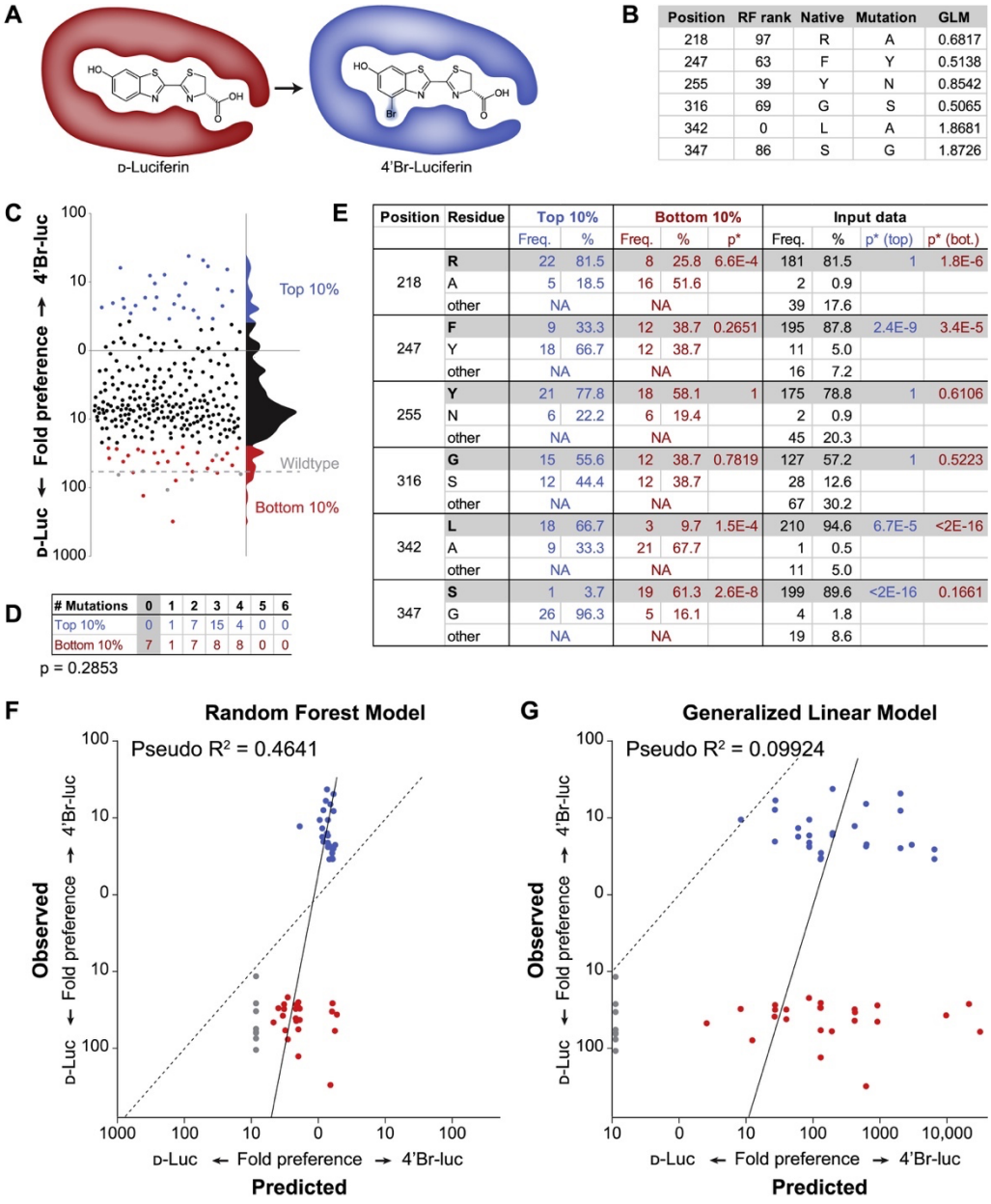

Position	RF rank	Native	Mutation	GLM
218	97	R	A	0.6817
247	63	F	Y	0.5138
255	39	Y	N	0.8542
316	69	G	S	0.5065
342	0	L	A	1.8681
347	86	S	G	1.8726

Position	Residue	Top 10% Freq.	Top 10% %	Bottom 10% Freq.	Bottom 10% %	Bottom 10% p*	Input data Freq.	Input data %	Input data p* (top)	Input data p* (bot.)
218	**R**	22	81.5	8	25.8	6.6E-4	181	81.5	1	1.8E-6
	A	5	18.5	16	51.6		2	0.9		
	other	NA		NA			39	17.6		
247	**F**	9	33.3	12	38.7	0.2651	195	87.8	2.4E-9	3.4E-5
	Y	18	66.7	12	38.7		11	5.0		
	other	NA		NA			16	7.2		
255	**Y**	21	77.8	18	58.1	1	175	78.8	1	0.6106
	N	6	22.2	6	19.4		2	0.9		
	other	NA		NA			45	20.3		
316	**G**	15	55.6	12	38.7	0.7819	127	57.2	1	0.5223
	S	12	44.4	12	38.7		28	12.6		
	other	NA		NA			67	30.2		
342	**L**	18	66.7	3	9.7	1.5E-4	210	94.6	6.7E-5	<2E-16
	A	9	33.3	21	67.7		1	0.5		
	other	NA		NA			11	5.0		
347	**S**	1	3.7	19	61.3	2.6E-8	199	89.6	<2E-16	0.1661
	G	26	96.3	5	16.1		4	1.8		
	other	NA		NA			19	8.6		

Figure S3.1. Development of a Machine-Learning-Guided Library Design Paradigm, Related to Figure 3.1

A. Schematic showing the evolution of substrate preference from D-luc to 4'Br-luc.

B. Random forest (RF) modeling and generalized linear modeling (GLM) were performed on 222 variants (see Table S3.2).

C. The combination library in (B) was generated and 276 variants were screened for their preference for D-luc or 4'Br-luc. The top and bottom 10% of variants were sequenced.

D. Table showing no difference between the mutation rate of the top and bottom 10% of variants (Fisher's Exact test). Variants with no mutations were omitted from statistical analysis.

E. Table showing the frequency of different mutations predicted by statistical modeling. ∗p values were calculated by Fisher's exact test, comparing the mutated amino acid(s) to the native amino acid, and the top 10% to either the bottom 10% or the input data as noted.

F, G. Comparison between the RF (F) and GLM (G) prediction and the actual data

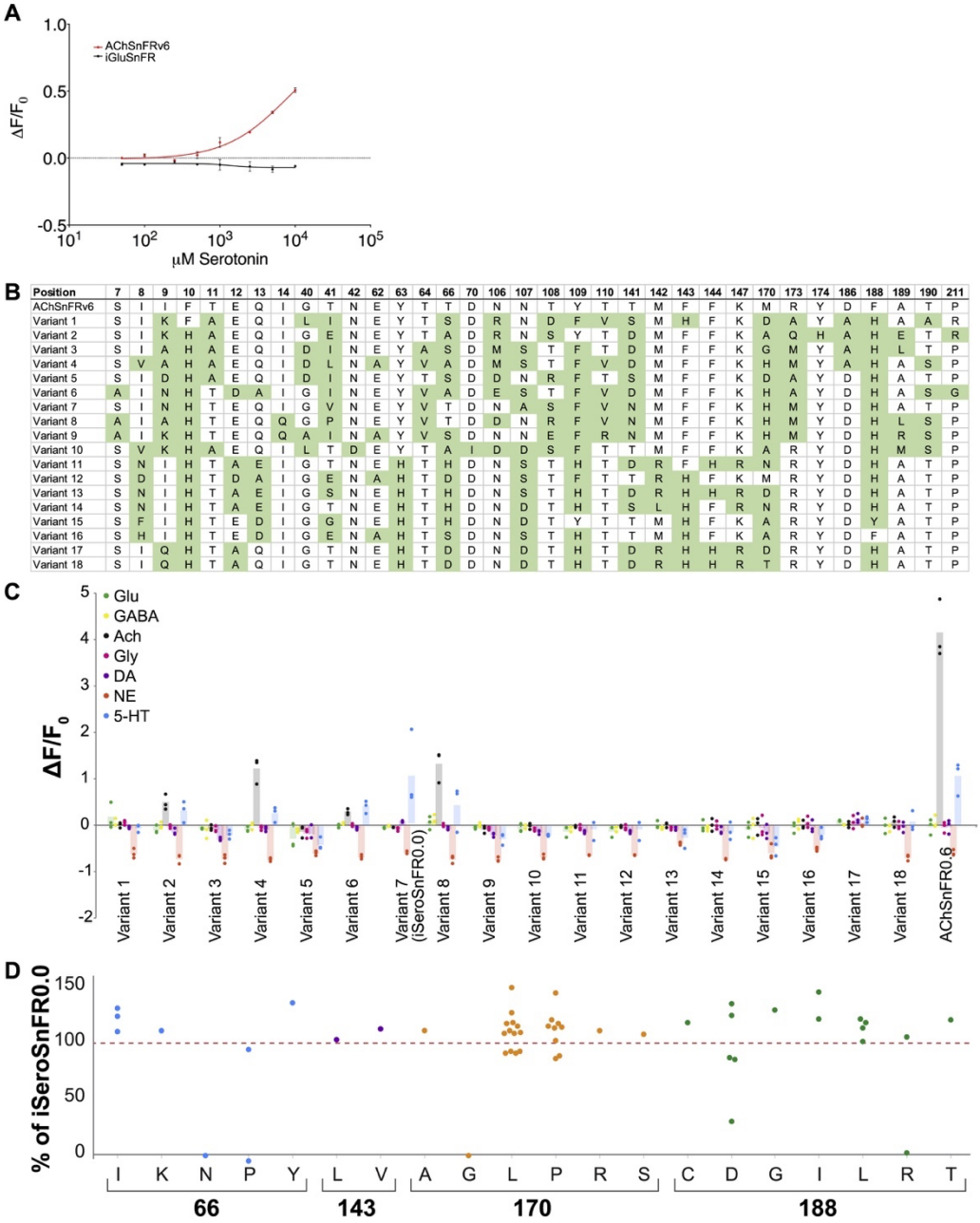

Position	7	8	9	10	11	12	13	14	40	41	42	62	63	64	66	70	106	107	108	109	110	141	142	143	144	147	170	173	174	186	188	189	190	211
AChSnFRv6	S	I	I	F	T	E	Q	I	G	T	N	E	Y	T	T	D	N	N	T	Y	T	T	M	F	F	K	M	R	Y	D	F	A	T	P
Variant 1	S	I	K	F	A	E	Q	I	L	I	N	E	Y	T	S	D	R	N	D	F	V	S	M	H	F	K	D	A	Y	A	H	A	A	R
Variant 2	S	I	K	H	A	E	Q	I	G	E	N	E	Y	T	A	D	R	N	S	Y	T	D	M	F	F	K	A	Q	H	A	H	E	T	R
Variant 3	S	I	A	H	A	E	Q	I	D	I	N	E	Y	A	S	D	M	S	T	F	T	D	M	F	F	K	G	M	Y	A	H	L	T	P
Variant 4	S	V	A	H	A	E	Q	I	D	L	N	A	Y	V	A	D	M	S	T	F	V	D	M	F	F	K	H	M	Y	A	H	A	S	P
Variant 5	S	I	D	H	A	E	Q	I	D	I	N	E	Y	T	S	D	D	N	R	F	T	S	M	F	F	K	D	A	Y	D	H	A	T	P
Variant 6	A	I	N	H	T	D	A	I	G	I	N	E	Y	V	A	D	E	S	T	F	V	D	M	F	F	K	H	A	Y	D	H	A	S	G
Variant 7	S	I	N	H	T	E	Q	I	G	V	N	E	Y	V	T	D	N	A	S	F	V	N	M	F	F	K	H	M	Y	D	H	A	T	P
Variant 8	A	I	A	H	T	E	Q	Q	G	P	N	E	Y	V	T	D	D	N	R	F	V	N	M	F	F	K	H	M	Y	D	H	L	S	P
Variant 9	A	I	K	H	T	E	Q	Q	A	I	N	A	Y	V	S	D	N	N	E	F	R	N	M	F	F	K	H	M	Y	D	H	R	S	P
Variant 10	S	V	K	H	A	E	Q	I	L	T	D	E	Y	T	A	I	D	D	S	F	T	T	M	F	F	K	A	R	Y	D	H	M	S	P
Variant 11	S	N	I	H	T	A	E	I	G	T	N	E	H	T	H	D	N	S	T	H	T	D	R	F	H	R	N	R	Y	D	H	A	T	P
Variant 12	S	D	I	H	T	D	A	I	G	E	N	A	H	T	D	D	N	S	T	F	T	T	R	H	F	K	M	R	Y	D	H	A	T	P
Variant 13	S	N	I	H	T	A	E	I	G	S	N	E	H	T	H	D	N	S	T	H	T	D	R	H	H	R	D	R	Y	D	H	A	T	P
Variant 14	S	N	I	H	T	A	E	I	G	T	N	E	H	T	H	D	N	D	T	H	T	S	L	H	F	R	N	R	Y	D	H	A	T	P
Variant 15	S	F	I	H	T	E	D	I	G	G	N	E	H	T	H	D	N	D	T	Y	T	T	M	H	F	K	A	R	Y	D	Y	A	T	P
Variant 16	S	H	I	H	T	E	D	I	G	E	N	A	H	T	S	D	N	S	T	H	T	T	M	H	F	K	A	R	Y	D	F	A	T	P
Variant 17	S	I	Q	H	T	A	Q	I	G	T	N	E	H	T	D	D	N	D	T	H	T	D	R	H	H	R	D	R	Y	D	H	A	T	P
Variant 18	S	I	Q	H	T	A	Q	I	G	T	N	E	H	T	D	D	N	D	T	H	T	D	R	H	H	R	T	R	Y	D	H	A	T	P

Figure S3.2. iSeroSnFR Design, Related to Figure 3.1

A. Purified protein of iAChSnFR0.6 and iGluSnFR were tested against multiple concentrations of 5-HT. n = 3. Data represent mean ± s.e.m.s.e.m.

B. Table showing the top 18 variants predicted by Rosetta modeling. Mutations are highlighted in green, compared to iAChSnFR0.6.

C. The top 18 variants were synthesized and tested as purified protein against multiple ligands. Protein concentration: 100 nM, ligand concentration: 10 mM. Shaded bars represent the mean.

D. Single mutants from the first SSM screen were tested with 10 mM 5-HT and compared to iSeroSnFR0.0. Red dashed line indicates iSeroSnFR0.0 (set to 100%).

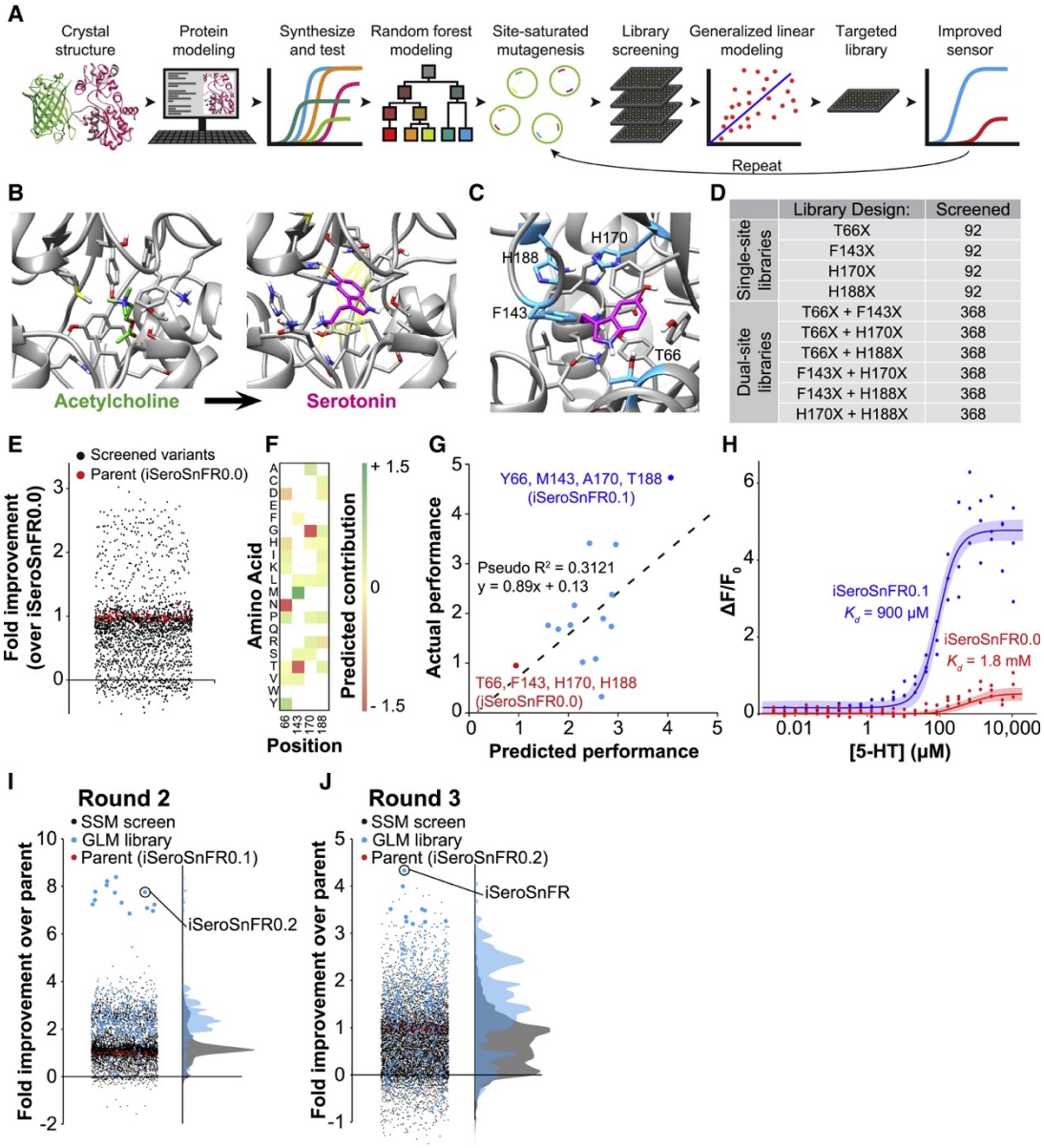

Figure 3.1. Using Machine Learning to Evolve Binding Proteins.
(A) Overview of machine learning method.
(B) Schematic showing conversion of an acetylcholine (ACh)-binding protein to a serotonin (5-HT)-binding protein. ACh and 5-HT were docked into the binding pocket of AChSnFR0.6 using Rosetta. Statistical modeling was performed on these models, and promising mutations were synthesized and tested (see Figure S3.2 and Table S3). iSeroSnFR0.0 was chosen as a starting point for statistical modeling. Positions 66, 143, 170, and 188 were selected for further mutation.
(C) The binding pocket of iSeroSnFR0.0 was simulated using Rosetta and 5-HT (magenta) docked. Top-ranked positions are labeled (cyan).
(D) Table of DNA libraries created, and number of variants screened from each library.
(E) DNA libraries were generated, transformed into bacteria, grown, and lysed. Lysate was then screened with 10 mM 5-HT and compared to the parent sensor (iSeroSnFR0.0).
(F). Heatmap of the contribution of each mutation at each position screened, as predicted by the generalized linear model (GLM) (for additional information see Table S3).
(G) Combinations of mutations predicted to be better than the parent (iSeroSnFR0.0) were synthesized and tested as purified protein with 10 mM 5-HT. Dashed line represents the linear regression.

(H) Protein from iSeroSnFR0.0 and the top variant (iSeroSnFR0.1) was purified and tested against multiple concentrations of 5-HT. Fits were determined using the Hill equation. Shaded area denotes 95% confidence interval. The apparent Kd is defined as the concentration of the ligand producing 50% of the maximum fluorescence change.
(I) Raincloud plot where iSeroSnFR0.1 was used as the parent for a second round of screening followed by GLM analysis. A small library (32 possible combinations) was generated based on the GLM results and screened (cyan), which led to the discovery of iSeroSnFR0.2.
(J) Raincloud plot similar to (I), but using iSeroSnFR0.2 as the parent. This GLM-guided targeted library (96 possible combinations) was created and screened, leading to the discovery of iSeroSnFR.
See also Figures S1 and S2 and Data S3.1.

(xii) Step I: Computational Binding-Pocket Redesign

To perform computational modeling, we started with the structures of open, ligand-free iAChSnFR0.6 (6URU) and closed, choline-bound Bacillus subtilis OpuBC (3R6U), and created a model of the closed, ACh-bound form of iAChSnFR using Rosetta (Figure 3.1B). 5-HT conformers (rotation of the β-aminoethyl and hydroxy moieties) were generated using Open Eye Omega (Hawkins et al., 2010), and docked into the closed-iAChSnFR model using RosettaLigand (Bender et al., 2016; Davis and Baker, 2009) (Figures 1B and 1C). Next, Rosetta protein redesign (Taylor et al., 2016; Tinberg et al., 2013) was used to optimize the 5-HT binding pocket. In total, 250,000 variants were predicted and ranked based on computed ligand interaction (Methods). The top 18 predicted variants were synthesized, purified, and examined for fluorescence response to 5-HT and other ligands including ACh (Figures S2B and S2C). Among the 18 variants, variant 7 showed the largest fluorescence response to 10 mM 5-HT ($\Delta F/F0 = 87\% \pm 20\%$) with no ACh response ($\Delta F/F0 = -4\% \pm 1\%$), representing an 18-fold improvement in 5-HT selectivity (Figure S3.2C). This mutated variant, named iSeroSnFR0.0 (Table S3.2), was then selected for further optimization.

(xiii) Step II: Random Forest Modeling

We next optimized iSeroSnFR0.0 with SSM to improve 5-HT affinity. We used a random forest (RF) model to estimate the importance of each position interrogated by computational design (Table S3.2). We took the four highest-ranked positions from RF (66 > 170 > 143 > 188) (Figure 3.1D) and performed SSM at each site separately and in pairs (using degenerate NNK codons). We screened a total of 2,576 variants, including 92 from each single-site library and 368 from each dual-site library, for fluorescence response to 5-HT (10 mM). The library size was determined using the TopLib online library calculator (Nov, 2012). Of the screened variants, ~100 variants showed an improved response (~2- to 3-fold) compared to iSeroSnFR0.0 (Figure 3.1E). Subsequent analysis showed that top-performing variants frequently contained mutations at multiple positions, and the ordered contribution of each position (66 > 143 > 170 > 188) (Table S3.2) to the fluorescence response was nearly identical to that predicted by RF (66 > 170 > 143 > 188) (Figure 3.1F). No single mutation drastically improved 5-HT affinity, but combinations of mutations were frequently better than single mutations (Figure S3.2D). These results suggest that RF effectively predicts important positions contributing to sensor response, and simultaneous, beneficial contributions of multiple residues are essential to large-scale improvements.

(xiv) Step III: Generalized Linear Model

Because single mutations offered only small improvements, whereas combinations gave much better results, mutations were clearly not additive. For example, we found a top-performing variant containing T66Y/H170A with 140% improved response, whereas T66Y and H170A alone showed only 40% and 10% improvements,

respectively (Figure S3.2D). We next applied GLM to our dataset. This allowed us to identify individual mutations from our libraries that contribute to synergistic interactions—allowing us to design small targeted libraries.

GLM predicted that several amino acid mutations at each position would be beneficial (Figure 3.1F; Table S3), with 66Y, 66P, 143M, 170A, 188G, 188P, and 188T showing the strongest positive predictions. Given the beneficial T66Y/H170A mutant that we had already identified, we decided to synthesize variants combining those with GLM-predicted amino acid residues at positions 143 and 188. Out of 13 variants synthesized, 12 showed larger fluorescence response to 10 mM 5-HT than iSeroSnFR0.0 (Figure 3.1G) (GLM was moderately predictive: pseudo-R2 = 0.31). One variant displayed 4.5-fold improved response over iSeroSnFR0.0, well above any SSM-screened variant. In purified protein, this variant (T66Y/F143M/H170A/H188T, named iSeroSnFR0.1) showed >9-fold increased fluorescence response ($\Delta F/F0$)max relative to iSeroSnFR0.0 (($\Delta F/F0$)max = 480% ± 14% versus 50% ± 4%), and 2-fold increased 5-HT affinity (900 ± 110 µM versus 1.8 ± 0.5 mM) (Figure 3.1H).

In light of the substantial improvements from a single round of GLM-guided mutagenesis, we performed two more rounds of screening followed by GLM prediction, recruiting additional positions predicted by RF, and added others based on prior experience optimizing biosensors (e.g., linkers connecting the cpGFP to the binding protein, the interface between cpGFP and binding protein, and random mutations from previous rounds of screening) (Table S3.2). These subsequent rounds were screened at progressively lower 5-HT concentrations (round 2: 500 µM and round 3: 50 µM) to enrich

for variants with tighter affinity. After each round, the top-performing variants were sequenced and reanalyzed using GLM to create a focused library; in total, ~13,000 variants were tested, of which 244 were sequenced. The best variant from round 2 (Figure 3.1I) came from the GLM-driven focused library, had 8-fold improved response over its parent iSeroSnFR0.1, and was named iSeroSnFR0.2. The best variant from round 3 (Figure 3.1J) was 5-fold improved over its parent iSeroSnFR0.2 (Figure 3.2A; Table S3.2). We named this final version iSeroSnFR, which contains 19 mutations relative to iAChSnFR0.6 (Figure 3.2A, PDB: 6PER); In purified protein, this variant exhibits 310 ± 30 μM affinity for 5-HT, and 800% $(\Delta F/F0)max$ (Figure 3.2B).

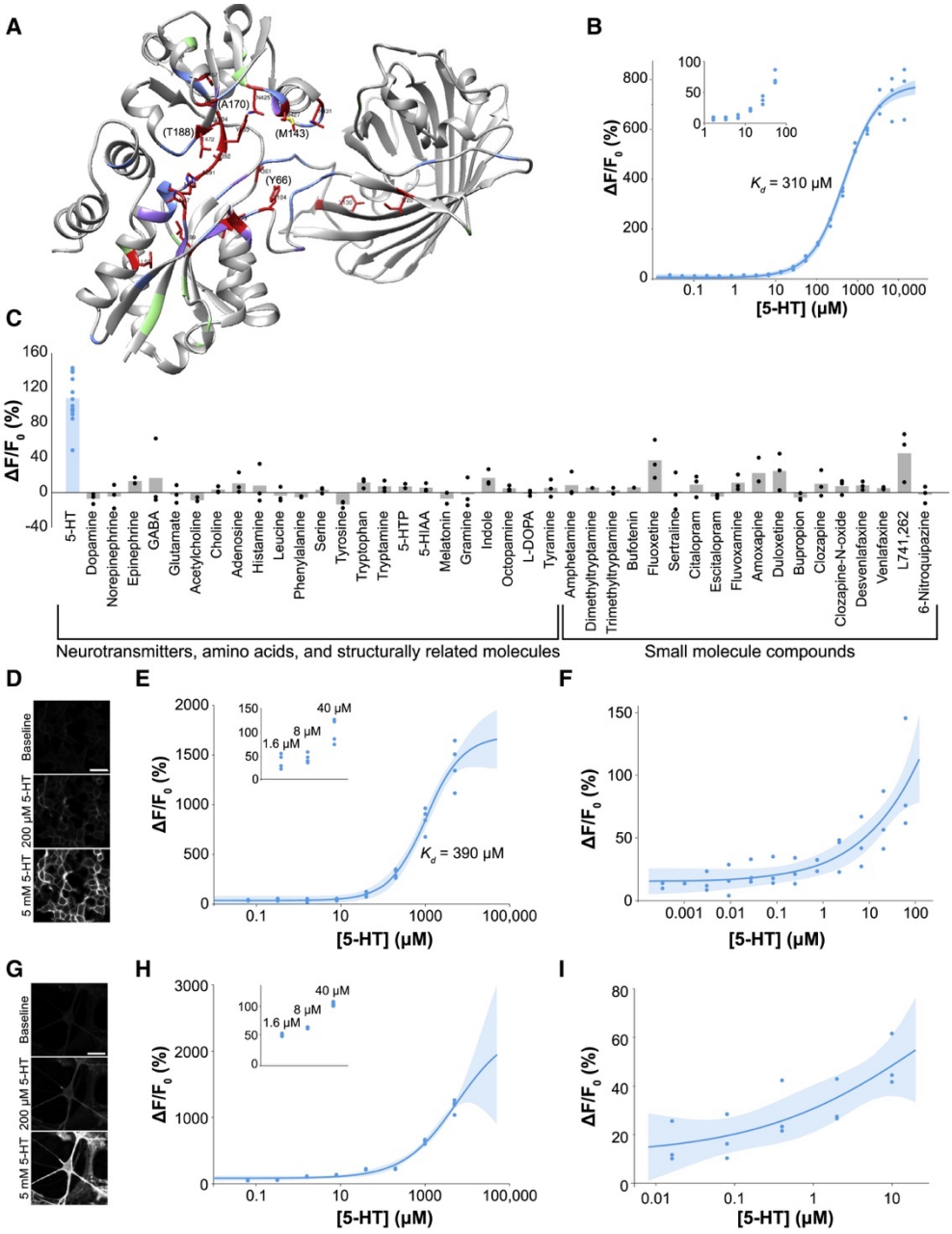

Figure 3.2. Affinity and Specificity of the Sensor.
(A) Crystal structure of unliganded iSeroSnFR (PDB: 6PER). Mutations in iSeroSnFR relative to iAChSnFR0.6 are mapped onto the crystal structure (red). Positions interrogated by site-saturated mutagenesis (but not mutated in iSeroSnFR) are displayed in blue, mutations interrogated by Rosetta, but not SSM, in purple, and positions that were randomly mutated, in green
(B) Purified iSeroSnFR binding to 5-HT.
(C) Purified iSeroSnFR binding to multiple ligands. Due to differential compound solubility, the values displayed match the following concentrations: octopamine, L-phenylalanine, 80 μM; 5-HTP, 85 μM; sertraline, 110 μM; L-DOPA, tyramine, escitalopram, citalopram, amoxapine, 125 μM; all other compounds were tested at either 100 or 105 μM. For the full concentration curve for each compound, see Figure S3.3.
(D–F) Response of membrane-displayed iSeroSnFR in HEK293T cells. Representative images (D), and dose-response curves for higher concentrations (E) and lower concentrations (F). n = 3–4.

(G–I) Response of membrane-displayed iSeroSnFR-PDGFR in cultured neurons. (G–I) Representative images (G), and dose-response curve for higher concentrations (H) and lower concentrations (I). n = 3–4. For raw traces, see Figure S4.
(B, E, F, H, and I) Fits were determined using the Hill euqation. Shaded area denotes 95% confidence interval. Scale bars represent 50 μm. Insets show magnifications of the points at low concentrations.

Our data show that GLM is highly effective at identifying beneficial mutations (Figures 1I and 1J): the average performance of GLM variants was significantly higher than SSM variants (1st, 2nd, and 3rd rounds: $p < 0.001$, Wilcoxon rank-sum test) and more importantly, the top variants in each round (including the top 15 variants from round 2) were from the GLM-inspired library as opposed to the SSM library. Thus, our machine-learning-guided mutagenesis pipeline can improve protein-ligand binding selectivity and affinity even for target molecules structurally distant from cognate ones, while still maintaining sensor function.

(xv) In Vitro Characterization

iSeroSnFR is highly specific for 5-HT over a wide array of endogenous molecules and drugs (Figures 3.2C and S3.3). Only tryptamine and dopamine showed detectable responses, but with 8- and 16-times weaker affinity (apparent Kd = 2.4 mM for tryptamine and 5.6 mM for dopamine), respectively. Other endogenous molecules showed marginal responses, with very low or negative responses, and/or titrations that did not fit a single-site binding isotherm.

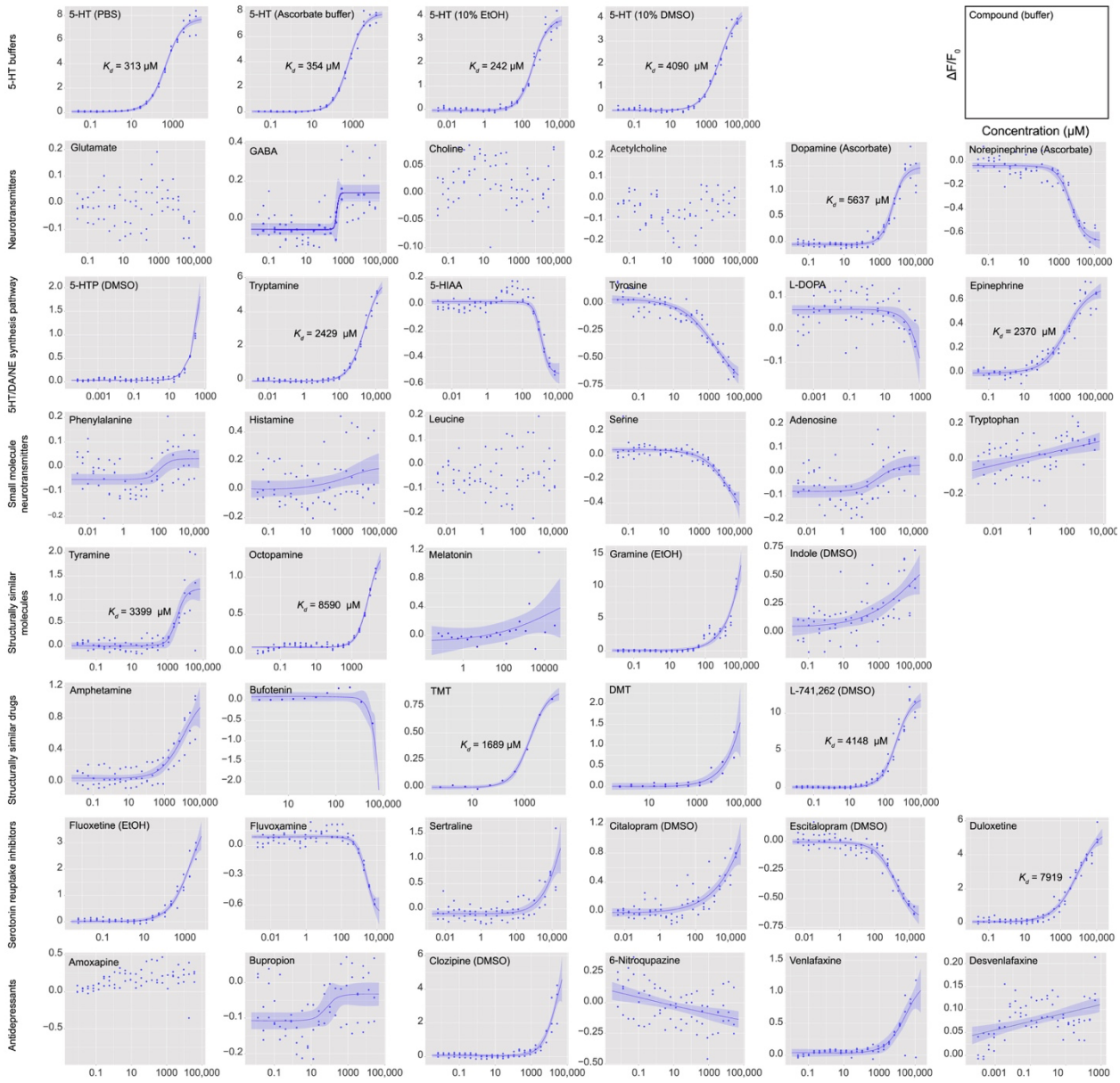

Figure S3.3. Specificity of iSeroSnFR, Related to Figure 3.2.
iSeroSnFR was purified and tested at 100 nM against multiple ligands as noted. Some ligands were tested in alternative buffers as noted. If no buffer is listed, the ligand was dissolved in PBS. Lines were fitted and Kd's were determined using the drc package in R. Shaded areas represent the 95% confidence interval. If no line is present, convergence failed, and no fit was calculated.

To determine the in-situ affinity in mammalian (HEK293T) cells, we cloned iSeroSnFR into the pMinDisplay expression vector (pDisplay lacking the HA epitope tag) (Marvin et al., 2013) such that iSeroSnFR would be displayed on the outer cell surface; we also cloned a version targeted to the post-synapse using full-length neuroligin (Nlgn)

(Methods). We observed robust membrane localization (Figure 3.2D) and clear response to 1.6 µM 5-HT (~50% ΔF/F0) (Figures 3.2E and S3.4A). The in situ affinity of the sensor on HEK293T cells was similar (390 ± 110 µM) to that in purified protein.

Fortuitously, the fluorescence response of iSeroSnFR on HEK293T cells was significantly increased ([ΔF/F0]max = 1,700%). To characterize the utility of iSeroSnFR for physiologically relevant concentrations, we focused on the range from high-pM (338 pM) to mid-µM (60 µM) (Figures 3.2F and S3.4B). We observed small but reliable responses to all concentrations tested (ΔF/F0 = 16.8% ± 1.9% at 338 pM; similar responses up to 246 nM 5-HT) (Figure S4B). We quantified the ability of iSeroSnFR to faithfully report 5-HT by comparing 5-HT responses to Hank's balanced salt solution (HBSS) buffer responses (Figure S4C) with two metrics from signal detection theory: the receiver operating characteristic (ROC) (Figure S4D) and the discriminability index (d′) (Figure S4E). ROC analysis indicates that 5-HT responses show essentially perfect discrimination (area under the curve = 0.990) (Figure S4D, bottom) of true-positives from false-positives, whereas buffer responses have no power (Figure S4D, top). Similarly, d′ analysis shows that 5-HT responses have very strong separation from system noise (d′ > 3) (Figure S4E, bottom), but buffer responses show essentially no separation (Figure S4E, top). Results on the surface of dissociated hippocampal neurons were similar to those on HEK293 cells (ΔF/F0 = 15.8% ± 2.0% at 16 nM 5-HT) (Figures 3.2G–3.2I and S3.4F).

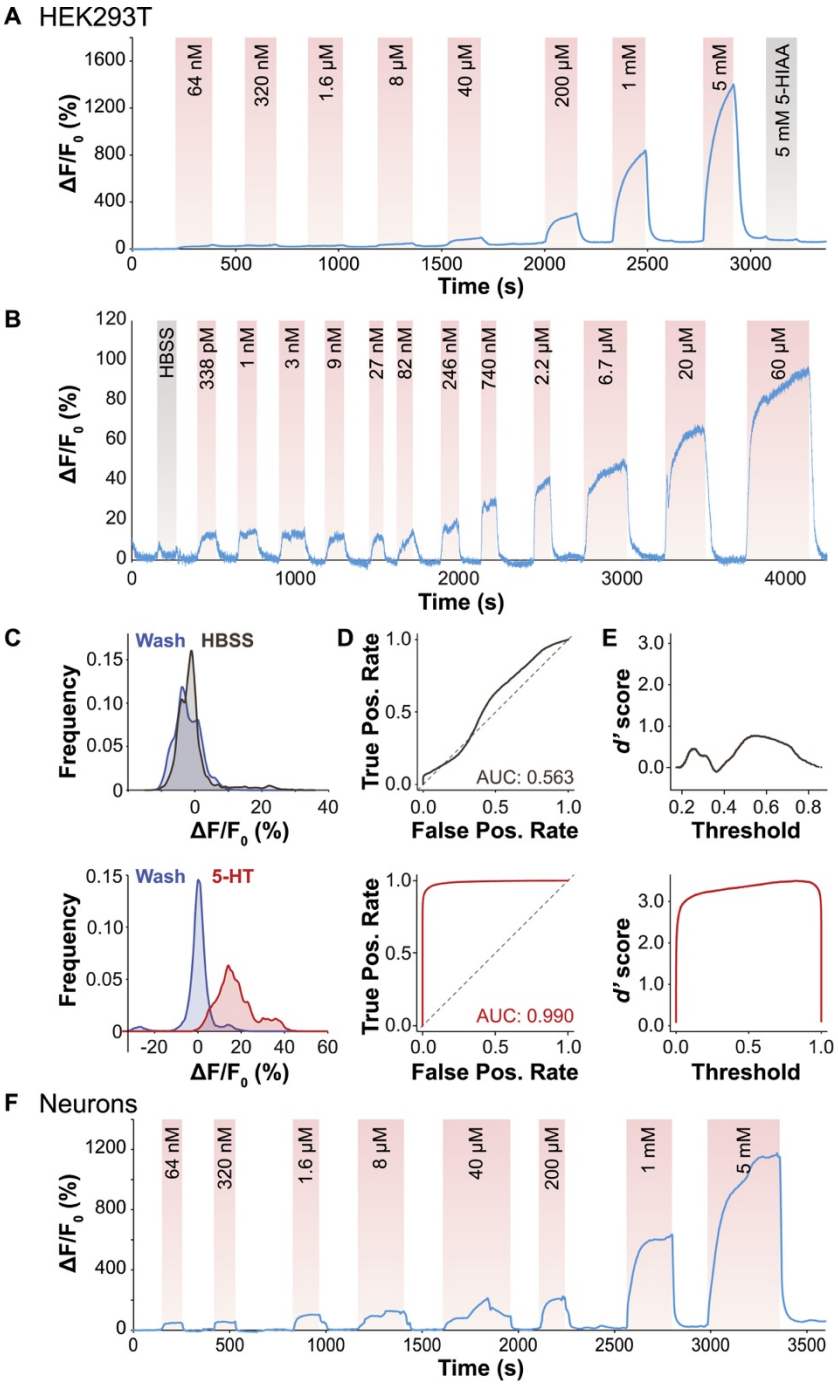

Figure S3.4. In Situ Titration, Related to Figure 3.2.
Representative traces from HEK293T cells (A,B) and primary cultured E18 rat hippocampal neurons (F) for which the images and dose response curves are displayed in Figures 2D–2F (HEK cells) and Figures 2G and 2H (neurons).
C-E. HBSS (top) and concentrations of 5-HT between 338 pM and 246 nM (bottom) were further analyzed for sensor sensitivity.
C. Distribution of responses is shown.
D. ROC analysis was performed where responses during the "wash" period were defined as a false positive, and responses during the "HBSS" or "5-HT" period were defined as a true positive.

E. A d' score was calculated based on the ROC analysis.
(A) and (F) were imaged at 1 Hz, (B) was imaged at 5 Hz. n = 3-4 dishes.

Discussion

Use of Machine Learning to Accelerate Directed Evolution

Our combined Rosetta and machine-learning-guided directed evolution approach was quite effective. After just one round of each, we screened fewer than 2,600 variants, but made dramatic improvements to the sensor's affinity, specificity, and fluorescence response. After just two more rounds of machine-learning-guided directed evolution, we had screened a total of ~16,000 variants, interrogated more than 60 different protein scaffold positions, and introduced 19 mutations into our final sensor, increasing its 5-HT affinity by >5,000-fold, abolishing choline/ACh binding, and increasing fluorescence response by 3-fold compared to the starting scaffold, iAChSnFR0.6. The efficacy of the design cycle diminished somewhat with each round. However, these results validate the rankings of the initial RF model, which predicted high impacts for the top 4 positions and progressively lower impacts for each successive position. Nonetheless, in each round, the best variant came from the GLM-predicted library; in rounds 1 and 2, these variants were nearly twice as good as the best-performing variant from the SSM library. Because RF uses an ensemble method, we could identify the most important features (protein positions) and provide guidance for subsequent stages. GLM is a good classifier even for small (<10,000) training datasets and is ideal for first-pass data analysis (Yang et al., 2019a). Our entire dataset was used for training (no test data), because our models were used only to guide one round of library design at a time.

Headroom remains in the iSeroSnFR scaffold, particularly for higher-affinity versions for better detection of sparse signaling events. It is likely that the machine-learning-guided approach detailed here can produce further gains, although each round thus far produced diminishing returns. A high-resolution structure of ligand-bound iSeroSnFR could reinvigorate this process, but we have been as yet unable to obtain such a structure. Alternatively, the addition of more biophysical parameters to the model, or more advanced ML models such as universal transformers (Dehghani et al., 2019), Bayesian optimization (Yang et al., 2019b), or neural networks (Kato et al., 2005), could extract sequence/function relationships that we missed. On a related note, it will be broadly useful for the field to somehow incorporate ML-gleaned insights back into the biophysical potential functions underlying structure-based computational protein design. Regardless, the method described here was highly effective for our purposes, and we expect that it can be used to engineer other PBP-based neuromodulator sensors, and more generally to tackle other challenging protein-engineering tasks.

Author Contributions

E.K.U., J.P.K., M.A., L.L.L., and L.T. conceived of and designed the study. E.K.U. designed the machine-learning method, screened and optimized sensors, and characterized them in purified protein, mammalian cells, cultured neurons, and brain slice, with significant contribution from C.D., D.A.J., and J.S. J.P.K., S.S., and G.R. designed OSTA and stopped-flow experiments, and J.P.K. performed them. M.A. and V.G. designed and performed in vivo fiber photometry and EEG/EMG recording in BLA and mPFC in fear learning and sleep/wake cycles. O.J.H., M.E.F., and T.L.K. designed and performed in vivo fiber photometry experiments in BLA, OFC, and BNST during

social interaction. R.L. and V.Y.-Y. designed and performed computational Rosetta modeling. Z.Y. and J.A.P. provided luciferase experimental data for establishing machine-learning methods. J.C. and D.T.L. provided significant insight for the machine-learning methods. J.S. characterized the sensor in acute slice using two-photon imaging. A.M. and V.A.A. designed and performed photometry imaging in acute slice. S.H. and A.J.F. performed crystallography. J.S.M., P.M.B., A.V.S., H.A.L., and L.L.L. provided iAChSnFR0.6 and performed preliminary experiments on serotonin binding. S.B. and L.D.L. synthesized caged serotonin. G.O.M. provided dissociated neuronal cultures. L.P.C. and D.E.O. produced chemical reagents. S.M.U. and S.G.A. provided SSRIs and guidance in cell-assay design. E.K.U., J.P.K., L.L.L., and L.T. wrote the manuscript with significant input from other authors.

Acknowledgments

We would like to thank Drs. Liqun Luo (Stanford University) and Jing Ren (MRC) for their critical reading and feedback. This work is based upon research conducted at the Northeastern Collaborative Access Team beamlines, which are funded by the National Institute of General Medical Sciences from the NIH (P30-GM124165). The Pilatus 6M detector on the 24-ID-C beamline is funded by an NIH-ORIP HEI grant (S10-RR029205). This research used resources of the Advanced Photon Source, a US Department of Energy (DOE) Office of Science User Facility operated for the DOE Office of Science by Argonne National Laboratory under contract DE-AC02-06CH11357. This work was supported by funding to L.T. (BRAIN Initiative U01NS090604, U01NS013522, and DP2MH107056 from NIH), to E.K.U. (Mistletoe Foundation Research Fellowship), and to G.O.M. (ARCS Scholarship), as well as by the Howard Hughes Medical Institute. V.G. is a Heritage

Principal Investigator supported by the Heritage Medical Research Institute, the NIH (BRAIN RF1MH117069), the Center for Molecular and Cellular Neuroscience of the Chen Institute, and the Beckman Institute for CLARITY, Optogenetics and Vector Engineering Research. V.A.A. is funded by Intramural Programs of NIAAA and NINDS ZIA-AA000421 and Innovation Award from NIH-DDIR. T.L.K. is funded by the NIH (R01AA019454, P60AA011605, and U24AA025475), and O.J.H. is funded by the NIH (5T32NS007431-20).

Method Details

Materials Availability

The following plasmids have been deposited in Addgene:

128483	pRSET-iSeroSnFR
128484	pMinDisplay-iSeroSnFR
128485	pAAV-CAG.iSeroSnFR-Nlgn
128486	pAAV-CAG.FLEx.iSeroSnFR-PDGFR
128941	pMinDisplay-iSeroSnFR-EnhancedExport
129180	pAAV-CAG.FLEx.iSeroSnFR-PDGFR-EnhancedExport

AAV viruses are available through the Canadian Neurophotonics Centre.

Data And Code Availability

The full sequence of iSeroSnFR, and has been deposited in GenBank:MN083270. The crystal structure has been deposited in the Protein Data Bank:6PER). Code has been provided directly in this STAR Methods section. Code updates will be provided at https://github.com/ekunger/iSeroSnFR.

Experimental Model And Subject Details

The experimental procedures performed on animals followed the guidelines of the Animal Care and Use Committees at the University of California Davis, the California Institute of Technology, the University of North Carolina, Chapel Hill, and the National Institute on Drug Abuse. Mice and rats were housed in a barrier facility with a 12:12 hr light:dark cycle, and food and water were available ad libitum. Animals were group housed by sex wherever possible. RosaAi14/Ai14 (Madisen et al., 2010) mice were maintained as homozygous breeding pairs or crossed to wild-type C57BL/6J (Jax # 000664). SERTCre/+ (Zhuang et al., 2005) mice were bred as male SERTCre/+ x female wild-type C57BL/6J (Jax # 000664) as recommended by the depositing lab. Both male and

female animals were used in experiments and were between the age of 2 and 9 months. For in vivo mouse experiments, SERT-Cre (Zhuang et al., 2005; (Gong et al., 2003)) were crossed to wild-type C57BL/6J (Jax # 000664). Both wild-type mice and mice heterozygous for the Cre transgene were used for experiments. Following surgery, subjects were singly housed for at least five days in a residence room for full recovery before animals were moved to a behavioral room. Animals were habituated to the new light/dark cycle and behavioral room for at least 2 weeks before experiments were started. Rats were ordered as timed-pregnant females and sacrificed shortly after arrival in the facility.

Methods specific to luciferase

Development of a machine learning-guided library design paradigm

Before pursuing the ambitious goal of drastically shifting the specificity of a choline-binding protein to 5-HT, we first established our machine learning approach on a more modestly modified ligand/binding pocket pair. We selected firefly luciferase, an enzyme that has been engineered for multicomponent imaging (Jones et al., 2017). We synthesized a brominated analog (4'Br-Luc) of the cognate substrate -luciferin (-Luc) and mutated the enzyme active site to accommodate the substitution (Figure S1A).

We first chose random forest (RF) (Liaw and Wiener, 2002) because it is tolerant of missing data points and capable of extracting information from relatively small training datasets, which are a practicality of most protein mutagenesis studies. Importantly, a strength of RF is "feature importance" detection, giving us the ability to prioritize protein positions for SSM (Figure 1A). Second, we chose generalized linear modeling (GLM, Gaussian regression) (Dobson et al., 2008) because it is a better classifier, while still tolerating small training datasets, and its linear nature provides precise, interpretable predictions about the effects of individual mutations that we could easily translate into new variants and combinations thereof (Figure 1A).

To build the models, we used sequence information from 222 published and unpublished luciferase variants as our input variables, and the experimentally determined preference for -Luc versus 4'Br-Luc as the output variable. Each position within the protein was an independent variable with a categorical distribution (amino acid), and the preference for -Luc versus 4'Br-Luc (fold-preference as calculated by the

amplitude of photon output in the presence of -Luc versus 4'Br-Luc) was our target with a continuous numerical distribution. We then compared the importance of each position using the RF model, and the contribution of each mutation using the GLM (identity link), followed by experimental validation of these predictions. We found that RF was effective at predicting positions, and GLM made correct predictions, but only at positions highly ranked by RF. We therefore decided that for future sensor design, we would use the two models in a sequential fashion: first we would use the RF to rank the positions for SSM, and then we would analyze the results of our SSM libraries with the GLM to identify the best individual mutations at each position.

The top residues predicted by the RF model were positions 218, 347, 316 and 247, which were frequently mutated to accommodate other 4'-substituted analogs in a previous screen (Jones et al., 2017). The GLM predicted S347G, L342A, S347A, Y255N, R218A, F247Y, and G316S as the top mutations. To experimentally validate these predictions, we created a small library covering both high-ranked and lowranked positions predicted by RF, all of which had very statistically significant GLM predictions of improved 4'Br–Luc specificity. We tested 276 variants from this library for their photon output with D-Luc and 4'Br–Luc and sequenced the top 10% favoring 4'Br–Luc (~1000x increased binding compared to the starting variant), as well as the bottom 10% favoring D-Luc. The number of mutations per variant was not significantly different between the two populations, indicating a similar overall mutation rate. However, the incidence of specific mutations was different between the two populations, and when compared to the input data. For example, at position 347, which was highly ranked by both RF and

GLM, the incidence of the glycine mutation compared to the native serine was 26:1 (G:S) in the top 10% of variants but 5:19 in the bottom ones. Conversely, at position 342, which was not ranked highly by RF, a leucine-to-alanine mutation was predicted by the GLM to heavily bias the preference toward 4'Br–Luc. This mutation appeared more frequently in the bottom variants (L:A, 18:9 – top 10% versus 3:21 – bottom 10%), demonstrating a correct prediction by the RF model, and an incorrect prediction for the GLM. In general, the RF more linearly predicted the preference (pseudo-R2 = 0.45), than GLM (pseudo-R2 = 0.10) (Figure S3.1)

Construction of luciferase library and mutants

DNA inserts for the luciferase shuffle library and point mutants were generated as described by Jones et al. (2017). Two sections of the luciferase gene (pgl4-luc2), denoted R1 and R2, were targeted for gene assembly. The R1 region comprises amino acids 199-275 and was assembled with primers R1-F0 to R1-F235 (forward primers, Table M1) and R1-R0 to R1-R119 (reverse primers). The R2 region comprises amino acids 275-347 and was assembled with primers R2-F0 to R2-F264 (forward, Table M2) and R2-R0 to R2-R228 (reverse). The gene assembly primers were designed using gene2oligo (Rouillard et al., 2004) to identify desirable Tm values. To assemble the genes encoding point mutants, primers containing the codon(s) of interest were used in place of the primers coding for the wild-type sequence. For the shuffle library inserts, mutagenic primers were mixed with wild-type primers in a 1:1 molar ratio. Libraries were assembled as described by Bessette et al. (2003). All PCR reactions were performed using Q5 High-Fidelity DNA polymerase.

Library DNA was inserted into linearized template vector pET28-R1del-mRFP as described by Rathbun et al. (2017). Library inserts were assembled with the linearized pET vectors using Gibson assembly (Gibson et al., 2009). Gibson assembly master mixes were prepared following the Prather recipe on https://www.openwetware.org/wiki/Gibson_Assembly, with all materials purchased from New England BioLabs. For each assembly, 50 ng of DpnI digested, linearized vector was combined with insert (5:1 insert:vector ratio) and added to 10 mL of master mix. The mixtures were incubated at 50°C for 60 min, then 2 mL was transformed into chemically competent cells (TOP10 E. coli, Thermo-Fisher). Transformants were plated on square, agar plates containing kanamycin. Cells were plated to exceed 3X the library size. Cells were scrapped of the plates, combined, and pelleted. DNA was isolated using ZymoPURE Plasmid Miniprep Kit and saved for screening.

Primer lists

All primers were purchased from Integrated DNA Technologies, Inc. (San Diego, CA) and are written in the 5′→3′ direction. Upper case letters denote bases coding for the luciferase gene. Lower case letters denote bases added to ensure similar melting temperatures (Tm) for all primers. Bases highlighted in red denote sites targeted for mutagenesis.

Forward Primers	
R1-F0	GGATCCACCGGATTGCCCAAGGGCGTAGCCCTACC
R1-F35	GCACCGCACCGCTTGTGTCCGATTCAGTCATGCCC
R1-F70	GCGACCCCATCTTCGGCAACCAGATCATCCCCGACA
R1-F106	CCGCTATCCTCAGCGTGGTGCCATTTCACCACGGC
R1-F141	TTCGGCATGTTCACCACGCTGGGCTACTTGATCTGCG
R1-F178	GCTTTCGGGTCGTGCTCATGTACCGCTTCGAGGAG
R1-F213	GAGCTATTCTTGCGAAGCTTcggccctgtacagtcgctg
R1-F235	cagcgactgtacagggc
Reverse Primers	
R1-R0	GGGCAATCCGGTGGATCC
R1-R18	ACAAGCGGTGCGGTGCGGTAGGGCTACGCCCTT
R1-R51	GCCGAAGATGGGGTCGCGGGCATGACTGAATCGGAC
R1-R87	CCACGCTGAGGATAGCGGTGTCGGGGATGATCTGGTT
R1-R124	CGTGGTGAACATGCCGAAGCCGTGGTGAAATGGCA
R1-R159	AGCACGACCCGAAAGCCGCAGATCAAGTAGCCCAG
R1-R194	cgAAGCTTCGCAAGAATAGCTCCTCCTCGAAGCGGTACATG

Region 1 (R1, wild-type luc2 primers). Lower case letters denote non-luciferase sequences included for maintaining proper Tm and do not appear in the final assembled gene.

Forward Primers	
R2-F0	acacatCGAGGAGGAGCTATTCTTGCGAAGCTTGCA
R2-F36	AGACTATAAGATTCAATCTGCCCTGCTGGTGCCCACAC
R2-F74	TATTTAGCTTCTTCGCTAAGAGCACTCTCATCGACAAGTACGAC
R2-F117	CTAAGCAACTTGCACGAGATCGCCAGCGGCGGG
R2-F150	GCGCCGCTCAGCAAGGAGGTAGGTGAGGCC
R2-F181	GTGGCCAAACGCTTCCACCTACCAGGCATCCG
R2-F213	CCAGGGCTACGGCCTGACAGAAACAACTAGTGCCA
R2-F248	TTCTGATCACCCCCgtcgcctccggaggaga
R2-F264	tctcctccggaggcg
Reverse Primers	
R2-R0	TAGCTCCTCCTCGatgtgt
R2-R19	GGGCAGATTGAATCTTATAGTCTTGCAAGCTTCGCAAGAA
R2-R59	GCTCTTAGCGAAGAAGCTAAATAGTGTGGGCACCAGCA
R2-R97	TCGTGCAAGTTGCTTAGGTCGTACTTGTCGATGAGAGT
R2-R135	TTGCTGAGCGGCGCCCCGCCGCTGGCGATC
R2-R165	GGAAGCGTTTGGCCACGGCCTCACCTACCTCC
R2-R197	AGGCCGTAGCCCTGGCGGATGCCTGGTAGGT
R2-R228	acGGGGGTGATCAGAATGGCACTAGTTGTTTCTGTC

Region 2 (R2, wild-type luc2 primers). Lower case letters denote non-luciferase sequences included for maintaining proper Tm and do not appear in the final assembled gene.

Forward Primers	
R1-F35_A	GCACCGCACCGCTTGTGTCGCCTTCAGTCATGCCC
R1-F141_Y	TACGGCATGTTCACCACGCTGGGCTACTTGATCTGCG
R1-F141_N	TTCGGCATGTTCACCACGCTGGGCAATTTGATCTGCG
R1-F141_Y+N	TACGGCATGTTCACCACGCTGGGCAATTTGATCTGCG
R2-F117_S	CTAAGCAACTTGCACGAGATCGCCAGCGGCTCT
R2-F213_A	CCAGGGCTACGGCGCCACAGAAACAACTAGTGCCA
R2-F213_G	CCAGGGCTACGGCCTGACAGAAACAACTGGGGCCA
R2-F213_A+G	CCAGGGCTACGGCGCCACAGAAACAACTGGGGCCA
Reverse Primers	
R1-R51_A	GCCGAAGATGGGGTCGCGGGCATGACTGAAGGCGAC
R1-R124_Y	CGTGGTGAACATGCCGTAGCCGTGGTGAAATGGCA
R1-R159_N	AGCACGACCCGAAAGCCGCAGATCAAATTGCCCAG
R2-R135_S	TTGCTGAGCGGCGCAGAGCCGCTGGCGATC
R2-R197_A	GCGCCGTAGCCCTGGCGGATGCCTGGTAGGT
R2-R228_G	acGGGGGTGATCAGAATGGCACTAGTTGTTTCTGTG

Primers used to construct luciferase point mutants and shuffle library. The bases highlighted in red denote sites targeted for mutagenesis.

R1 insert amplifaction primers	
R1-insert-Fwd	GACAAAACCATCGCCCTGATCATGAACAGTAGT GGATCCACCGGATTGCCCAA
R1-insert-Rev	CACCAGCAGGGCAGATTGAATCTTATAGTCTTGCAAGCTTCGCAAGA ATAGCTCCTCCTC
R2 insert amplifaction primers	
R2-insert-Fwd	CGAGGAGGAGCTATTCTTGCG
R2-insert-Rev	CTTCGGGGGTGATCAGAAT
Vector amplifcation primers	
R1-vector-Rev	GCAAGACTATAAGATTCAATCTGCCCTGCTGGTG
R2-vector-Fwd	ATTCTGATCACCCCCGAAG

Primers used to amplify inserts for the R1 or R2 regions, along with the pET vector backbone.

General bioluminescence imaging protocol

All analyses were performed with bacterial cell lysates in black 96-well plates (Greiner Bio One). Plates containing luminescent reagents were imaged in a light-proof chamber with an IVIS Lumina (Xenogen) CCD camera chilled to −90°C. The stage was kept at 37°C during the imaging session, and the camera was controlled using Living Image software. Exposure times were set to 60 s, and data binning levels were set to medium. Regions of interests were selected for quantification, and total flux values were

analyzed using Living Image software. All data were exported to Microsoft Excel for further analyses.

Lysate screening of combination library

The shuffle library was screened following the protocol previously described in Jones et al. (2017), with modifications. Library DNA was transformed into chemically competent BL21-DE3 E. coli cells. Transformants were plated on square, agar plates containing kanamycin. Colonies were picked and expanded in LB-Kan media in a 96-well deep well plate (500 mL/well). The plate was incubated at 37°C overnight. An aliquot of the overnight culture (4 mL) was used to inoculate 400 mL of auto-induction LB media (Studier, 2005), and the cells were incubated at 30°C with shaking (200 rpm) for 24 h. The remaining starter cultures were stored at 4°C and used for subsequent plasmid recovery and sequencing analysis. The cells were pelleted and lysed in lysis buffer (600 mL). Cell lysate (90 mL) was added to 96-well black plates, followed by 10X luciferin and ATP solution (10 mL, 100 mM luciferin and 1 mM ATP final concentration) in phosphate buffer (250 mM phosphate buffer, pH = 7.8). The plate was then imaged as described above.

Methods specific to iSeroSnFR

Rosetta Modeling

Rotamers for 5-HT were generated with OMEGA from OpenEye Scientific. The closed conformation PDB structure of Thermoanaerobacter spX513 OpuBC was combined with the open structure of iAChSnFR0.4 (provided by PMB). We used rosetta_script in Rosetta 3 (2015.19.57819) for docking with protein-ligand interface design instructed by design.xml (below). Residues within 6Å of the ligand, as well as

those within 8Å and facing toward the ligand, were mutated. Residues within 10Å, as well as those within 12Å and facing the ligand, were repacked. We restricted aromatic residues (Trp, His, Tyr, and Phe) to only be mutated into other aromatic residues. We designed 48,000 models and filtered them with total_score for the top 5% and then picked the top 10 models according to the interface_delta_X score. These 10 models were further re-designed with a protocol to couple protein side-chain and backbone flexibility from the Kortemme lab (Ollikainen et al., 2015). Shape complementarity scores for the top redesigns were calculated with Sc routine in CCP4. Top designs were chosen for synthesis and characterization.

Cloning

The bacterial expression vector pRSET-A was used for library screening, which contains a His6-tag for purification. The mammalian expression vector pMinDisplay, which contains a myc-tag, an IgK-leader secretion tag, a Kozak sequence, and a PDGFR transmembrane domain for tethering to the membrane, was used for transfection into HEK293 cells. The viral expression vector pAAV was used for infection of HEK293 cells, primary neurons, mouse brain slices, and in vivo fiber photometry. All vectors were cloned with a combination of QuikChange, circular polymerase extension cloning (Quan and Tian, 2011), overlap extension cloning (Bryksin and Matsumura, 2010), digestion/ligation, or Kunkel mutagenesis (Kunkel, 1985). Due to issues arising from double-stranded break repair machinery in the bacteria, which drastically reduced the cloning efficiency into FLEx backbones, sequences inserted into pAAV containing FLEx

sites were first subcloned into a custom shuttle vector, then cut with SacI and HindIII and ligated into a matching custom pAAV.

Library generation

Libraries were constructed by Kunkel mutagenesis (Kunkel, 1985). Single stranded dU-DNA was generated by transforming the plasmid to CJ236 cells and infecting with M13K07 bacteriophage. Chloramphenicol was used initially to ensure an F-pilus+ host; ampicillin was used to ensure the presence of the plasmid, and kanamycin was used to ensure bacteriophage infection. Single stranded dU-DNA was harvested using a kit according to the manufacturer's instructions. Phosphorylated primers were designed in the reverse direction with either a specific mutation or a degenerate codon (NNK), and at least 10 bp on either side of the mutation. An additional primer was included in each reaction to destroy a cut site (either NheI or XbaI) in order to allow easy enrichment for mutated sequences (Huang et al., 2012). Primers were annealed to the sequence by raising the temp to 95°C and lowering it slowly to 25°C (2°/min) using a thermocycler. Gaps were filled in and ligated using T7 polymerase and T4 ligase. DNA was transformed to Top10 cells and grown at 37°C overnight. DNA was extracted using a miniprep kit according to the manufacturer's instructions, and digested with either NheI or XbaI. DNA was purified using a PCR cleanup kit according to the manufacturer's instructions.

Library screening

Library size was determined using the TopLib online library calculator (Nov, 2012). DNA libraries were transformed to BL21(DE3) cells, plated on LB-agar with ampicillin, and allowed to grow at 37°C overnight. Colonies were picked at random into 2.3 mL

deep-well 96-well plates and grown in 1 mL of autoinduction medium (2xYT + 0.5% glycerol, 0.5% glucose, 0.2% α-lactose, 25 mM Na2HPO4, 25 mM KH2PO4, 50 mM NH4Cl, 5 mM Na2SO4, 20 mM MgSO4) for 8 h at 37°C, then for 24-36 h at 18°C, shaking at 250-300 rpm. 4 wells of each plate were designated for the parent protein, which was transformed and plated at the same time as the libraries. At the end of the growth period, 50 µL was removed and stored at −80°C in 25% glycerol for subsequent DNA recovery. Cultures were then pelleted by centrifugation and washed 3x with PBS. Pellets were dried briefly, then frozen at −80°C for 15 mins, and thawed. Pellets were resuspended in 100 µL of B-PER Complete reagent and incubated shaking at 30°C for 1 h. Cell debris was pelleted by centrifugation and the supernatant was transferred to a clean plate. 96-well plates were expanded into optically clear 384-well plates containing 45 µL PBS and 4 µL lysate, then read on a fluorescent plate reader. Following the initial read, 5-HT was prepared fresh and 1 µL was added to experimental wells, and 1 µL of PBS was added to control wells, and the plate was read again. The performance of each variant was calculated as the difference between the first and second read, divided by the first read, and normalized to the PBS well, then compared to the parent wells. Any variant showing considerable improvement over the parent was subsequently retested at multiple concentrations, then regrown from the glycerol stock, DNA extracted by miniprep, and sequenced.

Protein purification

Plasmids were regrown from glycerol stock or transformed to LOBSTR-BL21(DE3) cells. For small yields, cells were grown in 5 mL of autoinduction medium at 37°C for 8 h, then 18°C for 24-36 h, shaking at 250-300 rpm. Then cultures were pelleted by centrifugation and the supernatant removed. Pellets were subjected to 3 rounds of freeze-thaw, first at −80°C, followed by 37°C waterbath. Then pellets were resuspended in 500 µL of B-PER Complete and incubated at 30°C for 1 h, shaking at 250-300 rpm. Cell debris was pelleted by centrifugation and supernatant was transferred to a 96-well deep-well plate. Protein was purified using the His-tag with prepacked NiNTA tips (IMAC20) connected to an electronic multichannel with a preset protein purification protocol. Briefly, NiNTA beads were washed with 10 mM imidazole, then the lysate was bound to the NiNTA beads, and washed 8X with 25 mM imidazole, then eluted with 250 mM imidazole.

For large yields, plasmids were first grown in 5 mL of autoinduction medium at 37°C, then expanded to 100 mL and grown at 18°C for 36-48 h, shaking at 250-300 rpm. Then cultures were pelleted by successive rounds of centrifugation followed by supernatant removal. Pellets were subjected to 3 rounds of freeze-thaw cycles as above, then resuspended in 10 mL of B-PER Complete and incubated at 30°C for 1 h, shaking at 250-300 rpm. Then NiNTA beads were washed with 10 mM imidazole in PBS and incubated with the lysate in 10 mM imidazole on a rotator at 4°C for 18 h. Beads were then washed with 25 mM imidazole in PBS 6 times (600-1000 mL total wash volume), then eluted with 250 mM imidazole in PBS. Protein was then dialyzed in 1X PBS

(specificity and affinity assays) or 0.1X TBS (crystallization), and subsequently concentrated using concentrator columns (10 kDa MWCO).

Specificity screening

Purified protein was measured by nanodrop, and diluted with 1X PBS to reach a final concentration of 100 nM. 40 µL was added to a 384-well plate, and read on a fluorescent plate reader. Small molecule neurotransmitters, drugs and other compounds were dissolved in either 1X PBS, ascorbate buffer (to reduce oxidation: Na-(L) Ascorbate 137 mM, KCl 5.3 mM, CaCl2 952 µM, MgSO47H2O 833 µM, MgCl26H2O 1 mM, Na2PO42H2O 423 µM, KH2PO4 345 µM, glucose 5.6 mM, NaHCO3 4.2 mM), 10% ethanol, or 10% DMSO. pH was carefully maintained at 7.4 for all experiments. Then 10 µL of either vehicle or compound was added to the protein and read again on the plate reader. Due to maximum solubility issues, not all compounds were tested at the same concentration.

Table S3.1: Additional information related to figure 3.1.

Position	Native Amino Acid	Frequency	Random Forest Ranking	Mutation	Frequency	Estimate (log(D-luc/4'Br)	Standard Error	t value	Pr(>|t|)	Significance
211	P	196	18.67	A	7	0.30839	0.18982	1.625	0.10762	
				S	6	-0.0713	0.23635	-0.302	0.76367	
				T	2	0.08635	0.27811	0.31	0.75689	
214	T	208	10.42	A	2	0.22054	0.25565	0.863	0.39053	
				S	1	0.31082	0.31859	0.976	0.33179	
218	R	181	97.4	A	2	-0.6817	0.23314	-2.924	0.00434	**
				H	5	-0.1292	0.31859	-0.405	0.68605	
				K	23	0.66895	0.09273	7.214	1.43E-10	***
220	S	198	19.33	N	13	0.16193	0.33322	0.486	0.62813	
226	I	209	-3.28	V	2	-0.4745	0.73781	-0.643	0.52173	
227	F	198	0.35	C	1	-0.2112	0.31843	-0.663	0.5089	
				W	4	-0.0487	0.28951	-0.168	0.86683	
				Y	8	0.07492	0.13087	0.572	0.5684	
229	N	190	15.7	T	21	-0.2349	0.18888	-1.244	0.21673	
232	I	210	0	T	1	0.17555	0.32366	0.542	0.58883	
237	I	200	-4.78	V	11	0.05426	0.15272	0.355	0.72317	
239	S	196	-2.99	I	1	0.55528	0.46132	1.204	0.23177	
				T	13	0.30491	0.20534	1.485	0.14096	
				V	1	-0.3416	0.39311	-0.869	0.38714	
240	V	194	22.89	A	9	0.27524	0.17373	1.584	0.11652	
				G	1	0.23078	0.3638	0.634	0.52741	
				I	3	-0.0028	0.25232	-0.011	0.99113	
				L	2	0.62078	0.3638	1.706	0.09128	.
				M	2	0.11961	0.29372	0.407	0.68477	
241	V	198	8.13	A	9	0.00528	0.18827	0.028	0.97767	
				F	1	-0.9705	0.48142	-2.016	0.0467	*
				L	1	NA	NA	NA	NA	
				M	2	-0.4318	0.29795	-1.449	0.15067	
243	F	201	15.33	L	1	-0.0997	0.39904	-0.25	0.80329	
				M	9	-0.0694	0.13886	-0.5	0.61837	
246	G	192	9.84	A	19	-0.4631	0.24468	-1.893	0.06151	.
247	F	195	63.21	L	4	-0.2604	0.24334	-1.07	0.28725	
				S	1	NA	NA	NA	NA	
				Y	11	-0.5138	0.18159	-2.83	0.00571	**
249	M	150	35.41	F	9	0.19395	0.2297	0.844	0.40065	
				I	6	0.44579	0.27541	1.619	0.10892	
				L	46	0.03409	0.08591	0.397	0.69239	
250	F	178	23.77	A	4	-0.2625	0.2519	-1.042	0.30012	
				C	6	0.25221	0.19822	1.272	0.20641	
				G	1	0.57044	0.46814	1.219	0.22611	
				H	2	-0.5907	0.23678	-2.495	0.01437	*
				M	6	-0.2362	0.1506	-1.568	0.12021	
				S	2	0.72441	0.30415	2.382	0.01927	*
				T	7	-0.08	0.19599	-0.408	0.68395	
				V	1	0.15515	0.4816	0.322	0.74807	
				Y	4	-0.1121	0.16827	-0.666	0.5068	
251	T	210	0	I	1	NA	NA	NA	NA	
252	T	208	-4.28	S	3	-0.0501	0.54804	-0.091	0.92729	
255	Y	175	39.24	F	21	-0.4338	0.19608	-2.212	0.02938	*
				H	12	-0.4664	0.17548	-2.658	0.00926	**
				I	1	-0.7957	0.67763	-1.174	0.24332	
				N	2	-0.8542	0.31773	-2.688	0.00851	**
256	L	196	5.34	I	7	-0.2893	0.24769	-1.168	0.24579	
				M	6	-0.0489	0.21685	-0.225	0.82224	
				V	2	-0.1631	0.47519	-0.343	0.73221	
257	I	159	30.32	A	1	-0.5082	0.31734	-1.602	0.11266	
				C	3	-0.0694	0.38171	-0.182	0.85618	
				F	5	0.38618	0.28158	1.371	0.17353	
				L	14	0.06181	0.20057	0.308	0.75864	
				M	13	0.12343	0.17659	0.699	0.48633	
				R	3	0.27062	0.22695	1.192	0.23612	
				S	3	-0.0553	0.23705	-0.233	0.81617	
				V	8	0.42431	0.23297	1.821	0.07178	.
				Y	2	0.75755	0.40014	1.893	0.06144	.

Position	Native Amino Acid	Frequency	Random Forest Ranking	Mutation	Frequency	Estimate (log(D-luc/4'Br)	Standard Error	t value	Pr(>|t|)	Significance
260	F	207	9.51	G	1	-0.1392	0.31859	-0.437	0.66321	
				I	1	-0.2192	0.31859	-0.688	0.49317	
				N	1	-0.2792	0.31859	-0.876	0.38311	
				Y	1	0.10082	0.31859	0.316	0.75238	
264	L	189	31.8	F	1	-0.2897	0.37298	-0.777	0.43932	
				M	13	-0.3601	0.21138	-1.704	0.09179	.
				V	8	0.00896	0.2792	0.032	0.97448	
265	M	210	0	T	1	-0.8745	0.73781	-1.185	0.23893	
266	Y	209	2.65	H	2	-0.0988	0.87985	-0.112	0.91087	
267	L	210	0	F	1	0.05555	0.32366	0.172	0.86409	
269	E	209	2.47	G	2	-0.0795	0.25565	-0.311	0.75664	
279	D	210	0	N	1	0.7202	0.7657	0.941	0.34936	
281	K	210	0	E	1	-0.064	0.7331	-0.087	0.93062	
282	I	209	-5.28	T	1	NA	NA	NA	NA	
				V	1	0.08489	0.49072	0.173	0.86304	
283	Q	210	0	R	1	0.17555	0.32366	0.542	0.58883	
284	S	208	-2.78	V	3	0.08257	0.21939	0.376	0.70749	
286	L	196	24.55	I	2	-0.9751	0.48336	-2.017	0.04654	*
				M	4	-0.281	0.20038	-1.402	0.16411	
				V	9	0.55493	0.31594	1.756	0.08231	.
287	L	196	17.08	A	1	0.43402	0.46005	0.943	0.34791	
				I	1	-0.6259	0.42133	-1.486	0.14079	
				M	4	-0.2324	0.24791	-0.938	0.35089	
				V	9	0.36644	0.20177	1.816	0.07257	.
288	V	188	20.36	A	4	0.10941	0.42788	0.256	0.79875	
				F	2	0.78822	0.285	2.766	0.00685	**
				G	1	-0.2254	0.65275	-0.345	0.73062	
				I	1	0.65384	0.7185	0.91	0.36517	
				L	8	0.05214	0.23996	0.217	0.82845	
				M	6	-0.2228	0.32173	-0.693	0.49029	
				N	1	0.86248	0.63283	1.363	0.17621	
290	T	210	0	A	1	0.00446	0.50387	0.009	0.99295	
293	S	210	0	N	1	0.19511	0.85279	0.229	0.81953	
294	F	208	-2.12	L	1	-0.0444	0.32366	-0.137	0.89107	
				S	2	0.06635	0.38763	0.171	0.86446	
295	F	203	-11.5	L	8	0.23481	0.66098	0.355	0.72321	
301	I	210	0	T	1	NA	NA	NA	NA	
305	D	210	0	E	1	NA	NA	NA	NA	
310	H	209	6.41	R	2	0.10082	0.31859	0.316	0.75238	
311	E	197	22.44	C	14	0.16082	0.31859	0.505	0.61491	
312	I	209	0.37	V	2	-0.0492	0.31859	-0.154	0.87764	
313	A	197	22.27	G	14	NA	NA	NA	NA	
314	S	88	43.43	A	2	0.24328	0.23923	1.017	0.31181	
				C	51	-0.021	0.10384	-0.202	0.84049	
				T	58	-0.0921	0.10553	-0.873	0.38493	
				V	12	0.12736	0.14241	0.894	0.37344	
315	G	209	3.81	H	1	-0.3713	0.39338	-0.944	0.3477	
				T	1	-0.2377	0.48899	-0.486	0.62805	
316	G	127	68.74	A	13	-0.3285	0.12704	-2.586	0.01126	*
				R	1	NA	NA	NA	NA	
				S	28	-0.5065	0.08789	-5.763	1.07E-07	***
				T	42	-0.1567	0.09474	-1.654	0.10148	
321	L	209	-0.74	R	2	NA	NA	NA	NA	
326	A	207	-7.86	V	4	NA	NA	NA	NA	
334	P	208	3.67	S	3	-0.2754	0.48692	-0.566	0.57299	
337	R	208	-14.1	K	2	-0.6126	0.25525	-2.4	0.01838	*
				P	1	-0.0598	0.33262	-0.18	0.85769	
338	Q	207	25	C	2	-0.4257	0.42175	-1.009	0.31547	
				L	1	-0.69	0.46969	-1.469	0.14521	
				V	1	-0.4423	0.47466	-0.932	0.35384	
342	L	210	0	A	1	-1.8681	0.32673	-5.718	1.30E-07	***
347	S	199	86.35	A	8	-1.2661	0.1773	-7.141	2.02E-10	***
				G	4	-1.8726	0.22135	-8.46	3.68E-13	***
348	A	210	0	G	1	NA	NA	NA	NA	

Supplementary table 1. Additional information related to figure 1 · p < 0.1, * p < 0.05, ** p < 0.01 *** p < 0.001. Positive values in the "Estimate" column indicate a preference for D-luc, while negative values indicate a preferece for 4'Br-luc.

Table S3.2: Additional information related to figure 3.1.

					Round				Version					
Position	PDB#	Region	Rosetta	RF	1	2	3	AA's in sequenced variants	iAChSnFR0.6	iSeroSnFR0.0	iSeroSnFR0.1	iSeroSnFR0.2	iSeroSnFR	
3	41	Lower lobe					Rand.	F,V	V					
4	42	Lower lobe					Rand.	F,V	V					
7	45	Lower lobe	X	-2.01				A,S	S					
8	46	Binding pocket	X	0.28		SSM	SSM	E,H,I,L,P,Q,S,T,V,Y	I					
9	47	Binding pocket	X	2.30		SSM	SSM	A,D,I,K,L,N,P,Q,V,Y	I	N				
10	48	Binding pocket	X	-1.06		SSM	SSM	C,D,F,H,L,P	F	H				
11	49	Binding pocket	X	1.60			SSM	A,T	T					
12	50	Binding pocket	X	0.23			SSM	A,E,D	E					
13	51	Binding pocket	X	-1.55			SSM	A,D,E,Q,P,T	Q					
14	52	Lower lobe	X	-1.00				I,Q	I					
19	57	Lower lobe					Rand.	L,M	M					
20	58	Lower lobe					Rand.	L,V	V				L	
29	67	Lower lobe					SSM	D,P,Y	D					Random mutation in round 3 in improved variant
34	72	Lower lobe					SSM	A,C,R,T	R					Random mutation in round 3 in improved variant
38	76	Lower lobe					SSM	C,F,K,L	L					Random mutation in round 3 in improved variant
40	78	Binding pocket/lower lobe	X	-0.25				A,D,G,L	G					
41	79	Binding pocket/lower lobe	X	-0.02		SSM		A,E,F,G,I,L,P,Q,S,T,V	T	V				
42	80	Binding pocket/lower lobe	X	1.11				D,N	N					
55	93	Lower lobe				Rand.		N,Y	N					
59	97	Lower lobe					Rand.	F,I	I					Mutation occured after iSeroSnFR was discovered
61	99	Lower lobe				Rand.	SSM	A,G,L,M,V	V			L		
62	100	Binding pocket/lower lobe	X	-0.55				A,E	E					
63	101	Binding pocket/lower lobe	X	0.72				H,Y	Y					
64	102	Binding pocket/lower lobe	X	0.11			SSM	A,H,L,T,V	T	V				
65	103	Binding pocket/lower lobe					SSM	G	G					
66	104	Binding pocket/lower lobe	X	7.74	SSM			A,D,H,I,K,N,P,S,T,V,Y	T		Y			
70	108	Interface	X	-1.00				D,I	D					
73	111	Linker adjacent loop					SSM	A,S,T	T					
L1.1	112	Linker 1					SSM		Y					
L1.2	113	Linker 1					SSM	F,P	P					
L1.3	114	Linker 1					SSM	E,L,R	E					
L1.4	115	Linker 1					SSM		P					
GFP153	120	GFP/strand 7			Rand.		SSM	I,L,T	T		I			Effect of I was negligable by GLM, but was never confirmed
GFP157	124	GFP/7-8 loop					Rand.	H,Q	Q					Mutation occured after iSeroSnFR was discovered
GFP169	136	GFP/strand 8					SSM	H,L,Y	H			Y		
GFP192	159	GFP/9-10 loop					SSM		P			S	P	
GFP196	163	GFP/9-10 loop					SSM	A,L,P,S	P			L	P	L eliminates all mammalian expression
GFP231	198	GFP/11-1 linker					Rand.	F,L	L					
L2.1	357	Linker 2					SSM	P,S	P					
L2.2	358	Linker 2					SSM	A,K,Q,P	P					
L2.3	359	Linker 2					SSM	A,P	P					
L2.4	360	Linker 2					SSM	C,G,P,S,T	G					
77	361	Linker adjacent loop			Rand.	SSM		I,T	T			A		
102	386	Lower lobe				Rand.		L,P	P					
106	390	Binding pocket/hinge	X	0.71				D,E,M,N,R	N					
107	391	Binding pocket/hinge	X	-0.42		SSM		A,D,N,S	N	A				
108	392	Binding pocket/hinge	X	-2.21		SSM		A,D,E,P,R,S,T	T	S				
109	393	Binding pocket/upper lobe	X	0.39		SSM		F,H,W,Y	Y	F		Y		
110	394	Binding pocket/upper lobe	X	1.60				R,T,V	T	V				
112	396	Upper lobe				SSM	SSM	A,V	A					
130	414	Upper lobe					Rand.	A,S	A					Mutation occured after iSeroSnFR was discovered
140	424	Upper lobe					Rand.	A,V	A					
141	425	Binding pocket/upper lobe	X	0.72		SSM	SSM	D,N,Q,S,T	T	N				
142	426	Binding pocket/upper lobe	X	1.42			SSM	A,I,L,M,P,R,T	M					
143	427	Binding pocket/upper lobe	X	3.42	SSM			F,H,L,M,P,S,T,V	F		M			
144	428	Binding pocket/upper lobe	X	1.53				F,H	F					
147	431	Binding pocket/upper lobe	X	-0.46			SSM	D,K,N,Q,R,S,T	K				N	
148	432	Binding pocket/upper lobe					SSM	H,P	P					
149	433	Binding pocket/upper lobe					SSM	D,Y	D					
169	453	Binding pocket/upper lobe					SSM	A,D,V	D					
170	454	Binding pocket/upper lobe	X	4.57	SSM			A,D,G,H,L,M,N,P,R,S,T	M	H	A			
173	457	Binding pocket/upper lobe	X	-0.59			SSM	A,L,M,P,Q,R,T	R	M			P	
174	458	Binding pocket/upper lobe	X	0			SSM	A,F,H,P,S,Y	Y					
176	460	Upper lobe			Rand.			A,V	A					
186	470	Binding pocket/upper lobe	X	-1.16				A,D	D					
188	472	Binding pocket/upper lobe	X	2.51	SSM	SSM		C,D,F,G,H,I,K,L,M,P,R,T,Y	F		T			
189	473	Binding pocket/upper lobe	X	0.06			SSM	A,E,L,M,R	A					
190	474	Binding pocket/upper lobe	X	0.52			SSM	A,H,S,T	T					
191	475	Binding pocket/upper lobe					SSM	C,D,S	D					
211	495	Binding pocket/hinge	X	0.06				G,P,R	P					
212	496	Binding pocket/hinge				SSM		H,Y	Y					
221	505	Lower lobe					Rand.	D,E	D					
252	536	Binding pocket/lower lobe					SSM	R	R					

Supplementary table 2. Addiitonal information related to Figure 1. Summary of positions tested during sensor engineering, and mutations introduced.

Data S3.1: Excel file for machine learning. Refer to: https://www.cell.com/cms/10.1016/j.cell.2020.11.040/attachment/1a31be91-e1eb-4ff0-9795-6bcd3ec79ab0/mmc1.xlsx

Reference

Abdalla, A., Atcherley, C.W., Pathirathna, P., Samaranayake, S., Qiang, B., Pen˜ a, E., Morgan, S.L., Heien, M.L., and Hashemi, P. (2017). In Vivo Ambient Serotonin Measurements at Carbon-Fiber Microelectrodes. Anal. Chem. 89, 9703–9711.

Baker, D. (2019). What has de novo protein design taught us about protein folding and biophysics? Protein Sci. 28, 678–683.

Bang, S.J., Jensen, P., Dymecki, S.M., and Commons, K.G. (2012). Projec- tions and interconnections of genetically defined serotonin neurons in mice. Eur. J. Neurosci. 35, 85–96.

Bauer, E.P. (2015). Serotonin in fear conditioning processes. Behav. Brain Res. 277, 68–77.

Bedbrook, C.N., Yang, K.K., Robinson, J.E., Gradinaru, V., and Arnold, F.H. (2019). Machine learning-guided channelrhodopsin engineering enables mini- mally-invasive optogenetics. bioRxiv. https://doi.org/10.1101/565606.

Belmaker, R.H., and Agam, G. (2008). Major depressive disorder. N. Engl. J. Med. 358, 55–68.

Belmer, A., Klenowski, P.M., Patkar, O.L., and Bartlett, S.E. (2017). Mapping the connectivity of serotonin transporter immunoreactive axons to excitatory and inhibitory neurochemical synapses in the mouse limbic brain. Brain Struct. Funct. 222, 1297–1314.

Bender, B.J., Cisneros, A., 3rd, Duran, A.M., Finn, J.A., Fu, D., Lokits, A.D., Mueller, B.K., Sangha, A.K., Sauer, M.F., Sevy, A.M., et al. (2016). Protocols for Molecular Modeling with Rosetta3 and RosettaScripts. Biochemistry 55, 4748–4763.

Berger, M., Gray, J.A., and Roth, B.L. (2009). The expanded biology of seroto- nin. Annu. Rev. Med. 60, 355–366.

Bermingham, D.P., and Blakely, R.D. (2016). Kinase-dependent Regulation of Monoamine Neurotransmitter Transporters. Pharmacol. Rev. 68, 888–953.

Bessette, P.H., Mena, M.A., Nguyen, A.W., and Daugherty, P.S. (2003). Con- struction of designed protein libraries using gene assembly mutagenesis. Methods Mol. Biol. 231, 29–37.

Biswas, S., Kuznetsov, G., Ogden, P.J., Conway, N.J., Adams, R.P., and Church, G.M. (2018). Toward machine-guided design of proteins. bioRxiv. https://doi.org/10.1101/337154.

Bocchio, M., McHugh, S.B., Bannerman, D.M., Sharp, T., and Capogna, M. (2016). Serotonin, Amygdala and Fear: Assembling the Puzzle. Front. Neural Circuits 10, 24.

Borden, P.M., Zhang, P., Shivange, A.V., Marvin, J.S., Cichon, J., Dan, C., Podgorski, K., Figueiredo, A., Novak, O., Tanimoto, M., et al. (2020). A fast genetically encoded

fluorescent sensor for faithful in vivo acetylcholine detec- tion in mice, fish, worms and flies. bioRxiv. https://doi.org/10.1101/2020.02. 07.939504.

Bos, N., Dreier, S., Jørgensen, C.G., Nielsen, J., Guerrieri, F.J., and d'Ettorre, P. (2012). Learning and perceptual similarity among cuticular hydrocarbons in ants. J. Insect Physiol. 58, 138–146.

Breiman, L. (2001). Breiman and Cutler's Random Forests for Classification and Regression. Mach. Learn. 45, 5–32.

Broussard, G.J., Liang, R., and Tian, L. (2014). Monitoring activity in neural cir- cuits with genetically encoded indicators. Front. Mol. Neurosci. 7, 97.

Broussard, G.J., Unger, E.K., Liang, R., McGrew, B.P., and Tian, L. (2018). Im- aging glutamate with genetically encoded fluorescent sensors. In Biochemical Approaches for Glutamatergic Neurotransmission, S. Parrot and L. Denoroy, eds. (Springer New York), pp. 117–153.

Bryksin, A.V., and Matsumura, I. (2010). Overlap extension PCR cloning: a sim- ple and reliable way to create recombinant plasmids. Biotechniques 48, 463–465.

Bunin, M.A., and Wightman, R.M. (1998). Quantitative evaluation of 5-hydroxy- tryptamine (serotonin) neuronal release and uptake: an investigation of extra- synaptic transmission. J. Neurosci. 18, 4854–4860.

Bunin, M.A., Prioleau, C., Mailman, R.B., and Wightman, R.M. (1998). Release and uptake rates of 5-hydroxytryptamine in the dorsal raphe and substantia ni- gra reticulata of the rat brain. J. Neurochem. 70, 1077–1087.

Burghardt, N.S., Bush, D.E.A., McEwen, B.S., and LeDoux, J.E. (2007). Acute selective serotonin reuptake inhibitors increase conditioned fear expression: blockade with a 5-HT(2C) receptor antagonist. Biol. Psychiatry 62, 1111–1118.

Calhoon, G.G., and Tye, K.M. (2015). Resolving the neural circuits of anxiety. Nat. Neurosci. 18, 1394–1404.

Charnay, Y., and Le ́ger, L. (2010). Brain serotonergic circuitries. Dialogues Clin. Neurosci. 12, 471–487.

Chen, V.B., Arendall, W.B., 3rd, Headd, J.J., Keedy, D.A., Immormino, R.M., Kapral, G.J., Murray, L.W., Richardson, J.S., and Richardson, D.C. (2010). MolProbity: all-atom structure validation for macromolecular crystallography. Acta Crystallogr. D Biol. Crystallogr. 66, 12–21.

Cho, J.R., Treweek, J.B., Robinson, J.E., Xiao, C., Bremner, L.R., Greenbaum, A., and Gradinaru, V. (2017). Dorsal Raphe Dopamine Neurons Modulate Arousal and Promote Wakefulness by Salient Stimuli. Neuron 94, 1205–1219.

Cipriani, A., Furukawa, T.A., Salanti, G., Chaimani, A., Atkinson, L.Z., Ogawa, Y., Leucht, S., Ruhe, H.G., Turner, E.H., Higgins, J.P.T., et al. (2018). Compar- ative efficacy

and acceptability of 21 antidepressant drugs for the acute treat- ment of adults with major depressive disorder: a systematic review and network meta-analysis. Lancet 391, 1357–1366.

Clarke, R.J., and Khalid, M.A.A. (2015). Pumps, Channels and Transporters: Methods of Functional Analysis (John Wiley & Sons).

Cobb, R.E., Chao, R., and Zhao, H. (2013). Directed Evolution: Past, Present and Future. AIChE J. 59, 1432–1440.

Corre, J., van Zessen, R., and Pascoli, V. (2018). Dopamine neurons projecting to medial shell of the nucleus accumbens drive heroin reinforcement. eLife 7, e39945.

Correia, P.A., Lottem, E., Banerjee, D., Machado, A.S., Carey, M.R., and Mainen, Z.F. (2017). Transient inhibition and long-term facilitation of locomo- tion by phasic optogenetic activation of serotonin neurons. eLife 6, e20975.

Curzon, P., Rustay, N.R., and Browman, K.E. (2009). Cued and contextual fear conditioning for rodents. In Methods of Behavior Analysis in Neuroscience, J.J. Buccafusco, ed. (CRC Press/Taylor & Francis).

Davis, I.W., and Baker, D. (2009). RosettaLigand docking with full ligand and receptor flexibility. J. Mol. Biol. 385, 381–392.

Dehghani, M., Gouws, S., Vinyals, O., Uszkoreit, J., and Kaiser, L. (2019). Uni- versal Transformers (ICLR).

Dobson, A.J., Barnett, A.G., and Barnett, A.G. (2008). An Introduction to Generalized Linear Models (Chapman and Hall/CRC).

Ehren, J., Govindarajan, S., Moro´ n, B., Minshull, J., and Khosla, C. (2008). Pro- tein engineering of improved prolyl endopeptidases for celiac sprue therapy. Protein Eng. Des. Sel. 21, 699–707.

Emsley, P., and Cowtan, K. (2004). Coot: model-building tools for molecular graphics. Acta Crystallogr. D Biol. Crystallogr. 60, 2126–2132.

Evans, P.R., and Murshudov, G.N. (2013). How good are my data and what is the resolution? Acta Crystallogr. D Biol. Crystallogr. 69, 1204–1214.

Feng, J., Zhang, C., Lischinsky, J.E., Jing, M., Zhou, J., Wang, H., Zhang, Y., Dong, A., Wu, Z., Wu, H., et al. (2019). A Genetically Encoded Fluorescent Sensor for Rapid and Specific In Vivo Detection of Norepinephrine. Neuron 102, 745–761.

Ferre´ s-Coy, A., Pilar-Cuellar, F., Vidal, R., Paz, V., Masana, M., Corte´ s, R., Car- mona, M.C., Campa, L., Pazos, A., Montefeltro, A., et al. (2013). RNAi-medi- ated serotonin transporter suppression rapidly increases serotonergic neuro- transmission and hippocampal neurogenesis. Transl. Psychiatry 3, e211.

Forster, G.L., Feng, N., Watt, M.J., Korzan, W.J., Mouw, N.J., Summers, C.H., and Renner, K.J. (2006). Corticotropin-releasing factor in the dorsal raphe elicits temporally

distinct serotonergic responses in the limbic system in rela- tion to fear behavior. Neuroscience 141, 1047–1055.

Fujino, K., Yoshitake, T., Inoue, O., Ibii, N., Kehr, J., Ishida, J., Nohta, H., and Yamaguchi, M. (2002). Increased serotonin release in mice frontal cortex and hippocampus induced by acute physiological stressors. Neurosci. Lett. 320, 91–95.

Garcia-Garcia, A.L., Canetta, S., Stujenske, J.M., Burghardt, N.S., Ansorge, M.S., Dranovsky, A., and Leonardo, E.D. (2018). Serotonin inputs to the dorsal BNST modulate anxiety in a 5-HT1A receptor-dependent manner. Mol. Psychi- atry 23, 1990–1997.

Gibson, D.G., Young, L., Chuang, R.-Y., Venter, J.C., Hutchison, C.A., 3rd, and Smith, H.O. (2009). Enzymatic assembly of DNA molecules up to several hun- dred kilobases. Nat. Methods 6, 343–345.

Gong, S., Zheng, C., Doughty, M.L., Losos, K., Didkovsky, N., Schambra, U.B., Nowak, N.J., Joyner, A., Leblanc, G., Hatten, M.E., et al. (2003). A gene expression atlas of the central nervous system based on bacterial artificial chromosomes. Nature 425, 917–925.

Greenwood, B.N., Foley, T.E., Day, H.E.W., Burhans, D., Brooks, L., Campeau, S., and Fleshner, M. (2005). Wheel running alters serotonin (5-HT) transporter, 5-HT1A, 5-HT1B, and alpha 1b-adrenergic receptor mRNA in the rat raphe nuclei. Biol. Psychiatry 57, 559–568.

Hashimoto, S., Inoue, T., and Koyama, T. (1999). Effects of conditioned fear stress on serotonin neurotransmission and freezing behavior in rats. Eur. J. Pharmacol. 378, 23–30.

Hawkins, P.C.D., Skillman, A.G., Warren, G.L., Ellingson, B.A., and Stahl, M.T. (2010). Conformer generation with OMEGA: algorithm and validation using high quality structures from the Protein Databank and Cambridge Structural Database. J. Chem. Inf. Model. 50, 572–584.

Heinrich, T., Bo¨ttcher, H., Gericke, R., Bartoszyk, G.D., Anzali, S., Seyfried, C.A., Greiner, H.E., and Van Amsterdam, C. (2004). Synthesis and structure– activity relationship in a class of indolebutylpiperazines as dual 5-HT(1A) re- ceptor agonists and serotonin reuptake inhibitors. J. Med. Chem. 47, 4684–4692.

Helassa, N., Du¨rst, C.D., Coates, C., Kerruth, S., Arif, U., Schulze, C., Wiegert, J.S., Geeves, M., Oertner, T.G., and To¨ro¨k, K. (2018). Ultrafast glutamate sen- sors resolve high-frequency release at Schaffer collateral synapses. Proc. Natl. Acad. Sci. USA 115, 5594–5599.

Huang, R., Fang, P., and Kay, B.K. (2012). Improvements to the Kunkel muta- genesis protocol for constructing primary and secondary phage-display li- braries. Methods 58, 10–17.

Jaquins-Gerstl, A., and Michael, A.C. (2015). A review of the effects of FSCV and microdialysis measurements on dopamine release in the surrounding tis- sue. Analyst (Lond.) 140, 3696–3708.

Jarrett, M.E., Kohen, R., Cain, K.C., Burr, R.L., Poppe, A., Navaja, G.P., and Heitkemper, M.M. (2007). Relationship of SERT polymorphisms to depressive and anxiety symptoms in irritable bowel syndrome. Biol. Res. Nurs. 9, 161–169.

Jing, M., Zhang, Y., Wang, H., and Li, Y. (2019). G-protein-coupled receptor- based sensors for imaging neurochemicals with high sensitivity and speci- ficity. J. Neurochem. 151, 279–288.

Jing, M., Li, Y., Zeng, J., Huang, P., Skirzewski, M., Kljakic, O., Peng, W., Qian, T., Tan, K., Zou, J., et al. (2020). An optimized acetylcholine sensor for moni- toring in vivo cholinergic activity. Nat. Methods 17, 1139–1146.

Jones, K.A., Porterfield, W.B., Rathbun, C.M., McCutcheon, D.C., Paley, M.A., and Prescher, J.A. (2017). Orthogonal Luciferase-Luciferin Pairs for Biolumi- nescence Imaging. J. Am. Chem. Soc. 139, 2351–2358.

Kabsch, W. (2010). XDS. Acta Crystallogr. D Biol. Crystallogr. 66, 125–132.

Kato, R., Nakano, H., Konishi, H., Kato, K., Koga, Y., Yamane, T., Kobayashi, T., and Honda, H. (2005). Novel strategy for protein exploration: high- throughput screening assisted with fuzzy neural network. J. Mol. Biol. 351, 683–692.

Kawahara, H., Yoshida, M., Yokoo, H., Nishi, M., and Tanaka, M. (1993). Psy- chological stress increases serotonin release in the rat amygdala and prefron- tal cortex assessed by in vivo microdialysis. Neurosci. Lett. 162, 81–84.

Keller, J.P., and Looger, L.L. (2016). The Oscillating Stimulus Transporter Assay, OSTA: Quantitative Functional Imaging of Transporter Protein Activity in Time and Frequency Domains. Mol. Cell 64, 199–212.

Keller, J.P., Marvin, J.S., Lacin, H., Lemon, W.C., Shea, J., Kim, S., Lee, R.T., Koyama, M., Keller, P.J., and Looger, L.L. (2019). In vivo glucose imaging in multiple model organisms with an engineered single-wavelength sensor. bio- Rxiv. https://doi.org/10.1101/571422.

Khoury, G.A., Smadbeck, J., Kieslich, C.A., and Floudas, C.A. (2014). Protein folding and de novo protein design for biotechnological applications. Trends Biotechnol. 32, 99–109.

Kiser, D., Steemers, B., Branchi, I., and Homberg, J.R. (2012). The reciprocal interaction between serotonin and social behaviour. Neurosci Biobehav Rev 36, 786–798.

Koldsø, H., Noer, P., Grouleff, J., Autzen, H.E., Sinning, S., and Schiøtt, B. (2011). Unbiased simulations reveal the inward-facing conformation of the hu- man serotonin transporter and Na(+) ion release. PLoS Comput. Biol. 7, e1002246.

Kunkel, T.A. (1985). Rapid and efficient site-specific mutagenesis without phenotypic selection. Proc. Natl. Acad. Sci. USA 82, 488–492.

Li, Y., Zhong, W., Wang, D., Feng, Q., Liu, Z., Zhou, J., Jia, C., Hu, F., Zeng, J., Guo, Q., et al. (2016). Serotonin neurons in the dorsal raphe nucleus encode reward signals. Nat. Commun. 7, 10503.

Liao, J., Warmuth, M.K., Govindarajan, S., Ness, J.E., Wang, R.P., Gustafsson, C., and Minshull, J. (2007). Engineering proteinase K using machine learning and synthetic genes. BMC Biotechnol. 7, 16.

Liaw, A., and Wiener, M. (2002). Classification and Regression by randomFor- est. https://rdrr.io/cran/randomForest/.

Lin, M.Z., and Schnitzer, M.J. (2016). Genetically encoded indicators of neuronal activity. Nat. Neurosci. 19, 1142–1153.

Lobas, M.A., Tao, R., Nagai, J., Kronschla ̈ger, M.T., Borden, P.M., Marvin, J.S., Looger, L.L., and Khakh, B.S. (2019). A genetically encoded single-wave- length sensor for imaging cytosolic and cell surface ATP. Nat. Commun. 10, 711.

Looger, L.L., and Griesbeck, O. (2012). Genetically encoded neural activity in- dicators. Curr. Opin. Neurobiol. 22, 18–23.

Madisen, L., Zwingman, T.A., Sunkin, S.M., Oh, S.W., Zariwala, H.A., Gu, H., Ng, L.L., Palmiter, R.D., Hawrylycz, M.J., Jones, A.R., et al. (2010). A robust and high-throughput Cre reporting and characterization system for the whole mouse brain. Nat. Neurosci. 13, 133–140.

Madisen, L., Garner, A.R., Shimaoka, D., Chuong, A.S., Klapoetke, N.C., Li, L., van der Bourg, A., Niino, Y., Egolf, L., Monetti, C., et al. (2015). Transgenic mice for intersectional targeting of neural sensors and effectors with high specificity and performance. Neuron 85, 942–958.

Marcinkiewcz, C.A., Mazzone, C.M., D'Agostino, G., Halladay, L.R., Hard- away, J.A., DiBerto, J.F., Navarro, M., Burnham, N., Cristiano, C., Dorrier, C.E., et al. (2016). Serotonin engages an anxiety and fear-promoting circuit in the extended amygdala. Nature 537, 97–101.

Margoob, M.A., and Mushtaq, D. (2011). Serotonin transporter gene polymor- phism and psychiatric disorders: is there a link? Indian J. Psychiatry 53, 289–299.

Marvin, J.S., Schreiter, E.R., Echevarrı ́a, I.M., and Looger, L.L. (2011). A genet- ically encoded, high-signal-to-noise maltose sensor. Proteins 79, 3025–3036.

Marvin, J.S., Borghuis, B.G., Tian, L., Cichon, J., Harnett, M.T., Akerboom, J., Gordus, A., Renninger, S.L., Chen, T.-W., Bargmann, C.I., et al. (2013). An opti- mized fluorescent probe for visualizing glutamate neurotransmission. Nat. Methods 10, 162–170.

Marvin, J.S., Scholl, B., Wilson, D.E., Podgorski, K., Kazemipour, A., Mu¨ller, J.A., Schoch, S., Quiroz, F.J.U., Rebola, N., Bao, H., et al. (2018). Stability, af- finity, and chromatic variants of the glutamate sensor iGluSnFR. Nat. Methods 15, 936–939.

Marvin, J.S., Shimoda, Y., Magloire, V., Leite, M., Kawashima, T., Jensen, T.P., Kolb, I., Knott, E.L., Novak, O., Podgorski, K., et al. (2019). A genetically en- coded fluorescent sensor for in vivo imaging of GABA. Nat. Methods 16, 763–770.

Matsui, A., and Alvarez, V.A. (2018). Cocaine Inhibition of Synaptic Transmis- sion in the Ventral Pallidum Is Pathway-Specific and Mediated by Serotonin. Cell Rep. 23, 3852–3863.

McCoy, A.J. (2007). Solving structures of protein complexes by molecular replacement with Phaser. Acta Crystallogr. D Biol. Crystallogr. 63, 32–41.

Miller, D.A., Suen, G., Bruce, D., Copeland, A., Cheng, J.-F., Detter, C., Good- win, L.A., Han, C.S., Hauser, L.J., Land, M.L., et al. (2011). Complete genome sequence of the cellulose-degrading bacterium Cellulosilyticum lentocellum. J. Bacteriol. 193, 2357–2358.

Mizuno, G.O., Unger, E.K., and Tian, L. (2019). Real-time monitoring of neuro- modulators in behaving animals using genetically-encoded indicators. In Compendium on In Vivo Monitoring in Real-Time Molecular Neuroscience, G.S. Wilson and A.C. Michael, eds. (World Scientific), pp. 1–18.

Nov, Y. (2012). When second best is good enough: another probabilistic look at saturation mutagenesis. Appl. Environ. Microbiol. 78, 258–262.

Ohmura, Y., Tanaka, K.F., Tsunematsu, T., Yamanaka, A., and Yoshioka, M. (2014). Optogenetic activation of serotonergic neurons enhances anxiety- like behaviour in mice. Int. J. Neuropsychopharmacol. 17, 1777–1783.

Ollikainen, N., de Jong, R.M., and Kortemme, T. (2015). Coupling Protein Side- Chain and Backbone Flexibility Improves the Re-design of Protein-Ligand Specificity. PLoS Comput. Biol. 11, e1004335.

Ozaki, N., Goldman, D., Kaye, W.H., Plotnicov, K., Greenberg, B.D., Lappalai- nen, J., Rudnick, G., and Murphy, D.L. (2003). Serotonin transporter missense mutation associated with a complex neuropsychiatric phenotype. Mol. Psychi- atry 8, 933–936.

Packer, M.S., and Liu, D.R. (2015). Methods for the directed evolution of pro- teins. Nat. Rev. Genet. 16, 379–394.

Patriarchi, T., Cho, J.R., Merten, K., Howe, M.W., Marley, A., Xiong, W.-H., Folk, R.W., Broussard, G.J., Liang, R., Jang, M.J., et al. (2018). Ultrafast neuronal imaging of dopamine dynamics with designed genetically encoded sensors. Science 360, eaat4422.

Pen˜ alva, R.G., Lancel, M., Flachskamm, C., Reul, J.M.H.M., Holsboer, F., and Linthorst, A.C.E. (2003). Effect of sleep and sleep deprivation on serotonergic neurotransmission in the hippocampus: a combined in vivo microdialysis/EEG study in rats. Eur. J. Neurosci. 17, 1896–1906.

Portas, C.M., Bjorvatn, B., and Ursin, R. (2000). Serotonin and the sleep/wake cycle: special emphasis on microdialysis studies. Prog. Neurobiol. 60, 13–35.

Quan, J., and Tian, J. (2011). Circular polymerase extension cloning for high- throughput cloning of complex and combinatorial DNA libraries. Nat. Protoc. 6, 242–251.

Rathbun, C.M., Porterfield, W.B., Jones, K.A., Sagoe, M.J., Reyes, M.R., Hua, C.T., and Prescher, J.A. (2017). Parallel Screening for Rapid Identification of Orthogonal Bioluminescent Tools. ACS Cent. Sci. 3, 1254–1261.

Ren, J., Friedmann, D., Xiong, J., Liu, C.D., Ferguson, B.R., Weerakkody, T., DeLoach, K.E., Ran, C., Pun, A., Sun, Y., et al. (2018). Anatomically Defined and Functionally Distinct Dorsal Raphe Serotonin Sub-systems. Cell 175, 472–487.

Richter, F., Leaver-Fay, A., Khare, S.D., Bjelic, S., and Baker, D. (2011). De novo enzyme design using Rosetta3. PLoS ONE 6, e19230.

Ritz, C., Baty, F., Streibig, J.C., and Gerhard, D. (2015). Dose-Response Anal- ysis Using R. PLoS ONE 10, e0146021.

Rouillard, J.-M., Lee, W., Truan, G., Gao, X., Zhou, X., and Gulari, E. (2004). Gene2Oligo: oligonucleotide design for in vitro gene synthesis. Nucleic Acids Res. 32, W176-80.

Rudnick, G., and Sandtner, W. (2019). Serotonin transport in the 21st century. J. Gen. Physiol. 151, 1248–1264.

Rudnick, G., and Wall, S.C. (1992). p-Chloroamphetamine induces serotonin release through serotonin transporters. Biochemistry 31, 6710–6718.

Rueter, L.E., and Jacobs, B.L. (1996). A microdialysis examination of serotonin release in the rat forebrain induced by behavioral/environmental manipula- tions. Brain Res. 739, 57–69.

Saito, T., and Nakatsuji, N. (2001). Efficient gene transfer into the embryonic mouse brain using in vivo electroporation. Dev. Biol. 240, 237–246.

Schindelin, J., Arganda-Carreras, I., Frise, E., Kaynig, V., Longair, M., Pietzsch, T., Preibisch, S., Rueden, C., Saalfeld, S., Schmid, B., et al. (2012). Fiji: an open-source platform for biological-image analysis. Nat. Methods 9, 676–682.

Schultz, K.N., and Kennedy, R.T. (2008). Time-resolved microdialysis for in vivo neurochemical measurements and other applications. Annu. Rev. Anal. Chem. (Palo Alto, Calif.) 1, 627–661.

Seo, C., Guru, A., Jin, M., Ito, B., Sleezer, B.J., Ho, Y.-Y., Wang, E., Boada, C., Krupa, N.A., Kullakanda, D.S., et al. (2019). Intense threat switches dorsal raphe serotonin neurons to a paradoxical operational mode. Science 363, 538–542.

Shivange, A.V., Borden, P.M., Muthusamy, A.K., Nichols, A.L., Bera, K., Bao, H., Bishara, I., Jeon, J., Mulcahy, M.J., Cohen, B., et al. (2019). Determining the pharmacokinetics of nicotinic drugs in the endoplasmic reticulum using biosensors. J. Gen. Physiol. 151, 738–757.

Sneddon, J.M. (1969). Sodium-dependent accumulation of 5-hydroxytrypta- mine by rat blood platelets. Br. J. Pharmacol. 37, 680–688.

Studier, F.W. (2005). Protein production by auto-induction in high density shaking cultures. Protein Expr. Purif. 41, 207–234.

Sun, F., Zeng, J., Jing, M., Zhou, J., Feng, J., Owen, S.F., Luo, Y., Li, F., Wang, H., Yamaguchi, T., et al. (2018). A Genetically Encoded Fluorescent Sensor En- ables Rapid and Specific Detection of Dopamine in Flies, Fish, and Mice. Cell 174, 481–496.

Tatsumi, M., Groshan, K., Blakely, R.D., and Richelson, E. (1997). Pharmaco- logical profile of antidepressants and related compounds at human mono- amine transporters. Eur. J. Pharmacol. 340, 249–258.

Taylor, N.D., Garruss, A.S., Moretti, R., Chan, S., Arbing, M.A., Cascio, D., Rogers, J.K., Isaacs, F.J., Kosuri, S., Baker, D., et al. (2016). Engineering an allosteric transcription factor to respond to new ligands. Nat. Methods 13, 177–183.

R Development Core Team (2013). R: A language and environment for statis- tical computing (R Foundation for Statistical Computing).

Tinberg, C.E., Khare, S.D., Dou, J., Doyle, L., Nelson, J.W., Schena, A., Jan- kowski, W., Kalodimos, C.G., Johnsson, K., Stoddard, B.L., and Baker, D. (2013). Computational design of ligand-binding proteins with high affinity and selectivity. Nature 501, 212–216.

Wan, J., Peng, W., Li, X., Qian, T., Song, K., Zeng, J., Deng, F., Hao, S., Feng, J., Zhang, P., et al. (2020). A genetically encoded GRAB sensor for measuring serotonin dynamics in vivo. bioRxiv. https://doi.org/10.1101/2020.02.24. 962282.

Wang, H., Goehring, A., Wang, K.H., Penmatsa, A., Ressler, R., and Gouaux, E. (2013). Structural basis for action by diverse antidepressants on biogenic amine transporters. Nature 503, 141–145.

Wankerl, M., Miller, R., Kirschbaum, C., Hennig, J., Stalder, T., and Alexander, N. (2014). Effects of genetic and early environmental risk factors for depression on serotonin transporter expression and methylation profiles. Transl. Psychia- try 4, e402.

Wickham, H. (2016). ggplot2: Elegant Graphics for Data Analysis (Springer). Wickham, H., Averick, M., Bryan, J., Chang, W., McGowan, L., Franc ̧ois, R., Grolemund, G.,

Hayes, A., Henry, L., Hester, J., et al. (2019). Welcome to the Tidyverse. J. Open Source Softw. 4, 1686.

Williams, G. (2011). Data Mining with Rattle and R: The Art of Excavating Data for Knowledge Discovery (Springer-Verlag).

Wu, Z., Kan, S.B.J., Lewis, R.D., Wittmann, B.J., and Arnold, F.H. (2019). Ma- chine learning-assisted directed protein evolution with combinatorial libraries. Proc. Natl. Acad. Sci. USA 116, 8852–8858.

Yang, K.K., Wu, Z., and Arnold, F.H. (2019a). Machine-learning-guided directed evolution for protein engineering. Nat. Methods 16, 687–694.

Yang, K.K., Chen, Y., Lee, A., and Yue, Y. (2019b). Batched Stochastic Bayesian Optimization via Combinatorial Constraints Design. arXiv, arXiv:1904.08102.

Yokoyama, M., Suzuki, E., Sato, T., Maruta, S., Watanabe, S., and Miyaoka, H. (2005). Amygdalic levels of dopamine and serotonin rise upon exposure to conditioned fear stress without elevation of glutamate. Neurosci. Lett. 379, 37–41.

Zhang, Y.-W., Turk, B.E., and Rudnick, G. (2016). Control of serotonin trans- porter phosphorylation by conformational state. Proc. Natl. Acad. Sci. USA 113, E2776–E2783.

Zhou, X., Lu, J.Y.-F., Darling, R.D., Simpson, K.L., Zhu, X., Wang, F., Yu, L., Sun, X., Merzenich, M.M., and Lin, R.C.S. (2015). Behavioral training reverses global cortical network dysfunction induced by perinatal antidepressant expo- sure. Proc. Natl. Acad. Sci. USA 112, 2233–2238.

Zhuang, X., Masson, J., Gingrich, J.A., Rayport, S., and Hen, R. (2005). Tar- geted gene expression in dopamine and serotonin neurons of the mouse brain. J. Neurosci. Methods 143, 27–32.

Unlocking opioid neuropeptide dynamics with genetically-encoded biosensors

Preface

The text of this chapter is a modified version of a manuscript that was submitted to the *Nature Neuroscience* on April 28, 2023, and pending external revisions by the time of submitting this thesis. The layout has been adjusted in accordance with the requirements of a doctoral thesis. The authors on the original manuscript are listed as Chunyang Dong†, Raajaram Gowrishankar†, Yihan Jin, Xinyi Jenny He, Achla Gupta, Huikun Wang, Nilüfer Sayar Atasoy, Rodolfo Floresgarcia, Karan Mahe, Ruqiang Liang, Grace Or Mizuno, Darren Kirin Lo, Qingtao Sun, Jennifer L. Whistler, Bo Li, Ivone Gomes, Hugo A Tejeda, Deniz Atasoy, Lakshmi A Devi, Michael R. Bruchas, Matthew R. Banghart, Lin Tian.

(† authors contributed equally to this work)

Abstract

Neuropeptides are ubiquitous in the nervous system. Research into neuropeptides has been limited by a lack of experimental tools that allow for the precise dissection of their complex and diverse dynamics in a circuit-specific manner. Opioid peptides comprise a clinically relevant family that modulates pain, reward, and aversion. To illuminate the spatiotemporal dynamics of endogenous opioid signaling in the brain, we developed a class of genetically-encoded fluorescent sensors based on kappa, delta, and mu opioid receptors: κLight, δLight, and μLight, respectively. We used κLight to identify electrical stimulation parameters that trigger endogenous opioid release and the spatiotemporal scale of dynorphin volume transmission ex vivo. Using in vivo fiber photometry, we characterized optogenetically-driven opioid release, and observed differential opioid signaling in response to fearful and rewarding conditions in the nucleus accumbens. These sensors reveal the dynamics of endogenous opioid neuropeptide release in vivo, in awake freely moving behavior.

Introduction

Neuropeptides (NPs) are small proteins that modify neural activity, regulate brain states, and control blood flow in the nervous system[1-5]. Neurons synthesize and release neuropeptides (NP) in addition to fast-acting neurotransmitters (NT) such as glutamate and GABA[6]. NPs activate select G protein-coupled receptors to modulate synaptic strength, neuronal excitability, and circuit dynamics. Unlike small molecule NTs, NPs are hypothesized to be released into the extra-synaptic space and thought to be cleared by proteolysis and diffusion over a range of 100 micrometers to millimeters to affect neurons, leading to long-lasting modulatory effects [6,7,8]. A comprehensive understanding of the conditions that trigger NP release from neurons and the spatiotemporal extent of peptide release has been lacking, and yet is critical for understanding the actions of NPs at the molecular, cellular, circuit and network levels to their influence on animal behavioral states.

Among all known NPs, the opioid system is the most functionally diverse and clinically relevant family [9-15]. The opioid receptor family contains distinct receptor subtypes—kappa, delta, and mu (κOR, δOR, and μOR, respectively), as well as nociception receptors — which can be activated by at least 20 endogenous opioid peptides with differential affinity and selectivity [12,16,17]. Kappa, delta, and mu and nociception opioid receptors activate inhibitory $G_{i/o}$ G proteins, which leads to reductions in cellular excitability and neurotransmitter secretion in receptor-expressing neurons. Opioid peptides and their receptors are widely distributed across cortical and subcortical brain regions [18,19]. It is thought, that the diversity of opioid peptides is essential for modulating complex behavior and physiological processes, such as pain,

reward, substance abuse/dependence, and stress [20]. Opioids drugs targeting these receptors are used to treat severe pain, but prolonged use can lead to addiction and overdose [21]. Newer efforts have isolated opioid receptors as potential targets for anxiety, depression, and addiction [22,23]. Some of these efforts have been hindered by a lack of high-resolution methods for studying endogenous neuropeptide release in vivo.

Studies into neuropeptide systems, especially opioid systems, have been historically challenging due to a lack of sensitive experimental tools in the spatial temporal domain which can facilitate understanding the complexity and diversity of NP signaling in a circuit-specific manner. The endogenous opioid peptides have similar structures and bind to different opioid receptors with relatively lower selectivity than some neuropeptide molecules at their cognate receptors[16]. Physiologically relevant NP release by neurons are thought to be difficult to trigger and the released concentration may also be at orders of magnitude lower than classical neurotransmitters (nanomolar vs. micromolar or even submillimolar) [24], making it extremely difficult to adequately probe the conditions to trigger the endogenous peptide release and measure the released concentration ex vivo and in vivo[25]. As a result, it has been exceedingly difficult to study the processes that regulate opioid neuropeptide release. Recent technological advances have begun to reveal the anatomical and spatiotemporal features of opioid signaling [26,27]. Transcriptomics studies have documented the distribution of opioid peptide-receptor pairs across cell types in the cortex, highlighting the functional significance of opioid signaling in mediating trans-cellular communication in neural circuits [28]. Features of peptide diffusion and clearance have been revealed by combining light-triggered photo-

release of caged enkephalin with electrophysiological measurements of peptide-evoked currents in brain slices [29]. In vivo, optogenetically-driven peptide release has been detected using high-speed micro-dialysis [30]. Despite these successes, it remains challenging to quantify behaviorally relevant endogenous opioid peptide release with subsecond and subregional resolution.

To bridge this gap in technology, we developed a class of genetically encoded opioid peptide indicators, κLight, δLight, and μLight, based on κOR, δOR, and μOR respectively. We used these sensors to systematically evaluate ligand binding-induced conformational changes at all three receptors and thereby established the binding specificity and efficacy of 14 opioid peptides and 8 opioid drugs. In acute hippocampal slice, we used κLight to determine electrical parameters that can trigger endogenous opioid peptide release and quantified the diffusion rate of dynorphin using photoactivatable peptide. Using optogenetics to stimulate opioid peptide release, we detected circuit-specific endogenous opioid signaling in vivo. Finally, we used these sensors to reveal rapid opioid peptide release in a subregion-specific manner in response to fear and reward conditions within the nucleus accumbens of awake, behaving mice.

Results

(xvi) Design and Engineering of Opioid Sensors

We replaced amino acids between R2.57 and R6.24 of the human κ receptor, S2.47 and K6.24 of the human δ receptor, and S6.23 and K6.24 of human μ receptors, respectively, with a circularly permuted green fluorescent protein (cpGFP), to generate κLight, δLight, and μLight sensors (Figure 4.1A-B, Figure S4.1A-B). The dynamic range of each sensor was optimized by screening linker compositions. In total, the dynamic range of 698 κLight variants, 64 δLight variants, and 233 μLight variants were examined in response to U50,488, met-enkephalin (ME) and DAMGO, respectively (Figure S4.1C). To promote excellent membrane localization; we fused a telencephalin (TlcnC) tag [31] or endoplasmic reticulum (ER) export motif (FCYENEV) [32] followed by a chain of GS linker and the proximal restriction and clustering (PRC) tag [33] to the c-terminus of κLight, δLight, and μLight. We named these new variants κLight1.3, δLight1, and μLight1, respectively. In addition, we mutated D3.22 of KOR and D3.32 in DOR in the binding pockets to attenuate the ligand-binding, which led to two control sensors κLight0 and δLight0.

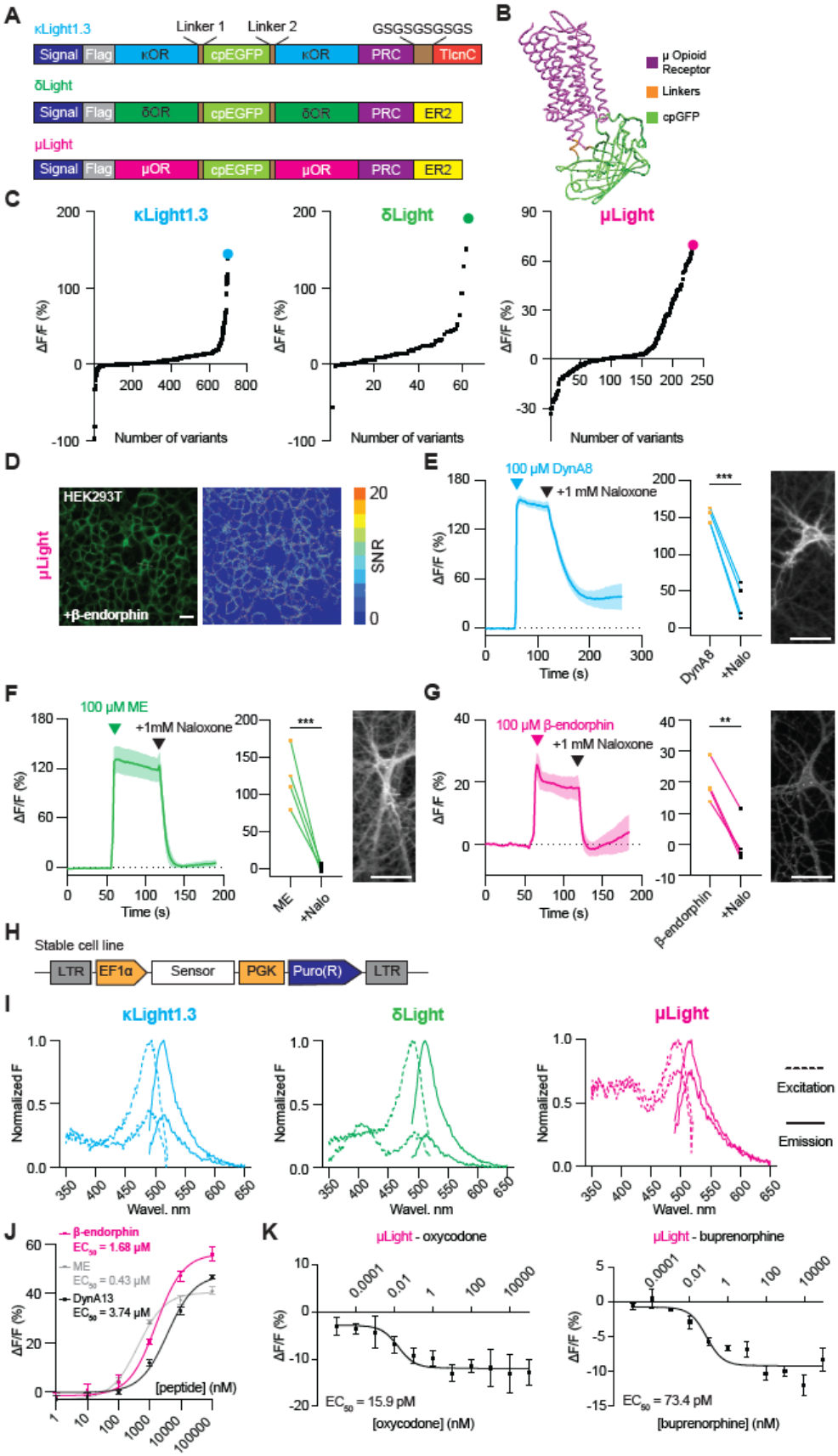
A
κLight1.3
Linker 1
Linker 2
GSGSGSGSGS
Signal
Flag
κOR
cpEGFP
κOR
PRC
TlcnC
δLight
Signal
Flag
δOR
cpEGFP
δOR
PRC
ER2
μLight
Signal
Flag
μOR
cpEGFP
μOR
PRC
ER2
B
μ Opioid Receptor
Linkers
cpGFP
C
κLight1.3
δLight
μLight
ΔF/F (%)
Number of variants
D
HEK293T
μLight
+β-endorphin
SNR
20
0
E
100 μM DynA8
+1 mM Naloxone
ΔF/F (%)
Time (s)
***
DynA8
+Nalo
F
100 μM ME
+1mM Naloxone
ΔF/F (%)
Time (s)
***
ME
+Nalo
G
100 μM β-endorphin
+1 mM Naloxone
ΔF/F (%)
Time (s)
**
β-endorphin
+Nalo
H
Stable cell line
LTR
EF1α
Sensor
PGK
Puro(R)
LTR
I
κLight1.3
δLight
μLight
Normalized F
Wavel. nm
Excitation
Emission
J
β-endorphin
EC50 = 1.68 μM
ME
EC50 = 0.43 μM
DynA13
EC50 = 3.74 μM
ΔF/F (%)
[peptide] (nM)
K
μLight - oxycodone
ΔF/F (%)
EC50 = 15.9 pM
[oxycodone] (nM)
μLight - buprenorphine
ΔF/F (%)
EC50 = 73.4 pM
[buprenorphine] (nM)

Figure S4.1. Screening and characterization of the opioid sensors.

(a) Schematic diagrams showing the components of recombinant DNA for each opioid sensor.

(b) Simulated structure of μLight. Mu opioid receptor (MOR, magenta), linkers (orange), cpGFP (light green).

(c) Optimization of the opioid sensor variants. Dots representing ΔF/F (%) of variants screened along optimizations, including cpGFP insertion sites, linker screening, and point mutations. A ligand concentration of 100 μM was used for screening; U50,488 for κLight (blue), ME for δLight (green) and DAMGO for μLight (magenta). Variants with the highest ΔF/F (%) indicated as κLight1.3 (144.47%) with 698 variants screened; δLight (191%) with 63 variants screened; μLight (69.6%) with 233 variants screened.

(d) (Left) Representative image showing transient transfection of μLight in HEK293T cells. (Right) Heatmap indicating signal-to-noise-ration (SNR) upon addition of 100 μM β-endorphin. Scale bar, 20 μm.

(e) (Left) Agonist (100 μM DynA8) and antagonist (1 mM naloxone) response of κLight1.3 transiently expressed in dissociated hippocampal neuron cultures. n = 4 wells. Solid blue line represents the mean, and shaded area represents SEM. (Middle) ΔF/F (%) comparison between two states: agonist response (151 ± 5.0 %), + antagonist response (36.9 ± 11.7 %), unpaired t test, ***p = 0.0001. (Right) Representative image show expression of κLight1.3 in neurons, scale bar, 50 μm. Nalo = Naloxone

(f) (Left) Agonist (100 μM ME) and antagonist (1 mM naloxone) response of δLight transiently expressed in dissociated hippocampal neuron cultures. n = 4 wells. Solid green line represents the mean, and the shaded area represents SEM. (Middle) ΔF/F (%) comparison between two states: agonist response (123 ± 19.4 %), + antagonist response (1.82 ± 2.4 %), unpaired t test, ***p = 0.0008. (Right) Representative image showing expression of δLight in neurons, scale bar, 50 μm. Nalo = Naloxone

(g) (Left) Agonist (100 μM β-endorphin) and antagonist (1 mM naloxone) response of μLight transiently expressed in dissociated hippocampal neuron cultures. N = 4 wells. Solid magenta line represents the mean, and the shaded area represents SEM. (Middle) ΔF/F (%) comparison between two states: agonist response (19.6 ± 3.2 %), + antagonist response (0.75 ± 3.6 %), unpaired t test, ***p = 0.0082. (Right) Representative image showing expression of μLight in neurons, scale bar, 50 μm. Nalo = Naloxone

(h) Schematic diagram showing the components of recombinant DNA for lentiviral production.

(i) Excitation-emission spectra of the three opioid sensors under both bound (upper lines, 100μM DynA8 for κLight -blue, 100μM ME for δLight -green, and 100μM β-endorphin for μLight -magenta) and unbound (lower lines) states. Excitation (dotted lines) of all three sensors peaks at ~490 nm, and emission (solid lines) of all three sensors peaks at ~515 nm.

(j) Concentration-response curves of μLight-expressing HEK293T cells to three peptide ligands (β-endorphin – magenta, ME – gray, DynA13 – black). Error bars represent SEM.

(k) Concentration-response curve of μLight-expressing HEK293T cells to oxycodone and buprenorphine. Error bars represent SEM.

When transiently expressed in mammalian HEK293 cells and dissociated neuronal culture, we observed excellent membrane expression of κLight1.3, δLight, and μLight. All three sensors were activated by their endogenous receptor agonists (100 μM), dynorphin A1-8 (DynA8), ME and β-endorphin, respectively (Signal to noise ratios (SNR) values for κLight1 (HEK) = 7.5 ± 0.45, κLight1.3 (neuron) = 5.6 ± 0.2, δLight (HEK) = 16 ±

0.62, δLight (neuron) = 8.9 ± 0.43, μLight (HEK) = 4.7 ± 0.26) (Figure 4.1C-D, Figure S4.1D). The ligand-induced responses (κLight1.3 ΔF/F (neuron) = 151 ± 5.1%; δLight ΔF/F (neuron) = 123 ± 19.4%; μLight ΔF/F (neuron) = 19.6 ± 3.2%) were blocked by naloxone (1 mM), which is an antagonist for all three receptors (Figure S4.1E-G).

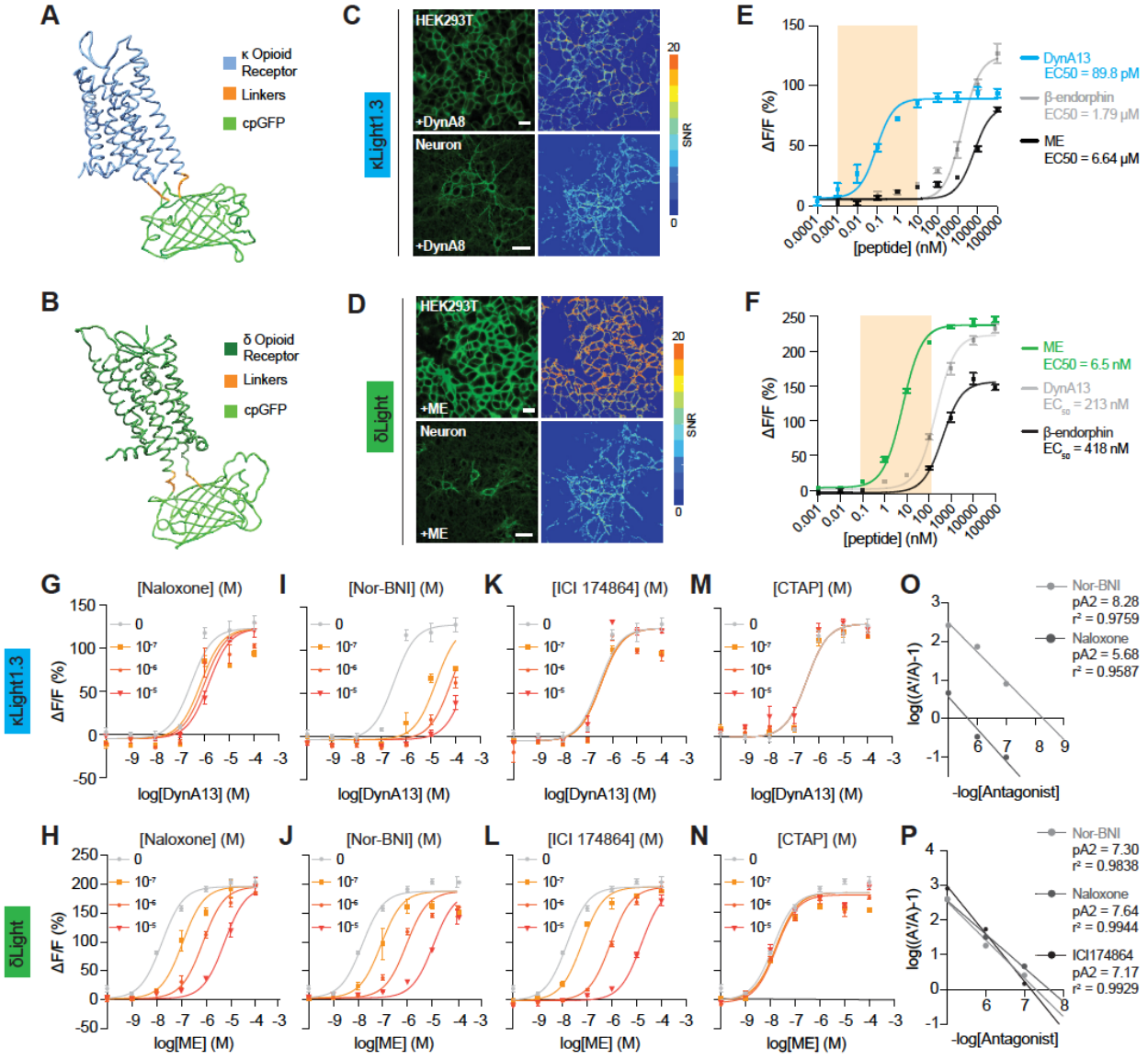

Figure 4.1. Development of the opioid sensors.

(a) Simulated structure of κLight. Kappa opioid receptor (KOR, blue), linkers (orange), circularly permuted GFP (cpGFP, light green).

(b) Simulated structure of δLight. Delta opioid receptor (DOR, dark green), linkers (orange), cpGFP (light green).

(c) Representative images of transient transfection of κLight1.3 in HEK293T cells and dissociated hippocampal neurons. Heatmap indicates signal-to-noise ratio (SNR) upon addition of DynA8 (100 μM). HEK293T images scale bar, 20 μm. Neuron images scale bar, 50 μm.

(d) Representative images of transient transfection of δLight in HEK293Tcells and dissociated hippocampal neurons. Heatmap indicates signal-to-noise ratio (SNR) upon addition of ME (100 μM). HEK293T images scale bar, 20 μm. Neuron images scale bar 50 μm.

(e) κLight1.3-expressing HEK293T cells respond to ligands in a concentration-dependent manner (DynA13 – blue, β-endorphin – gray, ME – black). Error bars represent SEM. The highlighted area corresponds to a concentration range from 1 pM to 10 nM. n = 4 wells each. Dyn = dynorphin, ME = met-enkephalin.

(f) δLight-expressing HEK293T cells respond to ligands in a concentration-dependent manner (ME – green, DynA13 – gray, β-endorphin – black). Error bars represent SEM. The highlighted area corresponds to a concentration range from 100 pM to 100 nM. n = 4 wells each. Dyn = dynorphin, ME = met-enkephalin.

(g) Schild plot of κLight1.3 dose response with 100 nM, 1 μM, and 10 μM of Naloxone. n = 4 wells. Error bars represent SEM. Dyn = dynorphin

(h) Schild plot of δLight dose response with 100 nM, 1 μM, and 10 μM of Naloxone. n = 4 wells. Error bars represent SEM. ME = met-enkephalin.

(i) Schild plot of κLight1.3 dose response with 100 nM, 1 μM, and 10 μM of Nor-binaltorphimine (Nor-BNI). n = 4 wells. Error bars represent SEM. Dyn = dynorphin

(j) Schild plot of δLight dose response with 100 nM, 1 μM, and 10 μM of Nor-BNI. n = 4 wells. Error bars represent SEM. ME = met-enkephalin.

(k) Schild plot of κLight1.3 dose response with 100 nM, 1 μM, and 10μM of ICI174864. n = 4 wells. Error bars represent SEM. Dyn = dynorphin

(l) Schild plot of δLight dose response with 100 nM, 1 μM, and 10 μM of ICI174864. n = 4 wells. Error bars represent SEM. ME = met-enkephalin.

(m) Schild plot of κLight1.3 dose response with 100 nM, 1 μM, and 10 μM of CTAP. n = 4 wells. Error bars represent SEM. Dyn = dynorphin

(n) Schild plot of δLight dose response with 100 nM, 1 μM, and 10 μM of CTAP. n = 4 wells. Error bars represent SEM. ME = met-enkephalin.

(o) Combined Schild regression with Nor-BNI and Naloxone on κLight1.3.

(p) Combined Schild regression with Nor-BNI, Naloxone, and ICI174864 on δLight.

To eliminate response variability due to inconsistent expression level of sensors via transient transfection, we developed HEK293T cell lines stably expressing κLight1.3, δLight, and μLight, respectively (Figure S4.1H). Using these cell lines, we characterized the promiscuity of endogenous opioid peptides on activating sensors [34]. First, all three sensors have consistent excitation peak wavelength at 495 nm and emission peaks at 515

nm (Figure S4.1I). Second, in situ titration showed that all three sensors can be activated by three distinct endogenous opioid peptides but with different potency and efficacy. κLight1.3 responded to dynorphin A1-13 (DynA13) with an apparent EC50 of 89.8 pM, which is three magnitudes higher than β-endorphin and ME. However, at higher concentrations (>10 μM), κLight1.3 displayed higher fluorescent changes to β-endorphin, followed by DynA13 and ME (ΔF/F (κLight - DynA13) = 93.6 ± 3.9%; ΔF/F (κLight - β-endorphin) = 126.9 ± 8.6%; ΔF/F (κLight - ME) = 80.3 ± 1.8%) (Figure 4.1E). δLight is activated by ME with an EC50 of 6.5 nM, which is two orders of magnitude greater than DynA13 and β-endorphin, and has higher fluorescent efficacy compared to these two peptides (ΔF/F (δLight - DynA13) = 232.6 ± 6.8%; ΔF/F (δLight - β-endorphin) = 147.9 ± 4.1%; ΔF/F (δLight - ME) = 246.1 ± 4.6%) (Fig. 1F). Together, at presumed physiological conditions (pM-100 nM), both κLight1.3 and δLight are selective and sensitive to endogenous opioid peptides. In contrast, all three endogenous opioid peptides showed similar sensor potency and efficacy for μLight activation (Figure S4.1J).

By running the in-situ titration in antagonist mode [35], we were able to determine the selectivity of antagonists acting on κLight and δLight. In addition to naloxone, we chose nor-binaltorphimine (Nor-BNI), ICI 174864, and CTAP, which selectively antagonize κOR, δOR, and μOR, respectively. As expected, increasing the concentration of naloxone (100 nM to 10 μM) shifted the apparent EC50 to the right for DynA13 and ME for κLight1.3 and δLight, respetively: naloxone inhibited δLight with 2-fold greater affinity than κLight (p2A (δLight - naloxone) = 7.64, pA2 (κLight - naloxone) = 5.68). Nor-BNI displayed slightly higher affinity in blocking κLight than δLight (pA2 = 8.28 and 7.3

respectively) (Figure 4.1G-J, O-P). We did not observe apparent antagonism of κLight by ICI 174864, whereas it effectively inhibited activation of δLight by ME (pA2 δLight – ICI 174864 = 7.17) (Figure 4.1K, L, O-P). The μOR-selective antagonist CTAP did not affect the EC50 of DynA13 or ME in either κLight or δLight, respectively (Figure 4.1M, N, O-P).

(xvii) Selectivity and Pharmacology of the Opioid Biosensors

We next used a low concentration (10 nM) of a broad panel of endogenous and synthetic ligands to evaluate their rank order of response for inducing sensor fluorescence. We found that known κOR selective endogenous peptides induced significantly greater fluorescence changes at κLight compared to δOR- or μOR-selective ligands. Among the dynorphin peptides, the shorter form dynorphin DynA1-8 induced lower activation of κLight compared to DynA1-13. Interestingly, nalfurafine, a synthetic κOR agonist, elicited an almost two-fold greater fluorescent change compared to the dynorphins (Figure 4.2A). For δLight cells, enkephalins and δOR-selective agonists elicited larger responses compared to other ligands; deltorphin I displayed similar efficacy as ME and LE for δLight activation (Figure 4.2B). Endogenous opioid peptide agonists at μOR, including β-endorphin, endomorphin, metorphinamide, and BAM18, displayed various efficacies for κLight1.3 and δLight activation, although to a much smaller extent compared to κOR- and δOR-specific peptides. Notably, U50,488 and U69,593 selectively activated κLight over δLight, while SNC80 and SNC162 activated δLight over κLight, confirming the sensors' specificity to receptor-specific small molecule agonists (Figure 4.2A, B).

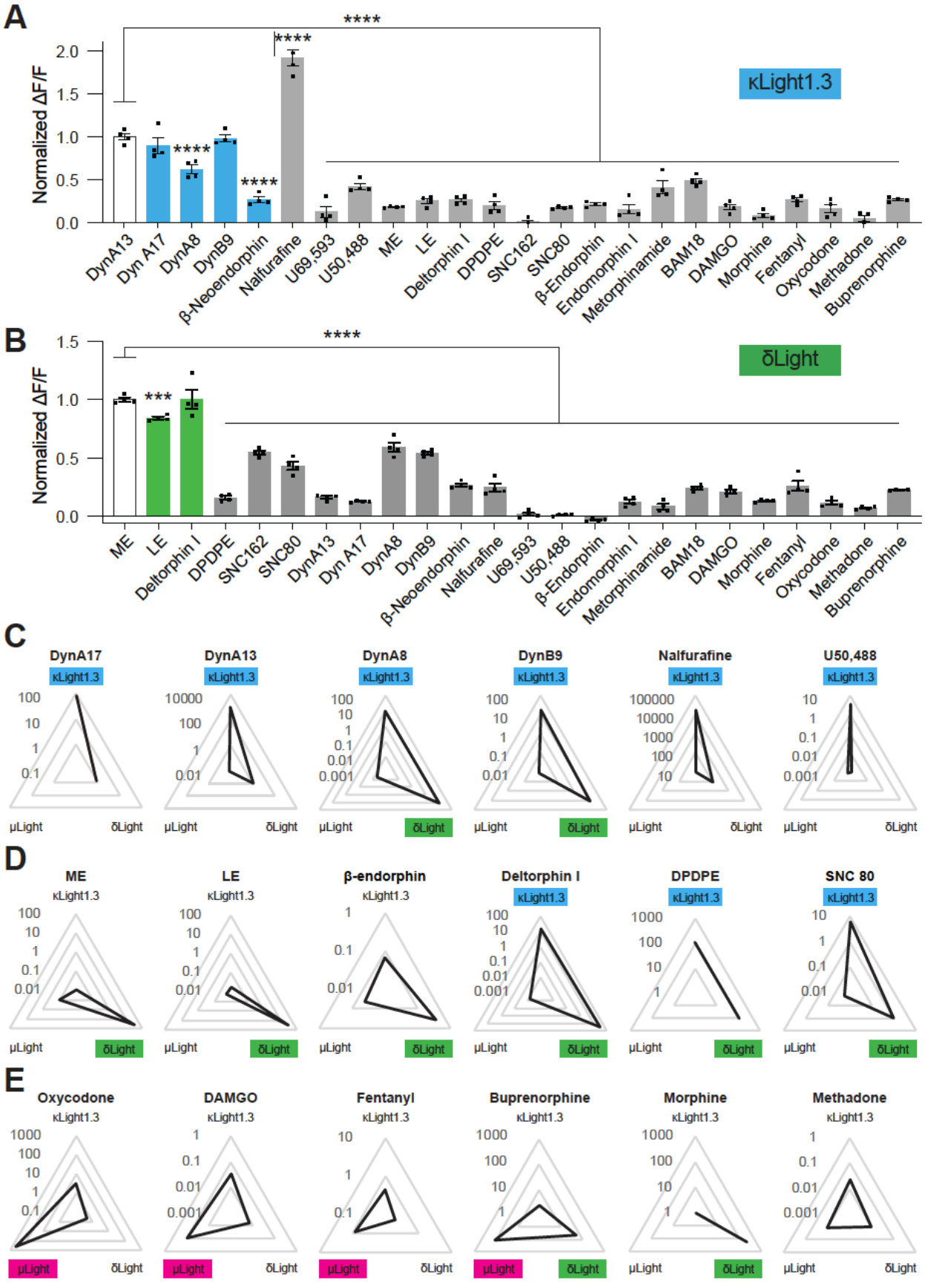
A
Normalized ΔF/F
κLight1.3
****
****
****
****
DynA13
Dyn A17
DynA8
DynB9
β-Neoendorphin
Nalfurafine
U69,593
U50,488
ME
LE
Deltorphin I
DPDPE
SNC162
SNC80
β-Endorphin
Endomorphin I
Metorphinamide
BAM18
DAMGO
Morphine
Fentanyl
Oxycodone
Methadone
Buprenorphine
B
Normalized ΔF/F
δLight
****
***
ME
LE
Deltorphin I
DPDPE
SNC162
SNC80
DynA13
Dyn A17
DynA8
DynB9
β-Neoendorphin
Nalfurafine
U69,593
U50,488
β-Endorphin
Endomorphin I
Metorphinamide
BAM18
DAMGO
Morphine
Fentanyl
Oxycodone
Methadone
Buprenorphine
C
DynA17
DynA13
DynA8
DynB9
Nalfurafine
U50,488
κLight1.3
μLight
δLight
D
ME
LE
β-endorphin
Deltorphin I
DPDPE
SNC 80
κLight1.3
μLight
δLight
E
Oxycodone
DAMGO
Fentanyl
Buprenorphine
Morphine
Methadone
κLight1.3
μLight
δLight

Figure 4.2. Pharmacological characterization of κLight and δLight.

(a) Normalized change in fluorescence (ΔF/F) of κLight1.3 upon addition of the listed compounds (10 nM). ΔF/F of all compounds are normalized to DynA13 (DynA13: 1 ± 0.03, DynA17: 0.89 ± 0.08, DynA8: 0.61 ± 0.04, DynB9: 0.97 ± 0.03, β-Neoendorphin: 0.26 ± 0.03, Nalfurafine: 1.91 ± 0.09, U69,593: 0.12 ± 0.06, U50,488: 0.42 ± 0.03, ME: 0.18 ± 0.005, LE: 0.24 ± 0.02, Deltorphin I: 0.26 ± 0.02, DPDPE: 0.19 ± 0.04, SNC162: 0.009 ± 0.02, SNC 80: 0.17 ± 0.008, β-Endorphin: 0.21 ± 0.01, Endomorphin I: 0.15 ± 0.05, Metorphinamide: 0.41 ± 0.06, BAM18: 0.48 ± 0.03, DAMGO: 0.17 ± 0.03, Morphine: 0.08 ± 0.02, Fentanyl: 0.26 ± 0.02, Oxycodone: 0.16 ± 0.04, Methadone: 0.04 ± 0.03, Buprenorphine: 0.27 ± 0.01, n = 4 wells each, ****p < 0.0001, ***p < 0.001, one-way ANOVA compared to DynA13 with Šídák's multiple comparisons test).

(b) Normalized change of fluorescence (ΔF/F) of δLight upon addition of the listed compounds (10 nM). ΔF/F of all compounds are normalized to met-enkephalin (ME) (ME: 1 ± 0.01, LE: 0.84 ± 0.01, Deltorphin I: 1 ± 0.07, DPDPE: 0.15 ± 0.01, SNC162: 0.54 ± 0.02, SNC80: 0.42 ± 0.03, DynA13: 0.15 ± 0.01, DynA17: 0.12 ± 0.004, DynA8: 0.58 ± 0.03, DynB1-9: 0.53 ± 0.01, β-Neoendorphin: 0.26 ± 0.01, Nalfurafine: 0.24 ± 0.03, U69,593: 0.014 ± 0.014, U50,488: 0.009 ± 0.004, β -Endorphin: -0.03 ± 0.004, Endomorphin I: 0.12 ± 0.01, Metorphinamide: 0.07 ± 0.02, BAM18: 0.23 ± 0.01, DAMGO: 0.2 ± 0.01, Morphine: 0.12 ± 0.005, Fentanyl: 0.25 ± 0.04, Oxycodone: 0.11 ± 0.01, Methadone: 0.06 ± 0.006, Buprenorphine: 0.22 ± 0.003, n = 4 wells each. ****p < 0.0001, one-way ANOVA compared to DynA13 with Dunnett's multiple comparisons test).

(c) Log s-slope values (in nM^{-1}) of KOR-specific ligands plotted in triangle plots with κLight (blue) on top, δLight (green) on the bottom right corner, and μLight (magenta) on the bottom left corner. Higher s-slope values are located on the outer ring. Dyn = dynorphin, Enk = enkephalin.

(d) Log s-slope values (in nM^{-1}) of DOR-specific ligands plotted in triangle plots with κLight (blue) on top, δLight (green) on the bottom right corner, and μLight (magenta) in the bottom left corner. Higher s-slope values are located on the outer ring.

(e) Log s-slope values (in nM^{-1}) of MOR-specific ligands plotted in triangle plots with κLight (blue) on top, δLight (green) on the bottom right corner, and μLight (magenta) in the bottom left corner. Higher s-slope values are located on the outer ring.

We then used radar plots to compare the proportionality constant (s-slope) of various receptor-selective ligands for activating each sensor (Figure 4.2C-E, Table 4.1). The s-slope is a constant that links the variables of dynamic range ($\Delta F/F_{max}$) and EC50 of a given sensor response to a drug, defined as $\Delta F/F_{max}$ / EC50. It highlights both the efficacy and potency of drugs on sensor responses [36]. By plotting s-slope values of individual ligands on three sensors as a radar plot, we found that the long forms of Dyn are more potent in activating κLight1.3 than the short forms, the latter of which displayed considerable activity at δLight as well. Both nalfurafine and U50,488 were selective for κLight1.3 (Figure 4.2C). The enkephalins (both ME and Leu-Enk (LE)), as well as β-

endorphin, were highly selective for δLight, whereas deltorphin I and DPDPE displayed similar s-slopes for κLight1.3 and δLight. Despite low efficacy at κLight1.3, the s-slope of SNC80 was slightly higher at κLight1.3 than that at δLight (Figure 4.2D). Notably, μLight was insensitive to morphine, whereas the latter induced slight fluorescent increases at κLight1.3 and δLight. In contrast, methadone activated all three sensors with similar efficacy and potency. Buprenorphine activates all three sensors but showed higher potency for μLight and δLight. On the other hand, other μOR-selective synthetic drugs, including DAMGO, fentanyl, and oxycodone, engaged μLight with higher s-slopes compared to κLight1.3 and δLight (Figure 4.2E). Interestingly, oxycodone and buprenorphine suppressed, rather than enhanced, μLight fluorescence; thus, the s-slope was calculated using the absolute $\Delta F/F_{max}$ (Figure S4.1K).

To determine whether the insertion of cpGFP perturbs the ligand-binding properties of these receptor-based opioid sensors, we conducted a radioligand binding assay using cells expressing each sensor and a panel of ligands that includes several endogenous peptides [16,37,38]. For μLight cells, endogenous opioid peptides displaced [^{3}H] diprenorphine binding with nM IC_{50} \except for metorphamide (μM IC_{50}). Specific binding detected in the presence of these peptides ranges from 34 ± 2% for peptide F to 82 ± 2% with BAM18. In the case of synthetic agonists, we see that DAMGO and oxycodone have nM IC_{50} while morphine and fentanyl have μM IC_{50}. Interestingly, in the case of fentanyl we find that it exhibits nM IC_{50} in CHO cells stably expressing μ receptors (Table 4.2). For δLight cells, the endogenous opioid peptides and the synthetic agonists displace [^{3}H] diprenorphine binding with nM IC_{50} except for peptide E (μM IC_{50}).

Specific binding detected in the presence of the endogenous peptides ranges from 32 ± 3% for BAM18 to 77 ± 4% with ME (Table 4.2). For κLight1.3 cells, the endogenous opioid peptides and the synthetic agonist, U69,593 displace [^{3}H] diprenorphine binding with nM $IC_{50.}$ Specific binding detected in the presence of the endogenous peptides ranges from 10 ± 5% for ME to 76 ± 2% with DynB13 (Table 4.2). For the peptides DynA8, β-endorphin, and ME, we used s-slope analysis to compare binding parameters with the sensors to those reported for opioid receptors under similar assay conditions [16]. We found that they correlate in all three cases (Figure S4.2A-C). Similarly, the s-slope determined by the fluorescence assay was also correlated to that determined by radio-ligand binding (Figure S4.2D-F). Most importantly, we found that the effects of these peptides on receptors' confirmation can be differentiated by the fluorescence assay ($\Delta F/F_{max}$), but not by radio-ligand binding approach (E_{max}) (Figure S4.2G-I).

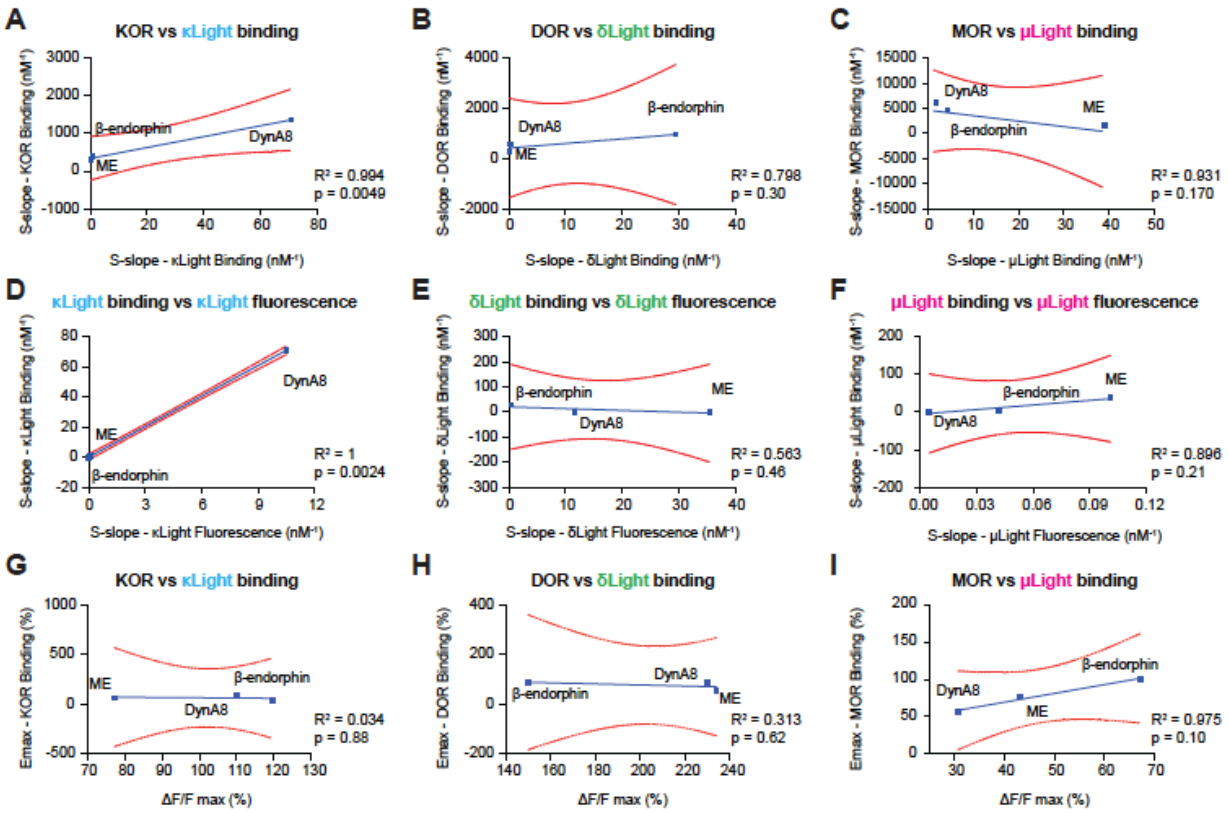

Figure S4.2. Binding studies of selected compounds on the opioid sensors and receptors.

(a) Regression plot between the s-slope (maximum displacement / IC50, in nM^{-1}) for KOR (S-slope - KOR Binding) and κLight1.3 (S-slope - κLight Binding) measured with a radio-ligand binding assay. Red curves indicate 95 % confidence interval.

(b) Regression plot between the s-slope (maximum displacement / IC50, in nM^{-1}) for DOR (S-slope - DOR Binding) and δLight (S-slope - δLight Binding) measured from radio-ligand binding assay. Red curves indicate 95 % confidence interval.

(c) Regression plot between the s-slope (maximum displacement / IC50, in nM^{-1}) for MOR (S-slope - MOR Binding) and μLight (S-slope - μLight Binding) measured from radio-ligand binding assay. Red curves indicate 95 % confidence interval.

(d) Regression plot between the s-slope (maximum displacement / IC50, in nM^{-1}) for KOR measured from radio-ligand binding assay (S-slope - κLight Binding) and the s-slope ($\Delta F/F_{max}$ / EC50, in nM^{-1}) for κLight1.3 measured from sensor imaging (S-slope - κLight Fluorescence). Red curves indicate 95 % confidence interval.

(e) Regression plot between the s-slope (maximum displacement / IC50, in nM^{-1}) for DOR measured from radio-ligand binding assay (S-slope - δLight Binding) and the s-slope in ($\Delta F/F_{max}$ / EC50, in nM^{-1}) for δLight measured from sensor imaging (S-slope - δLight Fluorescence). Red curves indicate 95 % confidence interval.

(f) Regression plot between the s-slope (maximum displacement / IC50, in nM^{-1}) for MOR measured from radio-ligand binding assay (S-slope - μLight Binding) and the s-slope ($\Delta F/F_{max}$ / EC50, in nM^{-1}) for μLight measured from sensor imaging (S-slope - μLight Fluorescence). Red curves indicate 95 % confidence interval.

(g) Regression plot between the maximum displacement in (%) of indicated ligands from KOR (Emax - KOR Binding) measured with a radio-ligand binding assay and maximum fluorescence change in (%) of κLight1.3 ($\Delta F/F_{max}$) measured from sensor imaging. Red curves indicate 95% confidence interval.

(h) Regression plot between the maximum displacement in (%) of indicated ligands from DOR (Emax - DOR Binding) measured with a radio-ligand binding assay and maximum fluorescence change in (%) of δLight ($\Delta F/F_{max}$) measured from sensor imaging. Red curves indicate 95% confidence interval.

(i) Regression plot between the maximum displacement in (%) of indicated ligands from MOR (Emax - MOR Binding) measured with a radio-ligand binding assay and maximum fluorescence change in (%) of μLight (ΔF/Fmax) measured from sensor imaging. Red curves indicate 95% confidence interval.

Together, these data suggest that the cpGFP insert is not likely to perturb the binding pockets of the patent receptor. Our studies demonstrate that peptide binding to an opioid sensor triggers fluorescence changes that correlate with the binding of the peptide to the receptor, making the sensors serve as useful tools to quantify differences in ligand-driven conformational changes between peptides.

(xviii) Probing Dynorphin Release by Simultaneous Photo-Stimulation and κLight Dynamics

Photoactivatable or "caged" synthetic variants of opioid NPs or photosensitive nano-vesicles (nVs) can be activated with millisecond precision using short flashes of light and have been optimized for spectrally orthogonal use with GFP-based probes [39]. The spatiotemporal scale over which NP volume transmission occurs in brain tissue has been determined by combining photoactivatable NPs or nVs, electrophysiological recording or cell-based NP biosensors. We thus asked whether κLight is capable of reporting opioid peptide volume transmission in brain tissue using photo-uncaging experiments.

To choose the most appropriate κLight variant that balances dynamic range and sensitivity, we first examined the responses and kinetics of various κLight variants using photoactivable Dyn8 (CYD8) [29]. We injected AAV9-hSyn-κLight1.x (top kLight variants including 1.2a, 1.2b, 1.2c, 1.3) into the dorsal striatum (dStr) of C57 mouse pups (P0 – P3) and prepared the brain slices after 3 weeks of expression (Figure 4.3A). On the day of imaging, CYD8 was circulated in the bath and photo-uncaged with 50 ms flash of 355 nm laser light over an area of 700 μm^2, while imaging the responses of κLight with a 473 nm LED within the same region (Figure 4.3B). Among all the κLight variants tested (Figure S4.3A), κLight1.3 yielded the greatest response ($\Delta F/F$=11 ± 1.4 %) (Figure 4.3C, D), followed by κLight1.2a ($\Delta F/F$=9.09 ± 0.81 %), κLight1.2c ($\Delta F/F$=6.84 ± 0.65 %), and κLight1.2b ($\Delta F/F$=5.1 ± 0.51 %) (Supplementary Fig. 3B, C). The uncaging response was completely blocked by the presence of naloxone (0.5 ± 0.1 %) (Figure 4.3D), confirming that the fluorescence change is due to ligand-dependent sensor activation, as opposed to being an artifact of the UV light flash. While κLight1.3 had the greatest $\Delta F/F$, we noticed that its response was slow to decay in comparison to most of the other variants (tau_{off} - κLight1.3 = 202.1 sec, tau_{off} - κLight1.2a = 179.7 sec, tau_{off} - κLight1.2b = 246.1 sec, tau_{off} - κLight1.2c = 165.0 sec) (Figure 4.3C, Figure S4.3B), presumably due to the higher affinity for dynorphins that results in slower peptide dissociation (Figure S4.3D).

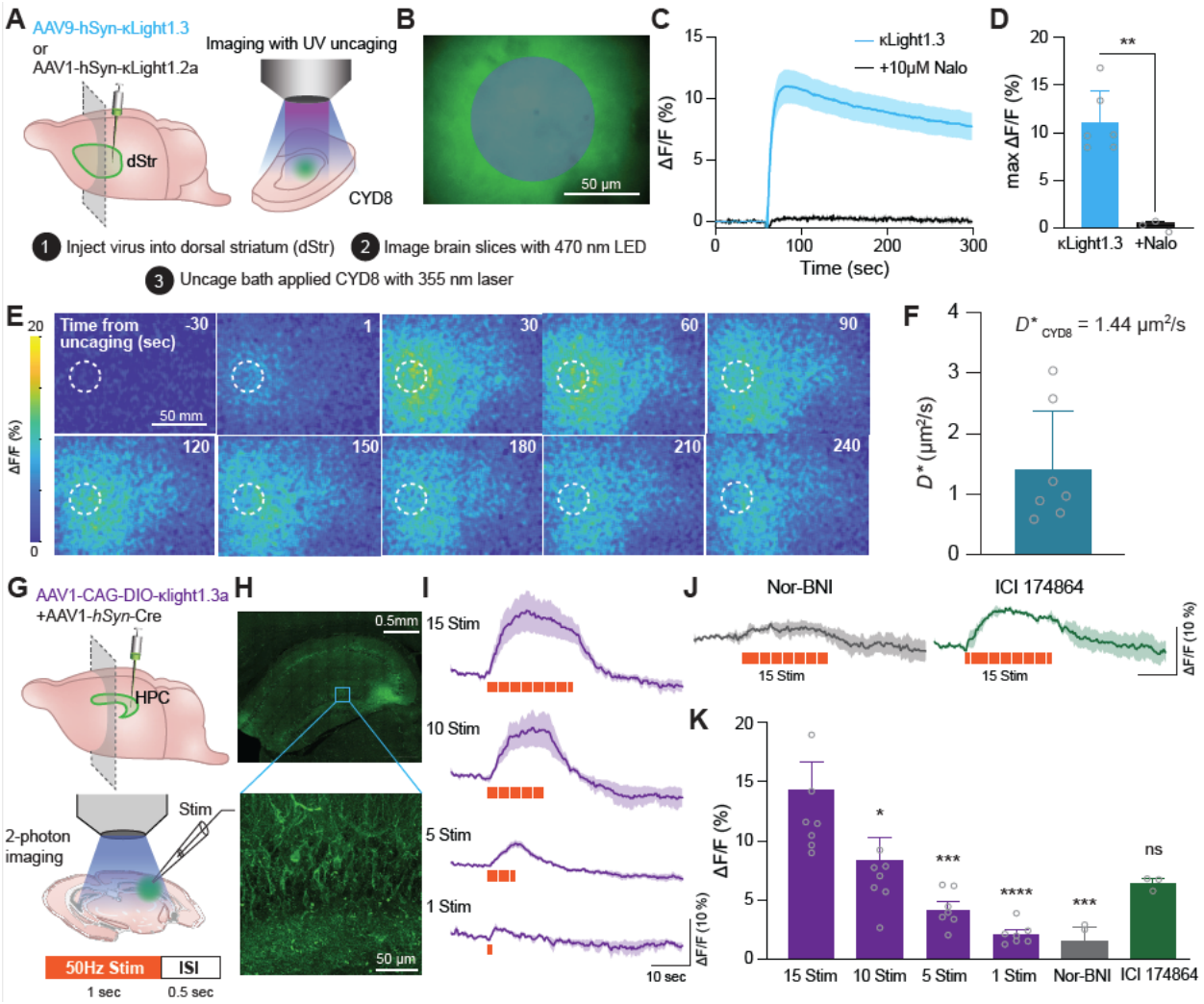

Figure 4.3. κLight1.3 characterization in acute brain slices.

(a) Experimental schematics indicating virus injections in the dorsal striatum (dStr), followed by imaging of acute brain slices and photouncaging CYD8 with a 355 nm laser.

(b) Image of tissue as acquired through video acquisition, with a semitransparent gray circle indicating the field of UV illumination with a collimated 355 nm laser. Scale bar, 50 μm.

(c) Response of κLight1.3 to CYD8 photouncaging (blue, n = 6 slices) in the absence and presence of naloxone (Nalo, 10 μM) (black, n = 3 slices). Solid lines represent the mean and the shaded areas represent SEM.

(d) Quantification of the peak ΔF/F evoked by CYD8 photouncaging. κLight1.3 (blue); 11.1 ±.1.36 %, + naloxone (black); 0.51 ± 0.12 %, p = 0.0011, unpaired t test. Error bar represents SEM.

(e) Time course of κLight1.2a photoactivation after CYD8 (5 μM) photouncaging in the dorsal striatum. The dotted circle indicates the site of UV illumination. Heatmap indicates ΔF/F (%). Scale bar, 50 μm.

(f) Summary of experiments determining the apparent diffusion coefficient, n = 7 slices from 4 mice. D* = 1.4 μm²/s. Error bar represents SD.

(g) Experimental schematics indicating virus injections in the hippocampal complex (HPC), followed by local electrical stimulation with trains of 1 second, 50 Hz stimuli with a 0.5 sec inter-stimulation-interval.

(h) Representative image showing expression of κLight1.3a in CA3 (top), scale bar 0.5 mm, and zoomed in to visualize the localization of localization κLight1.3a to the membranes of neuronal processes in the dentate gyrus (bottom), scale bar 50 μm.

(i) Average κLight1.3a responses to electrical stimulation with varying numbers of stimuli (Stim). Solid lines represent the mean, and shaded areas represent SEM.

(j) Average κLight1.3a response to electrical stimulation in the presence of antagonists Nor-BNI (gray) and ICI174864 (green). Solid lines represent the mean, and shaded areas represent SEM.

(k) Bar graph summarizing the peak fluorescence response to each stimulation condition. 15 stim (n = 6 slices): 14.3 ± 2.4 %, 10 stim (n = 6 slices): 8.39 ± 1.9 %, 5 stim (n = 6 slices): 4.28 ± 0.6 %, 1 stim (n = 6 slices): 2.12 ± 0.3 %, Nor-BNI (100 μM, n = 3 slices): 1.57 ± 1.2 %, ICI174864 (100 μM, n = 3 slices): 6.44 ± 0.3 %. Ordinary one-way ANOVA with Bonferroni's multiple comparisons test, individual conditions compared to 15 stim, 15 stim vs. 10 stim: *p = 0.0492, 15 stim vs. 5 stim: ***p = 0.0005, 15 stim vs. 1 stim: ****p<0.0001, 15 stim vs. Nor-BNI: ***p = 0.0007, 15 stim vs. ICI174864: ns, p = 0.0557).

We next examined whether sensor expression might alter the ability of peptide ligands to engage endogenous opioid receptors. For this experiment, we used κLight1.2a, which exhibited faster decay kinetics than κLight1.3 upon DynA8 photorelease, yet still produced a relatively large ΔF/F. AAVs encoding κLight1.2a or GFP control were injected into the hippocampus of C57 pups (P0 – P3) and allowed to express for a minimum of 3 weeks before acute slices were prepared for electrophysiology (Supplementary Fig3E). Parvalbumin interneurons in the CA1 region of the hippocampus express MOR and DOR, which act presynaptically to suppress synaptic transmission [40]. Although DynA8's primary target is KOR, it also binds to MOR and DOR (e.g. Fig 2B and Table 4.1) [41]. This allowed us to ask whether the activation of MOR and DOR by DynA1-8 is altered by the expression of κLight1.2a. To assay opioid receptor function, we recorded inhibitory currents (IPSCs) in pyramidal cells, evoked with a stimulation protocol that favors MOR- and DOR-sensitive parvalbumin synapses [40] (Figure S4.3F). Photorelease of DynA1-8 using 5 ms flashes of 355 nm light produced a rapid, power-dependent reduction in IPSC amplitude that reversed over the course of

several minutes (Figure S4.3G,H). Compared to GFP control, κLight1.2a expression altered neither the degree of IPSC suppression, nor the time-course of IPSC recovery in response to DynA8 photorelease across all light powers densities examined (Figure S4.3I,J). These results suggest that κLight1.2a expression does not result in sufficient ligand buffering as to perturb the activation of endogenous opioid receptors.

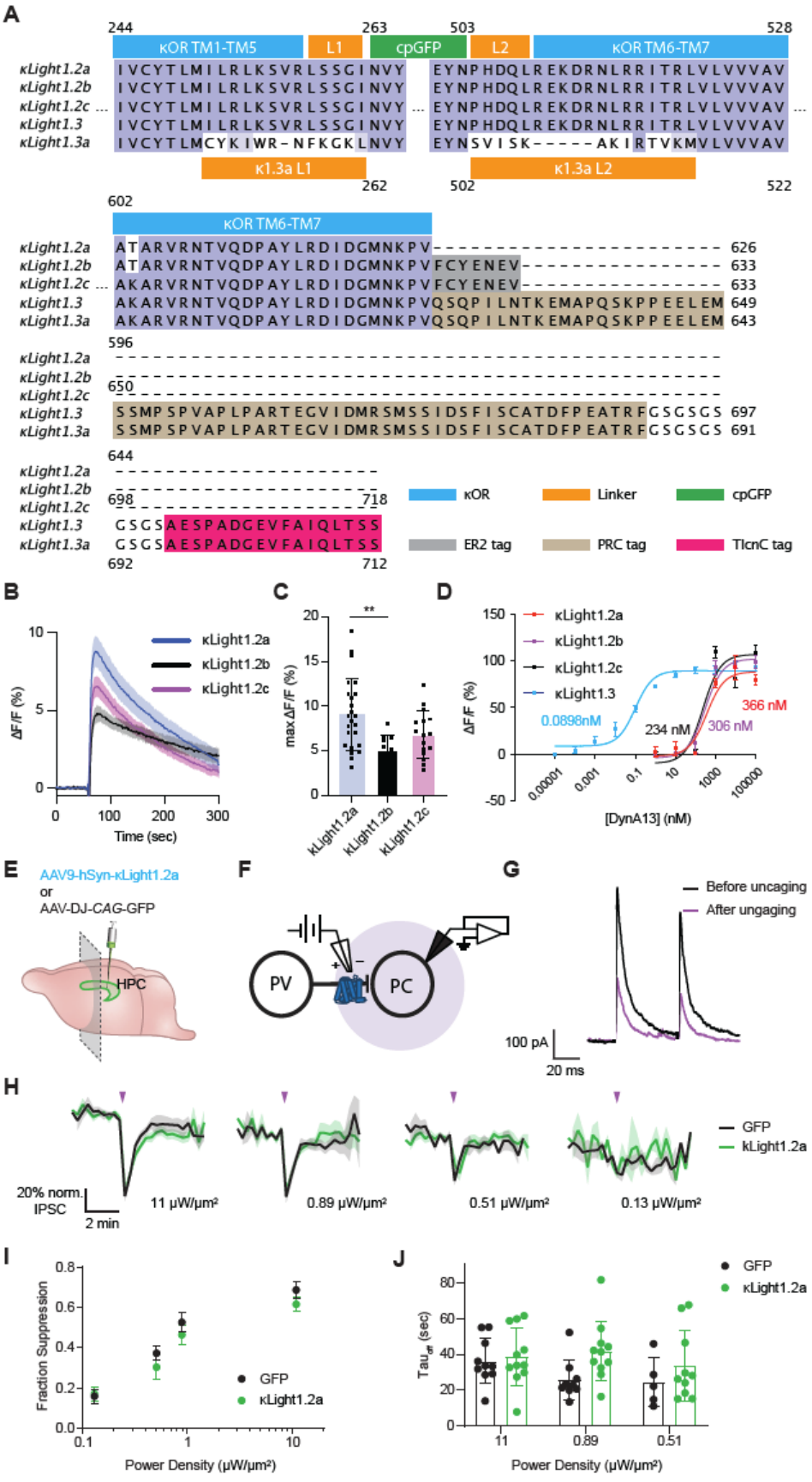
A
244
263
503
528
κOR TM1-TM5
L1
cpGFP
L2
κOR TM6-TM7
κLight1.2a
κLight1.2b
κLight1.2c
κLight1.3
κLight1.3a
κ1.3a L1
κ1.3a L2
262
502
522
602
κOR TM6-TM7
626
633
633
649
643
596
650
698
718
644
692
712
κOR
Linker
cpGFP
ER2 tag
PRC tag
TlcnC tag
B
ΔF/F (%)
Time (sec)
C
max ΔF/F (%)
**
D
ΔF/F (%)
0.0898nM
234 nM
306 nM
366 nM
[DynA13] (nM)
E
AAV9-hSyn-κLight1.2a
or
AAV-DJ-CAG-GFP
HPC
F
PV
PC
G
Before uncaging
After ungaging
100 pA
20 ms
H
20% norm. IPSC
2 min
11 μW/μm²
0.89 μW/μm²
0.51 μW/μm²
0.13 μW/μm²
GFP
κLight1.2a
I
Fraction Suppression
Power Density (μW/μm²)
J
Tau_off (sec)
Power Density (μW/μm²)

Figure S4.3. Comparison of top κLight variants and buffering effect study.

(a) Sequence alignment of κLight1.2a, κLight1.2b, κLight1.2c, κLight1.3, and κLight1.3a. Purple indicates the same residues across all variants. Blank indicates different residues. Blue color indicates KOR sequence. Orange indicates linkers. Green indicates cpGFP sequences. Gray indicates the sequence for the ER2 tag. Khaki indicates the sequence for the PRC tag, and magenta indicates the TlcnC tag.

(b) CYD8 uncaging response comparison between κLight1.2a (blue, n = 19 videos), κLight1.2b (black n = 11 videos), and κLight1.2c (magenta, n = 16 videos) expressed in dStr in acute brain slices. The solid line represents the mean, and the shaded area represents SEM.

(c) Max ΔF/F (%) at the peak of the CYD8 uncaging responses for κLight1.2a (blue, n = 19 videos), κLight1.2b (black, n = 11 videos), and κLight1.2c (magenta, n = 16 videos). κLight1.2a: 9.09 ± 0.8 %, κLight1.2b: 5.1 ± 0.5 %, κLight1.2c: 6.84 ± 0.7 %. **p = 0.0027, ordinary one-way ANOVA with Dunnett's multiple comparisons test. Error bars represent SEM.

(d) Dose response curves for DynA13 at κLight1.2a (red, n = 3 wells, EC50 = 366 nM), κLight1.2b (purple, n = 5 wells, EC50 = 306 nM), κLight1.2c (black, n = 4 wells, EC50 = 234 nM), and κLight1.3 (blue, n = 4 wells, 0.0898 nM). Error bars represent SEM.

(e) Schematic indicating injection of C57/B6J pups with AAV1-hSyn-κLight1.2a or AAV-DJ-CAG-GFP in the hippocampus followed by 3 weeks of expression prior to preparation of acute brain slices for electrophysiology.

(f) Schematic of the electrophysiological recording configuration. Whole-cell voltage-clamp recordings are obtained from pyramidal cells (PCs) held at 0 mV while parvalbumin (PV) basket cell axons are preferentially stimulated with a narrow-tipped theta-glass-based bipolar stimulating electrode. Two electrical stimuli are applied 50 ms apart to drive synaptic inhibition. A 5 ms flash of 355 nm light (semitransparent purple circle) is applied to photorelease DynA8, which acts on presynaptic mu and delta opioid receptors on the PV cell to suppress the synaptic output.

(g) Example inhibitory post-synaptic currents (IPSCs) before (black) and after (purple) DynA8 photorelease.

(h) Time-course of IPSC suppression in response to DynA8 photorelease in slices expressing κLight1.2a (n = 13 cells from 3 mice, green) or GFP (n = 10 cells from 3 mice, black) using different intensities of UV light. Traces indicate the mean peak IPSC (normalized to 100%) over time, which was probed every 20 sec. Purple arrows indicate the application of UV light. The solid lines represent the mean, and the shaded areas represent SEM.

(i) Power-response curve summarizing the fraction of the baseline IPSC suppressed by DynA8 photorelease in slices expressing κLight1.2a (n = 13 cells from 3 mice, green) or GFP (n = 10 cells from 3 mice, black). No significant differences were detected at different power densities (Multiple Mann-Whitney tests between GFP and κLight1.2a at different power densities: 0.13 $\mu W/\mu m^2$: p = 0.91, 0.51 $\mu W/\mu m^2$: p = 0.71, 0.89 $\mu W/\mu m^2$: p = 0.71, 11 $\mu W/\mu m^2$: p = 0.70, non-significant).

(j) Average time constant of IPSC recovery after DynA8 photorelease in slices expressing κLight1.2a (n = 11-12 cells from 3 mice, green) or GFP (n = 6-9 cells from 3 mice, black). No significant differences were detected (Multiple Mann-Whitney tests between GFP and κLight1.2a at different power densities: 0.51 $\mu W/\mu m^2$: p = 0.52, 0.89 $\mu W/\mu m^2$: p = 0.04, 11 $\mu W/\mu m^2$: p = 0.56, non-significant).

We next measured the spread of DynA1-8 in space and time. AAV1-hSyn-κLight1.2a was injected into dStr and imaging was performed three weeks post-injection (Figure 4.3A). Small volumes of DynA1-8 were rapidly photoreleased using a focused 25

μm diameter spot of 355 nm light (Figure 4.3E) while monitoring sensor activation at distances of up to 125 μm away. We observed that the peak ΔF/F decreased with increased time from uncaging and with distance from the uncaging site (Figure S4.4A). For each video frame post-uncaging, we plotted the fluorescence profile as a function of distance from the uncaging spot and extracted the ΔF/F half-width, which was used to compute an effective diffusion coefficient (D^*) of 1.4 ± 0.4 $\mu m^2/s$ (n = 7 slices from 4 mice) for DynA8 in dStr (Figure S4.4B-D). These results suggest that DynA1-8 can reach receptors over 100 μm away from release sites within several seconds of release in the hippocampus.

(xix) Two-Photon Imaging of Endogenous Dynorphin Release Triggered by Electrical Stimulation

It has been historically difficult to determine the electrical parameters that can effectively trigger the release of endogenous opioid peptides in brain tissue. We thus examined if κLight is capable of detecting endogenous opioid peptide release triggered by electrical stimulation ex vivo. To do so, we first improved the basal fluorescence of κLight1.3 by integrating CYKIWRNFKGK as linker 1 and SVISKAKIRTV as linker 2 derived from the oxytocin sensor $MTRIA_{OT}$ [42] (Figure S4.3A). This new variant, named κLight1.3a, displayed a similar dynamic range (κLight1.3 at 155 ± 11.6%, κLight1.3a at 152 ± 29.5%, p=0.92, unpaired t test), but >2x the basal brightness compared to κLight1.3 (κLight1.3 at 25 ± 0.08, κLight1.3a at 61.8 ± 7.6, p=0.0075, unpaired t test) (Figure S4.4E, F). Immunoreactivity studies have shown abundant dynorphin stored in dentate granule cells, dynorphin dynamics in CA3 have also been shown to have an association with

stress under various behavior paradigms, and dynorphins have been shown to inhibit excitatory neurotransmission and prevent the induction of long-term potentiation (LTP) in hippocampus [43-45]. We sparsely expressed κLight1.3a in CA3 by delivering AAV1-CAG-DIO-κLight1.3a in combination with AAV1-hSyn-Cre (Figure 4.3G). After 3 weeks of expression, we observed bright labeling of neurons in CA3 and dentate gyrus with clear processes in the basal state using two-photon imaging (Figure 4.3H).

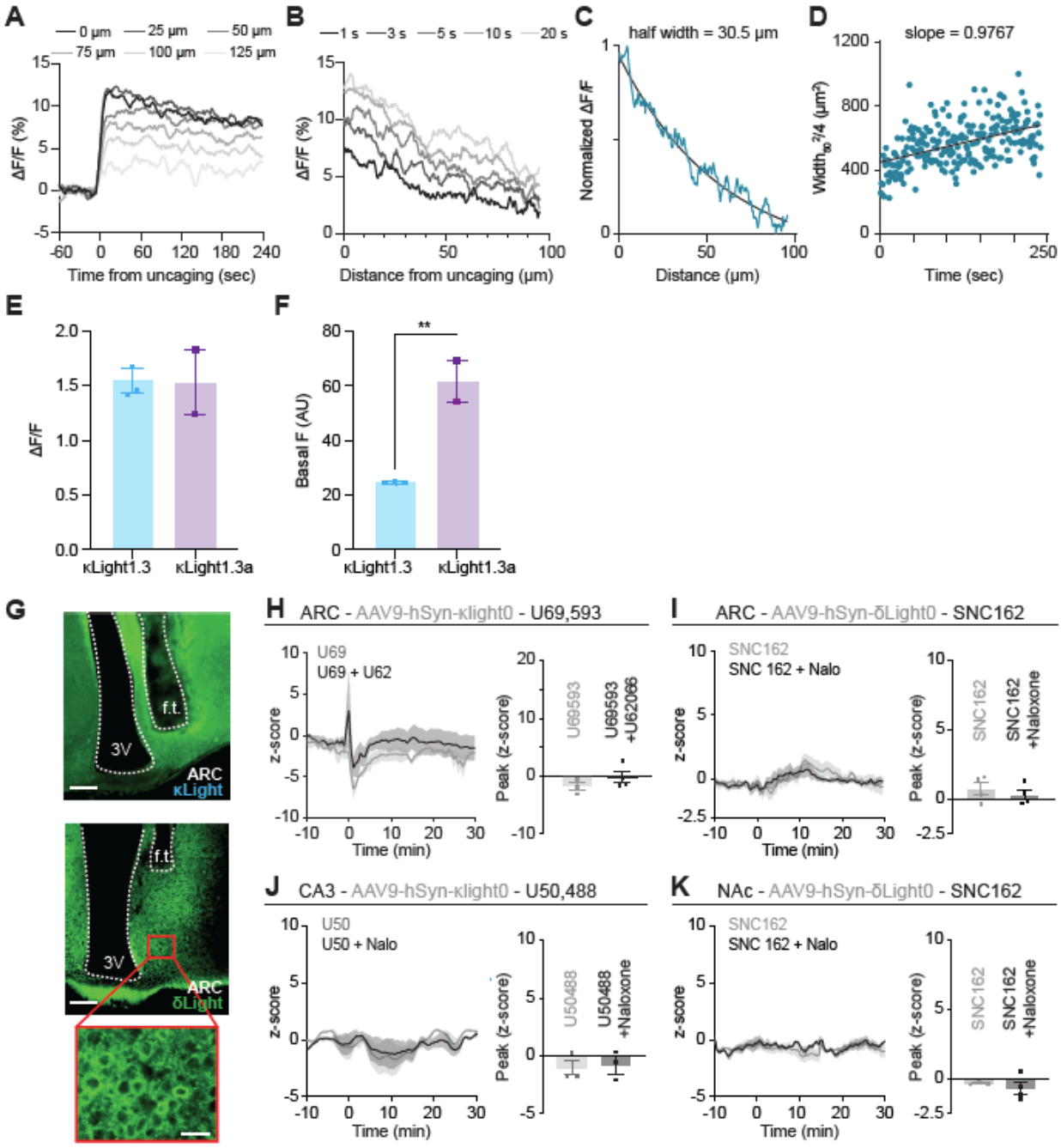

Figure S4.4. Dynorphin diffusion analysis and in vivo pharmacology with control sensors.

(a) Representative example of the fluorescence response of κLight1.2a for single pixels along the center of the imaging field at various distances from the site of DynA8 photorelease.

(b) Representative examples of fluorescence profile as a function of distance from the uncaging site at differing time points after uncaging.

(c) Representative example of a fluorescence profile at a single time (5 sec, as in **Supplementary Figure 4B**), normalized and fit to an exponential function in order to extract the half width (30.5 µm).

(d) Representative example plot of the half-width squared/4 vs. time for determination of the apparent diffusion coefficient *D**. The fluorescence profile fits (e.g. Supplementary Fig.4C) were repeated in 1 second time bins to extract the half-width. The slope of this linear regression is the apparent diffusion coefficient *D**.

(e) Fluorescence response (ΔF/F) to U50,488 (100 μM) compared between κLight1.3 (blue, n = 3 wells), and κLight1.3a (magenta, n = 2 wells). κLight1.3: 1.56 ± 0.12, κLight1.3a: 1.53 ± 0.3, unpaired t test, p = 0.93, non-significant. Error bar represents SEM.

(f) Basal fluorescence compared between κLight1.3 (blue, n = 3 wells), and κLight1.3a (magenta, n = 2 wells). κLight1.3: 25.0 ± 0.08, κLight1.3a: 61.8 ± 7.7, unpaired t test, **p = 0.0075. Error bar represents SEM.

(g) Representative images showing κLight (top), δLight (middle), and zoomed-in image for δLight (bottom) expression in ARC. Scale bar 150 μm for both κLight and δLight. δLight zoomed insert has scale bar = 30 μm. Abbreviations: ventricle (3V), fiber track (f.t.).

(h) (Left) κLight0 response to 3 mg/kg U69,593 (gray, n = 3 animals), and 3 mg/kg U69,593 + 1 mg/kg U62,066 (black, n = 4 animals) in ARC, Solid lines represent the mean, and shaded areas represent SEM. (Right) bar graph indicating the peak z-score of each response, U69,593: -1.9 ± 0.7 %, U69,593 + U62,066: -0.2 ± 1 %, unpaired t test, p = 0.2625, non-significant. U69 = U69,593, U62 = U62,066.

(i) (Left) δLight0 response to 5 mg/kg SNC162 (gray, n = 4 animals), and 5 mg/kg SNC162 + 4 mg/kg naloxone (black, n = 4 animals) in ARC. Solid lines represent the mean, and shaded areas represent SEM. (Right) bar graph indicating the peak z-score of each response, SNC162: 0.77 ± 0.5 %, SNC162 + naloxone: 0.33 ± 0.4 %, unpaired t test, p = 0.4948, non-significant. Nalo = Naloxone.

(j) (Left) κLight0 response to 10 mg/kg U50,488 (gray, n = 3 animals), and 10 mg/kg U50,488 + 10 mg/kg naloxone (black, n = 3 animals) in CA3. Solid lines represent the mean, and shaded areas represent SEM. (Right) bar graph indicating the peak z-score of each response, U50,488: -1 ± 0.7 %, U50,488 + naloxone: -0.75 ± 0.8 %, unpaired t test, p = 0.8123, non-significant. U50 = U50,488, Nalo = Naloxone.

(k) (Left) δLight0 response to 5 mg/kg SNC162 (gray, n = 4 animals), and 5 mg/kg SNC162 + 4 mg/kg naloxone (black, n = 3 animals) in ARC, Solid lines represent the mean, and shaded areas represent SEM. (Right) bar graph indicating the peak z-score of each response, SNC162: -0.61 ± 0.4 %, SNC162 + naloxone: -0.27 ± 0.07 %, unpaired t test, p = 0.5451, non-significant. Nalo = Naloxone.

Next, we evaluated the responses of κLight1.3a to a range of electrical stimuli parameters applied locally via a stimulating electrode in CA3. Trains of electrical stimuli (1 s, 50 Hz, 0.5 sec inter-stimulus-interval) produced sustained fluorescence increases that rapidly decayed upon cessation of the stimulus (Figure 4.3I), with increasing number of stimuli driving larger maximum fluorescence responses (15 stimulations: 14.3 ± 2.4%, 10 stimulations: 8.39 ± 1.9%, 5 stimulations: 4.28 ± 0.6%, 1 stimulation: 2.12 ± 3.3%) (Figure 4.3K). The response to 15 stimuli was strongly attenuated by the addition of the KOR antagonist nor-BNI (100 μM, ΔF/F=1.57 ± 1.2%), consistent with the observed

fluorescence increase resulting from activation by endogenous peptide. In the presence of DOR antagonist ICI 174864 (100 μM), the responses were decreased but not statistically significant (Figure 4.3J, K) (ΔF/F=6.44 ± 0.3%).

(xx) Detecting the Dynamics of Opioid Receptor-Selective Ligand Binding in Vivo

We next determined if κLight and δLight can be activated by systemic administration of exogenous small molecule drugs *in vivo*. We injected AAV encoding κLight1.3 or δLight in the hypothalamus (ARC) [46], CA3 [43], and NAc [30], areas abundant in KOR and DOR. We next implanted fiber optic ferrules above each injection site and recorded the fluorescence of κLight and δLight upon intraperitoneal (i.p) injection of opioid receptor selective ligands using fiber photometry (Figure 4.4A, Figure S4.4G).

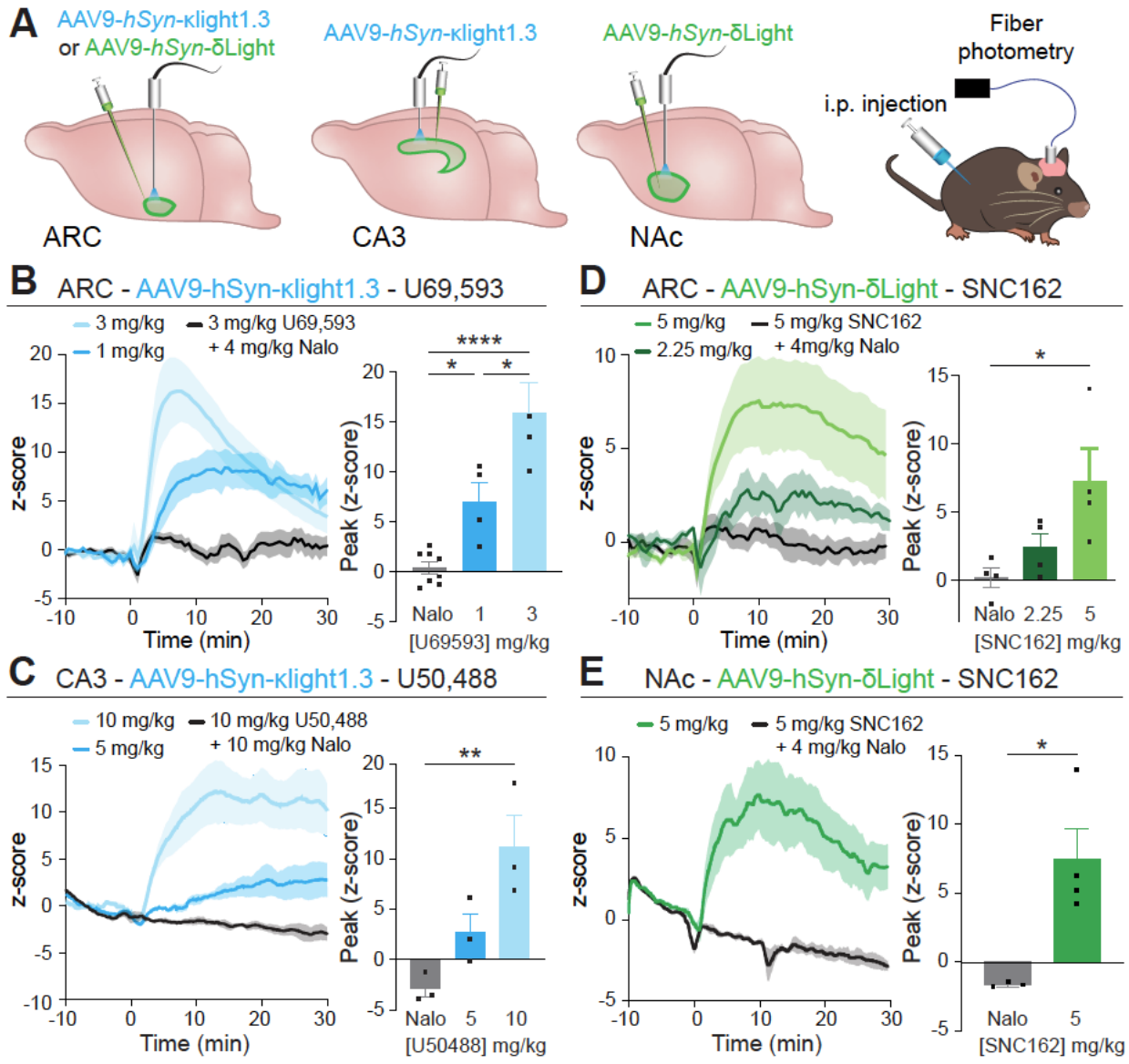

Figure 4.4. In vivo drug pharmacology imaged with κLight and δLight.

(a) Experimental schematics indicating κLight1.3 and δLight injection sites in the hypothalamus (ARC), hippocampal CA3 region (CA3), and nucleus accumbens (NAc). κLight1.3 was injected into ARC and CA3, δLight was injected into ARC and nucleus accumbens (NAc), followed by imaging with fiber photometry during drug injection.

(b) (Left) κLight1.3 response in ARC to different doses of U69,593 in ARC, 3 mg/kg (light blue), 1 mg/kg (blue), and 3 mg/kg U69,593 + 4 mg/kg naloxone (black), n = 7 animals. Solid lines represent the mean, and the shaded area represents SEM. (Right) Bar graph indicating the peak z-score of each response, 3 mg/kg + naloxone: 0.4 ± 0.6 %, 1 mg/kg: 7.0 ± 1.9 %, 3 mg/kg: 15.9 ± 3.1 %, ordinary one-way ANOVA with Tukey's multiple comparisons test, *p < 0.05, ****p < 0.0001.

(c) (Left) κLight1.3 response to different doses of U50,488 in CA3, 10 mg/kg (light blue), 5 mg/kg (blue), and 10 mg/kg U50,488 +10 mg/kg naloxone (black) in CA3, n = 3 animals. Solid lines represent the mean, and shaded areas represent SEM. (Right) Bar graph indicating the peak z-score of each response, 10 mg/kg

+ naloxone: -2.9 ± 0.8 %, 5 mg/kg: 2.7 ± 1.8 %, 10 mg/kg: 11.1 ± 3.2 %, ordinary one-way ANOVA with Dunnett's multiple comparisons test, **p < 0.01.

(d) (Left) δLight response to different doses of SNC162 in ARC, 5 mg/kg (light green), 2.25 mg/kg (green), and 5 mg/kg SNC162 + 4 mg/kg naloxone (black) in ARC, n = 3 animals. Solid lines represent the mean, and shaded areas represent SEM. (Right) Bar graph indicating the peak z-score of each response, 5 mg/kg + naloxone: 0.2 ± 0.7 %, 2.25 mg/kg: 2.4 ± 1.0 %, 5 mg/kg: 7.3 ± 2.4 %, ordinary one-way ANOVA with Tukey's multiple comparisons test, *p < 0.05.

(e) (Left) δLight response to compounds SNC162 in Nac, 5 mg/kg (green), 5 mg/kg SNC162 + 4 mg/kg naloxone (black), n = 4 animals. Solid lines represent the mean, and shaded areas represent SEM. (Right) Bar graph indicating the peak z-score of each response, 5 mg/kg + 4 mg/kg naloxone: -1.7 ± 0.1 %, 5 mg/kg: 7.5 ± 2.2 %, unpaired t test, *p = 0.0185.

In each case, we observed dose-dependent fluorescence increases in response to systemic drug i.p. treatment which were blocked by the non-selective opioid receptor antagonist naloxone. In ARC, κLight1.3 responded to the KOR-selective agonist U69,593 with a robust increase in fluorescence within a few minutes of drug injection (1 mg/kg: z-score$_{peak}$ = 7.0 ± 1.9, 3 mg/kg: z-score$_{peak}$ = 15.9 ± 3.05). Co-injection of naloxone (4 mg/kg) drastically attenuated the response to U69,593 (3 mg/kg) (U69,593+naloxone z-score$_{peak}$ = 0.39 ± 0.59) (Figure 4.4B). In CA3, the KOR selective agonist U50,488, similarly activated κLight1.3 in a dose-dependent manner. Again, the response to U50,488 (10 mg/kg) was completely blocked by co-injecting naloxone (10 mg/kg) (5 mg/kg: z-score$_{peak}$ = 2.68 ± 1.8; 10 mg/kg: z-score$_{peak}$ = 11.1 ± 3.2; U50,488+Naloxone: z-score$_{peak}$ = -2.86 ± 0.83) (Figure 4.4C).

In ARC, SNC162 administration produced increases δLight fluorescence that were blocked by naloxone (4 mg/kg co-injected with SNC162 (5 mg/kg)). (2.25 mg/kg: z-score$_{peak}$ = 2.4 ± 1.0; 5 mg/kg: z-score$_{peak}$ = 7.28 ± 2.4; SNC162+naloxone: z-score$_{peak}$ = 0.19 ± 0.72) (Figure 4.4D). In NAc, the administration SNC162 (5 mg/kg) also increased δLight

fluorescence, and this was again blocked by naloxone (4 mg/kg) (SNC162: z-score$_{peak}$ = 7.45 ± 2.2; SNC162+naloxone: z-score$_{peak}$ = -1.66 ± 0.11) (Figure 4.4E).

Importantly, we did not observe fluorescent changes in response to agonist when then non-functional mutant sensors κLight0 or δLight0 were expressed in ARC, CA3, and NAc (Figure S4H-K). These results suggest that both sensors can be faithfully activated by receptor-specific agonists in vivo.

(xxi) Measuring Evoked Endogenous Dynorphin Release Induced by Photo-Stimulation of Neural Circuits

Though optogenetics has been broadly used to trigger neuromodulator release and neural activity, direct monitoring of peptide release triggered by optogenetic stimulation in vivo, especially in a circuit-specific manner with high temporal resolution, has not been measured optically. NAc contains abundant dynorphin and previous studies have demonstrated that targeting the Dyn-KOR system in the NAcSh can modulate both rewarding and aversive behaviors [47,48]. Furthermore, previous work has demonstrated the ability to measure the optogenetically-evoked release of dynorphin in the NAcSh using in vivo opto-dialysis [30]. Studies have also shown that the basolateral amygdala (BLA) sends dense, functional excitatory projections to the NAcSh and that these terminals are sensitive to modulation by Dyn-KOR [49,50]. We, therefore, set out to determine if κLight can detect photo-stimulated release in vivo in BLA to NAcSh projection.

To detect dynorphin signaling at KOR-expressing neurons, we injected KOR-Cre mice with AAV1-CAG-DIO-κLight1.3a and implanted optical fibers in the NAcSh. A subset of mice were also injected with the red-shifted opsin ChRimson (AAV5-DIO-EF1a-ChRimson-tdTomato) in the BLA (Figure 4.5A-C, Figure S4.5A); ChRimson-lacking mice served as a negative control to determine if optical stimulation produced artifactual dynamics in κLight1.3a fluorescence. To ensure a good dynamic range, adequate expression, and fiber-expression alignments as a foundation for the following optogenetic stimulation experiments, we first examined the response of κLight1.3a to the agonist U50,488 in these mice (Figure 4.5D). U50488 (10 mg/kg; i.p) administration resulted in a rapid, sustained, and robust increase in the fluorescence of κLight1.3a. This increase was significantly attenuated when the animals were pre-treated with the short-acting, reversible KOR antagonist, JNJ-67953964 [51] (aticaprant, 3 mg/kg; i.p) ($p = 0.034$, paired t test), demonstrating the selectivity of κLight1.3a responses *in vivo* (Norm peak, $p = 0.0344$, paired t test. Norm AUC, $p = 0.0138$, paired t test) (Figure 4.5E-H).

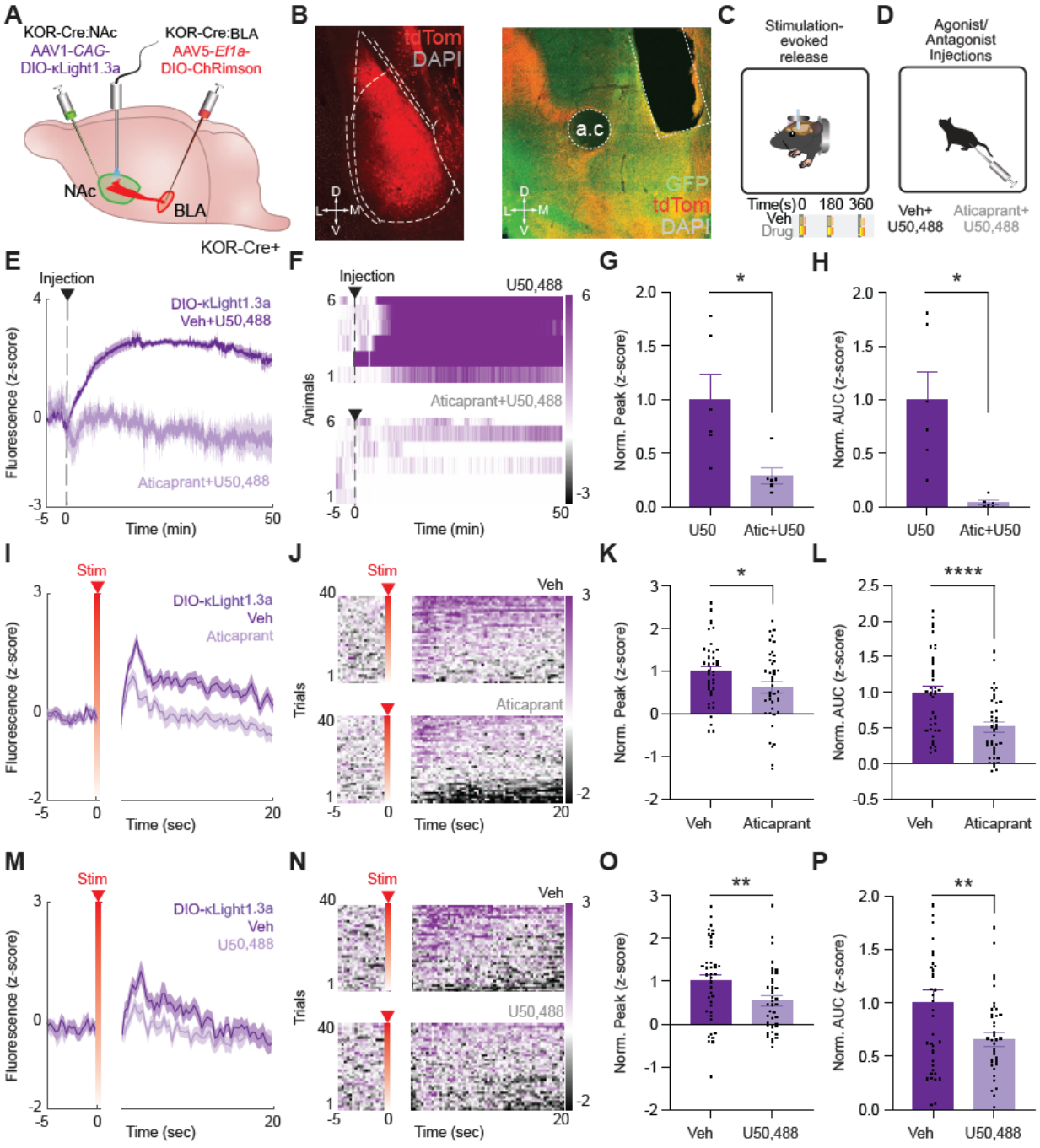

Figure 4.5. Imaging optogenetically-stimulated dynorphin release with κLight1.3a.

(a) Schematic of viral injection sites for κLight1.3a into NAcSh and ChRimson into BLA of KOR-Cre+ mice.

(b) Representative 20X coronal image (left panel) showing expression of κLight1.3a (green), ChRimson (red), DAPI (blue), and fiber placement in NAcSh (top; scalebar – 200 µm), and ChRimson (red) and DAPI (blue) in BLA (bottom; scalebar – 200 µm).

(c) Schematic of in vivo head-fixed stimulation-evoked Dyn release experiments. The bottom schematic shows a trial consisting of three stimulations (yellow) at time 0, 180, and 360 sec, respectively.

(d) Schematic of in vivo agonist/antagonist drug injection experiments, comparing between 10mg/kg U50,488 and 3mg/kg aticaprant + 10mg/kg U50,488.

(e) Mean recorded κLight1.3a activity averaged across all animals following i.p injections of vehicle (veh)+U50,488 (dark) and aticaprant+U50,488 (light; n = 6 animals). Solid lines represent the mean, and shaded areas represent SEM.

(f) Heatmap raster plot of recorded κLight1.3a activity averaged across all animals following i.p injections of vehicle+U50,488 (top) and aticaprant+U50,488 (bottom; n = 6 animals) displayed in animal ascending order by average activity following injection.

(g) Normalized peak fluorescence during injection period (0-50 min; U50: 1 ± 0.23, Atic+U50: 0.29 ± 0.07; paired t test, *p = 0.034, n = 6 animals). Data represented as mean ± SEM. Atic = Aticaprant, U50 = U50,488.

(h) Normalized fluorescence area under the curve of single trails during injection period (0-50 min; U50: 1 ± 0.26, Atic+U50: 0.04 ± 0.02; paired t test, *p = 0.014, n= 6 animals). Data represented as mean ± SEM. Atic = Aticaprant, U50 = U50,488.

(i) Mean recorded κLight1.3a activity averaged across all trials following vehicle (dark) and aticaprant (light) treatment during ChRimson stimulation-evoked trials (n = 4 animals). Solid lines represent the mean, and shaded areas represent SEM. Stim indicates the time of stimulus application.

(j) Heatmap raster plot of recorded κLight1.3a activity averaged across all trials following vehicle (top) and aticaprant (bottom) treatment during ChRimson stimulation-evoked trials (n = 4 animals) displayed in ascending trial order by average activity across trials. Stim indicates the time of stimulus application.

(k) Normalized peak fluorescence across vehicle and aticaprant treatment during all ChRimson stimulation-evoked trials (0-20 sec; veh: 1 ± 0.12, Atic: 0.63 ± 0.14; paired t test, *p = 0.037, n = 4 animals). Data represented as mean ± SEM.

(l) Normalized fluorescence area under the curve of single trails across vehicle and aticaprant treatment during all ChRimson stimulation-evoked trials (0-20 sec; veh: 1 ± 0.09, Atic: 0.51 ± 0.068; paired t test, ****p<0.0001, n = 4 animals). Data represented as mean ± SEM.

(m) Mean recorded κLight1.3a activity averaged across all trials following vehicle (dark) and U50,488 (light) treatment during ChRimson stimulation-evoked trials (n = 4 animals). Solid lines represent the mean, and shaded areas represent SEM.

(n) Heatmap raster plot of recorded κLight1.3a activity averaged across all trials following vehicle (top) and U50,488 (bottom) treatment during ChRimson stimulation-evoked trials (n = 4 animals) displayed in ascending trial order by average activity across trials.

(o) Normalized peak fluorescence across vehicle and U50,488 treatment during all ChRimson stimulation-evoked trials (0-20 sec; veh: 1 ± 0.15, U50: 0.55 ± 0.12; paired t test, **p = 0.002, n = 4 animals). Data represented as mean ± SEM.

(p) Normalized fluorescence area under the curve of single trails across vehicle and U50,488 treatment during all ChRimson stimulation-evoked trials (0-20 sec; veh: 1 ± 0.12, U50: 0.65 ± 0.06; paired t test, **p = 0.007, n = 4 animals). Data represented as mean ± SEM.

Next, we tested whether κLight1.3a can detect endogenous dynorphin release in the NAc evoked via stimulation of glutamatergic BLA terminals, known to densely innervate the NAc [49]. A 1 s, 20 Hz, 5 ms pulse-width stimulation produced a brief artifact,

followed by a significant increase in κLight1.3 fluorescence (Figure S4.5B, C). Importantly, this stimulus artifact was present to the same extent in all animals, with and without ChRimson expression in the BLA terminals (Figure S4.5D). However, the subsequent increase in κLight1.3a fluorescence was present only in the animals expressing ChRimson in BLA, suggesting that this elevation is due to the BLA terminal stimulation-evoked release of dynorphin ($p < 0.0001$, Welch's t test) (Figure S4.5E). To determine the appropriate stimulation parameters for stimulation-evoked dynorphin release, we performed a battery of experiments modulating stimulation number (1-5 stim), laser intensity (0.5 – 5 mW), and stimulation time (1-30 sec) within the same session in a randomized order (Figure S4.5F-H). Varying the length of stimulation from 1-5 sec revealed, somewhat paradoxically, that 1 sec of photo-stimulation produced the most κLight1.3a activation, while the magnitude of the artifact (fluorescence minimum) remained constant throughout ($p = 0.0082$, Brown-Forsythe and Welch ANOVA test) (Figure S4.5I-J). Based on these results, we performed all our subsequent experiments using 1s, 20 Hz, 5 ms pulse-width stimulation.

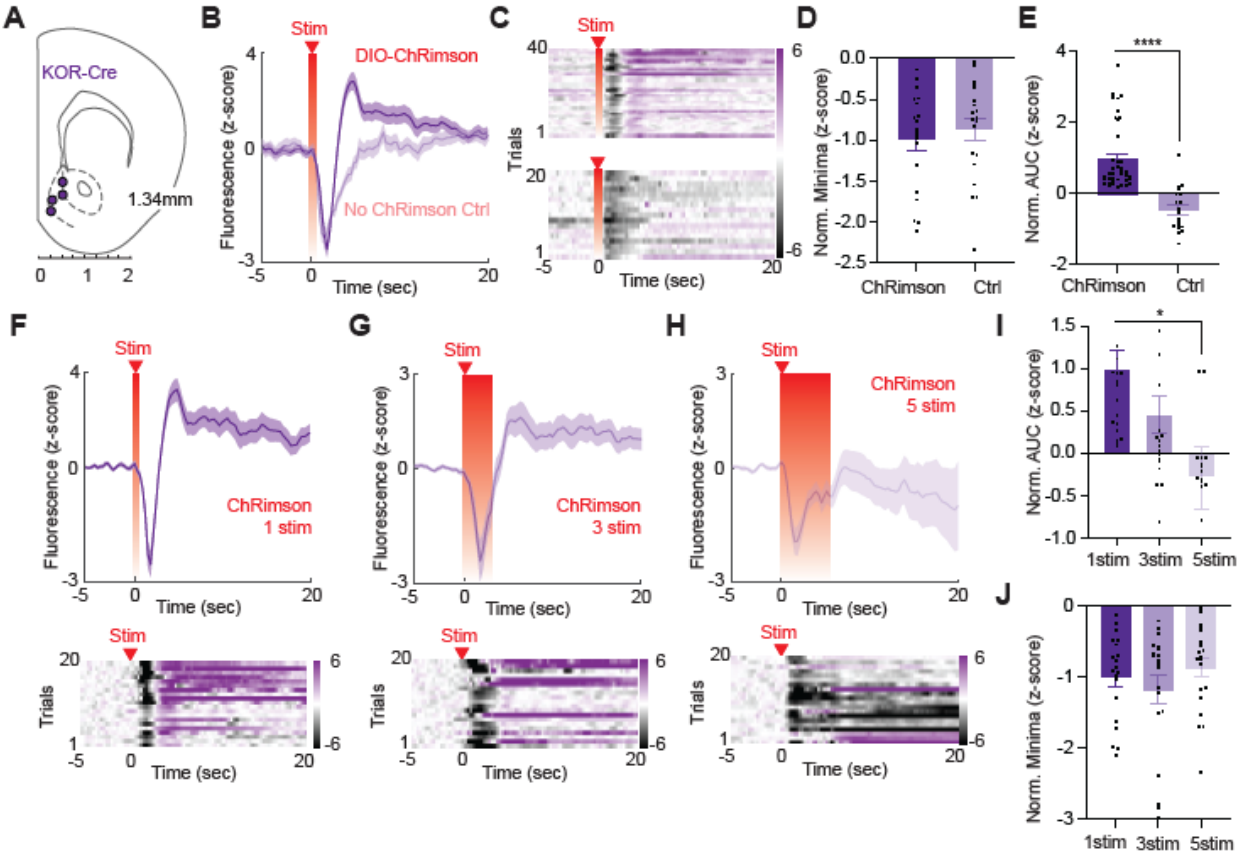

Figure S4.5. Controls for in vivo fiber photometry with optogenetics and other stimulation parameters.

(a) Coronal brain schematic showing photometry fiber placements in the NAcSh of KOR-Cre+ mice.

(b) Mean recorded κLight1.3a fluorescence averaged across all stimulation-evoked trials in ChRimson-injected (dark purple; n = 4 mice) or control mice (light purple; n = 2 mice).

(c) Heatmap raster plot of recorded κLight1.3a fluorescence averaged across all stimulation-evoked trials in ChRimson-injected (top; n = 4 mice) or control mice (bottom; n = 2 mice).

(d) Normalized fluorescence minima during all stimulation-evoked trials (0-20 sec; ChRimson – n = 4 animals: 0.98 ± 0.15, Control - n = 2 animals: -0.45 ± 0.13, unpaired t test, ****p<0.0001). Data represented as mean ± SEM.

(e) Normalized fluorescence area under the curve of single trails during all stimulation-evoked trials (0-20 sec; ChRimson – n = 4 animals: -1 ± 0.14, Control - n = 2 animals: -0.87 ± 0.14, unpaired t test, p = 0.51, non-significant). Data represented as mean ± SEM.

(f) Mean trace and heatmap raster plot of recorded κLight1.3a fluorescence averaged across all 1 second stimulation-evoked trials in ChRimson-injected mice (n = 4 animals). Stim indicates the time of stimulus application.

(g) Mean trace and heatmap raster plot of recorded κLight1.3a fluorescence averaged across all 3 second stimulation-evoked trials in ChRimson-injected mice (n = 4 animals). Stim indicates the time of stimulus application.

(h) Mean trace and heatmap raster plot of recorded κLight1.3a fluorescence averaged across all 5 second stimulation-evoked trials in ChRimson-injected mice (n = 4 animals). Stim indicates the time of stimulus application.

(i) Normalized fluorescence area under the curve of single trails during all stimulation-evoked trials (0-20 sec; 1 stim (dark purple): 1 ± 0.22, 3 stim (medium purple): 0.46 ± 0.22, 5 stim (light purple): -0.29 ± 0.37, ordinary one-way ANOVA with Dunnett's multiple comparisons test, *p = 0.0167, n = 4 animals). Data represented as mean ± SEM.

(j) Normalized fluorescence minima during all stimulation-evoked trials (0-20 sec; 1 stim (dark purple): -1 ± 0.14, 3 stim (medium purple): -1.18 ± 0.2, 5 stim (light purple): -0.87 ± 0.14, ordinary one-way ANOVA with Dunnett's multiple comparisons test, p > 0.05, n = 4 animals). Data represented as mean ± SEM.

We then determined the pharmacological selectivity of BLA terminal stimulation-evoked κLight1.3a activation. We first pre-treated animals with vehicle or aticaprant (3 mg/kg; i.p), followed by 10 trials/animal of BLA terminal stimulation, while simultaneously monitoring κLight1.3a fluorescence. We observed that KOR antagonism significantly decreased stimulation-evoked κLight1.3a activity *in vivo* (Norm peak, p =0.0365, paired t test. Norm AUC, p < 0.0001, paired t test) (Figure 4.5I-L). We then posited that if this is due to KOR antagonism, wherein the antagonist prevents endogenous dynorphin from binding κLight1.3a, we should obtain a similar result following KOR agonism due to κLight1.3 occupancy by U50,488. Hence, we injected animals with vehicle or U50,488 (10 mg/kg; i.p) and performed the aforementioned recordings of stimulation-evoked κLight1.3 activity. As with aticaprant, we found that U50,488 significantly blunted evoked-κLight1.3a activation (Norm peak, p =0.0022, paired t test. Norm AUC, p = 0.0072, paired t test) (Figure 4.5M-P). This suggests that U50,488 occupied and competed for the binding of evoked endogenous dynorphin to κLight1.3a. Altogether, these results demonstrate that we can use optogenetics to trigger and measure terminal dynorphin release with κLight in a circuit-specific manner.

(xxii) Monitoring Dynorphin and Enkephalin Release Dynamics During Fear and Reward Seeking Behavior

After successfully detecting optogenetically-evoked dynorphin release, we next sought to use κLight and δLight to monitor longitudinal opioid peptide signaling dynamics in behaving animals under fear-inducing and rewarding conditions. Previous studies have demonstrated that dynorphin neurons in ventral and dorsal NAcSh subregions (vNAc and dNAc, respectively) have a distinct role in aversive and reward behavior [47]. Furthermore, sub-region-specific dynorphin and enkephalin release have been measured in vNAc versus dNAc using an opto-dialysis method [30]. We thus decided to examine the utility of κLight1.3 and δLight in probing subregion-specific release of opioid peptides in NAc during fear-learning. To do so, AAV9-hSyn-κLight1.3 or AAV9-hSyn-δLight was injected in dNAc and vNAc, followed by fiber implantation. Three weeks post-surgery, we measured peptide transients during an auditory fear conditioning experiment consisting of 30 presentations of a 30 s tone co-terminating with a 1.5 sec foot-shock (0.5 mA) (Figure 4.6A, Figure S4.6A). In the case of κLight, both dNAc and vNAc, we observed a quick rise in fluorescence intensity after the onset of the tone, which was sustained during tone presentation, followed by a small dip at the onset of the shock and a large rise immediately after the foot-shock. The fluorescence signal then gradually decreased to the baseline after ~40 sec (Tau - κLight1.3 in dNAc = 28.7 sec; Tau - κLight1.3 in vNAc = 21.7 sec) (Fig. 6B-C). To assess differences in release between NAc subregions, we calculated the area under the curve (AUC) of individual trials. The AUC to the tone was similar between dNAc and vNAc, whereas the AUC of the post-shock response was significantly higher in dNAc compared to vNAc (AUC dNAc; 194 ± 24,

AUC vNAc; 135 ± 15, p = 0.0355, unpaired t test) (Figure 4.6D). We did not observe fluorescent changes during fear-learning when AAV1-hSyn-κLight0 was expressed either in dNAc or vNAc. (Figure S4.6B-D).

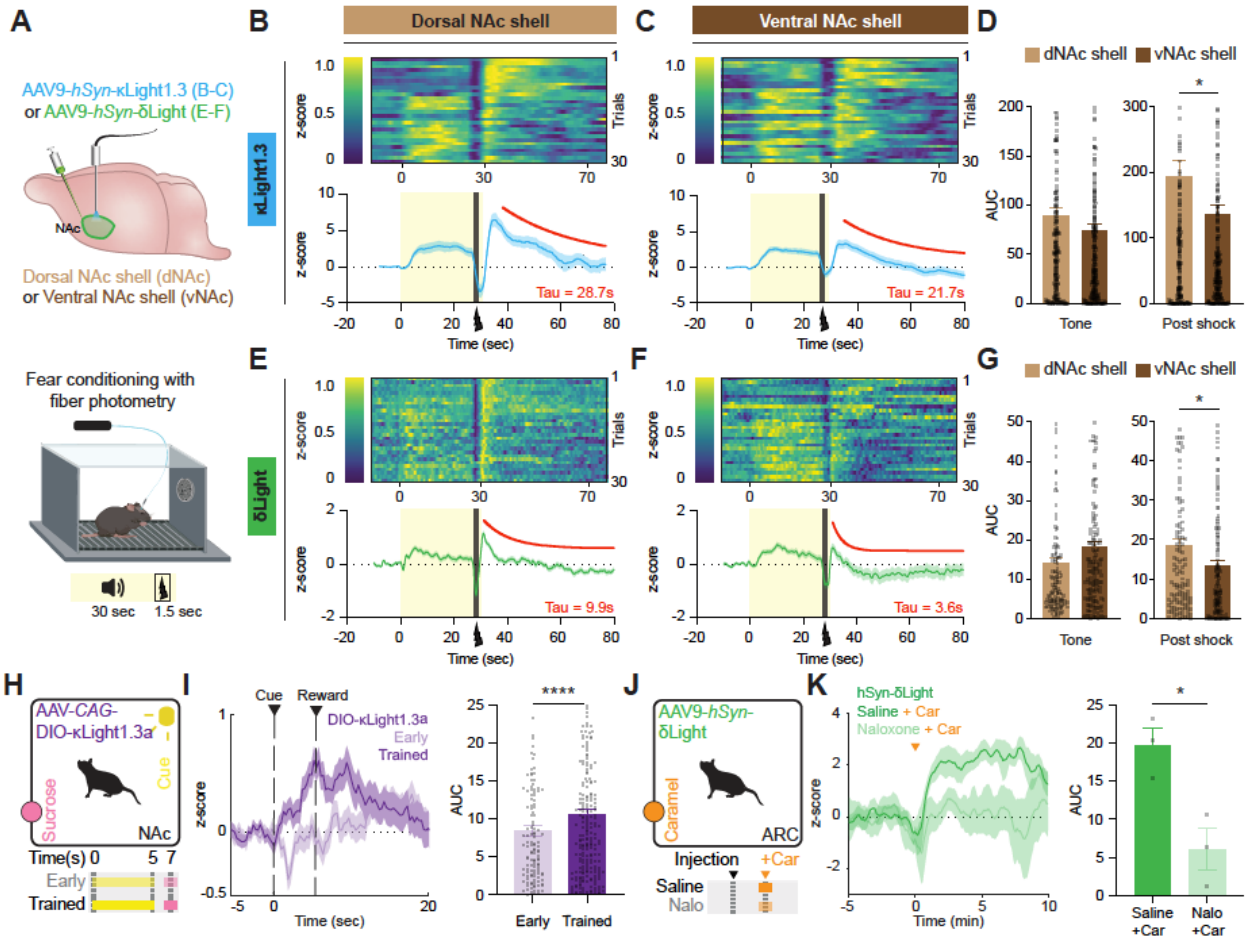

Figure 4.6. Imaging dynorphin and enkephalin dynamics during aversive and rewarding behavior.

(a) Experimental schematics indicating injection site for κLight1.3 or δLight into dorsal nucleus accumbens shell (dNAc) or ventral nucleus accumbens shell (vNAc) (top), followed by a fear conditioning protocol (30 sec tone, co-terminated with 1.5 sec shock), recorded with fiber photometry (bottom).

(b) κLight1.3 response in dNAc: (Top) Sorted shock trials averaged across animals from top to bottom in chronological order (trial 1 at the top, trial 30 at the bottom). (Bottom) Average trace of κLight1.3 response (blue) during fear conditioning, tone (0-30 sec, yellow shaded area), shock, (27.5-29 sec, black). Solid blue line represents the mean, and shaded area represents SEM. n = 7 animals. One-phase decay fit from 35 sec to 80 sec (red), Tau = decay constant.

(c) κLight1.3 response in vNAc: (Top) Sorted shock trials averaged across animals from top to bottom in chronological order (trial 1 at the top, trial 30 at the bottom). (Bottom) Average trace of κLight1.3 response (blue) during fear conditioning, tone (0-30 sec, yellow shade), shock, (27.5-29 sec, black). Solid blue line

represents the mean, and shades represent SEM. n = 8 animals. One-phase decay fit from 35 sec to 80 sec (red), Tau = decay constant.

(d) Area under the curve of single trails in **(Fig.6B)** and **(Fig.6C)** during tone and post-shock. Tone AUC in dNAc: 89 ± 8.5, tone AUC in vNAc: 74 ± 7, unpaired t test, p = 0.1829, non-significant. Post-shock AUC in dNAc: 194 ± 24, post-shock AUC in vNAc: 135 ± 15, unpaired t test, *p = 0.0355. Error bars represent SEM.

(e) δLight response in dNAc: (Top) Sorted shock trials averaged across animals from top to bottom in chronological order (trial 1 at the top, trial 30 at the bottom). (Bottom) Average trace of δLight response (green) during fear conditioning, tone (0-30 sec, yellow shaded area), shock, (27.5-29 sec, black). Solid green line represents the mean, and shaded area represents SEM. One-phase decay fit from 31 sec to 80 sec (red), Tau = decay constant.

(f) δLight response in vNAc: (Top) Sorted shock trials averaged across animals from top to bottom in chronological order (trial 1 at the top, trial 30 at the bottom). (Bottom) Average trace of δLight response (green) during fear conditioning, tone (0-30 sec, yellow shaded area), shock, (27.5-29 sec, black). Solid green line represents the mean, and shaded area represent SEM. One-phase decay fit from 31 sec to 80 sec (red), Tau = decay constant.

(g) Area under the curve of single trails in **(Fig.6E)** and **(Fig.6F)** during tone and post-shock. Tone AUC in dNAc: 14 ± 1.4, tone AUC in vNAc: 18 ± 1.5, unpaired t test, p = 0.0582, non-significant. Post-shock AUC in dNAc; 18 ± 1.8, post-shock AUC in vNAc; 13 ± 1.4, unpaired t test, *p = 0.0276. Error bars represent SEM.

(h) Experimental schematics indicating injection of κLight1.3a into NAc and performed classical Pavlovian conditioning with house light (yellow) illumination as the conditioned stimulus and 20 mg sucrose pellet (pink) as unconditioned stimulus. Bottom schematics show a trial consisting of 5 seconds of CS presentation, and a single sucrose pellet is dropped 7 seconds after CS onset. Intertrial interval is randomized between 60-120 seconds. A total session is 1 hour.

(i) (Left) Mean recorded κLight1.3a activity averaged across all trials during day 1 (early; light purple) and day 7 (trained; dark purple) of Pavlovian conditioning (n = 6 animals). (Right) Area under the curve of single trails across early and trained stages of Pavlovian conditioning, early: 8.4 ± 0.74, trained: 10.51 ± 0.77, paired t test, ****p<0.0001. Error bars represent SEM.

(j) Experimental schematics indicating injection of δLight in ARC and performed caramel retrieval experiment, where caramel (Car, orange) is put into the arena 15 mins after i.p. injection of either saline or 4mg/kg naloxone (nalo).

(k) (Left) Averaged δLight activity upon caramel retrieval after injection of saline (dark green) or naloxone (light green) (n = 3 animals). Solid line represents the mean, and shaded area represent SEM. (Right) Area under the curve of single trails compared between saline and naloxone conditions, saline: 20 ± 2.3, naloxone: 6 ± 2.7, *p = 0.0197, unpaired t test. Error bars represent SEM.

In the case of δLight in dNAc, we observed a brief increase in fluorescence triggered by the tone that gradually decreased to the baseline during the course of tone presentation. The foot shock also triggered a large fluorescence increase followed by a sharp decay over 10 sec after the shock (Tau - δLight in dNAc = 9.9 sec; Tau - δLight in vNAc = 3.6 sec) (Figure 4.6E-F). Although the AUC of the tone-evoked response in vNAc

was slightly larger in amplitude than in dNAc, the difference was not significant. Again, the AUC of the shock-evoked response in dNAc was significantly higher than in vNAc (AUC dNAc; 18 ± 1.8, AUC vNAc; 13 ± 1.4, $p = 0.0276$, unpaired t test) (Figure 4.6G). We observed significantly attenuated fluorescence changes to the tone and shock in the animals expressing the control sensor δLight0 (Figure S4.6E, F).

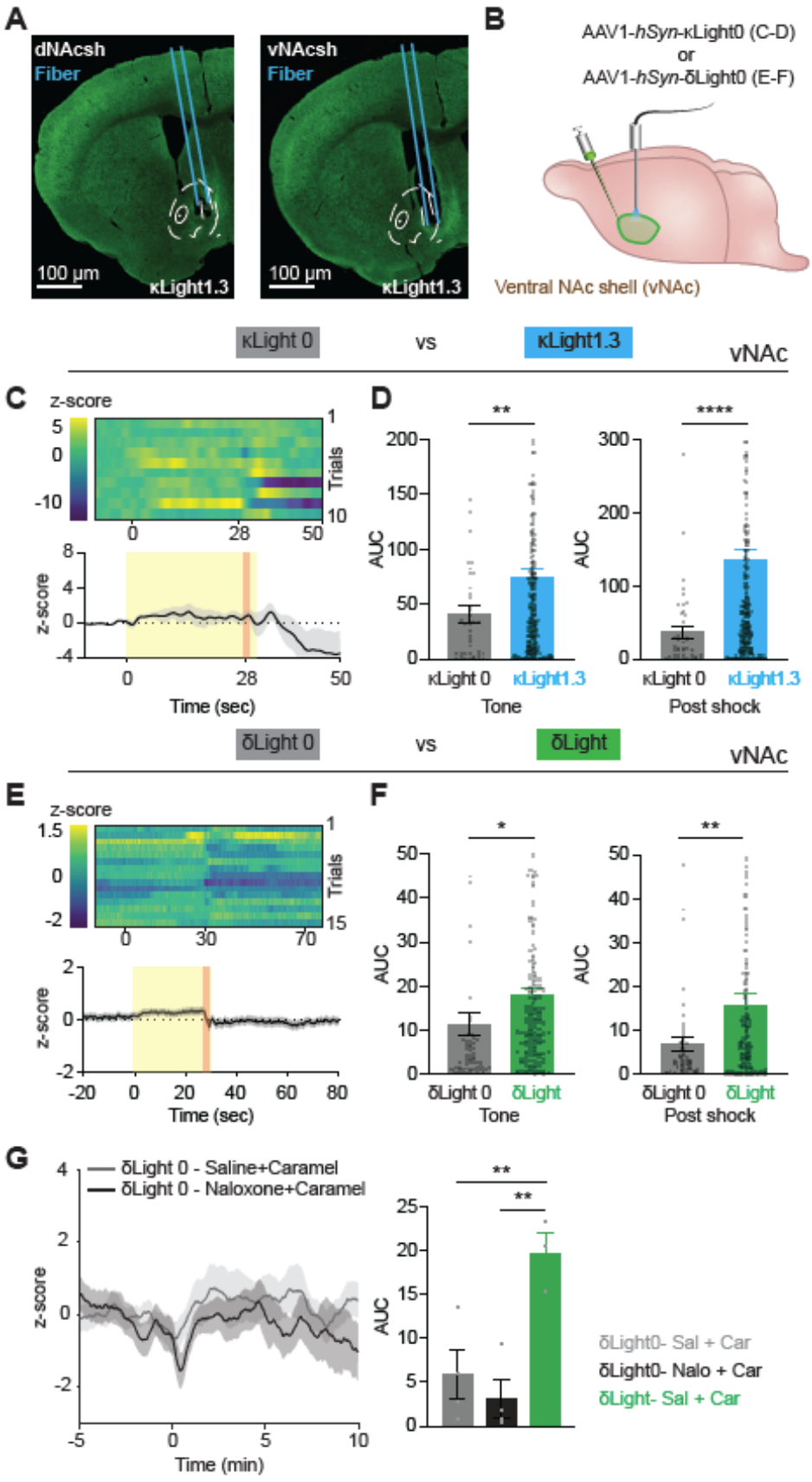
A
dNAcsh
Fiber
100 µm
κLight1.3
vNAcsh
Fiber
100 µm
κLight1.3
B
AAV1-hSyn-κLight0 (C-D)
or
AAV1-hSyn-δLight0 (E-F)
Ventral NAc shell (vNAc)
κLight 0
vs
κLight1.3
vNAc
C
z-score
Trials
Time (sec)
D
AUC
κLight 0
κLight1.3
Tone
Post shock
δLight 0
vs
δLight
vNAc
E
z-score
Trials
Time (sec)
F
AUC
δLight 0
δLight
Tone
Post shock
G
δLight 0 - Saline+Caramel
δLight 0 - Naloxone+Caramel
z-score
Time (min)
AUC
δLight0- Sal + Car
δLight0- Nalo + Car
δLight- Sal + Car

Figure S4.6. In vivo fiber photometry during aversive and rewarding behaviors with control sensors.

(a) Representative images indicating κLight1.3 expression in dNAcsh (left) and vNAcsh (right). Blue lines indicate the fiber tract. Scale bar = 100 μm.

(b) Experimental schematic indicating injection of κLight0 and δLight0 into vNAc individually, followed by fear conditioning protocol (30 sec tone, co-terminated with 1.5 sec shock, as described in **Figure 6A**), recorded with fiber photometry.

(c) κLight0 response in vNAc: (Top) Sorted shock trials averaged across animals from top to bottom in chronological order (trial 1 at the top, trial 10 at the bottom). (Bottom) Average trace of κLight0 response (black) during fear conditioning, tone (0-30 sec, yellow shade), shock, (27.5-29 sec, orange). Solid line represents the mean, and shaded areas represent SEM. n = 5 animals.

(d) Area under the curve of single trails in **(Supplementary Fig.6C)** and **(Fig.6C)** during tone and post-shock. Tone AUC κLight0 (gray): 41 ± 7.6, tone AUC κLight1.3 (blue): 74 ± 7, unpaired t test, **p = 0.0016. Post-shock AUC κLight0 (gray): 37 ± 8.5, post-shock AUC κLight1.3 (blue): 135 ± 15, unpaired t test, ****p = 0.0001. Error bars represent SEM.

(e) δLight0 response in vNAc: (Top) Sorted shock trials averaged across animals from top to down in chronological order (trial 1 at the top, trial 15 at the bottom). (Bottom) Average trace of δLight response (black) during fear conditioning, tone (0-30 sec, yellow shade), shock, (27.5-29 sec, orange). Solid line represents the mean, and shades represent SEM.

(f) Area under the curve of single trails in **(Supplementary Fig.6E)** and **(Fig.6F)** during tone and post-shock. Tone AUC δLight0 (gray): 11 ± 2.5, tone AUC δLight (green): 18 ± 1.5, unpaired t test, *p = 0.025. Post-shock AUC δLight0 (gray): 6.8 ± 1.5, post-shock AUC δLight (green): 16 ± 2.7, unpaired t test, **p = 0.0034. Error bars represent SEM.

(g) (Left) Averaged δLight0 fluorescence upon caramel retrieval after injection of saline (gray) or naloxone (black) (n = 4 animals). (Right) Area under the curve of single trails between δLight0-saline, δLight0-naloxone, and δLight-saline conditions, δLight0-saline (gray): 5.8 ± 2.8, δLight0-naloxone (black): 3.1 ± 2.1, δLight-saline (green): 20 ± 2.3, **p<0.01, ordinary one-way ANOVA with Dunnett's multiple comparisons test. Error bars represent SEM. Abbreviations: saline (Sal), naloxone (Nalo), caramel (Car).

Together, these data suggest κLight and δLight can faithfully report the sub-regional differences in endogenous opioid peptide release triggered during fear learning. More interestingly, the post-shock signals from κLight are much larger and longer lasting in early trials, and the response gradually shifted from the shock to tone as the number of trials increased (Figure 4.6B-C, heatmap). However, we did not observe this pattern signal shift from shock to tone in δLight (Figure 4.6E-F, heatmap). This result suggests that dynorphin, but not enkephalin, might actively track fear state in NAcSh.

To determine the utility of κLight to probe reward-trigger endogenous dynorphin release, we first recorded the response of κLight1.3a to Pavlovian conditioning in NAc (Figure 4.6H). To target KOR-expressing neurons, we again injected CAG-DIO-κLight1.3a into NAc of KOR-Cre mice and trained these animals using classical reward conditioning. Although reward delivery during early trials did not produce fluorescence increases, we found a significant increase in κLight1.3a fluorescence in during reward delivery and consumption following conditioning, as animals increased their reward consumption across training (AUC early: 8.4 ± 0.739, AUC trained: 10.51 ± 0.77, $p < 0.0001$, paired t test) (Fig. 6I). These results suggest that endogenous dynorphin is released during reward reinforcement, supporting our prior work showing that subpopulations of dynorphin neurons in the NAcSh are reinforcing [47].

Similarly, we monitored δLight fluorescence in ARC while mice retrieved caramel rewards (Figure 4.6J). We observed elevated δLight signals in animals injected with saline following caramel retrieval, and this response was blocked when naloxone (4 mg/kg) was injected prior to caramel retrieval (AUC saline: 20 ± 2.3, AUC naloxone: 6 ± 2.7, $p = 0.0197$, unpaired t test) (Figure 4.6K). We did not observe an increase of δLight0 in response to caramel retrieval under either condition (Figure S4.6G). Together, these results suggest that κLight and δLight can faithfully track dynamic changes in endogenous opioid release during the full course of aversive and rewarding behaviors in vivo.

Discussion

In this study, we develop, and characterize genetically encoded opioid receptor sensors for high-resolution tracking of opioid peptides under various experimental settings. GPCR-based sensors have been valuable in monitoring neuromodulator signals in awake animals[52,53], initially for biogenic amines and acetylcholine[35,54-60], and more recently for neuropeptides including oxytocin, orexin, and others[42,61-63]. The development of opioid sensors addresses a crucial need in the neuroscience toolkit due to opioids' widespread significance.

All three sensors, μLight, κLight, and δLight, collectively respond to a wide range of opioid ligands, including and endogenous opioid neuropeptides, with κLight and δLight retaining the pharmacological selectivity of the parent receptor. These sensors can detect and differentiate conformational changes of the receptor induced by various peptiides, which is difficult to do using traditional radio-ligand binding assays. However, μLight is weakly activated by small molecule drugs like morphine and fentanyl and has a lower binding efficacy for endogenous peptides. In fact, oxycodone was observed to suppress μLight fluorescence. Structural studies of μOR in active and inactive state revealed that conformational changes of TM5 and TM6 depends on an allosteric coupling between ligand-binding pockets and G-protein [64]. As cpGFP was inserted into intracellular loop3, it is possible that cpGFP insertion decreased such coupling. Future optimization of μLight is crucial for reliably detecting MOR-selective neuropeptide β-endorphin.

Neuropeptide receptors can be expressed at a significant distance(μm-mm) from putative peptide release sites, suggesting volume transmission as one mode of neuropeptidergic transmission, enabling small amounts of neuropeptides to widely impact brain function. We used κLight with spatially restricted peptide photorelease to measure DynA1-8 in the dorsal striatum, indicating that it can signal via volume transmission to activate receptors over 100 μm away within seconds, with an apparent diffusion coefficient of 1.4 $\mu m^2/s$. Diffusion coefficients for neuropeptides and similar molecules vary greatly depending on peptide type and brain region, peptidase content, as well as tissue tortuosity[8,62,65-67]. We measured diffusion in the striatum, a tortuous region with myelinated fiber bundles and patch-matrix microcircuits; peptides may exhibit higher mobility in less tortuous regions. Although peptide uncaging has advantages, it doesn't target endogenous release sites and may release larger quantities than dense core vesicles. Additionally, confining sensor expression to KOR-expressing cells could improve sensitivity to endogenous peptide release by minimizing background fluorescence from neurons potentially unexposed to locally released peptide which can further enhance the accuracy of measurement. Further studies on endogenously released peptide spread are needed.

Understanding the neural activity patterns required for evoking neuropeptide release remains a decades long challenge. Monitoring neuropeptide release in response to electrical or optogenetic stimulation ex vivo or in vivo offers a powerful method for identifying these activity patterns. We demonstrated κLight's utility in determining

electrical parameters to trigger endogenous release in hippocampal slices; this overcomes the challenge of using electrophysiological assays for endogenous receptor activation.

Identifying conditions that support endogenous peptide release may be most appropriately addressed in vivo, where neural circuits remain fully intact and endogenous neuromodulatory tone remains unaltered by brain slicing. To demonstrate circuit and cell-type specific release, rather than stimulating dynorphinergic cells within NAc directly, we optogenetically stimulated their glutamatergic inputs arising from the BLA. Prior work has established that optogenetic stimulation of BLA terminals in the NAc reliably drives action potentials in striatal neurons in brain slices, as well as facilitate reward seeking behavior [49]. In addition, synaptic stimulation of action potentials in peptidergic neurons via strong glutamatergic drive can activate metabotropic glutamate receptors, which have been implicated as gatekeepers for dynorphin secretion from striatal neurons in brain slices [68]. Using this optogenetic approach, we successfully identified stimulation conditions that result in κLight activation, presumably via dynorphin secretion from striatal neurons, as BLA neurons themselves express little to no *prodynorphin* mRNA (Allen Brain Atlas ISH data). Paradoxically, we found that increasing the duration of the stimulus beyond 1 sec *decreased* the degree of κLight activation. This is likely due to the stimulation artifact generated by red-light, as evidenced by the comparable minima observed in the animals expressing ChRimson and the controls that lack it (Supplementary Fig. 5B-D). Furthermore, increasing stimulation number also increased the width of the artifact (Supplementary Fig. 5F-H). While our data strongly suggest that this paradoxical suppression is likely due to stimulation

artifacts induced by red light, future studies are required to explore the possibility of recruitment of additional neurochemical signaling processes during sustained stimulation that may suppress dynorphin release. Moreover, KOR-mediated suppression of BLA synaptic output, via dyn-KOR signaling at BLA terminals following sustained stimulation, resulting in the dampening of further synaptic activation of NAc dynorphin neurons requires further study. Additionally, whether prolonged stimulation of opioid release, either via optogenetics, or in response to strong behavioral stimuli such as footshock, results in the transient quenching of sensor activity also warrants future exploration.

In this study, we further demonstrated utility of κLight and δLight sensors in tracking rapid dynamic changes in endogenous opioid peptide release triggered by both reward and aversion, which can vary between subregions. Collectively, κLight and δLight respond to most endogenous opioid neuropeptides, including various dynorphin forms and enkephalins. However, the promiscuity among opioid receptors and peptides present a disadvantage in specificity, as the sensors cannot reliably distinguish between the endogenous peptides that might activate them – indeed many brain areas are rich in multiple opioid neuropeptides. Further engineering effort combined with structural analysis may make it possible to reduce such promiscuity. We expect broad application of these opioid sensors to enable a new understanding of how endogenous opioid peptide signaling contributes to various physiological and pathological conditions, including pain, stress, reward, and drug addiction. Monitoring circuit-specific peptide release in behaving animals may reveal new opioid functions in behavioral state transitions and

associative learning. Detecting discrete peptide release events, evoked optogenetically or behaviorally, can help identify differences in opioid secretion under various pharmacological, behavioral, or disease states. While pharmacology, photopharmacology, and optogenetics have contributed significantly to opioid receptor signaling knowledge, these sensors enable a shift from focusing on receptor activation consequences to exploring endogenous neuropeptide secretion's impact on the brain's complex and diverse functions.

Author Contributions

L.T. conceived and led the project. K.M. and C.D. developed and optimized the opioid sensors. C.D. designed and performed key experiments, including in vitro sensor characterization, drug screening assays, part of the in vivo drug injection assay, and in vivo fear conditioning behavior experiments. C.D. also performed rodent surgeries for two-photon electrical stimulation experiments and in vivo fear conditioning experiments. R.G. worked with M.R. Bruchas to design and perform the optogenetics and pavlovian conditioning experiments. Y.J. led the design and implementation of the two-photon electrical stimulation experiments. X.J.H. worked closely with M.R. Banghart to design and execute the uncaging experiments and dynorphin diffusion constant measurement. H.W. and R.F. characterized sensor variants and control sensors using in vivo fear conditioning experiments with guidance from H.T. N.S.A played a crucial role in performing the majority of the in vivo drug injection and caramel retrieval experiments with guidance from D.A. A.G. and I.G. performed the radioligand binding assay under the guidance of L.A.D. R. L engineered viral vectors encoding sensors. D.K.L assisted in vitro characterization. J.L.W. provided compounds and helped design the sensor drug

screening assay. L.T., C.D., and M.R.Banghart wrote the manuscript with input from other authors.

Acknowledgements

This work is funded by NIH Brain Initiative (U01NS103522 and U01NS120820 to L.T., U01NS113295 to M.B.& L.T.). We thank NIDA Grants R37DA033396 and R61DA051489 to M.R.B. This research was supported, in part, by NIH grants DA008863 and DA058300 to L.A.D., and DK126740 to D.A. We thank the support from NIMH Intramural Research Program (ZIA-MH002970-04) to H.A.D. We thank Mark Von Zastrow (UCSF) and John Williams (Vollum) for providing key input to design and characterize early versions of sensors. We thank Sarah Gooding for assistance in drug injection experiments in vivo. We thank Brian Trainor (UC Davis) for insightful comments.

Ethics Declarations

L.T. is a co-founder of Seven Biosciences. All other authors declare no competing interests.

Table 4.1. Drug activation and affinity parameters in κLight, δLight, and μLight cells.

Compound	κLight		δLight		μLight	
	ΔF/F max (%)	EC50 (M)	ΔF/F max (%)	EC50 (M)	ΔF/F max (%)	EC50 (M)
β-endorphin	126.9±8.55	1.77E-06	147.9±4.07	4.18E-07	54.9±2.78	1.61E-06
BAM18	99.5±1.70	3.56E-08	155.0±1.73	1.82E-07	13.2±2.17	1.86E-07
β-neoendorphin	92.0±1.40	2.59E-08	157.5±3.66	3.31E-08	14.2±4.45	6.31E-06
Buprenorphin	58.6±3.31	1.58E-08	253.8±29.88	8.10E-10	-8.3±1.63	7.34E-11
DAMGO	52.9±2.09	1.34E-06	101.5±22.50	1.51E-05	50.5±1.95	5.05E-07
Deltorphin I	37.8±7.27	2.17E-09	253.8±29.88	7.36E-09	43.1±9.43	7.38E-06
DPDPE	20.5±1.67	1.66E-10	17.1±4.08	1.93E-10	n/a	n/a
DynA17	94.0±6.42	9.20E-10	167.4±3.65	1.96E-07	n/a	n/a
DynA13	93.6±3.93	8.98E-11	232.6 ± 6.82	2.13E-07	45.6 ± 0.83	3.74E-06
DynA8	112.6±2.21	1.05E-08	231.6 ± 15.57	1.97E-08	24.8 ± 0.63	6.51E-06
DynB9	177.2±3.94	1.00E-08	217.1±20.88	1.99E-08	42.3±3.28	3.76E-06
Endomorphin I	41.7±6.31	4.96E-08	11.6±1.074	1.75E-10	26.6±4.37	1.01E-07
Fentanyl	103.9±11.88	2.09E-07	134.1±5.97	6.00E-07	13.9±2.20	3.58E-08
LE	95.9±3.55	5.01E-06	214.9±5.53	7.22E-09	27.0±3.68	2.84E-06
ME	80.3±1.79	6.64E-06	246.1±4.56	6.58E-09	40.0±1.55	4.27E-07
Methadone	149.9±2.96	6.79E-06	146.7±3.20	1.80E-05	26.7±5.31	3.77E-06
Metorphinmide	105.3±8.15	1.52E-08	161.3±2.69	9.55E-08	40.9±1.55	6.39E-08
Morphine	40.1±2.78	3.77E-08	26.7±1.25	1.18E-10	n/a	n/a
Nalfurafine	199.4±25.33	9.61E-12	39.7±3.24	3.22E-10	-12.8±1.33	1.16E-09
Oxycodone	34.5±4.44	1.08E-08	45.0±6.45	6.97E-08	-12.8±2.78	1.59E-11
SNC162	12.2±2.39	8.28E-06	152.1±5.20	1.03E-08	2.9±1.69	8.73E-08
SNC80	42.4±3.39	6.65E-09	209.4±5.29	1.82E-07	38.8±0	1.52E-06
U50,488	189.7±2.79	5.29E-08	36.1±0.87	4.1E-5	13.4±1.61	1.08E-05
U69,593	163.4±4.97	2.78E-07	23.9±1.59	2.14E+10	30.8±9.63	2.43E-12

Dose-response assays from (1pM - 100μM) of each compound screened on kLight, δLight, μLight stable cell lines. ΔF/F max values are sensor responses at 100μM of each compound. EC50 values were calculated with the mean of ΔF/F values at each concentration of compounds. Data are represented by mean ± SEM, n/a = not applicable.

Table 4.2. Displacement binding parameters in κLight, δLight, and μLight cells.

Compound	κLight		δLight		μLight	
	IC_{50} [nM]	% bound at 10 μM	IC_{50} [nM]	% bound at 10 μM	IC_{50} [nM]	% bound at 10 μM
ME	130±3	10±5	947±1	77±4	2±2	77±3
LE	14±3	13±8	343±1	65±3	67±2	70±2
β-endorphin 31	81±2	62±4	2±2	59±2	12±4	46±3
DynA8	1±2	71±3	222±1	51±3	48±2	58±2
DynA17	47±2	74±4	47±2	47±2	15±2	60±2
DynB13	6±2	76±2	178±2	58±4	10±2	61±2
Metorphamide	13±2	28±3	56±1	53±3	1490±2	40±3
BAM 18	243±2	66±3	32±3	32±3	14±2	82±2
Peptide E	252±2	40±2	2278±2	51±7	154±2	65±2
Peptide F	18±3	21±6	901±2	40±4	13±3	34±2
α-neoendorphin	6±3	42±4	n.t.	n.t.	n.t.	n.t.
β-neoendorphin	13±2	25±5	n.t.	n.t.	n.t.	n.t.
DAMGO	n.t.	n.t.	n.t.	n.t.	2±2	79±3
Morphine	n.t.	n.t.	n.t.	n.t.	2249±2	77±2
Oxycodone	n.t.	n.t.	n.t.	n.t.	103±2	32±3
Fentanyl	n.t.	n.t.	n.t.	n.t.	2587±2 1±2*	62±3 88±4*
Deltorphin II	n.t.	n.t.	53±2	72±2	n.t.	n.t
DPDPE	n.t.	n.t.	215±2	83±2	n.t.	n.t.
SNC80	n.t.	n.t.	246±2	88±3	n.t.	n.t.
U69,593	110±2	72±2	n.t.	n.t.	n.t.	n.t.

Displacement binding assays were carried out with membranes (100 μg) from μLight, δLight or κLight cells, [3H] diprenorphine (3 nM final concentration) and different ligands (0- 10 μM final concentration) as described in Methods. Data are Mean±SE of 3 experiments in triplicate. Binding in the absence of cold ligand was taken as
100% bound. Binding in the presence of 10 μM ligand was taken as non-specific binding. % Specific binding at 10 μM = Total binding – non-specific binding. n.t.= not tested.
* Displacement binding assays were carried out with CHO-MOR membranes (100 μg).

Method Details

RESOURCE AVAILABILITY

Lead Contact

Further information and requests for resources and reagents should be directed and will be fulfilled by lead contact, Lin Tian, lintian@ucdavis.edu.

Materials Availability

The following plasmids and viral constructs have been deposited in Addgene and UNC neurotools:

Constructs	**Deposited at**	**Identifier**
pCMV- κLight1.3	Addgene	201223
pAAV-hSyn-κLight1.3	Canadian Neurophotonics	Lot 1952
pAAV-CAG-DIO-κLight1.3a	UNC Neurotools	NT-23-724
pCMV- δLight	Addgene	201224
pAAV-hSyn-δLight	UNC Neurotools	NT-23-485
pCMV- μLight	Addgene	201225

κLight1.3, δLight and μLight stable cell lines will be available upon request via MTA with UCD.

Data and Code Availability

All source data present in this manuscript and custom MATLAB code are available from https://github.com/lintianlab/opioid_sensorsV1.

Key Resources Table

Reagent or Resource	Source	Identifier
Bacterial and Virus Strains		
NEB 5-alpha competent E. coli (high efficiency)	NEB	C2987I
NEB10-beta competent E. coli (high efficiency)	NEB	C3019I
AAV1-hSyn-κLight1.2a	UC Davis viral core	N/A
AAV1-hSyn-κLight1.2b	UC Davis viral core	N/A
AAV1-hSyn-κLight1.2c	UC Davis viral core	N/A
AAV9-hSyn-κLight1.3	Canadian Neurophotonics	N/A
AAV1-hSyn-κLight0	Canadian Neurophotonics	N/A

AAV9-hSyn-δLight	Canadian Neurophotonics	N/A
AAV1-hSyn-δLight0	Canadian Neurophotonics	N/A
AAV1-CAG-DIO-κLight1.3a	UC Davis viral core	N/A
AAV5-DIO-ChrimsonR-tdTomato	UW NAPE Center viral vector core	N/A
AAV-DJ-CAG-GFP	Addgene	Plasmid #37825
Chemicals, Peptides, and Recombinant Proteins		
Dynorphin A17	sigma aldrich	D8147-1MG
Dynorphin A13	Phoenix Pharmaceuticals, Inc.	021-21
Dynorphin A8	Phoenix Pharmaceuticals, Inc.	021-10
Dynorphin B9	Phoenix Pharmaceuticals, Inc.	021-38
Met-enkephalin	Phoenix Pharmaceuticals, Inc.	024-35

Leu-enkephalin	Phoenix Pharmaceuticals, Inc.	024-21
Deltorphin I	Phoenix Pharmaceuticals, Inc.	050-05
DPDPE	Phoenix Pharmaceuticals, Inc.	024-16
DAMGO	Phoenix Pharmaceuticals, Inc.	024-10
β-endorphin	Phoenix Pharmaceuticals, Inc.	022-14
Endomorphin I	Phoenix Pharmaceuticals, Inc.	044-10
Metorphinamide	Phoenix Pharmaceuticals, Inc.	024-54
β-neo-endorphin	Phoenix Pharmaceuticals, Inc.	021-44
BAM18	Phoenix Pharmaceuticals, Inc.	024-06
U50488	Fisher scientific	04-952-5

SNC80	Fisher scientific	50-816-10001
Nalfurafine hydrochloride	AdooQ Bioscience	A12579
Morphine Sulfate	Mallinckrodt	0406-1521-53
Fentanyl citrate salt	Sigma-Aldrich	F3886-25MG
Oxycodone hydrochloride	Sigma-Aldrich	O1378-500MG
(±)-Methadone hydrochloride	Sigma-Aldrich	M0267-1G
Buprenorphine hydrochloride	Sigma-Aldrich	B9275-50MG
Naloxone	Tocris	05-991-00
Norbinaltorphimine	Millipore Sigma	5.08017.0001
ICI174864	Tocris	0820
CTAP	Tocris	1560/1
CYD8	Banghart Lab and NIDA Drug Supply Program	N/A
NBQX	HelloBio	Cat #HB0443
CPP	Tocris	Cat #0247

U69593	Millipore Sigma	U103-5MG
SNC162	Tocris	1529
Aticaprant	Research Triangle Institute	14240-115
Critical Commercial Assays		
DNA miniprep kit	QIAGEN	27104
PCR purification kitDNA miniprep kit	QIAGEN	27104
Endo-free plasmid maxi kitPCR purification kit	QIAGEN	28104
Lipofectamine2000 transfection reagentEndo-free plasmid maxi kit	QIAGEN	12362
Lipofectamine2000 transfection reagent	ThermoFisher	11668019
Experimental Models: Cell lines		
κLight stable line	Tian Lab	N/A

δLight stable line	Tian Lab	N/A
μLight stable line	Tian Lab	N/A
Experimental Models: Organisms/Strains		
C57/BL6J	The Jackson Laboratory	N/A
KOR-Cre	Bruchas Lab	N/A
Recombinant DNA		
pLVX_EF1a- vector	Tian Lab	N/A
pCMV_delta8.2	Addgene	12263
pAAV_hSyn- vector	Addgene	111068
pCMV-vector	Addgene	111054
pCMV_κLight1.3	Tian Lab	N/A
pCMV_δLight	Tian Lab	N/A
pCMV_μLight	Tian Lab	N/A
pCMV_μLight	Tian Lab	N/A
Software and Algorithms		
Matlab	Mathworks Inc	https://www.mathworks.com
ScanImage 5	Pologruto et al, 2003	http://scanimage.vidriotechnologies.com/

Ocular	Qimaging	https://www.qimaging.com/ocular
Igor Pro	WaveMetrics	https://www.wavemetrics.com
ImageJ	Schneider et al, 2012	https://imagej.nih.gov/ij/index.html
Illustrator CC	Adobe Systems Inc.	https://www.adobe.com/
Prism 9	GraphPad Inc	https://www.graphpad.com
Excel	Microsoft	https://www.microsoft.com/en-us/microsoft-365/excel
Equipment		
2-photon Microscope	Scientifica	
Small Animal Stereotax	David Kopf Instruments	1900
Leica Stellaris 8 Confocal	Leica	Stellaris 8
2-photon Microscope	Scientifica	

EXPERIMENTAL MODEL AND SUBJECT DETAILS

Animals

All experimental procedures involving animals were approved by the Institutional Animal Care and Use Committee (IACUC) at the University of California, Davis, the University of California San Diego, the University of Washington, the University of Iowa Cold Spring Harbor Laboratory, the National Institute of Mental Health, or Icahn School of Medicine, and adhered to principles described in the National Institutes of Health Guide for the Care and Use of Laboratory Animals. The University of California, Davis, the University of California San Diego, the University of Washington, the University of Iowa, Cold Spring Harbor Laboratory, the National Institute of Mental Health, and Icahn School of Medicine are accredited by the Association for Assessment and Accreditation of Laboratory Animal Care International (AAALAC).

METHOD DETAILS

Sensor Development and Characterization

Development of κLight, δLight, and μLight.

All constructs were designed using circular polymerase extension cloning (CPEC), restriction cloning, and gBlock gene fragments (Integrated DNA Technologies) [69]. Sequences coding for a FLAG epitope were placed at the 5′-end of the construct as previously described [70]. *HindIII* and *NotI* cut sites were placed at the 5′- and 3′-ends, respectively, for cloning into pCMV (Addgene) to generate all pCMV constructs. *BamHI*

and *HindIII* sites were introduced via PCR for final subcloning onto pAAV.hSynapsin1 vectors (Addgene). To maximize coupling between conformational changes and chromophore fluorescence, we chose to use a cpGFP module (LSS-LE-cpGFP-LP-DQL) from GCaMP6 [71] for insertion into the human OPRK1 (KOR), OPRD1 (DOR) and OPRM1 (MOR) using circular polymerase extension cloning (CPEC).

For screening linker variants, we generated linker libraries by first creating an insert DNA carrying a randomized 2 amino acid linker on each side of cpGFP (LSS-xx-cpGFP-xx-DQL). Cloned constructs were amplified and purified with the Qiagen PCR purification kit prior to NEB® 5-α competent *E. coli* transformation. Competent cells were plated onto kanamycin-containing agar plates. After allowing for 24 hours of growth at 37 °C, single colonies were manually picked and grown overnight as described previously [72]. Plasmids from the colonies were purified using the Qiagen miniprep kit. Top variants were sequenced by Genewiz. For the iteration of κLight variants: κLight1.1 was discovered after linker screen, resulted in linker GI-PH. κLight1.2a: V164K from κLight1.1. κLight1.2b is κLight1.2a with ER2 tag. κLight1.2c is κLight1.2b with T603K. κLight1.3 is κLight1.2a with TlcnC, PRC, and ER2 tag. κLight0 is κLight1.2a with D128N. δLight has linker GI-PH, V154K mutation with PRC and ER2 tag. δLight0 has D128N mutation. μLight has linker sequence CI-SH, V175Q mutation with PRC and ER2 tag. To make AAV plasmids, NEB® stable competent cells were transformed with pAAV plasmids. After growth on an agar plate at 30°C, a single colony was selected. After sequencing confirmed the presence of the sensor gene, the cells were expanded at 30°C

in 100 mL of growth medium (2xYT) and purified with a Qiagen Endo-free Plasmid Maxi kit and send to the UC DAVIS Virus Packaging Core for virus production.

Tissue Culture

HEK293T cells were grown in DMEM, supplemented with fetal bovine serum (FBS) and penicillin-streptomycin. Cells were transfected with Effectene according to the manufacturer's instructions. Prior to imaging, cells were washed with Hank's Balanced Salt Solution (HBSS) supplemented with 2 mM $MgCl_2$ and 2 mM $CaCl_2$. All images were collected in HBSS containing Mg^{2+} and Ca^{2+} (HBSS+).

Transient Transfection

HEK293T cells were plated and transfected concurrently 24 h prior to each experiment using the Qiagen Effectene Transfection Reagent kit according to the manufacturer's protocol.

Displacement binding assays

Membranes were prepared from μLight, δLight, κLight cells or CHO-MOR cells as described previously[37]**.** Displacement binding assays were carried out with membranes (100 μg), [^{3}H]diprenorphine (3 nM final concentration) and different ligands (0-10 μM final concentration) as described previously [16,38]**, except that the assay buffer consisted of 50 mM Tris-Cl (pH 7.4) containing 100 mM NaCl, 10 mM $MgCl_2$**, 0.2 mM EGTA and protease inhibitor cocktail (Sigma Aldrich; cat No.P2714), and incubation was carried out for 1 h at 30 °C.

Micro-confocal High-throughput Imaging Experiments

Glass bottom 96-well plates (P96-1.5H-N, Cellvis) were coated with 50 µg/mL of poly-D-lysine (Sigma, P6407-5MG) and 10 µg/mL of laminin (Sigma, L2020) overnight in an incubator (37°C, 5% CO_2). Plates were washed with Dulbecco's PBS (ThermoFisher, 14190-250) and PSYLI2 cells were suspended in DMEM (Fisher, 11995073) containing 10% FBS (Fisher, 26-140-079) with 5% penicillin-streptomycin (Fisher, 15140-163) and plated at a density of 40,000 cells/well 24 h prior to each experiment. Immediately prior to an experiment, stock solutions of drugs in DMSO (10 mM) were diluted 1:100 in imaging media distributed across an empty 96-well plate (treatment plate) in triplicate following a randomized plate map. The imaging media consisted of 1 x HBSS (Fisher, 14175103) containing 0.5 M $MgCl_2$ (Sigma, M8266-1KG) and 0.5 M $CaCl_2$ (Sigma, C5670-50G). Cells grown in a separate 96-well plate (assay plate) were gently washed 3x with imaging media, and the wells were filled with an appropriate volume of imaging media for the respective experiment (*vide infra*).

HEK cell titration

For titration experiments, 50 µL of imaging media was added to each well of the assay plate. Wells were then imaged with ImageXpress Micro Confocal High-Content Imaging system at 40x (N.A. = 0.6) with 4 regions of interest (ROI) taken per well with no bias to location and no overlap of the ROIs (exposure = 300 ms) with MetaXpress software. Next, 50 µL from the treatment plate was transferred to the assay plate containing a doubled desired final concentrations. As for titration dose and controls, ligand of interest from 1pM to 100 µM (final) dissolved in HBSS+ as vehicle were used. Blank controls with

vehicles were present on every plate with randomized locations. After 5 min of incubation, the same sites were re-imaged using the same settings.

Once imaging was complete, the images were exported and analyzed using a self-written MATLAB script. The script will be deposited onto Github. In short, segmentation was performed on individual images and a mask highlighting the membrane of the HEK293T cells was generated. Pixel intensities were obtained from the mask-highlighted area and exported into Excel. The ΔF/F values for each well were calculated using the following equation:

$$\frac{(average\ fluorescence\ after\ drug - average\ fluorescence\ before\ drug)}{average\ fluorescence\ before\ drug}$$

These values were then used to obtain the triplicate mean (n = 3).

SNR values are calculated by:

$$\frac{(average\ fluorescence\ after\ drug - average\ fluorescence\ before\ drug)}{\sqrt{average\ fluorescence\ before\ drug}}$$

Schild Regression Analysis

A treatment plate was prepared by pre-mixing various concentrations of antagonists with increasing concentrations of the sensors' specific agonist. The agonist and antagonist were premixed in doubled concentrations in a treatment plate in HBSS+. Wells were first imaged with 50uL HBSS+ in the well, and 50uL of the mix of ligands from the treatment plate was then added to the imaging plate, and the wells were imaged again under the same settings.

Slice Experiments

Stereotaxic Intracranial Injection

Male and female C57/B6J mice (postnatal day 0–3) were anesthetized with isoflurane and placed in a small animal stereotaxic frame (David Kopf Instruments). After puncturing the skin and skull under aseptic conditions, AAVs were injected (0.5–1 µl total volume) bilaterally through a pulled glass pipette at a rate of 100 nl/min using a UMP3 microsyringe pump (World Precision Instruments). Depending on the size of the mouse, injection coordinates ranged between 0 to +0.5 mm from bregma, 0.5 to 1.0 mm lateral, and 1.8 to 2.3 mm below pia for dorsal striatum. For targeting hippocampus to study buffering, injection coordinates ranged from +0.3-0.5 mm from lambda, 2.2-2.5 mm lateral, and 1.4 to 2.0 below pia. After surgical procedures, mice were returned to their home cage for >30 days to allow for maximal gene expression. For CA3 injection in hippocampus for electrical stimulation, we used the following coordinates [-1.7 mm AP, 1.75 mm ML, -2.3 mm DV]. To achieve sparse labeling of neurons in CA3, we injected AAV1-CAG-DIO-κLight1.3 into CA3 with a 1:1000 dilution of AAV1-hSyn-Cre virus. Male and female C57/B6J mice were injected 8-10 weeks postnatal.

Brain Slice Preparation

Postnatal day 30-60 mice were anesthetized with isoflurane and killed, and the brain was removed, blocked, and mounted in a VT1000S vibratome (Leica Instruments). For striatal imaging experiments, coronal slices (300 µm) were prepared in 34°C ACSF

containing (in mM), 127 NaCl, 2.5 KCl, 25 NaHCO3, 1.25 NaH2PO4, 2 CaCl2, 1 MgCl2, and 25 glucose, osmolarity 307, equilibrated with 95% O2/5% CO2. For hippocampal electrophysiology recordings, horizontal slices (300 µm) were prepared in ice-cold choline-ACSF containing (in mM) 25 NaHCO3, 1.25 NaH2PO4, 2.5 KCl, 7 MgCl2, 25 glucose, 1 CaCl2, 110 choline chloride, 11.6 ascorbic acid, and 3.1 pyruvic acid, equilibrated with 95% O2/5% CO2. Slices were transferred to a holding chamber with oxygenated ACSF and incubated at 32 °C for 30 min and then left at room temperature until recordings were performed.

Fluorescence Imaging with Peptide Uncaging

All video recordings were performed within 5 h of slicing in a submerged slice chamber perfused with ACSF warmed to 32 °C and equilibrated with 95% O2/5% CO2. Sensor-expressing tissue in the dorsal striatum was located and imaged through an eGFP filter cube (Semrock GFP-3035D-OMF) under a 60x, 0.8 NA objective using a SciCam CCD camera (Scientifica, Uckfield, UK) and illumination with the 470 nm LED (CoolLED, Andover, UK). Ocular image acquisition software (Qimaging) was used to acquire videos using a 100 ms exposure times at a frame rate of 1 Hz. For uncaging trials, 5 µM of CYD8 was circulated in the bath prior to beginning video acquisition. During uncaging trials, ScanImage was used to trigger video acquisition and the UV laser. Uncaging was carried out using 50 ms flashes of light from a 355 nm laser (DPSS Lasers, Santa Clara, CA). For full-field uncaging (**Figure 3C-D and Supplementary Figure 3B-C**), a 70 µm diameter area of tissue was illuminated with collimated UV light at a power density of 5 $\mu W/\mu m^2$, as measured in the sample plane. When measuring DynA8 diffusion, a 25 µm diameter

area of focused 355 nm light at a power density of 39 μW/μm^2 was applied near the edge of the imaging field.

Electrophysiology

All recordings were performed within 5 h of slicing in a submerged slice chamber perfused with ACSF warmed to 32 °C and equilibrated with 95% O2/5% CO2. Whole-cell voltage clamp recordings were obtained with an Axopatch 700B amplifier (Molecular Devices, San Jose, CA). Data were sampled at 10 kHz, filtered at 3 kHz, and acquired using National Instruments acquisition boards and a custom version of ScanImage written in MATLAB (Mathworks, Natick, MA). Cells were rejected if holding currents exceeded −200 pA or if the series resistance (<25 MΩ) changed during the experiment by more than 20%. For recordings measuring inhibitory synaptic transmission in mouse hippocampus, patch pipets (2.8−3.5 MΩ) were filled with an internal solution containing (in mM) 135 CsMeSO3, 10 HEPES, 1 EGTA, 3.3 QX-314 (Cl − salt), 4 Mg-ATP, 0.3 Na-GTP, and 8 Na 2 phosphocreatine (pH 7.3, 295 mOsm/kg). Cells were held at 0 mV to produce outward currents. Excitatory transmission was blocked by the addition to the ACSF of NBQX (10 μM) and CPP (10 μM).To electrically evoke IPSCs, stimulating electrodes pulled from theta glass with ~5 μm tip diameters were placed at the border between stratum pyramidale and straum oriens nearby the recorded cell (~50−150 μm) and a two brief pulses (0.5 ms, 50−300 μA, 50 ms interval) were delivered every 20 s. Uncaging was carried out using 5 ms flashes of collimated full-field illumination with a 355 nm laser at different power densities, which were measured at the sample plane.

Data Analysis

Video acquisition data were first analyzed in ImageJ and subsequently plotted in Igor Pro (Wavemetrics). The mean brightness of each frame was divided by the average baseline fluorescence of the first minute to calculate $\Delta F/F$. Then, the first minute before uncaging was fit with a biexponential curve to estimate the rate of bleaching during the video acquisition. The fitted bleaching curve was then subtracted from the recorded traces to correct for bleaching. A 700 μm^2 circle ROI was drawn at the center of the uncaging field and the mean brightness of this ROI was plotted per frame. Electrophysiology data were analyzed in Igor Pro (Wavemetrics). Peak current amplitudes were calculated by averaging over a 2 ms window around the peak IPSC. To determine magnitude of modulation by DynA8 photorelease (% IPSC suppression), the IPSC peak amplitude measured immediately after a flash was divided by the average peak amplitude of the three IPSCs preceding the light flash. To determine the time constant of recovery (tau off), the IPSC amplitudes were fit to a monoexponential function starting at the point of maximal IPSC suppression to the point at which the IPSC amplitude returned to baseline.

Diffusion coefficient calculation

Based on a derivation of Fick's law of diffusion that yields $\gamma_i^2 = 4D^*(t_i + t_0)$ [66], D^* is the slope of the linear regression between $\gamma^2/4$, where gamma is the half-width of the spatial fluorescence profile, and time (t), as demonstrated by diffusion of dextrans molecules or quantum dots in the cortex [73]. To reduce noise, we averaged 50 pixels in the y-axis around the center line of the image plane (parallel to the uncaging spot). .

Brain Slices for Two-Photon Imaging

3 to 4 weeks after viral injection, samples from adult mice were anesthetized with 2.5% avertin and perfused in ice-cold carborgen (95% O2 and 5% CO2) gassed cutting NMDG-HEPES artificial cerebrospinal fluid (aCSF) solution that contained (in mM): 92 NMDG, 2.5 KCl, 1.25 NaH2PO4, 30 NaHCO3, 20 HEPES, 24 D-Glucose, 2mM Thiourea, 5 sodium ascorbate, 3 sodium pyruvate, pH adjusted to 7.3-7.4 and supplemented with 0.5 CaCl2 and 10 MgCl2, before decapitated. Brains were quickly extracted and were cut (300 µm) with a vibratome (V1200, Leica) in ice-cold oxygenated NMDG-HEPES aCSF. Brain slices were incubated at 34-36°C for 10 min before transferring to HEPES holding aCSF that contained (in mM): 92 NaCl, 2.5 KCl, 1.25 NaH2PO4, 30 NaHCO3, 20 HEPES, 25 D-Glucose, 2 Thiourea, 5 sodium ascorbate and 3 sodium pyruvate, pH adjusted to 7.3-7.4 and supplemented with and 2 CaCl2 and 2 MgCl2, saturated with 95% O2 and 5% CO2[74]. Imaging was carried out at room temperature using a 2-photon microscope. The sensor was excited at 920 nm with a Ti: sapphire laser (Ultra II, Coherent) that was focused by an Olympus 40×, 0.8NA water immersion objective. Emitted fluorescence was separated by a 525/50 nm filter set, and detected by a photomultiplier (H7422PA-40, Hamamatsu). Data were acquired and collected with ScanImage5 software. Electrical stimulation was performed with a bipolar stimulating electrode (Array of 2 SNEX-100 PI concentric electrodes epoxied side-by-side, MicroProbes). The area within approximately 20 µm of the electrode was imaged. Rectangular voltage pulses were applied through a 9-channel programmable pulse stimulator (Master-9, A.M.P. Instruments LTD) and a stimulus isolation unit (Analog Stimulus Isolator, A-M SYSTEMS). Imaging and electrical stimulation were controlled by an Axon Digidata 1550B. Field potentials were applied at

1, 5, 10, and 15 trains with inter stimulation interval of 0.5 s, where 1 train at 5V, 50Hz with a duration of 1s. Experiments were carried out at a scan rate of 30 (512×512 pixels) Hz. Image analysis was performed with ImageJ, data analyses were calculated using MATLAB and SigmaPlot 12.0. Drugs were dissolved as a stock solution in imaging HBSS buffer and diluted to final concentration prior to application in the perfusion system.

In vivo Sensor Recordings

Experimental Subjects and Stereotaxic Surgery

Adult (25-35 g), 12-16 week old KOR-Cre mice or C57/B6J mice were group-housed, given access to food pellets and water ad libitum, and maintained on a 12 hr:12 hr light:dark cycle (lights on at 7:00 AM). All animals were kept in a sound-attenuated, isolated holding facility in the lab 1 week prior to surgery, post-surgery, and throughout the duration of the behavioral assays to minimize stress.

For surgery, mice were anesthetized in an induction chamber (2-4% isoflurane) and placed into a stereotaxic frame (Kopf Instruments, Model 1900) where they were maintained at 1%-2% isoflurane. Male and female mice were anesthetized, following which we performed a craniotomy and unilaterally injected as described below, using a blunt neural syringe (65457-01, Hamilton Company). For photo-stimulation experiments and κLight Pavlovian conditioning experiments: 300-400 nL of AAV5-DIO-ChrimsonR-tdTomato (UW NAPE Center Viral Vector Core, viral titer 5 x 10^{12} vg/mL) into the BLA (stereotaxic coordinates from bregma: -1.3 mm [AP], +- 3.2 mm [ML], -4.6 mm [DV]), and

AAV-DIO-κLight1.3 (UC Davis Viral Core, viral titer 3.6 x 10^{13} vg/mL) followed immediately by fiber optic implantation into the NAcSh (stereotaxic coordinates from bregma: +1.3 mm [AP], +- 0.5 mm [ML], -4.5 mm [DV]). For fear conditioning experiments: 300-400 nL of AAV9-hSyn-κLight1.3 (Canadian Neurophotonics, viral titer 1 x 10^{13} vg/mL) and AAV9-hSyn-δLight (Canadian Neurophotonics, viral titer 3.3 x 10^{12} vg/mL) separately into the dorsal NAcsh (dNAcsh, +1.3 mm [AP], +-0.5 mm [ML], -4.5 mm [DV]) and ventral NAcsh (vNAcsh, +1.3 mm [AP], +-0.5 mm [ML], -5 mm [DV]). For fear conditioning control experiments: 300-400 nL of AAV1-hSyn-κLight0 (Canadian Neurophotonics, viral titer 7.8 x 10^{12} vg/mL) and AAV1-hSyn-δLight0 (Canadian Neurophotonics, viral titer 9.5 x 10^{12} vg/mL) were injected into vNAcsh as controls. For δLight caramel reward retrieval experiments: 300- 500 nL virus (AAV9-hSyn-δLight, AAV-syn-δLight0) was injected bilaterally in the medio-basal hypothalamus (ARC, -1.25 mm [AP], +-0.25 mm [ML], -5.6 mm [DV] from surface of the brain) using a pulled glass pipette (Drummond Scientific, Wiretrol, Broomall, PA) controlled by a micromanipulator (Narishige, East Meadow, NY). Fiber cannula was then implanted at the injection site and secured the implants using two bone screws and a dental cement head cap (Lang Dental). ([AP] values are measured from bregma, and [ML] values are measured from the skull at bregma unless otherwise noted.)

Fiber Photometry

For fiber photometry studies, recordings were obtained throughout the entirety of drug injection, Pavlovian conditioning and head-fixed sessions as previously described [75]. Prior to recording, an optic fiber was attached to the implanted fiber using a ferrule

sleeve (Doric, ZR_2.5). Two LEDs were used to excite κLight1.3. A 531-Hz sinusoidal LED light (Thorlabs, LED light: M470F3; LED driver: DC4104) was bandpass filtered (470 ± 20 nm, Doric, FMC4) to excite κLight1.3 and evoke emission. A 211-Hz sinusoidal LED light (Thorlabs, LED light: M405FP1; LED driver: DC4104) was bandpass filtered (405 ± 10 nm, Doric, FMC4) to evoke isosbestic control emission. Laser intensity for the 470 nm and 405 nm wavelength bands were measured at the tip of the optic fiber and adjusted to 50 uW before each day of recording. κLight1.3 fluorescence traveled through the same optic fiber before being bandpass filtered (525 ± 25 nm, Doric, FMC4), transduced by a femtowatt silicon photoreceiver (Newport, 2151) and recorded by a real-time processor (TDT, RZ5P). The envelopes of the 531-Hz and 211-Hz signals were extracted in real-time by the TDT program Synapse at a sampling rate of 1017.25 Hz. For the ChrimsonR stimulation experiments, a 625 nm laser was used at 2 mW intensity to deliver red light through the tip of the same optic fiber used to excite BLA terminals for stimulation-evoked dynorphin release.

Drug Injection

Mice were pre-treated with either vehicle (17:1:1:1 – Saline:DMSO:Corn Oil, EtOH) or Aticaprant (Eli Lilly) at 3 mg/kg of body weight i.p for 30 minutes. Mice were then tethered to a photometry cable and placed in a chamber. Following a 5-minute baseline recording, mice were injected with either saline or U50,488 (Sigma Aldrich) at 10 mg/kg body weight i.p. Recordings were conducted for a total of 1 hour.

Pavlovian Behavior Paradigm

Mice were initially food deprived to 90% of their body weight and trained in a Pavlovian behavioral paradigm for a total of 7 days with a modular test chamber (17.8 x 15.2 x 18.4 cm) (Med Associates Inc.), as previously described [75]. Mice were tethered to a photometry cable and habituated to an operant chamber in which there is a house light and pellet receptacle. The house light illuminates as the conditioned stimulus (CS) and sucrose pellets (20 mg, BioServe) are the unconditioned stimulus (US). Each trial consists of 5 seconds of CS presentation and a single sucrose pellet dropped 7 seconds after CS onset. Inter-trial interval was randomized between 60-120 seconds. Total session was 1 hour.

Stimulation-evoked release

Mice were head-restrained in a custom-made head-fixation device [76] and tethered to a photometry cable. For initial parameter determination experiments, mice received 20 Hz, 5 ms pulse-width laser stimulation in a randomized order varying the stimulus intensity, duration or pulse number, separated by an inter-trial-interval of 5 minutes resulting in 5 trials per mouse per condition, every session. For drug pre-treatment experiments, mice were injected with aticaprant at 3 mg/kg or U50,488 at 10 mg/kg body weight i.p using the aforementioned vehicle 30 minutes prior to stimulation sessions. Mice received 10 trials/mouse with an inter-trial interval of 5 minutes.

Fear Conditioning Paradigm

Mice were placed into a fear conditioning chamber (Med Associates) with a patch cord connected for photometric recordings. A Doric fiber photometry system was used in this study with 465 nm and 405 nm light (LED, ~30 μW) used for generating the signal

and as an isosbestic control, respectively. Each animal received 15 presentations of a 27 sec tone (3,000 Hz) co-terminating with a foot-shock (0.5 mA for 1.5 s) delivered at 2 min intervals. Each animal received 15 tone/foot-shock pairings over the course of 40 min, and the responses for these trials were averaged to create a single trace per animal. Data analysis was performed with custom-written script in MATLAB. In brief, 405 nm traces were fit with a bi-exponential curve, and then the fit was subtracted from the signal to correct for baseline drift. ΔF/F% was calculated as [100*(465 signal - fitted signal) / fitted signal)]. Traces were then z-scored. A heatmap was plotted using a custom MATLAB script by plotting normalized single trials of traces from all animals tested per brain region.

Photometry Analysis

Custom MATLAB scripts were developed for analyzing fiber photometry data in context of mouse behavior. The isosbestic 405 nm excitation control signal was subtracted from the 470 nm excitation signal to remove movement artifacts. Baseline drift was evident in the signal due to slow photobleaching artifacts, particularly during the first several minutes of each recording session. A double exponential curve was fit to the raw trace and subtracted to correct for baseline drift. After baseline correction, the photometry trace was z-scored relative to the mean and standard deviation of the session. The post-processed fiber photometry signal was analyzed in the context of animal behavior during Pavlovian conditioning and operant task performance. Pearson correlations, one sample t-tests, two sample t-tests and two-way ANOVAs were performed using standard MATLAB functions “corr”, “ttest”, “ttest2” and “anovan”, respectively. Peak, mean and

minimum fluorescence was determined during pre-determined time windows for the injection period (0-5 min), reward period (5-20 sec), release period (0-20 sec) or artifact period (0-20 sec) subtracted from peak, mean or minimum fluorescence values in a baseline window (-5-0 sec). Code that supports the analysis will be made available from the corresponding author upon reasonable request.

Perfusion and Histology

Stock avertin was made by mixing 10 g of 2,2,2-tribromoethyl alcohol and 10 ml of tert-amyl alcohol. The working stock was diluted to 1.2% (v/v) with water and shielded from light. Animals were euthanized with 125 mg/kg 1.2% Avertin (i.p.) followed by transcardial perfusion with ice-cold 1x phosphate buffered saline (PBS) and subsequently perfused with ice-cold 4% paraformaldehyde (PFA) in 1x PBS. After extraction of the mouse brains, samples were post-fixed in 4% PFA at 4°C overnight. The mouse brains were cryo-protected by immersion in 10% sucrose in a 1x PBS solution overnight. Samples were next placed in 30% sucrose in a 1x PBS solution for >1 day, before embedding the samples in O.C.T. Samples were then transferred to a -80°C freezer for long-term storage or were sliced into 50 μm sections on a cryostat (Leica Biosystems) for histology. Histology samples were imaged on Leica Stellaris 8 confocal microscope.

QUANTIFICATION AND STATISTICAL ANALYSIS

Treatments were randomized, and the data were analyzed by experimenters blinded to the treatment conditions. Statistical analyses were performed using GraphPad Prism 9 unless noted otherwise. Measurements are taken from distinct samples, and the sample size is indicated as n numbers. All comparisons were planned prior to performing each experiment. A $p<0.05$ was considered significant. Data are represented as mean ± SEM, unless otherwise noted, with asterisks indicating *$p < 0.05$, **$p < 0.01$, ***$p < 0.001$, and ****$p < 0.0001$. Measurements are taken from distinct samples, and sample size is indicated as n numbers.

Reference

1 Greco, M. A. *et al.* Opioidergic projections to sleep-active neurons in the ventrolateral preoptic nucleus. *Brain Res* **1245**, 96-107 (2008). https://doi.org:10.1016/j.brainres.2008.09.043

2 Hökfelt, T. *et al.* Neuropeptide and Small Transmitter Coexistence: Fundamental Studies and Relevance to Mental Illness. *Front Neural Circuits* **12**, 106 (2018). https://doi.org:10.3389/fncir.2018.00106

3 Holden, J. E., Jeong, Y. & Forrest, J. M. The endogenous opioid system and clinical pain management. *AACN Clin Issues* **16**, 291-301 (2005). https://doi.org:10.1097/00044067-200507000-00003

4 Klenowski, P., Morgan, M. & Bartlett, S. E. The role of δ-opioid receptors in learning and memory underlying the development of addiction. *Br J Pharmacol* **172**, 297-310 (2015). https://doi.org:10.1111/bph.12618

5 Nummenmaa, L. & Tuominen, L. Opioid system and human emotions. *Br J Pharmacol* **175**, 2737-2749 (2018). https://doi.org:10.1111/bph.13812

6 Russo, A. F. Overview of Neuropeptides: Awakening the Senses? *Headache* **57 Suppl 2**, 37-46 (2017). https://doi.org:10.1111/head.13084

7 Fricker, L. D. Analysis of mouse brain peptides using mass spectrometry-based peptidomics: implications for novel functions ranging from non-classical neuropeptides to microproteins. *Mol Biosyst* **6**, 1355-1365 (2010). https://doi.org:10.1039/c003317k

8 van den Pol, A. N. Neuropeptide transmission in brain circuits. *Neuron* **76**, 98-115 (2012). https://doi.org:10.1016/j.neuron.2012.09.014

9 Burns, J. A. *et al.* Molecular Imaging of Opioid and Dopamine Systems: Insights Into the Pharmacogenetics of Opioid Use Disorders. *Frontiers in Psychiatry* **10** (2019). https://doi.org:10.3389/fpsyt.2019.00626

10 Corder, G., Castro, D. C., Bruchas, M. R. & Scherrer, G. Endogenous and Exogenous Opioids in Pain. *Annu Rev Neurosci* **41**, 453-473 (2018). https://doi.org:10.1146/annurev-neuro-080317-061522

11 Franchi, S., Moschetti, G., Amodeo, G. & Sacerdote, P. Do All Opioid Drugs Share the Same Immunomodulatory Properties? A Review From Animal and Human Studies. *Frontiers in Immunology* **10** (2019). https://doi.org:10.3389/fimmu.2019.02914

12 Higginbotham, J. A., Markovic, T., Massaly, N. & Morón, J. A. Endogenous opioid systems alterations in pain and opioid use disorder. *Frontiers in Systems Neuroscience* **16** (2022). https://doi.org:10.3389/fnsys.2022.1014768

13 Le Merrer, J., Becker, J. A., Befort, K. & Kieffer, B. L. Reward processing by the opioid system in the brain. *Physiol Rev* **89**, 1379-1412 (2009). https://doi.org:10.1152/physrev.00005.2009

14 Machelska, H. & Celik, M. Ö. Advances in Achieving Opioid Analgesia Without Side Effects. *Front Pharmacol* **9** (2018). https://doi.org:10.3389/fphar.2018.01388

15 Pathan, H. & Williams, J. Basic opioid pharmacology: an update. *Br J Pain* **6**, 11-16 (2012). https://doi.org:10.1177/2049463712438493

16 Gomes, I. *et al.* Biased signaling by endogenous opioid peptides. *PNAS* **117**, 11820-11828 (2020). https://doi.org:doi:10.1073/pnas.2000712117
17 Machelska, H. & Celik, M. Ö. Opioid Receptors in Immune and Glial Cells—Implications for Pain Control. *Frontiers in Immunology* **11** (2020). https://doi.org:10.3389/fimmu.2020.00300
18 Mansour, A. *et al.* Mu, delta, and kappa opioid receptor mRNA expression in the rat CNS: an in situ hybridization study. *J Comp Neurol* **350**, 412-438 (1994). https://doi.org:10.1002/cne.903500307
19 McGinty, J. F., van der Kooy, D. & Bloom, F. E. The distribution and morphology of opioid peptide immunoreactive neurons in the cerebral cortex of rats. *J. Neurosci.* **4**, 1104 (1984). https://doi.org:10.1523/JNEUROSCI.04-04-01104.1984
20 van Steenbergen, H., Eikemo, M. & Leknes, S. The role of the opioid system in decision making and cognitive control: A review. *Cognitive, Affective, & Behavioral Neuroscience* **19**, 435-458 (2019). https://doi.org:10.3758/s13415-019-00710-6
21 Kosten, T. R. & George, T. P. The neurobiology of opioid dependence: implications for treatment. *Sci Pract Perspect* **1**, 13-20 (2002). https://doi.org:10.1151/spp021113
22 Al-Hasani, R. & Bruchas, Michael R. Molecular Mechanisms of Opioid Receptor-dependent Signaling and Behavior. *Anesthesiology* **115**, 1363-1381 (2011). https://doi.org:10.1097/ALN.0b013e318238bba6
23 Bruchas, M. R. *et al.* Stress-induced p38 mitogen-activated protein kinase activation mediates kappa-opioid-dependent dysphoria. *J Neurosci* **27**, 11614-11623 (2007). https://doi.org:10.1523/jneurosci.3769-07.2007
24 Hoyer, D. & Bartfai, T. Neuropeptide Receptors–Drug Development. (2009).
25 Fricker, L. D., Margolis, E. B., Gomes, I. & Devi, L. A. Five Decades of Research on Opioid Peptides: Current Knowledge and Unanswered Questions. *Molecular Pharmacology* **98**, 96 (2020). https://doi.org:10.1124/mol.120.119388
26 Castro, D. C. *et al.* An endogenous opioid circuit determines state-dependent reward consumption. *Nature* **598**, 646-651 (2021). https://doi.org:10.1038/s41586-021-04013-0
27 Ma, X. *et al.* In vivo photopharmacology with a caged mu opioid receptor agonist drives rapid changes in behavior. *Nature Methods* (2023). https://doi.org:10.1038/s41592-023-01819-w
28 Smith, S. J. *et al.* Single-cell transcriptomic evidence for dense intracortical neuropeptide networks. *eLife* **8**, e47889 (2019). https://doi.org:10.7554/eLife.47889
29 Banghart, M. R. & Sabatini, B. L. Photoactivatable neuropeptides for spatiotemporally precise delivery of opioids in neural tissue. *Neuron* **73**, 249-259 (2012). https://doi.org:10.1016/j.neuron.2011.11.016
30 Al-Hasani, R. *et al.* In vivo detection of optically-evoked opioid peptide release. *eLife* **7**, e36520 (2018). https://doi.org:10.7554/eLife.36520
31 Mitsui, S., Saito, M., Hayashi, K., Mori, K. & Yoshihara, Y. A novel phenylalanine-based targeting signal directs telencephalin to neuronal dendrites. *J Neurosci* **25**, 1122-1131 (2005). https://doi.org:10.1523/jneurosci.3853-04.2005

32 Stockklausner, C., Ludwig, J., Ruppersberg, J. P. & Klöcker, N. A sequence motif responsible for ER export and surface expression of Kir2.0 inward rectifier K+ channels. *FEBS Letters* **493**, 129-133 (2001). https://doi.org:https://doi.org/10.1016/S0014-5793(01)02286-4

33 Lim, S. T., Antonucci, D. E., Scannevin, R. H. & Trimmer, J. S. A Novel Targeting Signal for Proximal Clustering of the Kv2.1 K+ Channel in Hippocampal Neurons. *Neuron* **25**, 385-397 (2000). https://doi.org:https://doi.org/10.1016/S0896-6273(00)80902-2

34 Tandon, N., Thakkar, K. N., LaGory, E. L., Liu, Y. & Giaccia, A. J. Generation of Stable Expression Mammalian Cell Lines Using Lentivirus. *Bio Protoc* **8** (2018). https://doi.org:10.21769/BioProtoc.3073

35 Dong, C. *et al.* Psychedelic-inspired drug discovery using an engineered biosensor. *Cell* **184**, 2779-2792.e2718 (2021). https://doi.org:https://doi.org/10.1016/j.cell.2021.03.043

36 Nichols, A. L. *et al.* Fluorescence activation mechanism and imaging of drug permeation with new sensors for smoking-cessation ligands. *eLife* **11**, e74648 (2022). https://doi.org:10.7554/eLife.74648

37 Gomes, I., Filipovska, J. & Devi, L. A. Opioid receptor oligomerization. Detection and functional characterization of interacting receptors. *Methods Mol Med* **84**, 157-183 (2003). https://doi.org:10.1385/1-59259-379-8:157

38 Gomes, I., Ijzerman, A. P., Ye, K., Maillet, E. L. & Devi, L. A. G protein-coupled receptor heteromerization: a role in allosteric modulation of ligand binding. *Mol Pharmacol* **79**, 1044-1052 (2011). https://doi.org:10.1124/mol.110.070847

39 Banghart, M. R., He, X. J. & Sabatini, B. L. A Caged Enkephalin Optimized for Simultaneously Probing Mu and Delta Opioid Receptors. *ACS Chem. Neurosci.* **9**, 684-690 (2018). https://doi.org:10.1021/acschemneuro.7b00485

40 He, X. J. *et al.* Convergent, functionally independent signaling by mu and delta opioid receptors in hippocampal parvalbumin interneurons. *eLife* **10**, e69746 (2021). https://doi.org:10.7554/eLife.69746

41 Toll, L. *et al.* Standard binding and functional assays related to medications development division testing for potential cocaine and opiate narcotic treatment medications. *NIDA Res Monogr* **178**, 440-466 (1998).

42 Ino, D., Tanaka, Y., Hibino, H. & Nishiyama, M. A fluorescent sensor for real-time measurement of extracellular oxytocin dynamics in the brain. *Nature Methods* **19**, 1286-1294 (2022). https://doi.org:10.1038/s41592-022-01597-x

43 Shirayama, Y. *et al.* Stress increases dynorphin immunoreactivity in limbic brain regions and dynorphin antagonism produces antidepressant-like effects. *Journal of Neurochemistry* **90**, 1258-1268 (2004). https://doi.org:https://doi.org/10.1111/j.1471-4159.2004.02589.x

44 Wagner, J. J., Terman, G. W. & Chavkin, C. Endogenous dynorphins inhibit excitatory neurotransmission and block LTP induction in the hippocampus. *Nature* **363**, 451-454 (1993). https://doi.org:10.1038/363451a0

45 Weisskopf, M. G., Zalutsky, R. A. & Nicoll, R. A. The opioid peptide dynorphin mediates heterosynaptic depression of hippocampal mossy fibre synapses and

modulates long-term potentiation. *Nature* **362**, 423-427 (1993). https://doi.org:10.1038/362423a0

46 Romero-Picó, A. *et al.* Hypothalamic κ-opioid receptor modulates the orexigenic effect of ghrelin. *Neuropsychopharmacology* **38**, 1296-1307 (2013). https://doi.org:10.1038/npp.2013.28

47 Al-Hasani, R. *et al.* Distinct Subpopulations of Nucleus Accumbens Dynorphin Neurons Drive Aversion and Reward. *Neuron* **87**, 1063-1077 (2015). https://doi.org:10.1016/j.neuron.2015.08.019

48 Castro, D. C. & Berridge, K. C. Opioid hedonic hotspot in nucleus accumbens shell: mu, delta, and kappa maps for enhancement of sweetness "liking" and "wanting". *J Neurosci* **34**, 4239-4250 (2014). https://doi.org:10.1523/jneurosci.4458-13.2014

49 Stuber, G. D. *et al.* Excitatory transmission from the amygdala to nucleus accumbens facilitates reward seeking. *Nature* **475**, 377-380 (2011). https://doi.org:10.1038/nature10194

50 Tejeda, H. A. *et al.* Pathway- and Cell-Specific Kappa-Opioid Receptor Modulation of Excitation-Inhibition Balance Differentially Gates D1 and D2 Accumbens Neuron Activity. *Neuron* **93**, 147-163 (2017). https://doi.org:10.1016/j.neuron.2016.12.005

51 Page, S. *et al.* Behavioral Pharmacology of Novel Kappa Opioid Receptor Antagonists in Rats. *Int J Neuropsychopharmacol* **22**, 735-745 (2019). https://doi.org:10.1093/ijnp/pyz054

52 Dong, C. *et al.* Fluorescence Imaging of Neural Activity, Neurochemical Dynamics, and Drug-Specific Receptor Conformation with Genetically Encoded Sensors. *Annual Review of Neuroscience* **45**, 273-294 (2022). https://doi.org:10.1146/annurev-neuro-110520-031137

53 Wu, Z., Lin, D. & Li, Y. Pushing the frontiers: tools for monitoring neurotransmitters and neuromodulators. *Nature Reviews Neuroscience* **23**, 257-274 (2022). https://doi.org:10.1038/s41583-022-00577-6

54 Borden, P. M. *et al.* A fast genetically encoded fluorescent sensor for faithful in vivo acetylcholine detection in mice, fish, worms and flies. *bioRxiv*, 2020.2002.2007.939504 (2020). https://doi.org:10.1101/2020.02.07.939504

55 Jing, M. *et al.* An optimized acetylcholine sensor for monitoring in vivo cholinergic activity. *Nature Methods* **17**, 1139-1146 (2020). https://doi.org:10.1038/s41592-020-0953-2

56 Patriarchi, T. *et al.* Ultrafast neuronal imaging of dopamine dynamics with designed genetically encoded sensors. *Science (New York, N.Y.)* **360**, eaat4422 (2018). https://doi.org:10.1126/science.aat4422

57 Patriarchi, T. *et al.* An expanded palette of dopamine sensors for multiplex imaging in vivo. *Nature Methods* **17**, 1147-1155 (2020). https://doi.org:10.1038/s41592-020-0936-3

58 Sun, F. *et al.* Next-generation GRAB sensors for monitoring dopaminergic activity in vivo. *Nature Methods* **17**, 1156-1166 (2020). https://doi.org:10.1038/s41592-020-00981-9

59 Unger, E. K. *et al.* Directed Evolution of a Selective and Sensitive Serotonin Sensor via Machine Learning. *Cell* **183**, 1986-2002.e1926 (2020). https://doi.org:10.1016/j.cell.2020.11.040
60 Wan, J. *et al.* A genetically encoded sensor for measuring serotonin dynamics. *Nat Neurosci* **24**, 746-752 (2021). https://doi.org:10.1038/s41593-021-00823-7
61 Duffet, L. *et al.* A genetically encoded sensor for in vivo imaging of orexin neuropeptides. *Nat Methods* **19**, 231-241 (2022). https://doi.org:10.1038/s41592-021-01390-2
62 Qian, T. *et al.* A genetically encoded sensor measures temporal oxytocin release from different neuronal compartments. *Nat Biotechnol* (2023). https://doi.org:10.1038/s41587-022-01561-2
63 Wang, H. *et al.* A toolkit of highly selective and sensitive genetically encoded neuropeptide sensors. *bioRxiv*, 2022.2003.2026.485911 (2022). https://doi.org:10.1101/2022.03.26.485911
64 Sounier, R. *et al.* Propagation of conformational changes during μ-opioid receptor activation. *Nature* **524**, 375-378 (2015). https://doi.org:10.1038/nature14680
65 Drake, C. T. *et al.* Dynorphin opioids present in dentate granule cells may function as retrograde inhibitory neurotransmitters. *J Neurosci* **14**, 3736-3750 (1994). https://doi.org:10.1523/jneurosci.14-06-03736.1994
66 Nicholson, C. & Tao, L. Hindered diffusion of high molecular weight compounds in brain extracellular microenvironment measured with integrative optical imaging. *Biophys J* **65**, 2277-2290 (1993). https://doi.org:10.1016/s0006-3495(93)81324-9
67 Xiong, H. *et al.* Probing neuropeptide volume transmission in vivo by a novel all-optical approach. *bioRxiv*, 2021.2009.2010.459853 (2021). https://doi.org:10.1101/2021.09.10.459853
68 Atwood, B. K., Kupferschmidt, D. A. & Lovinger, D. M. Opioids induce dissociable forms of long-term depression of excitatory inputs to the dorsal striatum. *Nature Neuroscience* **17**, 540-548 (2014). https://doi.org:10.1038/nn.3652
69 Quan, J. & Tian, J. Circular polymerase extension cloning for high-throughput cloning of complex and combinatorial DNA libraries. *Nat Protoc* **6**, 242-251 (2011). https://doi.org:10.1038/nprot.2010.181
70 Irannejad, R. *et al.* Conformational biosensors reveal GPCR signalling from endosomes. *Nature* **495**, 534-538 (2013). https://doi.org:10.1038/nature12000
71 Chen, T. W. *et al.* Ultrasensitive fluorescent proteins for imaging neuronal activity. *Nature* **499**, 295-300 (2013). https://doi.org:10.1038/nature12354
72 Tian, L. *et al.* Imaging neural activity in worms, flies and mice with improved GCaMP calcium indicators. *Nat Methods* **6**, 875-881 (2009). https://doi.org:10.1038/nmeth.1398
73 Thorne, R. G. & Nicholson, C. In vivo diffusion analysis with quantum dots and dextrans predicts the width of brain extracellular space. *PNAS* **103**, 5567-5572 (2006). https://doi.org:doi:10.1073/pnas.0509425103
74 Ting, J. T., Daigle, T. L., Chen, Q. & Feng, G. in *Patch-Clamp Methods and Protocols* (eds Marzia Martina & Stefano Taverna) 221-242 (Springer New York, 2014).

75 Al-Hasani, R. *et al.* Author Correction: Ventral tegmental area GABAergic inhibition of cholinergic interneurons in the ventral nucleus accumbens shell promotes reward reinforcement. *Nature Neuroscience* **24**, 1501-1501 (2021). https://doi.org:10.1038/s41593-021-00928-z

76 Sean, C. P. *et al.* Hyperactivity of indirect pathway-projecting spiny projection neurons drives compulsive behavior. *bioRxiv*, 2022.2002.2017.480966 (2022). https://doi.org:10.1101/2022.02.17.480966

Preliminary Data on the Engineering of GENI for Gastrin-Releasing Peptide

Disinhibitory neurons found throughout the mammalian cortex have a significant impact on circuit excitability and plasticity. Studies have shown that the expression of neuropeptide receptors differs in disinhibitory, inhibitory, and excitatory neurons, suggesting that distinct neuropeptidergic systems control each circuit motif. Previous research has revealed that a neuropeptide similar to bombesin, gastrin-releasing peptide (GRP), selectively targets and activates vasoactive intestinal peptide (VIP)-expressing cells to recruit disinhibitory cortical microcircuits (Melzer et al., 2021). The research conducted using a first-generation genetically encoded GRP sensor, grpLight1.0, optogenetic anterograde stimulation, and trans-synaptic tracing approach indicates that GRP regulates VIP cells through extrasynaptic diffusion from several local and long-range sources. Furthermore, the signaling of GRP-GRPR enhances auditory fear memories. However, grpLight1.0 is not able to detect functionally relevant GRP levels in vivo as analysis of intracellular Ca2+ in VIP cells shows that GRP infusion has functional effects on these cells in vivo well before photometric detection of changes in grpLight fluorescence (Melzer et al., 2021). This is primarily due to a lack of sensors with sufficient sensitivity to detect released peptide. An improved GRP sensors will be beneficial to identify detailed spatial and temporal release dynamics also under physiological conditions in vivo.

Thus, we focused on binding pocket mutations to improve the sensitivity of grpLight1.0. Studies have identified residue positions on GRP receptor that contributes

to the high affinity binding of GRP (Nakagawa et al., 2005), and we then identified the indicated residues on grpLight1.0 (Table 5.1)

distance to the binding pocket		Single mutations	position	Mutate to	Original property	Mutated property	fold decrease of affinity for GRP
>6A		K	101	H	+ charge	+ charge	11.3
>6A		R	106	G	+ charge	non-polar	0
>6A		D	181		- charge		
>6A		P	184	T	non-polar	polar	1.25–2.5
	<6A	H	186	R	+ charge	+ charge	1.25–2.5
>6A		V	187	D	non-polar	- charge	0
	<6A	K	188	P	+ charge	non-polar	1.25–2.5
	<6A	D	189	N	- charge	polar	1.25–2.5
>6A		Q	192	M	polar	non-polar	1.25–2.5
	<6A	A	198	T	non-polar	polar	1.25–2.5
	<6A	S	293	Q	polar	polar	1.25–2.5
	<6A	E	294	Y	- charge	polar	1.25–2.5
>6A		T	297	P	polar	non-polar	1.25–2.5
	<6A	T	304	F	polar	non-polar	1.25–2.5
	<6A	Q	121	R	polar	+ charge	100
		A	308	S	non-polar	polar	0
>6A		P	199	S	non-polar	polar	11.3
	<6A	R	288	H	+ charge	+ charge	1

Table 5.1. Residue positions and identities that contributes to the affinity of GRP binding on grpLight1.0.

We then surveyed positions in the GRPR and screened with site saturated mutagenesis with combinations between regions resulted in total of 15 top variants (Figure 5.1A, B). A variant with mutation E187K resulted both tighter EC50 and larger ΔF/F. This variant were named, grpLight2.0, and selected for further characterizations (Figure 5.1B).

When transiently expressed in mammalian HEK293T cells, we obtained the excitation and emission spectrum of grpLight2.0, with excitation absorbance peaking at 490nm and emission spectrum peaking at 520nm (Figure 5.1C). After, we quantified the signal to noise ratio (SNR) of grpLight2.0 compared to the parent grpLight1.0 on HEK293T cells by adding 100 μM of GRP. Surprisingly, SNR of grpLight2.0 was 4 times higher than the parent (SNR-grpLight2.0 = 110 ± 5.9, SNR-grpLight1.0 = 32 ± 2.7) (Figure

5.1D). We further performed an eight-point dose response of GRP onto the two sensor variants expressing HEK293T cells to characterize the affinity differences. We found that the E187K mutation shifted the affinity of grpLight2.0 to GRP 5-fold tighter than the parent grpLight1.0 (EC50 – grpLight2.0 = 49nM, EC50 – grpLight1.0 = 200nM) (Figure 5.1E). Furthermore, the dynamic range of grpLight2.0 showed nearly 2-fold increase compared to grpLight1.0 (ΔF/F max - grpLight2.0 = 554.5 ± 18.8 %, ΔF/F max – grpLight1.0 = 314.8 ± 12.7 %) (Figure 5.1E).

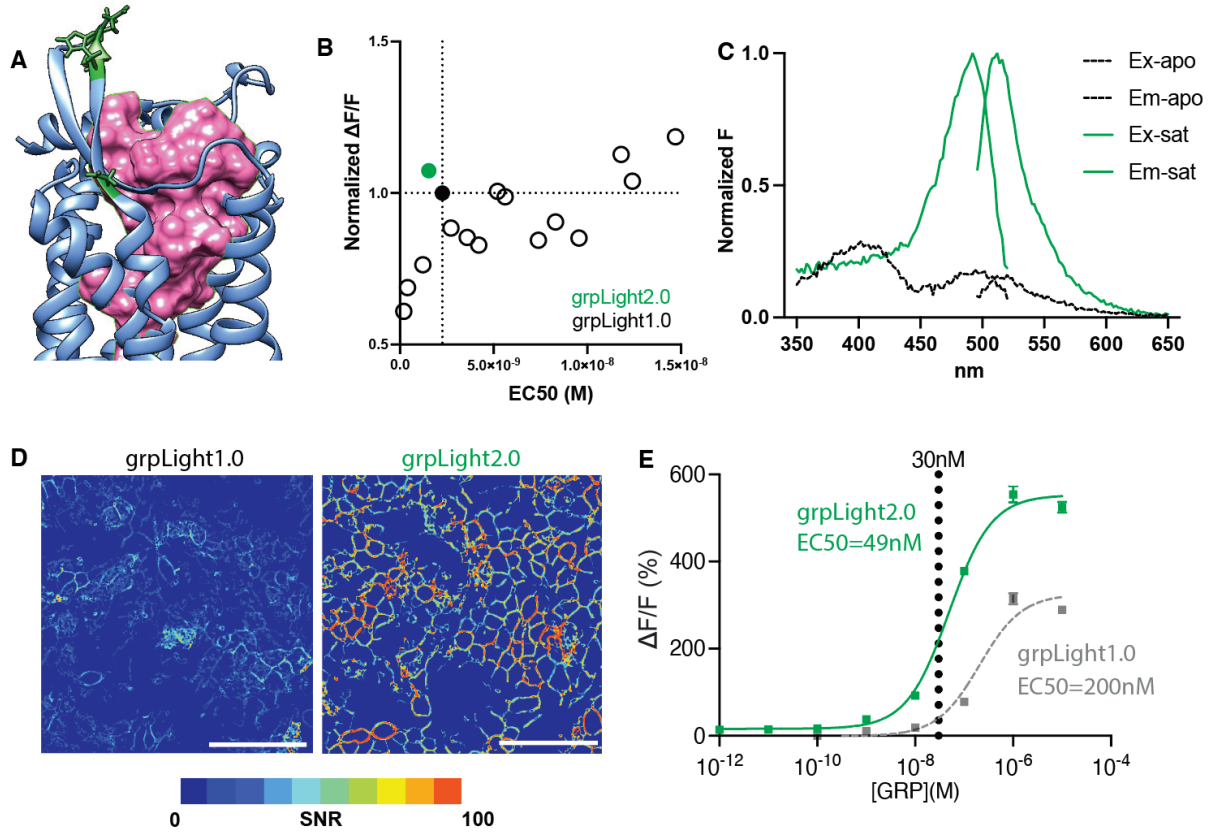

Figure 5.1. grpLight2.0 development and characterization in HEK293T cells.
A. Simulated structure of GRP receptor indicating the residue locations that influences GRP binding affinity.
B. grpLight variants with characterization of dynamic range normalized to the parent (grpLight1.0, black dot) (y-axis) and EC50 to GRP (x-axis). grpLight2.0 indicated as green dot.
C. Excitation emission spectrum of grpLight2.0.
D. SNR heatmap upon addition of 10uM GRP on grpLight1.0 (left, black) and grpLight2.0 (right, green) expressing HEK293T cells. Error bar 100um.
E. Dose response curve compare between grpLight2.0 (green) and grpLight1.0 (gray). Dotted line indicates 30nM GRP to indicate sensors performance differences at low concentration.

Next, we sought to address the question that whether grpLight2.0 is good enough to report functionally relevant GRP levels which grpLight1.0 was not able to achieve. We first looked at whether we could use electrical stimulation to trigger GRP release on acute brain slices. Hippocampus has been shown to express abundant GRP receptors in CA1 (Roesler et al., 2012). Thus, we packaged AAV1-hSyn-grpLight2.0 and injected to CA1 to assess if the sensor is capable of reporting electrically stimulated release of GRP (Figure 5.2A, B). With previous success of triggering opioid release, we applied the same electrical stimulation protocol, 1 sec 50Hz stimulation with 0.5 sec inter stimulation interval (ISI), to trigger GRP release in acute brain slices (Figure 5.2B). The hSyn driven grpLight2.0 has bright basal state and labels the processes and cell membranes clearly in CA1 after 2 weeks of expression post injection (Figure 5.2C). We then performed a dose response on the number of stimulations and recorded the signals of grpLight2.0 with 2-photon microscope. Expectably, we saw grpLight2.0 signals increases in a dose-dependent manner from 1 stimulation to 15 stimulations. To ensure the signals are indeed from GRP instead of a stimulation artifact, we performed 15 times stimulation with an incubation of GRP receptor antagonist RC3095. The signal of grpLight2.0 was significantly diminished by the application of antagonist (Figure 5.2D). Together, the results indicating we could use the aforementioned electrical stimulation protocol to trigger GRP release, and the triggered release can be detected by grpLight2.0.

With the success of monitoring triggered release of GRP in acute brain slices, we next sought to apply grpLioght2.0 in vivo and characterize GRP release under fear conditioning behavior in rodents to address the big question of whether grpLight2.0 can

monitor behavioral relevant GRP dynamics in vivo. Mechanism studies have shown activation of gastrin-releasing peptide receptors in the hippocampus CA1 interacts with multiple signaling pathways and growth factor systems to regulate memory formation and modulation (Roesler et al., 2012). We then decided to inject AAV1-hSyn-grpLight2.0 in CA1, and access if we could use grpLight2.0 to monitor transients of GRP release during fear conditioning (Figure 5.2E). The behavior paradigm consists of three days of recordings; day1: five trials of cue plus ten trials of cue shock pairs, day2: fifteen trials of cue shock pairs, and day3: five trials of cue shock pairs followed by ten trials of cue only. During cue trials, we observed slight increase of cue related signals during cue but not very robust (Figure 5.2F). However, during cue shock pair trials across three days, we were able to see substantial increase of grpLight2.0 signals during cue, followed by a shock motion artifact, grpLight2.0 signals retains at similar level and drop down to baseline sharply (Figure 5.2G). We didn't observe as strong signals during extinction on day3, but a slight increase and fluctuation after the "shock" times potentially indicates GRP might encodes fear memory (Figure 5.2H).

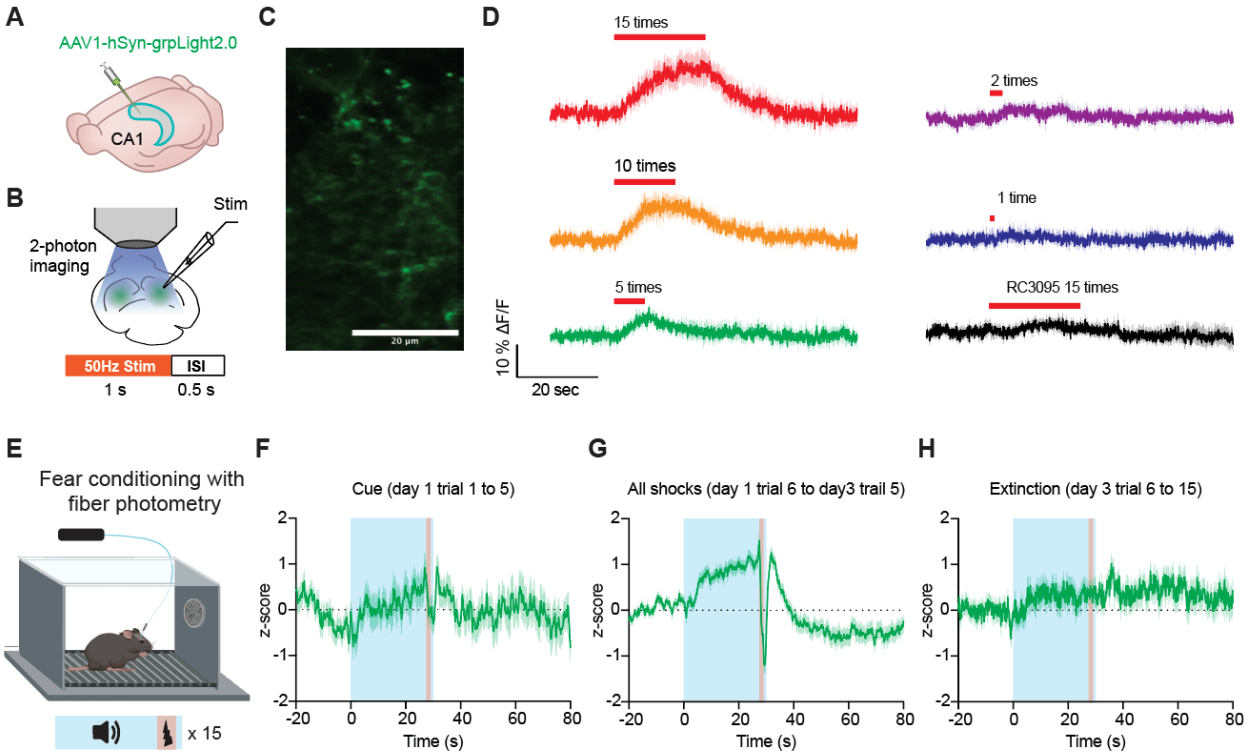

Figure 5.2 ex vivo and in vivo characterizations of grpLight2.0.
A. Schematic plot indicating viral injectionof hSyn-grpLight2.0 into CA1 in hippocampus.
B. Schematic plot showing two-photon imaging of grpLight2.0 expressing acute slices with electrical stimulation (top), and stimulation paradigm of 1 train of stimulation: 50Hz for 1 second (s) with inter stimulation interval (ISI) of 0.5 s (bottom).
C. Representative image showing the membrane localization of grpLight2.0 in CA1 under two-photon microscope. Scale bar 20 μm.
D. Averaged grpLight2.0 traces under numbers of stimulation in a dose-dependent manner (ranging from repeating the stimulation paradigm 1 time to 15 times, plus 15 times stimulation with bath application of 100 μM RC3095). Solid line indicates mean, and shades indicates SEM.
E. Schematics showing in vivo fear conditioning behavior recording with fiber photometry. Yellow bar indicates sound cue for 30 seconds, and lightning symbol represent a 1.5 s mild shock co-terminated with the sound cue.
F. Average trace of grpLight2.0 during cue trials (day1: 1-5 trials). Blue indicates tone time and red indicates shock time. Green solid line is average trace, and shade represents SEM.
G. Average trace of grpLight2.0 during cue shock trials (combined with day1: 6-15 trials, day2: 1-15 trials, and day3: 1-5 trials). Blue indicates tone time and red indicates shock time. Green solid line is average trace, and shade represents SEM.
H. Average trace of grpLight2.0 during extinction trials (day3: 6-15 trials). Blue indicates tone time and red indicates shock time. Green solid line is average trace, and shade represents SEM.

Discussion

GrpLight2.0 is an advancement over its predecessor, GrpLight1.0 in sensitivity. It can detect functionally relevant levels of GRP in real time through increased sensitivity

and dynamic range as demonstrated by SNR- and dose response experiments. Furthermore, this preliminary study shows how site saturated mutations can be used to optimize specific characteristic for sensor engineering, providing researchers with more tools for in-vivo neuroscience research. GrpLight2.0 has demonstrated in the detection of electrically stimulated GRP release from acute brain slices, which grpLight1.0 wasn't capable of. It is essential to confirm the sensor can be imaged with two-photon and identify optimal electrical stimulation protocol to trigger neuropeptide release.

GrpLight2.0's potential in-vivo applications were demonstrated through successful readout of fluorescent signals of during behavior stimulations. However, to further confirm the signal is from GRP, instead of pH, motion, or stimulation artifact, a control sensor that share the same design scaffold but with binding pocket ablated will be the next immediate step. Furthermore, while this study focused exclusively on GRP detection in the hippocampus region of the brain, it would be fascinating to see if grpLight2.0 can detect GRP across other brain regions under different conditions. Similar as psychLight and opioid sensos, potentially screen GRP receptor drug actions is also encouraged as next step to provide receptor level insights, i.e in inflammatory diseases (Petronilho et al., 2013).

Theoretic Considerations to Choose and Optimize GENIs

There are intrinsic limitations of every individual GENI. GPCR-based sensors have similar ligand affinity to endogenous receptors, which may reduce effective dynamic range and interfere with endogenous signaling pathways. PBP-based sensors, on the other hand, have large dynamic range but may have compromised sensitivity at lower concentrations of release. The appropriate combination of intrinsic parameters of a sensor, including brightness, expression, dynamic range, apparent affinity, and kinetics, must be matched to the extrinsic properties of the system, which include the size, shape, and frequency and concentration of release. To guide the selection of the sensor that is most appropriate to applications and future improvement, especially for NM sensors, we provide a simple model based on kinetics and dynamic ranges of GRAB5-HT1.0 and iSeroSnFR that illustrates the relationship between these parameters (Figure 5.3).

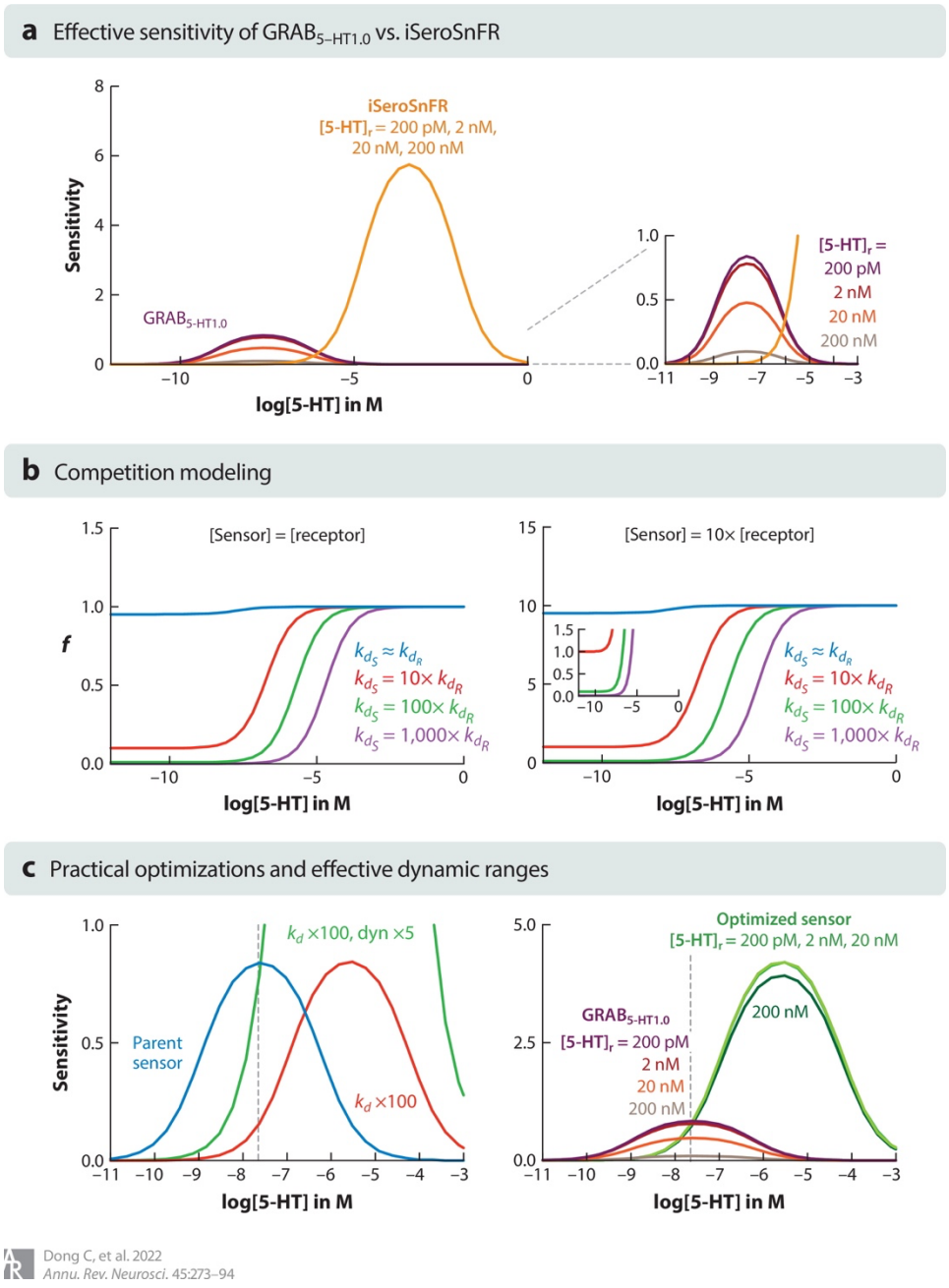

Dong C, et al. 2022
Annu. Rev. Neurosci. 45:273–94

Figure 5.3: Mathematical modeling to guide sensor optimizations.
(a) Modeling of effective sensitivity of GRAB5-HT1.0 (magenta) and iSeroSnFR (yellow) at resting serotonin concentration ([5-HT]r) of 200 pM, 2 nM, 20 nM, and 200 nM.
(b) A 100-fold (green) or greater increase in sensor kd relative to that of the native receptor minimizes ligand buffering effect when sensor and receptor expression are equal (left) and when sensor expression is 10 times higher than receptor expression (right).
(c, left) A practical optimization for GRAB5-HT1.0 to maintain or enhance sensitivity while minimizing competition is to increase both the kd and the maximum dynamic range of the parent sensor (blue). According to the model, this can be achieved with a 100-fold increase in kd and a 5-fold increase in maximum dynamic range (green). (Right) The optimized sensor is more tolerant to changes in [5-HT]r compared to the parent GRAB5-HT1.0, while maintaining similar sensitivity at the ligand concentration where the parent GRAB5-HT1.0 sensor has the peak sensitivity.

We define the dissociation and association rates of receptor or sensor and yield k_d as a rate constant at half of the maximum dynamic range:

$$k_{d_R} = \frac{[Ligand] \bullet [Receptor]}{[Ligand \cdot Receptor]} = \frac{k_{off_R}}{k_{on_R}} . 1.$$

$$k_{d_S} = \frac{[Ligand] \bullet [Sensor]}{[Ligand \cdot Sensor]} = \frac{k_{off_S}}{k_{on_S}} . 2.$$

When k_d of the sensor is similar to the endogenous receptor, we need to factor in the competition of ligand binding. We thus define *f* as the ratio of the fractional occupancy of sensor and native receptor with respect to ligand concentration, in which fractional occupancy (Θ) is defined as the fraction of receptors in a bound state (Motulsky & Neubig 2010):

$$f = \frac{\Theta_{[Ligand \cdot Sensor]}}{\Theta_{[Ligand \cdot Receptor]}} = \frac{[Sensor] \bullet (k_{d_R} + [Ligand])}{[Receptor] \bullet (k_{d_S} + [Ligand])} . 3.$$

We next define $\frac{\Delta F}{F}$ as the sensor's fluorescence change relative to its baseline fluorescence based on ligand binding, where *F* is fluorescence intensity. According to the specific binding equation, we can obtain a function of $\frac{\Delta F}{F}$ with respect to ligand concentration:

$$\frac{\Delta F}{F}_{([Ligand])} = \frac{F_{([Ligand])} - F_{([L]_0)}}{F_{([L]_0)}} = \frac{\left(\frac{\Delta F}{F}\right)_{max} \bullet [Ligand]}{k_{d_S} + [Ligand]} . 4.$$

We assume both PBP-based sensors and GPCR-based sensors have a Hill coefficient of one. $F_{([Ligand])}$is a function of fluorescence intensity with respect to ligand concentration. $F_{([L]_0)}$ is a constant calculated from the function $F_{([Ligand])}$ when ligand concentration is zero. $\left(\frac{\Delta F}{F}\right)_{max}$ is the maximum dynamic range of the sensor at its

saturation ligand concentration.

This leads to the definition of the sensitivity of the sensor as the first derivative of function $\frac{\Delta F}{F}_{([Ligand])}$:

$$\frac{\partial \frac{\Delta F}{F}_{([Ligand])}}{\partial [Ligand]} = \frac{\left(\frac{\Delta F}{F}\right)_{max} \bullet k_{d_S}}{(k_{d_S} + [Ligand])^2} \quad . 5.$$

When the resting ligand concentration is above zero, the effective sensitivity is affected. We finally define the effective sensitivity as

$$\frac{\partial \frac{\Delta F}{F}_{([Ligand])}}{\partial [Ligand]}' = \frac{\left(\frac{\Delta F}{F}\right)_{([Ligand])}' \bullet k_{d_S}}{(k_{d_S} + [Ligand])^2} \quad , 6.$$

where

$$\left(\frac{\Delta F}{F}\right)_{([Ligand])}' = \frac{F_{([Ligand])} - F_{([L]_r)}}{F_{([L]_r)}} = \frac{\left\{\left(\frac{\Delta F}{F}\right)_{max} - \frac{\left(\frac{\Delta F}{F}\right)_{max} \bullet [L]_r}{k_{d_S} + [L]_r}\right\} \bullet [Ligand]}{k_{d_S} + [Ligand]}$$

and $[L]_r$ is resting NM release concentration.

GRAB5-HT1.0 showed much higher sensitivity at a range of 1 nM to 1 μM compared to iSeroSnFR, while the sensitivity started to decrease when the release concentration was beyond 10 nM (Figure 5.3a). However, the effective sensitivity of GRAB5-HT1.0 significantly decreases with the increase of extracellular ligand concentration at equilibrium, whereas the effective sensitivity of iSeroSnFR remains unchanged (Figure 5.3a). Therefore, it is concerning that GRAB5-HT1.0 may have compromised sensitivity when the extracellular serotonin concentration is higher at resting state. In contrast, iSeroSnFR would theoretically be less affected by resting

concentration. Both serotonin sensors have shown capabilities of recording in vivo (Unger et al. 2020, Wan et al. 2021); iSeroSnFR may not fully utilize its dynamic range at nanomolar release range, whereas GRAB5-HT1.0 could potentially encounter saturation. In other words, the intrinsic properties of both sensors can be further optimized.

As the dissociation rate of GRAB5-HT1.0 is similar to the endogenous 5-HT2 receptor (kd of 5-HT2R = 20 nM) (Kelly & Sharif 2006), the potential competition with the endogenous receptor can be predominant, especially for long-term expression. Based on the model, if a sensor's dissociation rate can be increased about 100-fold higher than the endogenous receptor, the competition at the physiological range of release is minimal, which will significantly reduce the potential buffering effect (see the left side of Figure 5.3b). However, by simply increasing the dissociation rate, the sensitivity of the sensor will be reduced (see the left side of Figure 5.3c). To compensate for the loss of sensitivity, we also need to increase the dynamic range. Therefore, to maximize the effective sensitivity with minimal buffering, a practical optimization goal for GRAB5-HT1.0 is to increase the kd by 100-fold while increasing the dynamic range by fivefold as predicted by the model (see the right side of Figure 5.3c). On the other hand, to optimize iSeroSnFR, the model is predicted to decrease its kd by 100-fold while maintaining the dynamic range. Theoretically, if the dynamic range of iSeroSnFR can be further increased by fivefold, the sensitivity would be able to detect the release between 100 nM and 1 mM without compromised effective sensitivity or buffering effect. However, this ideal sensor may be practically difficult to engineer.

The other important factor affecting the SNR of imaging is the expression level of the sensor. We assume that the arbitrary sensor concentration is 10 times higher than that of native receptors to achieve sufficient SNR. Thus, the fraction will upshift and be more favorable to sensors than to endogenous receptors. However, a 100-fold-higher kd is still able to minimize the competition even when the sensor expression level is 10 times higher than that of the endogenous receptors (see the right side of Figure 5.3b). By increasing the maximum dynamic range and basal fluorescence, we can boost effective sensitivity at the lower release concentration. This modelling did not account for diffusion rate, distance of diffusion, ligand removal from transporter or enzyme, and assuming equilibrium is reached when binding. Together, our model suggests that an ideal sensor for a ligand of interest should have high dynamic range combined with a relatively higher dissociation rate compared to endogenous ligand-binding receptors. To practically achieve these end points, we have proposed a few strategies outlined in the workflow above. While optimizing both sensitivity and dynamic range can be guided by rational design, high-throughput screening of variants properties is needed, which can be a potential roadblock during the course of sensor optimization, especially for membrane-bound sensors. An optimal tool development pipeline requires both theoretical and experimental methods to engineer a sensor with great sensitivity and fast kinetics, while minimizing buffering effects.

Limitations of GENIs

We have pushed the spatiotemporal limitation of NM dynamics in a more precise way with GENIs, and unveiled many biological questions that are unachivable before.

However, there are many limitations still retains in many aspects. PsychLight, for example, although psychLight can predict hallucinogenic potential, the mechanisms underlying the effects of 5-HT2AR ligands at molecular, cellular, and circuit levels are still opaque. A critical step to understanding the molecular mechanisms of 5-HT2AR ligands will be to obtain and compare structures of psychLight bound to hallucinogenic and non-hallucinogenic ligands. Future work will need to rely on a combination of tools (e.g., imaging, electrophysiology, and behavior) to better understand the molecular and circuit-level mechanisms that give rise to hallucinogenic and antidepressant effects. Second, although psychLight provides direct examination of the conformational changes induced by biased 5-HT2AR ligands, the relationships between psychLight signals and other assays measuring downstream signaling have not been established. A detailed understanding of these relationships will be essential to reveal the mechanistic actions of biased ligands. Finally, a full pharmacological profile of AAZ-A-154 should be obtained and include information on mechanism of action, off-target effects, pharmacokinetics, full dose-response studies, potential toxicity, and efficacy validated using other established assays.

Conclusion and Outlook

The development of genetically encoded sensors has opened doors in neuroscience research that were previously untenable, particularly in the context of understanding neural circuit bases of complex, naturalistic behavior. By reducing restrictions on animal model and experimental design, these sensors allow for the broadening of circuits- and systems-level neuroscience to encompass a larger array of questions and permit unprecedented exploration of neurobehavioral systems in real-time.

To date, there are a vast amount of NT/NMs lacking precise detection tools, including neuropeptides and lipid transmitters. By taking advantage of naturally designed GPCRs, a similar strategy to GRAB sensor and Light sensor development pipeline can be generalized to cover more neurochemicals, which will greatly facilitate studies revealing their emergent roles under physiological and pathological conditions. In addition, the intrinsic properties of existing sensors demand further iterative optimization to be broadly applied to all microscopy techniques. The model we reported here provides theoretical guidance for future optimization. To achieve these goals, precise rational design aided by computational approach is expected for broad use, including machine leaning, as applied in iSeroSnFR (Unger et al 2020) or the recently developed AlphaFold 2.0 for protein structure prediction with unprecedented accuracy (Jumper et al 2021, Tunyasuvunakool et al 2021). A high-throughput screening system is crucial to maximize sensor optimization efficiency, since GPCR-based sensors can currently only be screened in mammalian cells. Fluorescence-activating cell sorting (FACS) combined with image-based screening or the well-known CRISPR/Cas9 system that has been applied in evolution of fluorescent proteins and voltage sensors (Erdogan

et al 2020, Lee et al 2020, Piatkevich et al 2018) hold great promise for screening of NT/NM sensors.

Extending the sensitivity, specificity, and color palette of neuromodulator sensors will continue to create rich opportunities for minimally invasive, multiplex imaging of neurochemical signaling dynamics. Together with advanced microscopy, opsin-based optogenetics and cell atlas, fluorescent imaging with next generation genetically encoded indicators will bring our experimental capabilities to previously impossible level, thus uncovering brain mechanisms, and potentially transform our understanding of how neurochemical inputs influence cell and circuit function in health and disease.

Reference

Erdogan M, Fabritius A, Basquin J, Griesbeck O. 2020. Targeted in situ protein diversification and intra-organelle validation in mammalian cells. *Cell Chem. Biol.* 27:610–21.e5

Jumper J, Evans R, Pritzel A, Green T, Figurnov M, et al. 2021. Highly accurate protein structure prediction with AlphaFold. *Nature* 596:583–89

Kelly CR, Sharif NA. 2006. Pharmacological evidence for a functional serotonin-2B receptor in a human uterine smooth muscle cell line. *J. Pharmacol. Exp. Ther.* 317:1254–61

Lee J, Liu Z, Suzuki PH, Ahrens JF, Lai S, et al. 2020. Versatile phenotype-activated cell sorting. *Sci. Adv.* 6:eabb7438

Melzer S, Newmark ER, Mizuno GO, Hyun M, Philson AC, Quiroli E, Righetti B, Gregory MR, Huang KW, Levasseur J, Tian L, Sabatini BL. Bombesin-like peptide recruits disinhibitory cortical circuits and enhances fear memories. *Cell*. 2021 Oct 28;184(22):5622-5634.e25

Nakagawa T, Hocart SJ, Schumann M, Tapia JA, Mantey SA, Coy DH, Tokita K, Katsuno T, Jensen RT. Identification of key amino acids in the gastrin-releasing peptide receptor (GRPR) responsible for high affinity binding of gastrin-releasing peptide (GRP). Biochem Pharmacol. 2005 Feb 15;69(4):579-93.

Petronilho F, Danielski LG, Roesler R, Schwartsmann G, Dal-Pizzol F. Gastrin-releasing peptide as a molecular target for inflammatory diseases: an update. Inflamm Allergy Drug Targets. 2013 Jun;12(3):172-7.

Piatkevich KD, Jung EE, Straub C, Linghu C, Park D, et al. 2018. A robotic multidimensional directed evolution approach applied to fluorescent voltage reporters. *Nat. Chem. Biol.* 14:352–60

Roesler R, Schwartsmann G. Gastrin-releasing peptide receptors in the central nervous system: role in brain function and as a drug target. Front Endocrinol (Lausanne). 2012 Dec 17;3:159.

Tunyasuvunakool K, Adler J, Wu Z, Green T, Zielinski M, et al. 2021. Highly accurate protein structure prediction for the human proteome. *Nature* 596:590–96

Unger EK, Keller JP, Altermatt M, Liang R, Matsui A, et al. 2020. Directed evolution of a selective and sensitive serotonin sensor via machine learning. *Cell* 183:1986–2002.e26

Villette V, Chavarha M, Dimov IK, Bradley J, Pradhan L, et al. 2019. Ultrafast two-photon imaging of a high-gain voltage indicator in awake behaving mice. *Cell* 179:1590–608.e23

Wan J, Peng W, Li X, Qian T, Song K, et al. 2021. A genetically encoded sensor for measuring serotonin dynamics. *Nat. Neurosci.* 24:746–52

Copyright Information

I. I am the first author on the following articles:

1. Fluorescence Imaging of Neural Activity, Neurochemical Dynamics, and Drug-Specific Receptor Conformation with Genetically Encoded Sensors, published in Annual Review of Neuroscience (Related to chapter 1 and Chapter 5).
2. Psychedelic-inspired drug discovery using an engineered biosensor, published in Cell (Related to chapter 2.1).
3. Unlocking opioid neuropeptide dynamics with genetically-encoded biosensors, pending revision in Nature Neuroscience (Related to chapter 4).

As the first author of these articles, I retain the right to include them in a thesis or dissertation, provided it is not published commercially.

II. I am an author on:

4. Directed evolution of a selective and sensitive serotonin sensor via machine learning, published in Cell (Related to chapter 3).

As per Elsevier journal author rights, as the author of this article, I retain the right to include it in a thesis or dissertation, provided it is not published commercially. Permission is not required.

III. I am an author on:

5. Psychedelics promote neuroplasticity through the activation of intracellular 5-HT2A receptors, published in Science (Related to chapter 2.2).

As per the Science journal's reprints and permissions guidelines, I have included the copyright information for article 5 on the following page.

THE AMERICAN ASSOCIATION FOR THE ADVANCEMENT OF SCIENCE LICENSE
TERMS AND CONDITIONS

May 02, 2023

This Agreement between University of California, Davis -- Chunyang Dong ("You") and The American Association for the Advancement of Science ("The American Association for the Advancement of Science") consists of your license details and the terms and conditions provided by The American Association for the Advancement of Science and Copyright Clearance Center.

License Number	5541101057610
License date	May 02, 2023
Licensed Content Publisher	The American Association for the Advancement of Science
Licensed Content Publication	Science
Licensed Content Title	Psychedelics promote neuroplasticity through the activation of intracellular 5-HT2A receptors
Licensed Content Author	Maxemiliano V. Vargas, Lee E. Dunlap, Chunyang Dong, Samuel J. Carter, et al.
Licensed Content Date	Feb 16, 2023
Licensed Content Volume	379
Licensed Content Issue	6633
Volume number	379
Issue number	6633
Type of Use	Thesis / Dissertation
Requestor type	Author of the AAAS published paper
Format	Print and electronic
Portion	Full Text
Title	Developing Genetically Encoded Optical Tools for Imaging Brain Circuits and Pharmacology
Institution name	University of California, Davis
Expected presentation date	Jun 2024
Requestor Location	University of California, Davis 4435 Tupper Hall One shield ave. DAVIS, CA 95616 United States Attn: University of California, Davis
Total	0.00 USD